$Ni_{0.05}Mo_3Sb_{5.4}Te_{1.6}$ Based Thermoelectric Nanocomposites

by

Nagaraj Nandihalli

A thesis

presented to the University of Waterloo

in fulfillment of the

thesis requirement for the degree of

Doctor of Philosophy

in

Chemistry (Nanotechnology)

Waterloo, Ontario, Canada, 2016

AUTHOR'S DECLARATION

I hereby declare that I am the sole author of this thesis. This is a true copy of the thesis, including any required final revisions, as accepted by my examiners.

I understand that my thesis may be made electronically available to the public.

Abstract

Thermoelectric (TE) materials have the capability to convert thermal energy into useful electrical energy. Sustainable energy production and its utilization are among the many challenges that humankind is facing today. In 2016 and 2017, the expected global production of hydrocarbon based automotive vehicles is expected to be 97.8 and 101.8 million respectively, and is expected to rise. The collective thermal energy losses from radiators and exhausts from these automotive vehicles are enormous. This is a big bottleneck in sustainable energy production and utilization. In mitigating this hurdle, TE materials will play a very important role. However, TE materials have low efficiency in thermal to electrical energy conversion owing to the reciprocal relation between the thermal and the electrical transport properties. Recent advances in nanotechnology tools have given a new dimension to decouple this relation. Back in 2003, our group reported a very promising TE material, $Ni_yMo_3Sb_{5.4}Te_{1.6}$ ($y < 0.1$). Improving the *figure-of-merit* of $Ni_{0.05}Mo_3Sb_{5.4}Te_{1.6}$ ("bulk") material through nanocomposite synthesis is one of the goals of my research. The main outcome of nanocomposite synthesis is the reduced thermal conductivity through arresting the coherent propagation of heat carrying acoustic waves in TE materials. To this end, I synthesized and characterized the transport properties of various nanocomposites. I have used fullerenes, oxides, carbides, and metal particles to fabricate nanocomposites.[1]

Chapter 3 addresses the effect of multi-wall carbon nanotubes (MWCNT) when added to $Ni_{0.05}Mo_3Sb_{5.4}Te_{1.6}$. We characterized these samples for their TE properties, and addressed the effect of porosity on transport properties. The effect of ball-milling on MWCNT was studied. Scanning and transmission electron microscopy were used to study the microstructural and nanostructural features of the samples. In a sample with 3 mass-% of MWCNT, the main contributing factor in elevating the *figure-of-merit* by 25% was the reduction in the thermal conductivity by 40%.

[1] Throughout our discussion, the notation for our composites is written as bulk/NM (or $Ni_{0.05}Mo_3Sb_{5.4}Te_{1.6}$/NP), where, NP stands for nanoparticles of a certain material.

In Chapter 4, we reported the results of $Ni_{0.05}Mo_3Sb_{5.4}Te_{1.6}$/SiC and $Ni_{0.05}Mo_3Sb_{5.4}Te_{1.6}/Al_2O_3$ composites consolidated through hot-pressing and spark-plasma sintering respectively. Samples with different volume fractions of SiC were prepared and characterized. Thermoelectric transport properties of these composites were characterized from 325 K to 740 K. For the sample with 0.01volume fraction of SiC, there was an enhancement in the *figure-of-merit* by an 18% compared to the reference sample, mainly due to an 18% reduction in the thermal conductivity. Microstructural information obtained through SEM, TEM, and BET was used to elucidate phase and transport properties. Spark-plasma sintered bulk sample has exhibited the highest *figure-of-merit*, which is 35% higher than the bulk consolidated through hot-pressing. Pore effect on thermal conductivity and electrical conductivity were investigated.

In Chapter 5, we covered various properties of bulk/NiSb composite. In this study, requisite amounts of bulk $Ni_{0.05}Mo_3Sb_{5.4}Te_{1.6}$ thermoelectric (TE) material and NiSb nanoparticles of ~60 nm were synthesized through solid-state reactions and solvothermal routes, respectively. NiSb nanoparticles were then manually mixed with $Ni_{0.05}Mo_3Sb_{5.4}Te_{1.6}$ in volume fractions of 0, 0.034, 0.074, and 0.16. All samples were consolidated by hot-pressing, and then their TE properties were characterized. The addition of NiSb nanoparticles elevated both the electrical conductivity and the thermal conductivity, but reduced the Seebeck coefficient. TEM images show highly electrically and thermally conductive NiSb nanoparticles settled within interstitial voids between bulk particles, thus, forming bridges between the balk particles. These networks of NiSb particles facilitate the electrical and thermal conductivity. Variation in lattice thermal conductivity from 330 K to 755 K for all samples shows that phonons are undergoing the same scattering mechanism. By adopting Callaway formalism for the lattice thermal conductivity, we made attempts to delineate the contribution of various scattering mechanism to the enhanced lattice thermal conductivity in bulk/NiSb composites. We concluded that electron-phonon scattering, which is the main factor for the increased lattice thermal conductivity in $Mo_3Sb_{7-x}Te_x$ ($0.0 < x \leq 1.8$) series was not the reason in our case, but rather that an overlap in the DOS of phonons of bulk and NiSb particles, was primarily responsible for the high phonon-phonon transfer efficiency from bulk

to NiSb particles and vice versa. We also speculated that there was a reduction in the umklapp process. Contribution from boundaries and interfaces was less in scattering phonons. Increase in hardness with respect to NiSb content provided an indication of increased Debye temperature of composites. Irrespective of extensive interfaces created by NiSb nanoparticles, there was no reduction in the thermal conductivity. Contrary to this, electrical conductivity of the bulk, 0.034, and 0.074 samples showed the same temperature dependence, whereas the 0.16 sample did not, revealing that the charge carrier scattering for the 0.16 sample was different from the rest. The existence of the electrical percolation phenomena was analyzed in detail and compared with other composites. SEM images of composites show that NiSb nanoparticles distributed homogeneously in 0.16 composite. HRTEM images of 0.16 composite shows crystalline nature of bulk and NiSb particles; we also used this information to interpret the enhanced lattice thermal conductivity. Furthermore, larger NiSb particles of 100 μm – 1000 μm size were synthesized through solid-state reaction and consolidated by hot-pressing. Their TE properties were characterized as well, in order to use these parameters to interpret the transport properties of the nanocomposites. Finally, there was a systematic improvement in the hardness of the composites with increasing NiSb content.

In Chapter 6, we extensively investigated the effective thermal properties and thermal boundary resistance of $Ni_{0.05}Mo_3Sb_{5.4}Te_{1.6}$/SiC and $Ni_{0.05}Mo_3Sb_{5.4}Te_{1.6}/Al_2O_3$ composites at 325K. Different effective media approximations (EMA) models were utilized to predict thermal boundary resistance (Kapitza resistance). The salient feature of this study is the comparison of these two composites based on their microstructure. This study shows that it is important to give credence to microstructures while addressing the effective thermal properties. Bounds for the effective thermal conductivity were determined using the Lipton–Vernescu model. The effect of SiC and Al_2O_3 nanoparticles on mechanical properties were analyzed and interpreted. Thermal properties in relation to mechanical properties were discussed.

In Chapter 7, we engineered the grain boundaries of bulk particles through a process called nanocoating. NiSb nanoparticles of 60 nm – 80 nm were coated on the bulk particles

through the solvothermal process. The actual process of solvothermal coating did not affect the bulk material. Layers of 300 nm – 500 nm NiSb nanoparticles were observed on the bulk sample with the 0.16 vol% NiSb nanoparticles.

In Chapter 8, we covered the effect of addition of C_{60} on the TE properties of bulk material. C_{60} was added in 1, 2, and, 3 mass%, respectively. Each part was hot-pressed at 150 MPa and 923 K. The sample with 1% C_{60} was characterized via a Rietveld refinement and TEM analysis. Measurements of the three thermoelectric key properties revealed that the Seebeck coefficient barely depends on the carbon amount added, while both the electrical and the thermal conductivity decrease with increasing amount of carbon. Depending on the amount of C_{60} used and on the temperature, the thermoelectric performance was either enhanced or decreased, depending on whether the electrical conductivity decreased less or more than the thermal conductivity. At the highest temperature measured, all carbon-containing samples performed better than the unmodified bulk sample, namely up to 14%. These improvements are within the error margin, however.

Acknowledgements

It was an immense pleasure to pursue my Doctor of Philosophy under the tutelage of Professor Holger Kleinke, who guided me very patiently in every research endeavor. His unparalleled expertise in the field of thermoelectrics has taken my career to a new level. I appreciated his offers for me to visit and work in foreign laboratories.

I would like to thank my committee members, including Professors Pavle Radovanovic, Dmitriy Soldatov, and Eric Prouzet, for their guidance and advice. My hearty thanks go to Dr. Jalil Assoud, crystallographer for his valuable help. I would like to thank Katja Kleinke, who helped me with various experimental techniques. The help of my senior group members, Dr. Michailo Guch, Dr. Savithree Bangarigadu-Sanasy, Susan Jeung, and Dr. Brian Kuropatwa, was greatly appreciated. My junior group members (Quansheng, Yixuan, Wenbin, Cheryl, Xiaoyu, Rafay, Mohamed, Mathew, Nader, and Parisa), all co-operated in ways that were very helpful. Over the years in my research, I have also interacted with researchers from various groups at the University of Waterloo; I truly appreciate all their assistance. In addition, I will not forget the continuing help of Dr. Howard Siu and Dr. Guerman Popov.

I would like to acknowledge the time and excellent feedback of Professor Mar on my thesis. Finally, the minute analysis of my thesis by Professor Bo Cui was truly invaluable.

Table of Contents

List of Figures

List of Tables

List of Abbreviations

BET	Brunauer-Emmett-Teller
BJH	Barrett-Joyner-Halenda
BPR	Balls to Powder Ratio
CNT	Carbon Nanotube
CR	Charge Ratio
CVD	Chemical-Vapor Deposition
DFT	Density Functional Theory
DOE	Department of Energy, US
DOS	Density of States
EDXS	Energy Dispersive X-Ray Spectroscopy
EMA	Effective Media Approximations
EMT	Effective Media Theory
ETC	Electronic-Thermal-Control
FEA	Finite Element Analysis
FWHM	Full width at Half Maximum
GB	Grain Boundaries
HP	Hot-press
HRTEM	High resolution Transmission Electron Microscopy
ICDD	International Center for Diffraction Data
ICE	Internal Combustion engines
ICSD	Inorganic Crystal Structure Database
INS	Inelastic Neutron Scattering
IUPAC	International Union of Pure and Applied Chemistry
IXS	Inelastic X-ray Scattering
LAST	lead, antimony, silver and tellurium
L–V	Lipton–Vernescu
MBE	Molecular-Beam-Epitaxy
MFP	Mean Free Path

MG-EMA	Maxwell Garnett Effective Media Approximation
MPa	Mega Pascal
MWCNT	Multi-Wall Carbon Nanotube
PCA	Process Control Agents
PIPS	Precision Ion Polishing System
PXRD	Powder X-Ray Diffraction
RTG	Radio Isotope Thermal Generator
SEI	Secondary Electron Image
SEM	Scanning Electron Microscopy
SPS	Spark-Plasma Sintering
TE	Thermoelectric
TEM	Transmission Electron Microscopy
TZM	Titanium Zirconium Molybdenum
VHN	Vickers Hardness Number
YSZ	yttria-stabilized zirconia

Chapter 1

Introduction

1.1 Motivation and Challenges

Energy is one of the key inputs to all global economic processes. Meticulous exploration, innovation, and implementation of renewable, energy efficient and sustainable technologies to fulfill our myriads of energy needs are challenging and in part difficult to realize. Greenhouse emission and volatile energy security, which were nonexistent on the radar of scientific research communities a decade ago, but now debated widely, have compelled humankind to come up with energy efficient green technologies. However, considering the enormity of the challenges, research communities should not confine their research endeavors to substitute fossil fuels with solar, wind power technology or hydrogen based technologies, but should also address improving the efficiency of internal combustion engines (ICE).

Most of the electrical energy produced in our society is lost in the form of heat during power generation and transportation. Therefore, only 35% of electricity produced reaches our homes. Despite enormous efforts to improve the economic and environmental performance of automotive fossil fuel engines, 55% of the energy from the internal combustion goes to waste.[1, 2] Energy losses from a typical urban vehicle from different processes are shown in Figure 1.1.

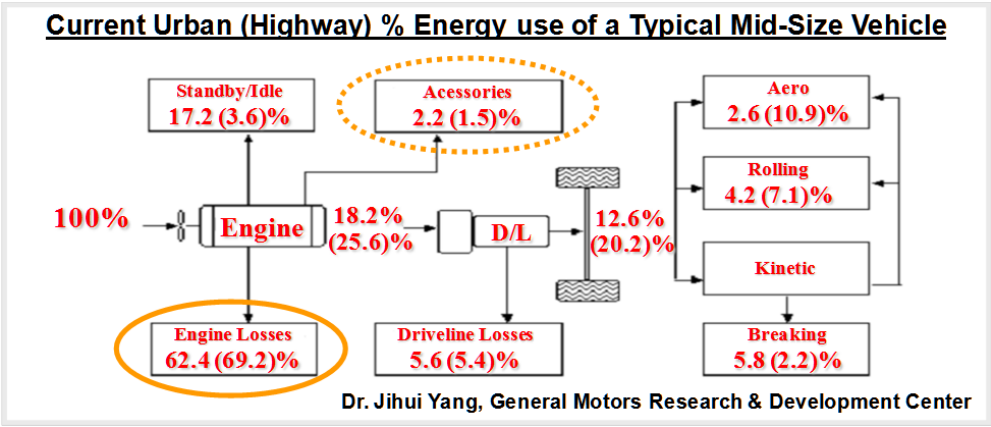

Figure 1.1: Energy losses from a typical urban automotive ICE engine.

Energy harnessing materials such as Thermoelectric (TE) materials have the ability to convert thermal energy into an electrical energy, when a certain temperature difference is established between two ends of these materials.

It is at this juncture that TE materials can contribute significantly to sustainable energy, taking into account their unique advantages: reliability, easy miniaturization, no moving parts, little maintenance, longlife, high-precision temperature control, and ability to function in a extreme environment. A key representative of these features is a TE Radioisotope Thermal Generator (RTG); a radio isotope material was used to develop a temperature difference in the TE device on board NASA's spacecraft Voyager, which was destined to travel beyond Mars and launched in 1977. Due to the TE device's longevity, the spacecraft is still sending data to earth and expected to do so until 2020.[3]

TE technology can be implemented in the field of new generation of vehicles. If we are able to scavenge waste heat from automotive radiators and exhaust gas and convert them into useful energy using TE devices, then we can use as produced energy to improve the vehicle kinetics; the economics of energy consumption could be improved – an improvement that can make a big difference in terms of overall natural gas consumption worldwide. Similarly, enormous heat generated in industrial plants and petrochemical refineries can be converted into useful energy.

1.2 Major Governing Phenomena in Thermoelectrics

There are two major governing phenomena in thermoelectrics: the Peltier effect and the Seebeck effect. A thermoelectric device operates in two modes: Peltier mode (refrigeration) and Seebeck mode (power generation). Refrigeration (to develop a temperature difference) is achieved when a DC current passes through one or more pairs of n-type and p-type semiconductor materials that are connected electrically in series and thermally in parallel with a temperature gradient. The temperature, T_C, of the interconnecting conductor decreases and heat is absorbed from the environment (Figure 1.2(a)). The absorption from the environment (cooling side) occurs when electrons pass from low energy levels in the p-type semiconductor through the

interconnecting highly conducting plate (usually copper) to higher energy levels in the n-type material. The absorbed heat carried by electrons is transferred through the semiconductor, to the other end of the junction (T_H), as the electrons return to lower energy levels in p-type material. This phenomenon is called Peltier effect. The Peltier effect is largely due to the difference in Fermi energies of the two materials.

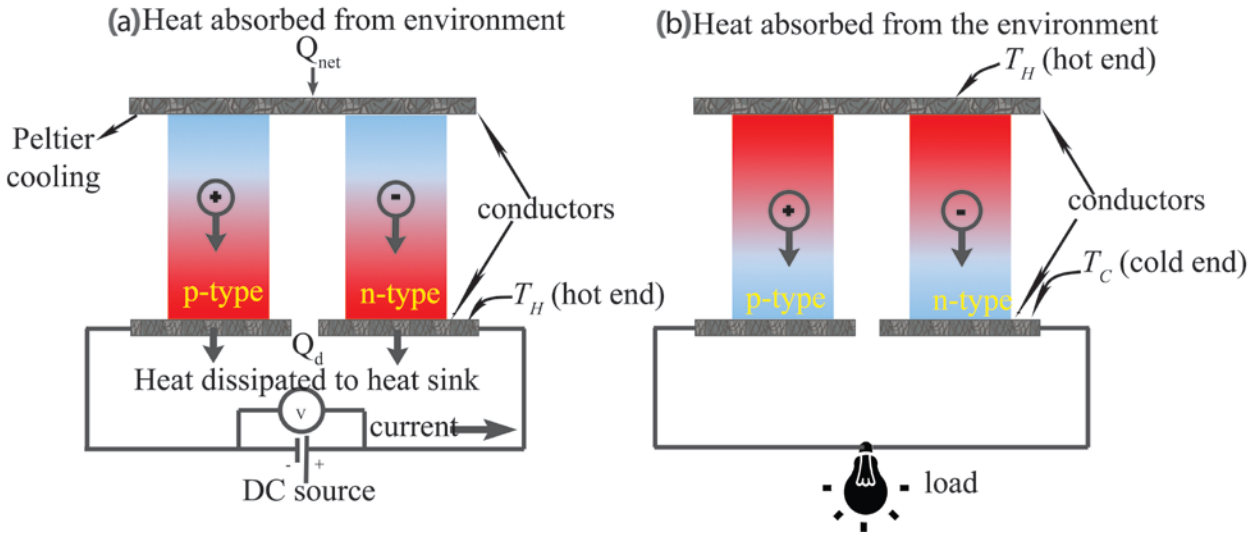

Figure 1.2: TE device in operation. (a) Refrigeration mode; (b) Power generation mode.

When a temperature difference is established between the hot and cold ends of p-type and n-type semiconductors, a voltage will be developed. Under the temperature difference, charge carriers (electrons or holes) at the hot side have more thermal energy than the carriers at the cold side of the materials; they start to diffuse to the cold side, causing accumulation of charge carriers at the cold end leading to the formation of an electric field, which opposes the further diffusion of charge carriers. In an open circuit mode, equilibrium will be established when the rate at which carriers move from the hot side to the cold side due to diffusion is balanced by the rate which carriers move from the cold side to the hot side due to established electric field. The voltage developed is called Seebeck voltage, and the amount of voltage developed per unit temperature gradient is called the Seebeck coefficient. When the TE device is connected to an external load, due to electrochemical potential, charge carriers will keep moving around supplying energy to external load as long as a certain temperature difference is maintained

between hot side and cold side. This mode of operation is called power generation mode. In Figure 1.2(a), if we reverse the polarity of applied power supply, the temperature starts to build at the top surface, thus TE devices can find applications in central heating and cooling applications in a common household.

In Peltier mode, the amount of heat absorbed at the cold end and the heat dissipated at the hot end are dependent on the product of current flowing through the semiconductor and the Peltier coefficient, which is defined as the product of Seebeck coefficient of the material and the absolute temperature.[4] The amount of heat absorbed at the cooling side is limited by two sources: conducted heat from the hot end to the cold due to temperature difference and Joule heating which is proportional to the square of the current and eventually becomes a dominant factor. At any supplied current, equilibrium will be established at the cold end when the Peltier effect at the cooling side is equal to the sum of conducted heat and ½ of Joule heat. The other half of Joule heating goes to the hot side. As the current is further increased, Joule heating becomes a dominant factor and a point is reached at which additional current results in less cooling.

To achieve the maximum power output, several TE devices needs to be cascaded as shown in Figure 1.3.

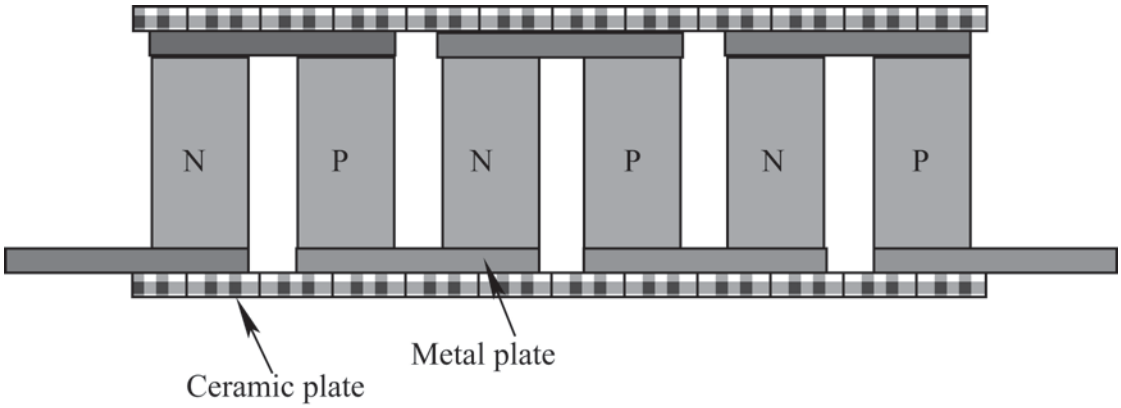

Figure 1.3: Cascaded TE device assembly. Combination of each n-type and p-type legs is called thermoelement.

Although the TE phenomenon was observed in the 1850s, TE devices were not developed until the discovery of semiconductors.[5] The performance of a thermoelectric material is dictated by what is called its *figure-of-merit*, a dimensionless quantity, $ZT = S^2\sigma\kappa^{-1}T$, where S is the Seebeck coefficient, σ is the electrical conductivity, κ is the thermal conductivity and, T is the operational temperature.

TE materials can also be used to tap solar energy.[6, 7] In high speed electronics, TE devices (when used in Peltier mode) have been employed in cooling high speed processors where the heat flux due to Joule heating can exceed hundreds of Watts cm^{-3}.[8] To keep the processors functioning reliably, it is very important to extract the dissipated heat. In such cases, electronic-thermal-control (ETC) systems [9-11] can be used to cool components that have temperatures above the ambient temperature. One such module is shown in Figure 1.4.

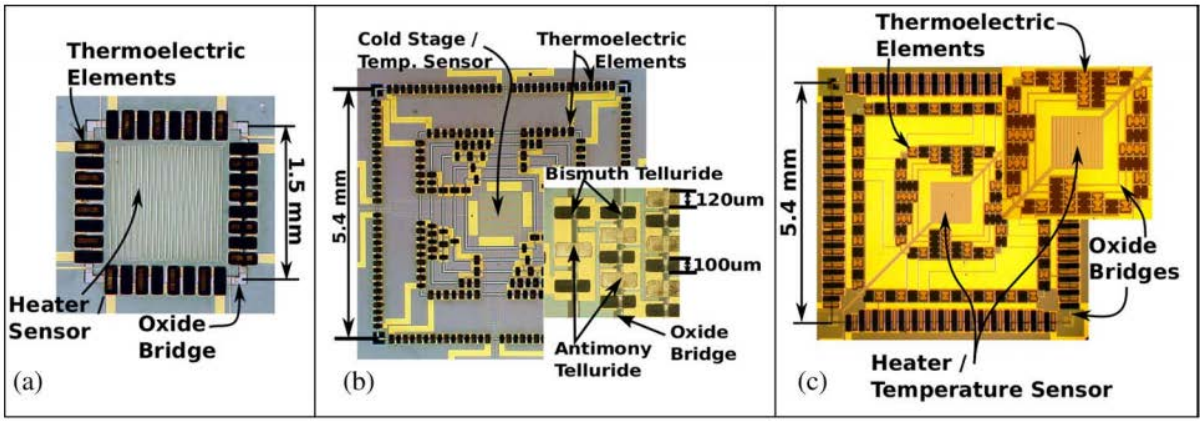

Figure 1.4: Thermoelectric micro-cooler for high speed processors.[2][10]

TE device applications are versatile. They find applications in cryogenics, [12] fluid flow sensors, [13] and thermal sensors.[14] Major applications are displayed in Figure 1.5.

---

[2] Reprinted, with permission, from [A. J. Gross, G. S. Hwang, B. Huang, H. Yang, N. Ghafouri, H. Kim, R. L. Peterson, C. Uher, M. Kaviany and K. Najafi, Multistage Planar Thermoelectric Microcoolers , IEEE, 2011]

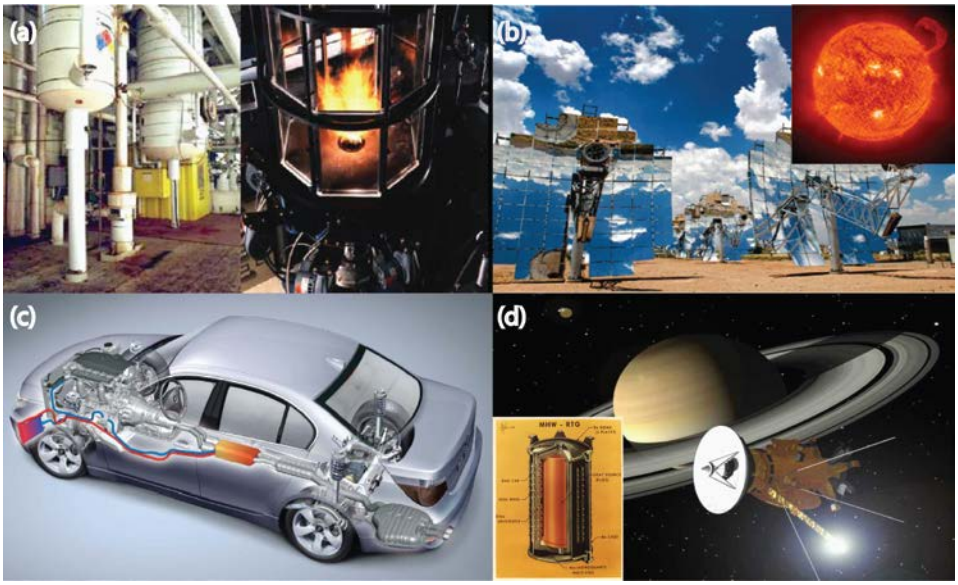

Figure 1.5: TE applications. (a) Industrial waste heat recovery (DOE); (b) Solar thermoelectric generation [3][14]; (c) Automotive waste heat recovery (BMW); (d) Deep space exploration (RTG).

1.3 Conversion Efficiency of a TE Material

The working principle of thermoelectric module is similar to that of a heat engine, where instead of heat, electrons and/or holes are being utilized as the energy carriers. The efficiency of thermoelectric material is governed by the Carnot efficiency, η, and material *figure-of-merit*, *ZT*, according to the following relation:

$$\eta = \frac{W}{Q_H} = \frac{T_H - T_C}{T_H} \cdot \frac{\sqrt{1+ZT} - 1}{\sqrt{1+ZT} + T_C / T_H} \qquad \textbf{Equation 1.1}$$

where W is the electrical power output and Q_H is the thermal power supplied. T_H and T_C are the average temperature of hot side and cold side, respectively.[7] For all heat engines, the upper limit of power generation efficiency is the Carnot efficiency, $[(T_H - T_C)/T_H]$. The device would approach the Carnot efficiency if *ZT* could reach infinity. Therefore, maintaining a large

[3] Reprinted (adapted) with permission from M. Xie and D. M. Gruen, J. Phys. Chem. B 114 (45), 14339-14342 (2010)). Copyright (2010) American Chemical Society.

temperature gradient and improving *ZT* are both effective means to increase the power generation efficiency. Shown in the Figure 1.6 are the conversion efficiency of state-of-the-art materials at different temperatures, with cold side = 300 K. Most state-of-the-art nanocomposites have a conversion efficiency, η, ranging from 8% – 16%.[15-18]

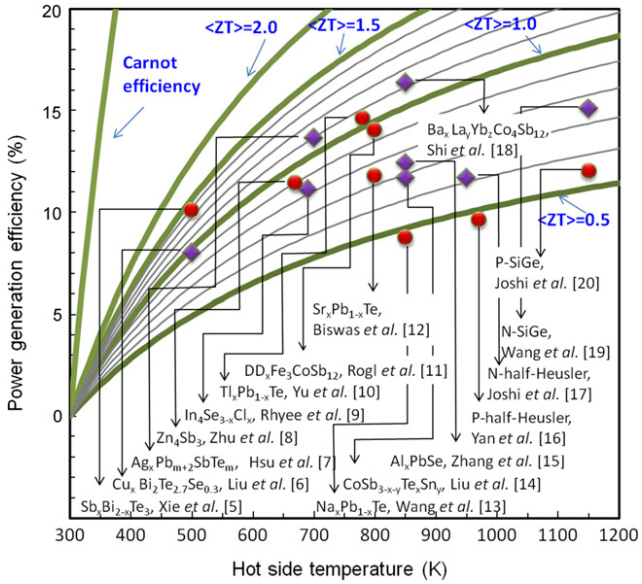

Figure 1.6: Comparison of conversion efficiency state-of-art materials[4].[19]

1.4 Thermoelectric Transport Parameters

1.4.1 Thermal Conductivity

Heat conduction is a transport phenomenon, in which a conserved quantity such as momentum, energy, mass, or charge is transferred as a result of a nonequilibrium situation in a system. The nonequilibrium situation is manifested by some kind of concentration gradient that causes the quantity to be transported in the direction of lower concentration area. For heat conduction we can define the thermal conductivity using the relation:

$$Q = \kappa A \, dT / dX \qquad \textbf{Equation 1.2}$$

[4] Reprinted from Nanoenergy, Elsevier, Vol. 1, Weishu Liu,Xiao Yan,Gang Chen,Zhifeng Ren, Recent advances in thermoelectric nanocomposites, 42-56, Copyright (2012), with permission from Elsevier

where Q is the energy current density or energy flux, A is the cross sectional area, and κ is the thermal conductivity (W $m^{-1}K^{-1}$). The thermal energy is the quantity transported as a result of the temperature gradient dT over dX (T = temperature, X = distance).

κ is related to Joule heating due to charge carriers and heat carrying acoustic phonons. κ consists of two major parts: κ_l, the lattice or phonon contribution and κ_e, the contribution from heat carrying charge carriers. κ_e is related to σ according to the Wiedemann–Franz law: $\kappa_e = L_0 \sigma T$, where L_0 is the Lorenz number, which is within a range of 1.6×10^{-8} V^2K^2 to 2.2×10^{-8} V^2K^2 for most thermoelectric materials. Though this relation is referred to as a law, the fact that Lorenz number is strictly not a constant, thus caution needs to be exercised against using it for rigorous quantitative analysis. However, it is a useful approximation for estimating the contribution of charge carriers to the total thermal conductivity. Thus, we can write the total thermal conductivity, $\kappa = \kappa_e + \kappa_l$.

Most of the comprehensive research in TE nanocomposites is to reduce κ_l, to enhance ZT. The lattice thermal conductivity based on the Boltzmann equation under relaxation time approximation is given by:

$$\kappa_l = 1/3 C_v l v \qquad \textbf{Equation 1.3}$$

where C_v is the specific heat, v is the phonons' group velocity, and l is the phonon free path. C_v can be determined experimentally, and v is the velocity of sound in a respective solid, which has to be determined by anharmonic collisions. We can heuristically assume that the mean free path of a phonon is inversely proportional to the number of phonons, i.e. phonon density, and therefore:

$$l \, \alpha \, \frac{1}{N_{phonons}} \text{ and we can write: } \kappa \, \alpha \, \frac{C_v \, v}{N_{phonons}}$$

At very low temperatures (< 40 K), κ_l is dictated by the Debye T^3 law for specific heat. At these temperatures, phonon scattering is insignificant because of the low number of excited

phonons, and also because of their long wavelength. At higher temperatures, that is, above Debye temperatures, C_v approaches the classical value of 3R, where R is the ideal gas constant. Thus, κ_l is primarily dependent on the phonon wavelength, which is determined by phonon scattering. Then phonons follow: $\kappa_l \approx 1/T$.[20] In the intermediate temperature regimes, a combined grain boundary scattering and point defect scattering is present.

Thus, one strategy to lower lattice thermal conductivity is to generate more phonons so that inter-phonon scattering dominates, reducing the lattice thermal conductivity. The variation of different scattering processes at different temperatures is shown in Figure 1.7.

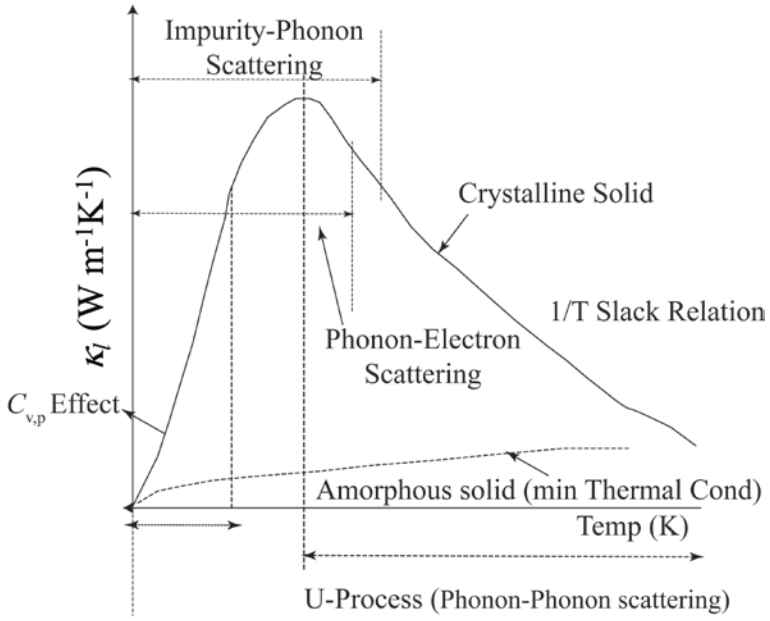

Figure 1.7: Variation of phonon thermal conductivity with respect to temperature in regimes of dominant scattering mechanisms.

1.4.1.1 Phonon Scattering Mechanisms

Phonon-Phonon Scattering

One pertinent question arises, namely, what kind of thermal conductivity is manifested in ideal crystals without any defects? In such structures, assuming that any phonon is considered a defect and atoms are disturbed from their ideal position, the likelihood that one phonon may collide with another phonon exists. However, in many ideal insulating crystals such as diamonds, sapphires etc., the rate of phonon scattering with another phonon is very small, and therefore, these crystals have very high thermal conductivity. Assuming the spring constant between atoms is ideal, there will be no phonon scattering. In practical situations, even with a small deviation from ideal behavior, one phonon may disturb many surrounding phonons, and the phonon-phonon scattering rate increases with increasing temperature simply because more phonons are present.

Point Defect and Alloy Scattering

A point defect means that one of the atoms making up the crystal is different from the rest (substitutional defect), or an atom is absent (vacancy defect), an atom is displaced (Frenkel defect) or defect is extended, forming a lamellar structure. A typical point defect is illustrated in Figure 1.8. In general, any type of defect scatters phonons, but in thermoelectric materials, the point defect is usually an atom with a mass very different from that of an atom of the host material, and these defects are introduced deliberately to lower the lattice part of the thermal conductivity; when this difference in mass is large, the scattering is called alloy scattering.[21] The presence of many defects facilitates more and more phonon scattering.

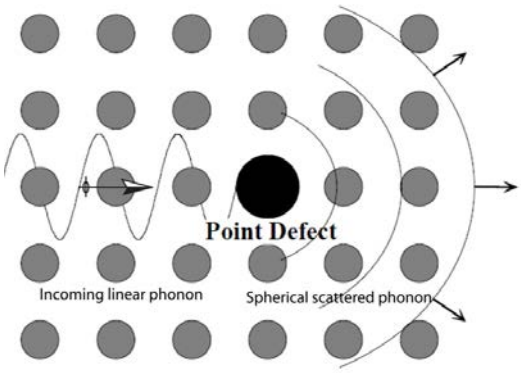

Figure 1.8: Point defect scattering.[5]

Different types of defects in a crystal are shown in the Figure 1.10

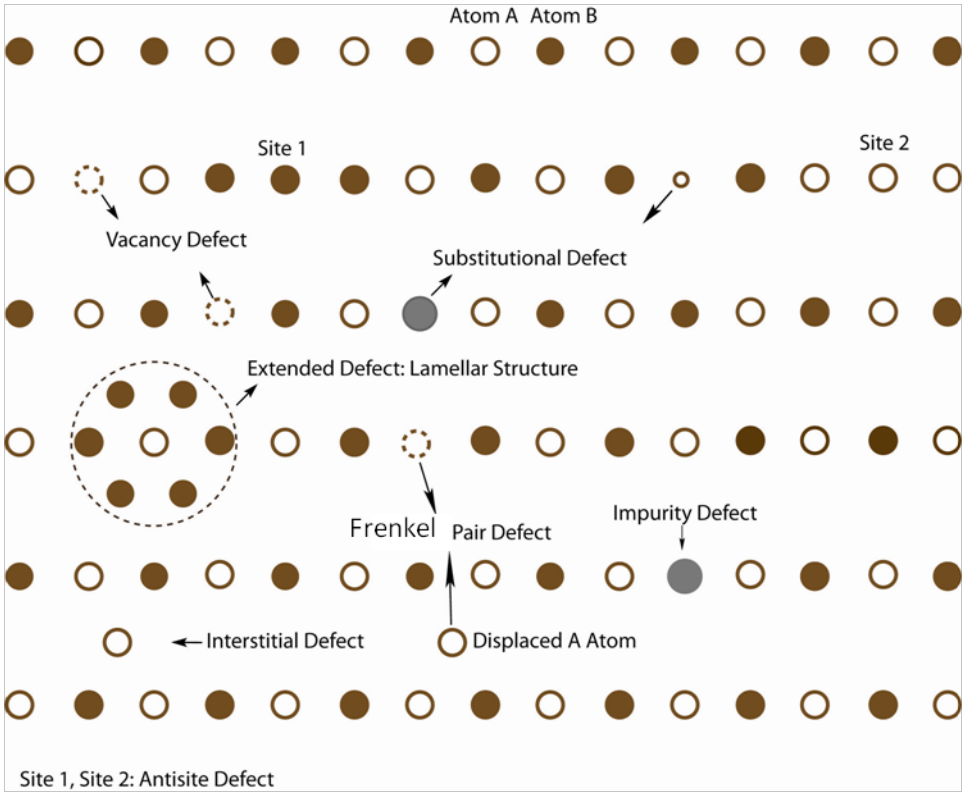

Figure 1.9: Different types of defects in crystal structures.

[5] Original Figure is modified, C.B. Vining, "Short course on thermoelectrics", Int'l TE soc. SCT-93, Japan

Phonon-Electron (or Hole) Scattering

When the crystal is doped with the aim of optimizing its charge carrier concentration, two mechanisms will increase the scattering of phonons. First, any type of defects such as donors, acceptors, vacancies, and interstitials, etc., will scatter phonons. However, a larger effect is the scattering of phonons by the charge carriers.[22] It is possible to substantiate this scattering mechanism with the following simple argument. We take the positions of atoms in the crystal in order to calculate the allowed energy levels of charge carriers. We assume that atoms are strictly confined to their respective lattice points (that is no phonons exist), and electronic band structures are calculated. However, a caveat exists here. Even if we generate only one single phonon, the entire band structure is modified. This small shift in electronic energy levels due to deformation in the lattice is called deformation potential and establishes a link between the system of phonons and charge carriers. Through this interaction, a phonon may impart its energy and momentum to one of the charge carriers, or a charge carrier can lose energy and momentum, creating a phonon. In both cases, a phonon and a charge carrier undergo scattering.

In general, low energy (long wavelength) phonons can interact with all the charge carriers. Above a certain phonon energy, there are no charge carriers to interact with. Thus, phonon-electrons (holes) interaction is dominant when phonons have long wavelengths.

Grain Boundary Scattering and Microstructure

Grain boundaries, pores, inclusions, and precipitates are essentially geometrical obstacles to phonons. In thermoelectrics, one strategy to lower the lattice part of thermal conductivity is to generate more interfaces per unit volume by either ball-milling or including nanoparticles. This increased interface per unit volume promotes more grain boundary scattering of phonons that leads to reduction in lattice thermal conductivity.[23-26] It is important to note that the sample walls themselves also scatter phonons. At a low temperature regime, interactions between phonons become small and the mean free path of phonon can become as large as the sample itself.

In TE composites, the comprehensive research to reduce lattice thermal conductivity is based on classical size effects, where physically and chemically stable particles of a certain size, shape, volume fraction, and thermal conductivity are incorporated into a bulk matrix, whose thermal conductivity is targeted to be reduced. When the size of the particle becomes small, its surface to volume ratio increases, and this size adds a new variable in controlling the thermal properties because the particle size becomes comparable to the phonon wavelength. The increased surface area facilitates diffusive phonon scattering at the grain boundaries and thus destroys the coherent propagation of phonons.[26-28]

1.4.1.2 Estimation of Lattice Thermal Conductivity Contribution to Total thermal Conductivity

We calculated the lattice thermal conductivity for all of our samples using the Wiedemann-Franz law, $\kappa_e = L_0 \sigma T$ (L_0 = Lorenz number) and subtracting it from the total thermal conductivity according to $\kappa = \kappa_e + \kappa_l$. Thus, κ_e may increase as the temperature rises, depending on the slope of σ, and κ_l decreases with increasing temperature because of increasing lattice vibrations, which leads to increased inter-phonon scattering. L_0 was calculated at various temperatures assuming our samples would follow the single parabolic model and mixed scattering mechanisms (i.e. alloy scattering and acoustic phonon scattering) and thus we used the scattering parameter $\lambda = 0$ [29, 30]. As estimated L_0 values at various temperature are included in the Supplementary Information of the respective composite chapters.

1.4.1.3 Effective Properties and Effective Media Approximation (EMA)

In composite synthesis, optimizing the nanoparticle's volume fraction, their shape, size (aspect ratio), their thermal properties, and most importantly their spatial distribution inside the bulk matrix is very challenging.[31] Since the time of Maxwell, literature is rife with models to predict thermal conductivity of composites.[32-35] These models are based on effective media theory or approximations (EMT or EMA), where the prevailing approach is to estimate the reduction in thermal conductivity due to the presence of guest particles inside the bulk matrix and to calculate the thermal boundary resistance.[36] These models follow classical Fourier heat conduction, but when the mean free path of phonons becomes comparable to the particle size,

these models deviate from experimental values as the interplay between the phonon wavelengths and their scattering cross-section becomes complex.[37] A Monte-Carlo simulation of Si–Ge composites (Si nanoparticles being randomly distributed in Ge host) yielded a dependence on nanoparticles of different sizes (which translates into interface per unit volume) on thermal conductivity that matched well the experimental results.[28] Similarly, SiC particles of varying sizes from 0.7 μm – 28 μm were reinforced into aluminum matrix, and the thermal conductivity of the composite was found to be decreasing with decreasing particle size.[38]

The thermal boundary resistance, R_{Bd}, is defined in terms of the heat flux, $\mathring{U}$, and temperature discontinuity, ΔT, across the interface by the equation: $\mathring{U} = \Delta T / R_{Bd}$. At the junction of embedded nanoparticle and the bulk particle, there exists a resistance to the heat flow and this resistance arises due to a discontinuity in temperature. This discontinuity in temperature in turn arises because of the difference in their physical properties such as sound velocity (what some authors call acoustic mismatch), differences in their electrical properties, differences in bulk densities, and chemical adherence at the interface. In 1941, Kapitza measured thermal boundary resistance on metal-liquid helium interfaces, [39] now commonly called Kapitza thermal boundary resistance (commonly called Kapitza resistance), and his analysis is the basis for theoretical predictions of R_{Bd}. As many experiments show, Kapitza resistance is a deterministic factor to predict how much we can lower or raise the thermal conductivity of a composite depending on the application.[38] In various references, interfacial thermal resistance and thermal boundary resistance are used interchangeably. Obtained parameters using EMTs are only approximates and heuristically important.

Every et al. applied their Bruggeman's asymmetric model (abbreviated as B–EMA in subsequent paragraphs) to study a ZnS/diamond composite with a large volume fraction of micron and sub-micron sized diamond particles to predict the effective thermal conductivity with respect to volume fraction of diamond particles.[33, 40] Similarly Nan et al., based on multiple scattering theory, formulated a model to predict the effective thermal conductivity of composites with arbitrarily arranged nanoparticles inside bulk materials. In this model, the effect of size, shape, volume fraction on the effective thermal conductivity of ZnS/diamond,

cordierite/diamond, and SiC reinforced Al matrix Al/ SiC was studied and compared with the experimental results.[35] Studying the effective properties can give us some design guidelines on how much we can reduce the thermal conductivity, which is a very important parameter in improving TE properties.

The notations for different parameters are as follows: κ_{bulk}, κ_{comp} ($\kappa_{eff,}$ effective thermal conductivity in some literature) κ_p, and f are the thermal conductivities of bulk, composites, embedded nanoparticles, and the volume fraction of embedded nanoparticles respectively.

All aforementioned models use a dimensionless quantity, $\alpha = (a_k / a)$, [40, 41],where a is the nanoparticle radius, a_k is the Kapitza radius, which in turn is related to the thermal boundary resistance, R_{Bd}, via the relation: $a_k = R_{Bd}\ \kappa_{bulk}$, and can take any values between 0 and ∞. When $a_k = 0$, the interface is perfect and gives zero thermal resistance. When α is large, R_{Bd} dominates and when α is small, R_{Bd} is negligible. The Kapitza radius can be related to the mean free path of phonons λ divided by the probability, η_p, of phonon transmission at the interface via $a_k = \lambda / \eta$. Simply put, a_k is the equivalent thickness of a region of the matrix having thermal resistance equal to R_{Bd}. Whenever $a >> a_k$ (small α), the particle is large enough that the thermal boundary resistance is small. Conversely, when $a << a_k$ (large α), R_{Bd} dominates. The transition region from one region to the other occurs in the neighborhood of $a = a_k$ ($\alpha = 1$). The Kapitza radius and its relation to the radius of embedded particle provide design guidelines to tune the thermal conductivity properties by mixing two different constituents. Since porosity can affect both the electrical and thermal properties, we have studied properties, with pores and pore corrected thermal properties.

We utilized Maxwell's EMA formula to find effective thermal property and this is given by: $\kappa_{comp} = \kappa_{bulk}\ [1– (3/2)\ f]$, where f, is the volume fraction of pores.[32] Such EMA was applied in the case of dense and porous yttria-stabilized zirconia (YSZ) ceramics.[42]

In B-EMA, $\kappa_p > \kappa_{bulk}$, and we used the following relation to calculate effective property[40]:

$$\frac{\kappa_{comp}}{\kappa_{bulk}} = \frac{1}{[1-f]^{3\frac{(1-\alpha)}{(1+\alpha)}}}$$ **Equation 1.4**

And for Nan et al.'s MG-EMA, for flat plates and strictly spheres respectively[35]:

$$\frac{\kappa_{comp}}{\kappa_{bulk}} = \frac{\kappa_p}{[\kappa_p - f(\kappa_p - \kappa_{bulk} - \alpha\kappa_p)]}$$ **Equation 1.5**

$$\frac{\kappa_{comp}}{\kappa_{bulk}} = \frac{\kappa_p\,(1+2\alpha) + 2\kappa_{bulk} + 2f\,[\kappa_p\,(1-\alpha) - \kappa_{bulk}\,]}{\kappa_p\,(1+2\alpha) + 2\kappa_{bulk} - f\,[\kappa_p\,(1-\alpha) - \kappa_{bulk}\,]}$$ **Equation 1.6**

The reciprocal of thermal barrier resistance is called thermal barrier conductance (h), which is being routinely used in literature depending on the prediction approach researchers follow to explain heat transfer.[43-45] As previously mentioned, a thermal boundary resistance exists at the junction of embedded nanoparticle and the bulk particle due to differences in physical and chemical properties of constituents. However, stress may develop at the junction owing to differences in thermal expansion coefficients of both nanoparticle and bulk particle, that can also change the thermal boundary resistance. As discussed by Bhatt et al.,[46] total interfacial thermal conductance, h, can be treated in series: $h = h_g + h_e + h_r = \kappa_{comp}/w$, where h_g, h_e, and h_r respectively are contributions due to: gaseous heat transfer, heat transfer through point of contact and radiative heat transfer; w is the thickness of the nanoinclusion (some authors treat these in parallel: $1/h = 1/h_g + 1/h_e + 1/h_r$.[47]). Thus, interfacial thermal conductance is limited by the nanoparticle's thickness as $w \rightarrow 0$, leaving κ_{comp}/w, finite. In most cases, the radiation component is very small at room temperature compared to the others, and in our case we neglect this component.

In a situation where there is a lack of detailed information on microstructures and isotropy of the composite, it is very appropriate to determine rigorous upper and lower bounds on effective properties of the material,[48] and these bounds should be as tight as possible. To find the bounds, the Lipton–Vernescu (abbreviated as L–V in subsequent discussion) model for

imperfect interfaces is very appropriate. This model predicts upper and lower bounds on effective thermal conductivity, provided volume fraction, *f*, of embedded particle and thermal conductivity of embedded and bulk matrix particles are known. It also predicts limits on interfacial barrier conductivity by taking into consideration the thermal conductivity of bulk matrix, embedded particles, their volume fractions and the radius of the embedded particles.[44, 45] Similarly, Rintoul et al.'s bounds for composites is very useful.[49] Imperfect interface is ascribed to the presence of discontinuous temperature field between two or multiple interfaces; the quantum jump in temperature is proportional to the heat flux across the interfaces. Both composites, bulk/SiC and bulk/Al_2O_3 in this article are assumed to have imperfect interfaces.

1.4.1.4 Percolation in Random Nanoparticle Composites

When particles of high thermal conductivity or electrical conductivity such as NiSb are randomly dispersed in a bulk matrix of relatively low electrical and thermal conductivity, clusters of particles form a percolation network.[50, 51] When the volumetric concentration of high conductivity crosses a certain limit called the percolation threshold, clusters of these nanoparticles will be formed. This threshold is determined by the geometric characteristics of particles or wires. Such clusters facilitate thermal conductivity and/or electrical conductivity.[50] When the characteristic size of the embedded nanoparticles is either comparable to or smaller than the phonon mean free path, phonon scattering at the boundary at the interfaces between two material can introduce a considerable thermal resistance even though the embedded minor phase has very high thermal conductivity. The effective thermal conductivity of nanocomposites depends on the interfacial area per unit volume.[24, 52, 53] Just beyond the percolation threshold, the effect of interfaces on diminishing the thermal conductivity will be reduced as highly conducting particles create a low resistance pathway for phonons or energy carrying charge carriers contributing to total thermal conductivity as they connect opposite ends of the material through the clusters they form. The thermal resistance in composites can be attributed to the following types of phonon scattering: inter-phonon scattering, phonon impurities, phonon dislocations and another category is interface between constituents due to acoustic mismatch. At

the junction of particles of two constituents, phonon interface scattering can be enhanced, and then the percolation network was not effective in enhancing the phonon transport.

Grain boundaries, nanoinclusions in composites, and pores all affect the scattering rates of phonons. A great deal of efforts, both theoretically and experimentally, was undertaken to explain the effect of microstructures on thermal conductivity.[54, 55]

In the phonon-interface scattering process are two types: one is diffusive, where phonons incident at the grain boundary generate multiple phonons with longer wavelength and these diffusively scattered phonons do not possess any preferential scattering when the roughness of the interface is much larger than the phonon wavelength. On the other hand, specular scattering occurs when the interface is smooth (just like a mirror).[56, 57] When the size of embedded nanoparticle of higher thermal conductivity is larger than the mean free path of the lower thermal conductivity material, the effective thermal conductivity of the composite increases monotonically with the volumetric concentration of high thermal conductivity particles. At low concentration of particles of higher thermal conductivity, percolation network is not yet formed and the effective thermal conductivity is dominated by interface scattering. However, as the volumetric concentration of the higher thermal conductivity is increased and approaches the percolation threshold, these particles begin to form a bridge between two or multiple bulk particles. If the particle is highly conductive electrically, high energy carrying charge carriers will cross the bridge and contribute to total thermal conductivity.

1.4.2 Electrical Transport Properties and *Figure-of-Merit*

1.4.2.1 *Figure-of-merit* (*ZT*)

As discussed in Section 1.2, the performance of the TE material is dictated by its *figure-of-merit*: $ZT = S^2\sigma\kappa^{-1}T$, where S is the Seebeck coefficient, σ is the electrical conductivity, and κ is the thermal conductivity. According to the above relation, good thermoelectric materials should possess high Seebeck coefficient S to have good voltage output, moderate electrical

conductivity, and low thermal conductivity, in order to minimize heat flow through the TE device.

A classical normal way to enhance material properties is to increase the power factor, $P.F. = S^2\sigma$, by optimizing the charge carrier concentration, n, and to reduce κ_l, by introducing phonon scattering centers. However, the strong coupling between these parameters (which will be discussed in coming paragraphs) made the improvement of ZT value beyond the benchmark of $ZT = 1$ cumbersome for a long time.

1.4.2.2 Seebeck Coefficient

The Seebeck coefficient (also called thermopower in some references), S, is a measure of the magnitude of an induced potential difference, ΔV, per unit temperature difference, ΔT, along the sample, and is expressed as: $S = \Delta V/\Delta T$.

S has the unit of microvolts per Kelvin ($\mu V\ K^{-1}$). A very good thermoelectric material should possess S within 150 – 250 $\mu V\ K^{-1}$ or above.[58] Thermoelectric materials in general are semiconductors with either holes (positive S) or electrons (negative S) as the dominant carriers. Since mixed types of charge carriers tend to cancel each other, a single type of charge carrier ensures a large Seebeck coefficient. For metals or degenerate semiconductors, the Seebeck coefficient is given by the equation from Mott [59]:

$$S = 8\pi^2 k_B^2 m^*/(3eh^2)\ (\pi/3n)^{2/3} \qquad \textbf{Equation 1.7}$$

Electrical conductivity is given by: $\sigma = ne\mu$, where k_B, e, h, m^*, n, and μ are Boltzmann constant, electronic charge, Planck's constant, effective mass of charge carrier, charge carrier concentration, and carrier mobility respectively. According to the above equations, the electrical conductivity increases with increase in charge carrier concentration, while the Seebeck coefficient decreases.

In nanocomposites, one approach to enhance the Seebeck coefficient is to filter out low energy charge carriers that contribute negatively to Seebeck coefficient by introducing

nanoinclusions in bulk matrix.[60-62] We discussed the filtering effect in Section 1.7 very briefly.

1.4.2.3 Electrical Conductivity

The electrical conductivity (σ) is a measure of the amount of electrical current a material can conduct. The first attempt to explain electrical conduction in solids was done by P. K. L. Drude, who made the assumption that metals comprise a sea of electrons or an electron gas. Electrical conductivity is also defined as the ratio of the current density (J) to the electric field strength (E), i.e. $\sigma = J/A$. Since current density $J = I/A$, and electric field, $E = -\mathrm{d}V/\mathrm{d}X$, where I is the current, A is the cross section of the sample, and X is length.

The inverse of σ is electrical resistivity, ρ, and defined as: $\rho = 1/\sigma$. For a wire of cross-sectional area A, length l with resistance R, the resistivity is given by: $\rho = RA/l$. The electrical conductivity is related to the carrier concentration (n) and the carrier mobility (μ) of charge carriers via the relation, $\sigma = ne\mu = ne^2\tau/m^*$. Where τ is the mean scattering time between the collisions of the carriers and m^* is the effective mass of charge carriers.

In metals, where charge carriers are free to move in the conduction band, n is constant, thus, the variation of σ is dictated by the variation in μ. On the other hand, in semiconductors, charge carriers will be promoted to the conduction band or donor level across the band gap; thus n always varies with the temperature. Since charge carrier concentration and the Seebeck coefficient have reciprocal relations, the maximum ZT is expected for a charge carrier concentration of 10^{19} cm^{-3} – 10^{21} cm^{-3} (Figure 1.9). Therefore, in thermoelectrics, heavily doped semiconductors and narrow band gap semiconductors with aforementioned charge carrier concentration prove to be favorable candidates for thermoelectric applications. Observing the relation between S and μ, effective mass, m^*, is another conflicting factor in electrical properties. A large effective mass of the charge carrier will be useful to enhance S; however, this reduces the electrical conductivity because heavier charge carriers move slowly thus reducing mobility.

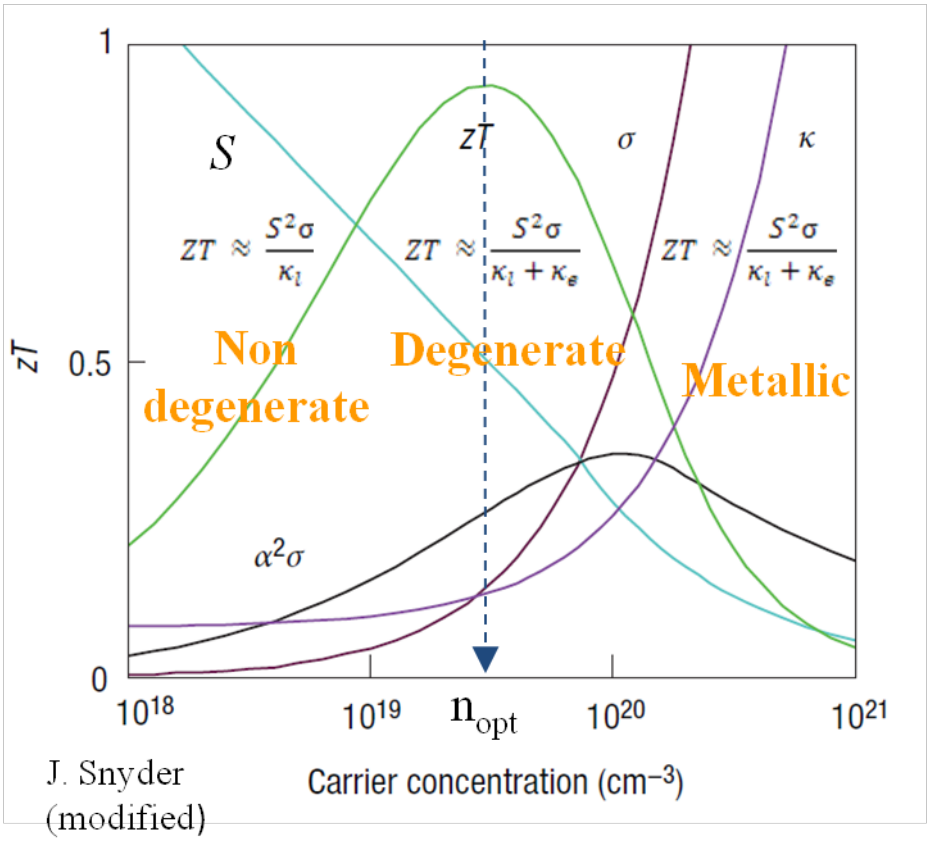

Figure 1.10: The effect of carrier concentration on the various thermoelectric properties.[6]

1.4.2.3.1 Charge Carrier Scattering Mechanisms

No Scattering

If the charge carriers are not scattered at all, they will be moving uninterrupted along the sample. In superconductors, this is the case, and Ohm's law is not applicable to superconductors.

Electron-Electron (hole-hole) Scattering

Charge carriers such as electrons or holes can interact with each other. In many simple calculations, this interaction will be ignored. This is not because the collision rate is small, but

[6] Reprinted by permission from Macmillan Publishers Ltd: Nature Publishing Group, G. J. Snyder and E. S. Toberer, Nature Mater. **7**, 105-114, Copyright 2008.

rather because this scattering mechanism has the unusual property that it does not tend to return the charge carriers system to equilibrium. In addition, when charge carriers collide with each other, momentum can be exchanged but not destroyed. Thus, even after the collision, the same amount of current exists and therefore the charge carrier collision will be ignored.[63] The Drude model disregards any long-range interaction between the electron and the ions or between the electrons.

Electron (or Hole)-Phonon Scattering

Charge carriers are also scattered by phonons. Assuming one charge carrier is being scattered by surrounding phonons, the total cross section of that collision should be added to the contribution from each phonon. A single phonon represents a displacement of a particular type and wavelength of all atoms in the crystal. However, the sum of all phonon contribution describes the average displacement of an atom due to thermal agitation. In other words, it gives the average size of an atomic wobble. This vibration of atom is an obstacle to the charge carrier movement.

In high temperature regimes, atomic agitation will increase, enhancing charge carrier scattering. For most metals and heavily doped semiconductors, resistivity increases with temperature because of charge carrier scattering (reducing mobility). We call this scattering mechanism acoustic charge carrier scattering, and it usually follows $T^{-3/2}$.[22, 64]

Charged Impurity Scattering

This is one of the most important scattering mechanisms for charge carriers due to impurities (or dopants) such as donors or acceptors, which themselves carry some charge. This is considered as a defect and since this defect possesses a charge, it can change the trajectories of passing charge carriers considerably. This kind of deflection is temperature independent.

Neutral Impurities and Alloy Scattering

Neutral impurities, such as unionized dopants or alloys of materials with the same number of outer shell electrons (for example, Ge and Si), are still considered as defects even if

they are not charged. These defects can still scatter charge carriers, reducing charge carrier mobility. This fact is one of the reasons why Cu alloyed with Ag possesses relatively higher resistivity than pure Cu or pure Ag. It has been observed that the majority of thermeoelectric materials are alloys because the lattice part of thermal conductivity can be reduced by alloy scattering. On the negative side, charge carrier mobility will also be reduced by alloying. Thus, alloying in thermoelectric materials is fruitful if the reduction in lattice thermal conductivity is far greater than the reduction in electrical conductivity due to the reduction in charge carrier mobility. The electrical transport properties in pure materials are better than alloys in general. In alloy scattering, a larger difference in atomic mass and size will generate a substantial local stress resulting in strong phonon scattering that leads to a reduction in the lattice part of thermal conductivity.

Grain Boundaries and Other Scattering

Grain boundaries and other types of crystalline defects can scatter charge carriers. A grain boundary by definition is a disruption in regular pattern of bonds in the crystal. Generally, strains in the bonds or incomplete bonds around the grain boundaries can reduce the mobility of charge carriers. It has been observed that ball-milled TE materials in general possess lower electrical conductivity than their bulk counterparts due to enhanced scattering of charge carriers by grain boundaries. Figure 1.11(a) shows the grain boundaries in one of our composites. The boundaries are very clean and do not interrupt charge carriers, but when there is an abrupt change in the periodic structure of atoms (as shown in Figure 1.11(b)), electrical conductivity will be reduced due to charge carrier scattering.

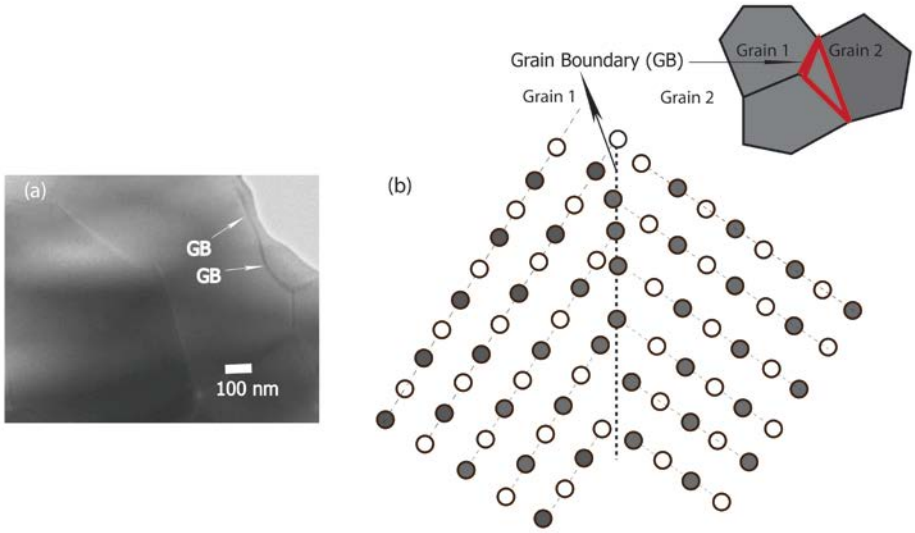

Figure 1.11: TEM images of grain boundaries of $Ni_{0.05}Mo_3Sb_{5.4}Te_{1.6}$/SiC composite.

1.4.2.3.2 Percolation in Electrical Conductivity

Readers are strongly advised to read Section 1.4.1.4 before proceeding further on percolation in electrical conductivity. According to the percolation theory, the conductivity of composites close to the percolation threshold, Φ_c, follows the scaling law given by, $\sigma_{comp} \alpha (\Phi - \Phi_c)^t$, where σ_{comp} is composite thermal conductivity, Φ is the volumetric concentration of the highly conducting material (NiSb in our bulk/NiSb case), Φ_c is the percolation threshold and t, is a conductivity exponent.[65]

Shown in the Figure 1.12 is the percolation network on an evaporated film above a percolation threshold. A section of infinite clusters and the resulting backbone that can actually conduct current is shown in Figure 1.12(a) and (b) respectively. The vast majority of clusters in the percolation network do not carry current as many of them have dead ends. Thus, only the backbone shown in Figure 1.12(b) conducts charge carriers. In bulk TE materials, using less amount of highly conductive material to generate a highly conductive backbone is very challenging.

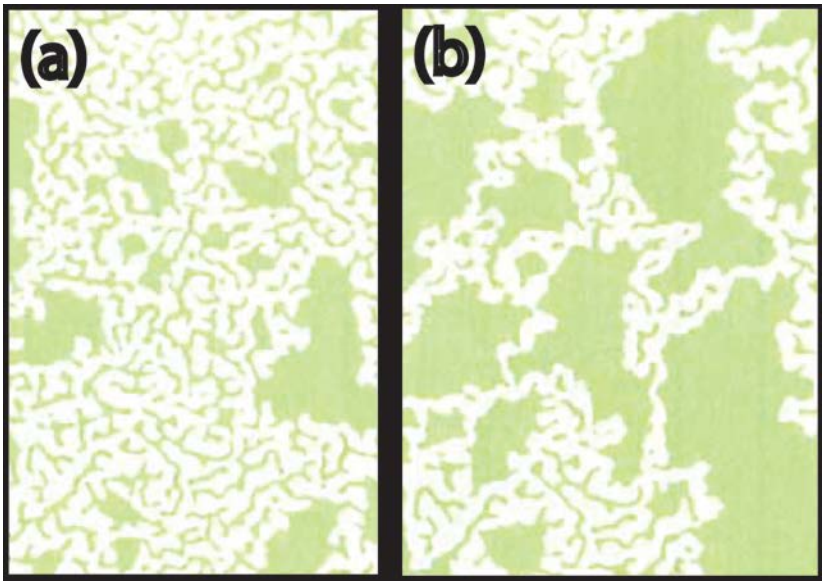

Figure 1.12: (a) Section of an infinite cluster just above percolation threshold (b) Backbones that actually conducts current.[7]

1.5 Progress in Thermoelectric Materials

Many classes of TE material systems are gaining more attention because they are endowed with good thermoelectric transport properties. These materials exhibit reasonable electrical conductivity, a relatively higher Seebeck coefficient, and moderate thermal conductivity–all giving rise to a *figure-of-merit* close to the benchmark of one or above. Over the past 20 years, many strategies to improve the transport properties of these materials have been developed and implemented, including nanostructured bulk materials. My work in the past 4 years was to improve the TE properties of existing thermoelectric materials.

1.5.1 Bismuth Telluride Based Thermoelectric Materials

Bi_2Te_3 based TE materials have been well studied materials since 1960 and have occupied a niche in TE refrigeration oriented applications in the market. The bulk Bi_2Te_3 has

[7] With permission from John Wiley and Sons and Copyright Clearance Center, D.S. McLachlan, M. Blaszkiewicz, R.E. Newnham, *J. Am. Ceram. Soc.* 73 (1990) 2187-2203. (Original figure is modified)

proven to possess *ZT* = 1. Nanocomposites synthesized by high energy ball-milling combined with DC-current assisted hot-pressing, [66] melt spinning, and spark-plasma sintering thereafter, [67] raised the *ZT* value of p-type $Bi_xSb_{2-x}Te_3$ up to 1.4 to 1.5 in comparison to their bulk counterpart with *ZT* =1. The main reason for the enhancement in *ZT* was the reduction in thermal conductivity from nanoinclusions of various sizes and the grain boundaries they generated. Ko et al.[68] have claimed enhanced Seebeck coefficient from 115.6 to 151.6 $\mu V\ K^{-1}$, when the bulk matrix Bi_2Te_3 was embedded with Pt nanoparticles. The increased Seebeck coefficient was due to the filtering effect. Studying the TE properties of both n-type and p-type Bi_2Te_3 dispersed with nanosize SiC particles has revealed that, in p-type material, *P.F*. was slightly increased, while in n-type, it was decreased. In Chapter 4, we compared the TE properties of these materials with our bulk dispersed with SiC nanoparticles.

ZT ~1.25 @420 K has been observed in micron sized/polycrystalline Bi_2Te_3 nanocomposite compared to bulk Bi_2Te_3.[69] Nanometer sized Bi_2Te_3 particles were embedded in micron sized Bi_2Te_3 power and the mixture was consolidated by hot-pressing. The reason for the improvement in the *ZT* was a slight increase in electrical conductivity and a reduction in thermal conductivity.

1.5.2 Nanostructured Silicon Germanium Bulk Alloys

Encouraged by the astounding reliability of the SiGe Radio Isotope Thermal Generator (RTG) for 16 years on board Voyager interplanetary missions, the research on SiGe TE alloys took a new turn in 1980s and is still attracting attention even today. SiGe alloys can operate up to a maximum temperature of 1275 K. Recently devised RTGs for interplanetary missions had a peak value of *ZT* ~0.5. The best reported p-type SiGe had the peak *figure-of-merit* close to 0.65.[70] Joshi et al. have shown that ball-milled SiGe powder (p-type) consolidated through the direct-current-induced hot-press compaction process showed improvement in *ZT* from 0.65 to 0.95 at 1073 K – 1173 K. The main factor behind this enhancement was the reduction in the thermal conductivity.[71] The improvement in *ZT* was 90% compared to RTGs, there was a 50% improvement over the results reported by Vining et al.[70]

Mechanically alloyed SiGe (n-type) and consolidated through DC hot-press showed a peak *ZT* of about 1.3 at 1073 K. Here again as in p-type SiGe alloy, the reason for the improvement in *ZT* was the reduction in thermal conductivity from 4.6 W $m^{-1}K^{-1}$ to 2.5 W $m^{-1}K^{-1}$.[72]

1.5.3 Lead Telluride Based Thermoelectric Materials

For several decades, researchers have used the *figure-of-merit* of pure PbTe systems with no nanostructuered features as a benchmark to evaluate the performance of nanostructured materials. The maximum reported *figure-of-merit* of PbTe is anywhere from 0.8 to 1 at 650 K. PbTe based TE devices are useful in 600 K–800 K range for various applications. PbTe belongs to the category of heavy element compound semiconductors, similar to Bi_2Te_3.

1.5.3.1 $AgPb_mSbTe_{m+2}$ (LAST-m)

The combination of $AgSbTe_2$ and PbTe results in the $AgPb_mSbTe_{m+2}$ family of materials. The thermoelectric properties of $AgPb_mSbTe_{m+2}$ (LAST-*m*; LAST stands for lead, antimony, silver and tellurium), were reported in 2004. $AgPb_{18}SbTe_{20}$ displayed a *figure-of-merit*, *ZT*, of ~2.2 at 800 K, and $AgPb_{10}SbTe_{12}$ reached ZT_{max} of 1.2 at 700 K.[16] Another approach to synthesize LAST type of materials is through mechanical alloying and spark-plasma sintering (SPS). Using this nanocomposite fabrication approach, very good TE transport properties were obtained.[73] Polycrystalline $Ag_{0.8}Pb_{18+x}SbTe_{20}$, formed by mechanical alloying of elemental starting materials and consolidated through spark-plasma sintering gave a *ZT* value of 1.5 at 673 K.[74] The average size of polycrystalline nanocomposite was ~1 μm, including 20 nm size precipitates and had a relative density of 95%. The 20 nm precipitates were found to play a role in reducing the lattice thermal conductivity. The lattice thermal conductivity of this family of compounds was found to be ranging from 2.1 W $m^{-1}K^{-1}$ at 300 K to 0.75 W $m^{-1}K^{-1}$ at 750 K.

Polycrystalline $Ag_{0.8}Pb_{18+xm}SbTe_{20}$ formed by mechanical alloying of elemental starting materials and consolidated through spark-plasma sintering gave a *ZT* value of 1.5 at 673 K.[74] The average size of polycrystalline nanocomposite was ~1 μm, including 20 nm size precipitate with a relative density of 95% was observed. 20 nm precipitates were found to play a role in

reducing the lattice thermal conductivity. The lattice thermal conductivity of this family of compounds was found to be ranging from 2.1 W $m^{-1}K^{-1}$ at 300 K to 0.75 W $m^{-1}K^{-1}$ at 750 K.

1.5.3.2 Tl and Sn Containing Tellurides

When a dopant energy level lies close to the fermi level, density of states (DOS) will be increased and this results in an enhanced Seebeck coefficient. ZT = 1.5 was reported at 773 K in Tl-doped PbTe [75], compared to PbTe (ZT ~0.76).[76] When a donor or acceptor level is introduced close to the Fermi level, the local DOS will be increased, leading to increased effective mass of charge carriers, without changing the carrier concentration. This increased effective mass leads to an enhanced Seebeck coefficient. Also, considerable reduction in lattice thermal conductivity has been reported in bulk PbTe containing <3% by mass of Sb nanoparticles.[77]

There exists another class of telluride with Sn. In $Tl_{10-x}Sn_xTe_6$ and $Tl_{10-x}Pb_xTe_6$, changing x from 1.9 to 2.05 resulted in ZT values in excess of 1.2; $Tl_{8.05}Sn_{1.95}Te_6$ and $Tl_{8.10}Pb_{1.90}Te_6$ exhibited ZT = 1.26 and ZT = 1.46 around 685 K, respectively.[78]

1.5.4 Antimonides

1.5.4.1 Filled Skutterudites

Since 1990, skutterudites have gained more and more attention because their lattice thermal conductivity can be reduced significantly by introducing void fillers. The skutterudite type ($CoAs_3$ type) is a cubic structure with MX_6 octahedra (M = Co, Rh, Ir; X = P, As, Sb) as depicted in Figure 1.13. The voids created at the center of $(MX_6)_8$ can be filled with atoms of lanthanides, alkali, alkaline-earth metals, and group 14 elements as “rattlers”.[79, 80] As already indicated, guest atoms act as phonon scattering centers to reduce the lattice thermal conductivity, this reduced thermal conductivity; this reduced thermal conductivity leads to an enhancement in thermoelectric properties. For example, filling 5% La or Ce in the voids reported to reduce the thermal conductivity by ~50% in $CoSb_3$.[81, 82] Higher $P.F.$ can be achieved by partially filling the voids through optimizing the charge carrier concentration, which leads to improved ZT

values.[83, 84] Skutterudites such as $LaFe_3CoSb_{12}$ and $CeFe_3CoSb_{12}$ have exhibited *ZT* close to 1 at 800 K.[80] Investigation of the effect of micron/nanosized bulk particles of p-type and n-type skutterudites, which were hot-pressed, has culminated in the observation that bulk material exhibits a record high *ZT* values, from *ZT* ~1.1 to 1.3 at 775 K for p-type and from 1.0 to 1.6 at 800 K for n-type. These *ZT* values were translated into respective efficiencies of 13% and 16% between 300 K – 850 K for p-type and n-type respectively.[85]

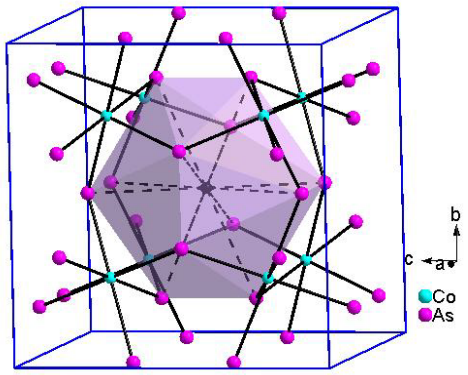

Figure 1.13: Crystal structure of skutterudite, guest atoms occupy the center of void.[86]

1.5.5 Mo_3Sb_7 Family of Compounds

Back in 2002, our research group started to improve the thermoelectric properties of Mo_3Sb_7, which adopts the Ir_3Ge_7 structure type, wherein the Sb and Te atoms occupy the Ge sites. Mo_3Sb_7 is metallic with its 53 valence electrons. Electronic band structure structure calculations predicted that the fermi level lies deep inside the valence band. This fermi level can be raised in a band gap of 0.5 eV if one substitutes two Sb atoms with two Te atoms to form $Mo_3Sb_3Te_2$.[87] This substitution increases the valence electrons from 53 to 55. More attempts were made to replace Sb with Te over time by other groups.[88]

In $Mo_3Sb_{7-x}Te_x$, Mo atoms are coordinated with eight Sb/Te atoms to form a square antiprism. Two such prisms share a face, resulting in an Mo–Mo bond. The eight Sb2 atoms form an empty cube, which can be occupied by a transition metal atom such as Ni, Cu, Co, and Cu. Each face of the Sb2 cube is part of a Mo $(Sb/Te)_8$ square antiprism. The chains of Mo_3Sb_{7-}

$_x$Te$_x$ are comprised of Sb2 cube–Mo–Sb1/Te square–Mo–Sb2 cube–Mo. Three such chains interpenetrate each other at the Sb2 cubes to construct a three dimensional structure as shown in Figure 1.14.

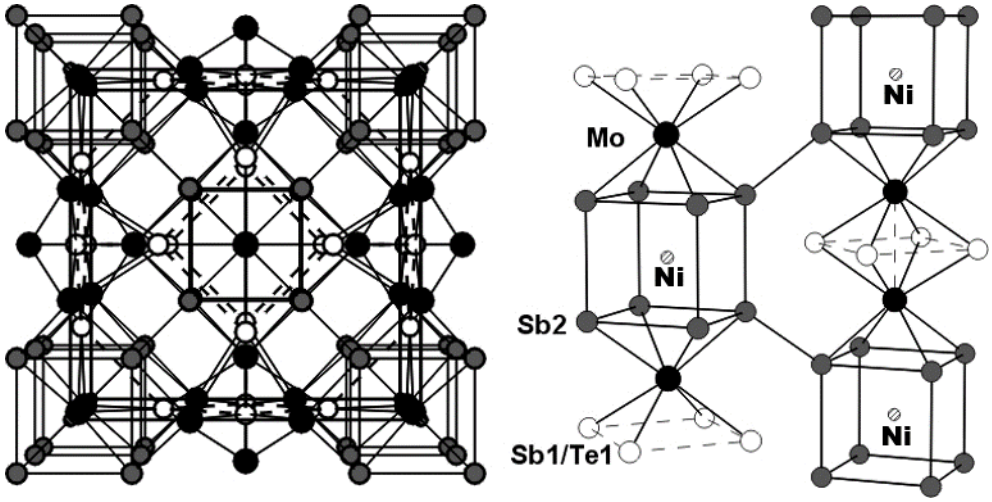

Figure 1.14: Crystal structure of $A_yMo_3Sb_{7-x}Te_x$ (left) and its chains (right)

In 2003, our group successfully intercalated different elements such as Mg, Cu, and Ni into the center of the Sb2 cubes, thereby decreasing the band gap.[89] In 2009, our group made further attempts to improve the TE properties of $Mo_3Sb_{7-x}Te_x$ by replacing Sb with Te, and we also successfully added transition metals such as Ni, Fe, Co, and Cu into the empty cubes formed by Sb atoms, thus significantly altering the band structure and the TE properties. Electronic band structure calculations showed that adding Ni slightly increased the charge carrier concentration, while increased Te content decreased charge carrier concentration. The outcome of these research culminated in the $Ni_{0.06}Mo_3Sb_{5.4}Te_{1.6}$ with ZT = 0.93, which is close to the benchmark of 1.[90] However, $Ni_{0.06}Mo_3Sb_{5.4}Te_{1.6}$ has a high thermal conductivity of 5.6 W $m^{-1}K^{-1}$ around 300 K. The main goal of my research is to reduce the thermal conductivity of this compound by synthesizing nanocomposites from this material.

1.6 Nanostructured Composites

To realize practical energy generation cost effectively using TE devices and to compete with other energy harnessing clean energy technologies, TE materials with *figure-of-merit ZT* greater than 3 are required. In contrast, current state-of-the-art materials exhibit *ZT* values of the order of 1 or slightly above 1. In spite of a substantial increase in research and some new breakthroughs in thermoelectrics over the last six decades, the design and synthesis of material with targeted *ZT* have proven to be still elusive mainly because of strong inverse coupling between electronic and thermal transport parameters. Decoupling between these parameters is a key to designing new materials.

1.7 Strategies to Improve Thermoelectric Performance

The arrival of nanotechnology has ushered a new era in the field of thermoelectrics. Back in 1993 Hicks and Dresselhaus theoretically predicted that low-dimensionality can enhance the Seebeck coefficient, *S*, over that of bulk through quantum confinement.[91] They proved that this confinement facilitates the decoupling of Seebeck coefficient and electrical conductivity, σ. Low dimensionality generated a highly structured density of states, $N(E)$. According to Mott's relation [59], *S* is related to the derivative of the electronic density of states, $N(E)$, at the Fermi level. Sharp changes in the density of states close to the Fermi level can enhance *S* thereby *ZT*. This theory led to efforts to fabricate reduced dimensionality structures comprising nanodots (0 dimension), quantum wires (1-dimension) and quantum wells (2-dimensions). Experimental verification of this theory was realized in PbTe quantum wells confined by $Pb_{0.927}Eu_{0.073}Te$ barrier layers, for which *ZT* was estimated to be 2.[92] Also Venkatasubramanian et al., reported 2-dimensional Bi_2Te_3/Sb_2Te_3 superlattice structures exhibiting *figure-of-merit*, *ZT*, as high as 2.4 at 300 K.[93]

However, the nanostructures mentioned in the above paragraph demand very expensive ultra-high quality thin films fabricated through molecular-beam-epitaxy (MBE) or chemical-vapor-deposition (CVD) and are not scalable for commercial production; their yield is also very poor.[94] Therefore, TE devices fabricated through these routes are not viable in the field of

energy recovery. Apart from these, these nanostructured TE devices are not well suited for high temperature applications, where there are issues regarding long-term thermal and mechanical stability as well as concerns about the effective stability between source and heat sinks linger.

Given the aforementioned bottlenecks, considerable efforts have been made to develop bulk nanostructured materials, in which reduced low dimensionality of nanomaterials can be used to optimize transport properties by creating more interfaces[95] and using classical size effects. These methods are cost-effective, and allow us to produce a large amount of material.

Acoustic phonons, the major carriers of heat have a spectrum of wavelengths and mean free paths (MFP).[96] Depending on their wavelengths, they contribute differently to thermal conductivity. While the short and medium wavelength phonons are scattered by point defects and nanostructures, long wavelengths phonons are largely unaffected and still able to propagate heat. Reducing the contribution of lattice thermal conductivity from long-wavelength phonons requires additional mechanisms. From the Boltzmann equation under relaxation time approximation, the lattice thermal conductivity is given by:

$$\boldsymbol{\kappa_l} = \left(\frac{\mathbf{1}}{\mathbf{3}}\right) \mathbf{C_v} \boldsymbol{l v_g} \qquad \textbf{Equation 1.8}$$

where C_v is the specific heat, v_g the group velocity of acoustic phonons, and l is the MFP between two scattering events. At very low temperatures (< 40 K), κ_l is dictated by the Debye's T^3 law for specific heat. At this temperature, phonon scattering is insignificant because of the low number of excited phonons and also because of their long wavelength. At higher temperatures, that is, above the Debye temperature, θ_D (temperature at which the wavelength of vibrations of the atoms in a lattice becomes close to the length of the unit cell), C_v approaches the classical value of 3R (R is the ideal gas constant). Thus, κ_l is primarily dependent on the phonon wavelength, which in turn is determined by the phonon scattering. Among all these parameters, controlling the phonon free path utilizing the classical size effect and interfacial phonon scattering effect are the most cost effective and feasible options.[58, 71] In addition to this, there is another advantage related to the specific heat of the composite material. In the case of single crystal diamond, coarse-grained polycrystalline and nanocrystalline diamond samples, no

measurable difference in specific heat between 323 K and 573 K was found.[97] Based on this information, we can conclude that grain-size dependent specific heat has little contribution to κ. In nanocomposites, the introduction of nanoparticles will scatter acoustic phonons thus reducing their mean free path (MFP). The principle idea in TE nanocomposite synthesis is to incorporate nanoparticles of certain shape and size inside an already promising TE material. Mid and long wavelength phonons will be scattered by grain boundaries and embedded nanoparticles; however, a reduction in electrical conductivity is imminent due to charge carrier scattering. Thus, it is very important to choose a suitable nanomaterial to reduce the thermal conductivity and simultaneously preserve or enhance the electrical conductivity.

Based on the Boltzmann equation mentioned above, thirty years ago, Rowe et al.[98] demonstrated that the thermoelectric properties of $Si_{80}Ge_{20}$ can be improved by grain size reduction. They were able to reduce the lattice thermal conductivity, κ_l, by 28% by milling the bulk powder to less than 5 μm. This finding led to an interest in bulk nanostructured materials in the scientific community. Using the same technique, Wang et al.,[72] showed that κ_l of $Si_{80}Ge_{20}$ can be reduced even further by ball-milling the bulk material, where the particle size distribution was reduced to 30 nm – 200 nm comprising crystallites of 5 nm – 15 nm. Despite the drop in charge carrier mobility, the authors were able to reduce κ_l by 46%, thereby enhancing the *ZT* to 1.3 at 1173 K, i.e. an approximately 40% increase compared to the bulk material. Another approach is to incorporate chemically and physically inert nanoparticles into bulk TE materials to arrest the coherent propagation of heat carrying acoustic waves without affecting the electrical conductivity and the Seebeck coefficient.[96, 99]

Ball-milling an already promising TE material and consolidating it either by hot-pressing or by spark-plasma sintering, creates an extensive interface per unit volume that facilitates diffusive scattering of phonons (reducing their MFP).[100] Poudel et al. obtained *ZT* of 1.2 at 300 K and 1.4 at 373 K from a ball-milled and hot-pressed p-type BiSbTe alloy.[25] Numerous studies have suggested that a wide distribution of nanoinclusions can also scatter phonons of different wavelengths. Hot-pressed $CoSb_3$, containing micron sized particles with nanoscale size particles from the same bulk material, enhanced the *figure-of-merit* by 54% at 700 K.[101]

Theoretical modeling on the contribution of κ_l vs. MFP of Si showed that 90% of κ in Si is due to phonons of wavelength > 20 nm.[102] Therefore, if the grain size is reduced to 20 nm, a considerable reduction in κ can be achieved without affecting the mobility of charge carriers as the MFP of electrons in Si is calculated to be only a few nanometers.[103]

Recently, numerous articles by various authors have demonstrated substantial reduction in lattice thermal conductivity, κ_l, over those of bulk representatives in composites made of bulk powder embedded with foreign nanoinclusions.[76, 104-107] These nanoinclusions stops the coherent propagation of heat carrying acoustic waves without deteriorating the electrical conductivity and the Seebeck coefficient.[96, 99] When the dimensions of the nanoinclusions are comparable to the MFP, the phonons will be scattered, reducing κ_l.

A plethora of literature proves that in composites, nanoinclusions and grain boundaries not only scatter phonons, but also scatter charge carriers thus reducing charge carrier mobility.[108, 109] However, with the optimum amount of nanoinclusions, it may be possible to enhance phonon scattering while simultaneously preserving the electrical conductivity.[23]

The mechanisms of phonon and charge carrier interaction with embedded nanoparticles, grain boundaries, and defects are depicted in Figure 1.15.

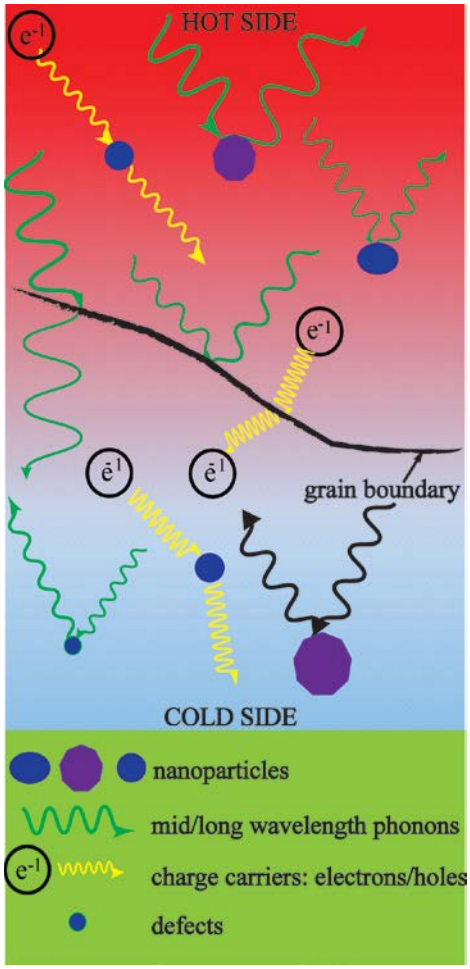

Figure 1.15: Mechanism of phonon and charge carrier interaction with embedded nanoparticles, grain boundaries, and defects.

Atomic defects can effectively scatter short wavelength phonons, but to scatter mid and long wavelength phonons, larger particles are needed. Also, grain boundaries are very efficient in scattering longer-wavelength phonons. When phonons incident at the interfaces, they generate multiple phonons of longer wavelengths beyond the grain boundaries, depending on the states available there. If the nanostructures are smaller than the phonon MFP, but greater than charge carrier MFP, phonons are more strongly scattered by the interfaces than the charge carriers, resulting in reduced thermal conductivity but not changing the mobility of the charge carrier.[110]

The energy barriers at the interfaces can lead to preferential scattering of low-energy charge carriers, thereby increasing the Seebeck coefficient.[61, 111, 112] This effect is called filtering effect, and was theoretically studied.[62] This approach was found to be useful only in some materials, and the concept of energy filtering is still not well understood.

It has been observed that MFPs of phonons typically vary from a single nanometer to several hundred nanometers; thus, preferential scattering is possible through the filtering effect. On the other hand, the charge carrier MFP is typically only a few nanometers.[53] Therefore, we can reduce the lifetime of phonons of various wavelengths by incorporating nanoparticles of different sizes. However, in many composites, introducing the nanoinclusions in a bulk thermoelectric matrix reduces mobility because each inclusion becomes a scattering center for charge carriers, thereby reducing electrical conductivity.[72] Thus, we need to study the tradeoff relation in reduced mobility due to defects, dispersed particles, grain boundaries, and corresponding reduction in lattice thermal conductivity.

Thus, any improvement in *ZT* must be determined from the relation of μ and κ_l. Although this is fruitful in many composites, many fundamental issues are still intangible. The MFP of phonons at a certain temperature is not known for many materials systems,[110] thus making theoretical prediction of electronic or thermal conductivity is difficult for nanocomposites.

The comparison of *figure-of-merit* between the current state-of-the-art bulk thermoelectric materials and nanostructured materials is shown in Figure 1.16.

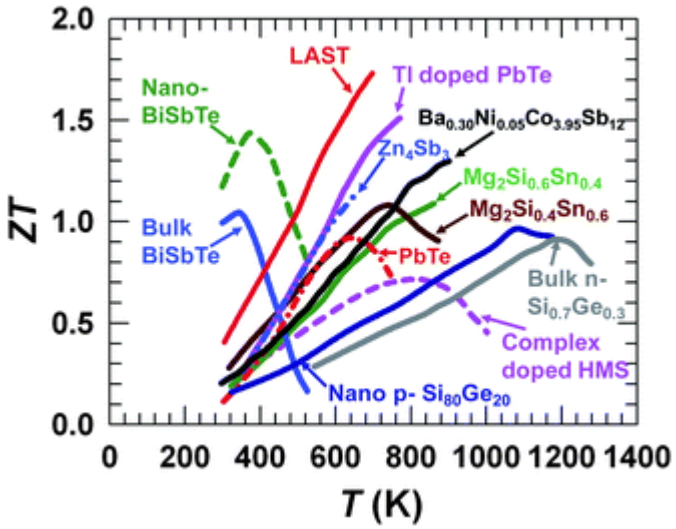

Figure 1.16: State-of-the-art nanostructured material.[8]

1.8 Research Objectives

As I discussed in Section 1.5.5, the main focus of my thesis, the reduction of the thermal conductivity of $Ni_{0.05}Mo_3Sb_{5.4}Te_{1.6}$, (5.6 W $m^{-1}K^{-1}$ at 325 K and 4.0 W $m^{-1}K^{-1}$ at 1000 K [113]) through various nanocomposites synthesis with $Ni_{0.05}Mo_3Sb_{5.4}Te_{1.6}$ as the starting material. With this in mind, I decided to synthesize different composites with carbides, fullerenes, oxides, and metal nanoparticles. The purpose of nanocomposite synthesis is to enhance phonon scattering by generating more interfaces through nanoinclusions and thereby stopping the coherent propagation of phonons according to Equation 1.8. Reduction in thermal conductivity in turn leads to increased *figure-of-merit*. My research involves different synthesis methods, such as manual mixing, mechanical mixing, and wet chemistry synthesis. By giving one simple example, I would like to explain the notations for one of our composites: bulk/SiC. Here bulk means 100s μ sized particles of $Ni_{0.05}Mo_3Sb_{5.4}Te_{1.6}$ and SiC means SiC nanoparticles.

[8] Reproduced from J. R. Szczech, J. M. Higgins and S. Jin, Journal of Materials Chemistry **21** (12), 4037-4055 (2011) with permission from the Royal Society of Chemistry.

Much literature on state-of-the-art TE composites and cermets prove that microstructures play a very important role in deciding the transport properties. Therefore, I am going to characterize the microstructural properties of composites using SEM, TEM, and BET, etc., and correlate their effects on TE transport properties. Readers are strongly advised to read Section 1.9 before reading any chapters.

1.9 Material Choice for Our Composites

The rationale behind the choice of nanomaterials is explained chapter wise in the following paragraphs.

Chapter 3: Multi-wall carbon nanotubes (MWCNT) are known to have outstanding electrical and mechanical properties.[114, 115] For example, in the p-type bismuth antimony telluride $(Bi_{0.2}Sb_{0.8})_2Te_3$, *ZT* increased by 42% after adding CNT,[116] and *ZT* of $MnSi_{1.75}Ge_{0.02}$ was enhanced by 20%.[117] In this study, we used CNT with the aim of achieving good electrical properties, reduced thermal conductivity, and thermally stable composites.

Chapter 4: Refractory materials such as silicon carbide (SiC, bulk M. P. 2973 K) and alumina (Al_2O_3, bulk M. P. 2945 K) are very inert at high temperatures.[118, 119] Incorporation of 0.4% SiC nanoparticles in the $Bi_{0.3}Sb_{1.7}Te_3$ matrix enhanced the *ZT* up to 1.33 from 1.2 at 373 K, resulting in an improvement of 11%.[120] Similarly, nano-SiC of 0.0024 by volume fraction added to Bi_2Te_3, consolidated through SPS, enhanced the *ZT* of bulk by 18% by aiding in reducing thermal conductivity.[121] In addition, SiC nanoparticles augmented the mechanical properties of some TE materials such as $Bi_{0.5}Sb_{1.5}Te_3$ and Bi_2Te_3, and SiC-whiskers reinforced alumina.[122, 123] Therefore, we studied composites of $Ni_{0.05}Mo_3Sb_{5.4}Te_{1.6}$ with nanoinclusions of β-SiC and Al_2O_3.

Chapter 5: There were three main reasons for the synthesis of the bulk/NiSb composite. The first goal was to reduce the thermal conductivity via NiSb nanoparticles as smaller particles have a larger surface to volume ratio and provide larger interfaces per unit volume. Incorporating Ag nanoparticles in Si nanoparticles reduced the thermal conductivity by two orders of

magnitude compared to the bulk counterpart.[124] The second goal was to enhance the electrical conductivity as NiSb exhibits very high electrical conductivity of $10^5\ \Omega^{-1}\ cm^{-1}$ at 300 K (data from our group). Furthermore, our decision was supported by the case of the Bi/Ag composite: incorporating highly conductive Ag particles in a Bi matrix resulted in an overall increase in *P.F.* = $S^2\sigma$ by 50%.[125]

The third goal was to enhance the mechanical properties of bulk/NiSb composites. In service conditions, TE materials undergo stresses from thermal gradients, the thermal mismatch of constituents, and applied external pressure. Therefore, studies of the mechanical integrity of thermoelectric materials are very important. Nanoparticles such as NiSb have a higher tolerance for changes in the surrounding volume, thereby mitigating the stress during heat cycling.[126] NiSb bulk has Vickers Hardness Number (VHN) of hardness of 5.5 and a measured density of 7.6 g cm^{-3} – 8.23 g cm^{-3},[127] which is close to the density of 8.28 g cm^{-3} of $Ni_{0.05}Mo_3Sb_{5.4}Te_{1.6}$. Knowing important mechanical properties such as elastic modulus, hardness, and responses of materials to imposed stress is advantageous. Since hardness is related to wear characteristics,[128] we characterized the hardness and elastic modulus.

Many effective media theories assume nanoparticles of either ceramics or oxides or metals retain their bulk thermal properties even when they are incorporated in another bulk matrix at room temperature.[35, 40, 42, 46, 129-131] For example, in ZnS/diamond composites, diamond with a room temperature thermal conductivity of 600 W $m^{-1}K^{-1}$, and ZnS with 17.4 W $m^{-1}K^{-1}$, were used to study composite thermal conductivity. We synthesized 100 μm – 1000 μm NiSb particles through a high temperature solid-state method; characterized their thermal and electrical transport properties and used as obtained parameters to interpret the thermal and electrical properties of our nanocomposites.

Chapter 6: We scrutinized the contribution of SiC and Al_2O_3 nanoparticles to the thermal boundary resistance of $Ni_{0.05}Mo_3Sb_{5.4}Te_{1.6}$. The first step was to fabricate $Ni_{0.05}Mo_3Sb_{5.4}Te_{1.6}$/SiC composites and consolidated them through hot-pressing. Next, we fabricated $Ni_{0.05}Mo_3Sb_{5.4}Te_{1.6}/Al_2O_3$ composites and consolidated them through spark-plasma sintering

(SPS). Then, we characterized the thermal conductivity transport properties of these composites and their bulk counterparts at 325 K; we used obtained data to grasp how thermal variables such as thermal boundary resistance and effective thermal conductivity vary with respect to the volume fraction, *f*, of embedded nanoparticles by adopting various Effective Media Theories (Section 1.6). To understand the relationship between the mechanical properties and the thermal properties of $Ni_{0.05}Mo_3Sb_{5.4}Te_{1.6}$/SiC, $Ni_{0.05}Mo_3Sb_{5.4}Te_{1.6}/Al_2O_3$ we tested our composites for Vickers hardness and Young's modulus, and correlated their effect on thermal boundary resistance.

Chapter 7: We covered the results of bulk coated with NiSb nanoparticles through a solvothermal treatment. In a typical nanocomposite synthesis, chemically and physically stable nanoparticles are mixed with an already promising material using one of several methods such as mechanical mixing or during the bulk material synthesis and then the mixture consolidated by either hot-pressing or spark-plasma sintering.[104, 132] These methods have their own limitations such as inhomogeneity.[103] In TE nancomposite materials, interfaces between bulk particles or the junction of bulk particles and foreign nanoparticles play a very important role in deciding the overall performance of a TE material.[104] Thus, engineering the interfaces following a suitable technique is very critical to achieve optimized transport properties. We studied pore sizes, and their volume distribution in depth to ascertain whether microstructures play an important role in deciding thermal boundary resistance.

Interfaces in thermoelectric materials can influence the Seebeck effect due to size quantization effects [91] and the energy filtering of low energy charge carriers.[60-62, 111] Interfaces are also found to reduce the thermal conductivity due to the diffusive scattering of phonons [100] and play an important role in deciding the electrical conductivity depending on the nature of interfaces. For a fixed Seebeck coefficient, enhancement in *figure-of-merit* requires that the reduction in mobility due to charge carrier scattering at interfaces must be smaller than the reduction in thermal conductivity [133]; achieving this balancing act is very challenging. There are numerous suggestions on the nature of interfaces; some already implemented and many still conceptual. For example, embedded nanoinclusions, nanocoated bulk grains,

polycrystalline microstructures, preferential alignment of grains along a favorable transport directions, reduced grain size to facilitate preferential scattering of charge-carriers, coherent inclusion, lamellar/multilayer structures, and nanomeshes to name a few.[19, 27, 134-136] There are several methods of solution based synthesis of nanoparticles for TE nanocomposites.[77, 137-139] Irrespective of the techniques followed, the final goal of these investigations is to engineer grain boundaries to facilitate good TE properties.

Recently, there were investigations of the concept of the interfacial nanocoating.[140-142] In this wet chemistry process suitable starting materials for a desired chemical process and a pulverized (powder) bulk material were added to a container, such as an autoclave. After the reactions, nanoparticles of the resulting compound were coated on the bulk material. For example, $La_{0.9}CoFe_3Sb_{12}$ coated with $CoSb_3$ nanoparticles enhanced the *figure-of-merit* by 15-30%. Three important conditions need to be fulfilled while executing this nanocoating process. Firstly, the very process of coating itself should leave the bulk material unaffected; secondly, the coating needs to be very homogeneous with respect to thickness (desired thickness), and thirdly the end product should be thermodynamically and chemically stable. Meeting all of these conditions is very cumbersome.

In this chapter, I have made preliminary efforts to coat NiSb nanoparticles on our bulk $Ni_{0.05}Mo_3Sb_{5.4}Te_{1.6}$ particles via a simple nanocoating process similar to $CoSb_3$ nanocoating on bulk $CoSb_3$ and $CoSb_3$ nanocoating on bulk $La_{0.9}CoFe_3Sb_{12}$.[143, 144] NiSb was chosen as a suitable nanoparticle for nanocoating as the synthesis process is simple,[145, 146] and because of its small size of 60 nm – 80 nm. Also, my initial investigation showed the nanocoating process itself did not affect the bulk material. I expected the outcome of this investigation would be that this grain boundary coating may aid in scattering phonons due to enhanced surface area on the bulk material. Since NiSb is highly conductive, its coating may help in enhancing the electrical conductivity of the composite and elevate (or leave unaffected) its Seebeck coefficient due to the filtering effect.

In Chapter 8, we considered C_{60} as a suitable nanoinclusion considering its inertness and nanoscale size (Van der Waals diameter of 1.1 nm). Compared to more common high

temperature thermoelectrics such as the filled skutterudites [79] or the clathrates [147], variants of Mo_3Sb_7 achieve their high *ZT* values with a moderate Seebeck coefficient, large electrical, and relatively large lattice thermal conductivity [148]. It has been reported that the introduction of many interfaces in thermoelectric materials reduces the thermal conductivity [104]. This can be accomplished by the formation of nanocomposites produced either via endogenous or exogenous routes [149] and [150]. Therefore, we are currently attempting to reduce the lattice thermal conductivity via forming various composites, such as the ones with the fullerene C_{60} as described in this contribution. Depending on the material and the C_{60} concentration, the C_{60} additions may cause an increase or a decrease in *ZT*, in dependence of how the (expected) decrease in thermal conductivity compares to the (possible) decrease in the electrical performance, i.e. the power factor $P.F.= S^2\sigma$. For example, any tested C_{60} addition to Bi_2Te_3 nanocrystals [151] and $(Bi,Sb)_2Te_3$ [152] decreased *ZT* of the bulk. Adding 6.5 mass% C_{60} to $CoSb_3$ ultimately enhanced *ZT*, while adding amounts between 0.5% and 4.8% to $CoSb_3$ decreased *ZT* [153]. Finally, the opposite trend was observed for composites of $(Bi,Sb)_2Te_3$ [154] and $Ba_{0.44}Co_4Sb_{12}$ with C_{60} [155], where *ZT* was improved at the smallest C_{60} concentration investigated, namely 0.5 vol% and 0.43 mass%, respectively, and adding more C_{60} resulted in a decrease of *ZT*. As in this work, these composites were consolidated by hot-pressing (or spark-plasma-sintering). The latter two also provide evidence that even an enhancement of the power factor is possible after C_{60} addition by the so-called energy-filtering [156], [157], [158] and [159]. This contribution is focused on composites of $Ni_{0.05}Mo_3Sb_{5.4}Te_{1.6}$ with carbon materials, the bulk material having the optimized Sb/Te ratio as well as apparently beneficial small amounts of nickel in the Sb_8 clusters.

Chapter 2

Experimental

2.1 Synthesis Methods

2.1.1 Solid-State Reaction

The synthesis of bulk thermoelectric materials, particularly in the form of polycrystalline powder, is often carried out by conducting a solid-state reaction. However, solid-state reactions are always very slow and difficult to complete and they also require high temperatures to enable the inner atoms to diffuse easily to the contact surfaces of the grains. In general, solid-state reactions can be divided into two steps: nucleation of the reaction products and subsequent growth.[160] Nucleation is generally difficult because a structural rearrangement of the lattice of reactants is required to form nuclei of the product. The reorganization of atoms requires significantly elevated temperatures. Once the nucleation of the product is done, the growth of the product layer will depend on the diffusion of reactants' ions, through the product layer to the reaction front.

The rate of thickness change of the product layer, $d(\Delta x)/dt$, is proportional to the atom or ion flux, and the growth rate is written as Equation (2.1), where k is a rate constant.

$$\frac{d(\Delta x)}{dt} = \frac{k}{\Delta x} \qquad \textbf{Equation 2.1}$$

This rate law can be integrated to give a parabolic equation: $(\Delta x)^2 = 2kt$, which has been confirmed experimentally.

The amount of the surface contact area between reactants is also a factor. Smaller particles react faster and produce a more homogeneous sample due to their higher surface to volume ratio. In my sample preparations, all the starting materials were thoroughly grounded and mixed intimately to optimize homogeneity of the final products.

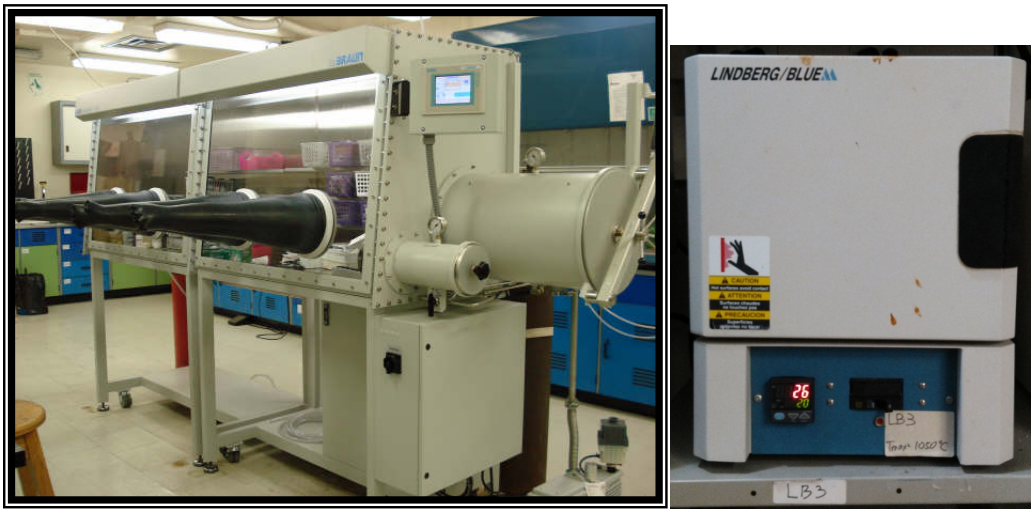

Figure 2.1: Glove box and programmable furnace

For all our composites, $Ni_{0.05}Mo_3Sb_{5.4}Te_{1.6}$ was the reference material (also called "bulk"). All the starting materials: Ni powder (99% nominal purity, –100+2000 mesh), Mo powder (99.95%, –100 mesh), Sb powder (99.95%, –100 mesh), and Te powder (99.8%, –325 mesh), all from Alfa Aesar, were stored and weighed in proper stoichiometry inside the argon filled glove box (Figure 2.1, left side). The starting materials were thoroughly mixed and transferred to fused silica ampoules and evacuated to 10^{-3} mbar. The tubes were then sealed using Oxy-Hydrogen torch. The tubes were transferred to a programmable furnace (Lindberg Blue with UP150 Control Module shown in Figure 2.1 on the right side) and heated at the rate of 1.5 K/min to 1000 K, and annealed at 1000 K for 10 days, and finally cooled to room temperature at a rate of 1.5 K/min. As obtained reaction mixtures in powder form were subjected to X-ray powder diffraction for phase purity using INEL powder diffractometer equipped with position-sensitive detector and Cu $K_{\alpha 1}$ radiation. Several reactions were carried out to obtain four samples of 2.2 g each. Phase-pure end-products from these reactions were transferred to 50 ml vial and subjected to high frequency vibrations in the Vortex-Mixture (Fisher-Scientific) for twenty minutes and divided into four heaps of equal mass, from which composites with different types of nanoinclusions were prepared.

2.1.2 Solvothermal Synthesis

It is a synthesis technique where starting materials are subject to react in certain solvents well above their boiling points in enclosed vessels that support high autogeneous pressure.[161]

The type of synthesis depends on the media: for water (hydrothermal); for alcohol (alcothermal); for ammonia (ammonothermal); and for glycol (glycothermal). Solvothermal reactions are very energy efficient and less time consuming unlike solid-state reactions that demand high temperature and longer time. In solvothermal synthesis, size and shape such as spheres, rods, tetrapods can be tuned by controlling the concentration of reactants, reaction time, surfactants, and temperature.[162] For more information on solvothermal synthesis readers can refer to Byrappa et al.[163]

In the thermoelectric field, solvothermal synthesis has played an important role since the nanoparticles synthesized through this technique have homogenous particle distribution and are mostly defect free. They are, unlike nanoparticles synthesized through the top-down approach such as high-energy ball-milling, which induce defects by broken bonds at the edges of the nanoparticles. The solvothermal process is scalable and materials in kilogram quantities can be synthesized. For our $Ni_{0.05}Mo_3Sb_{5.4}Te_{1.6}$/NiSb composite, we followed Kumari et al. for the solvothermal synthesis of NiSb nanoparticles.[145] Analytically pure $NiCl_2 \cdot 6H_2O$ and $SbCl_3$ were used as the precursors. Starting materials, Ni and Sb with a molar ratio of 1:1 were placed into a 40 ml Teflon-lined autoclave, and 80% of the volume of the Teflon tube was filled with pure ethanol. Excess amount of $NaBH_4$, a reducing agent, was added and stirred with glass rod and the reaction was allowed continue for 15 minutes. No surfactants were used for this synthesis. The autoclave was sealed immediately and placed in an oven, heated slowly to 240 ºC and maintained at this temperature for 72 hours. After the reaction, the autoclave was cooled to room temperature naturally. The reaction precipitate was filtered and washed several times with ethanol and Millipore water and dried at 100 ºC for several hours in nitrogen environment. The obtained NiSb powder was light pinkish in color. The synthesized powder was characterized for phase purity using X-ray powder diffraction and SEM for particle size and shape. The obtained

NiSb nanoparticles are shown in Figure 2.2. Figure 2.3 shows the autoclave used for NiSb nanoparticle synthesis and NiSb nanoparticle coating on the bulk material.

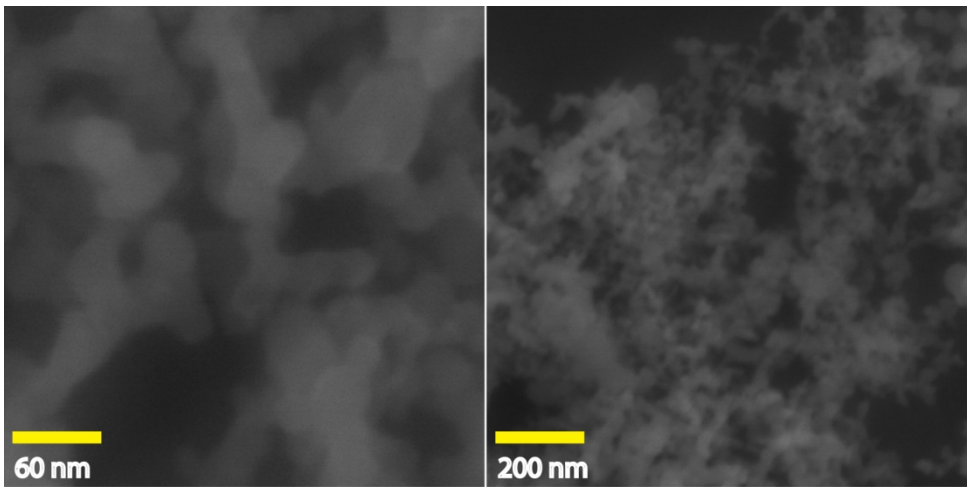

Figure 2.2: NiSb nanoparticles synthesized by a solvothermal process.

2.1.3 Growing Nanoparticles on Bulk Materials (nano - plating)

Another important aspect of solvothermal synthesis is to grow nanoparticles on bulk particles (which are usually larger than 500 microns). In thermoelectric materials, embedding nanometer size particles inside the bulk matrix scatters the phonons, thereby reducing the thermal conductivity. However, the method of dispersing these nanoparticles within the bulk matrix through mechanical means is extremely challenging, and this inhomogeneity is a great obstacle when it comes to reproducibility, as the distribution of nanoparticles for two samples may not be exactly same.

Figure 2.3: Teflon-lined autoclave used to synthesize NiSb nanoparticles and to coat them on bulk $Ni_{0.05}Mo_3Sb_{5.4}Te_{1.6}$.

In our investigation of a coating process, 2 g of bulk material and a respective amount of starting materials such as $NiCl_2 \cdot 6H_2O$, and $SbCl_3$ were added to a Teflon-lined autoclave containing 20 ml of ethanol. The mixture was mixed through sonication for 20 minutes. Separately, an appropriate amount of $NaBH_4$ was placed in a small beaker containing 10 ml of ethanol; the beaker was sonicated for 10 minutes. The solution containing $NaBH_4$ was added to the autoclave dropwise. The mixture in the autoclave turned very dark and vigorous effervescence was observed. The reaction was allowed to react for 20 minutes. The starting materials and reducing agent were added in such a way that the end product of the reaction yield would be 0.034, 0.074, and 0.16 NiSb nanoparticles by volume fraction. After 20 minutes, the autoclave was assembled and loaded into an oven and heated slowly until reaching 240 ^oC. The autoclave was kept in an oven for 72 hours, and thereafter it was cooled naturally. The final product, washed several times with deionized water and ethanol, was then dried under nitrogen atmosphere for 24 hours. The end product was subjected to powder XRD for phase analysis and SEM analysis for distribution of NiSb nanoparticles on bulk particles.[145] Particle size was determined using SEM and found to be 60 nm – 80 nm. The SEM images in Figure 2.4 show bulk particles coated with NiSb nanoparticles.

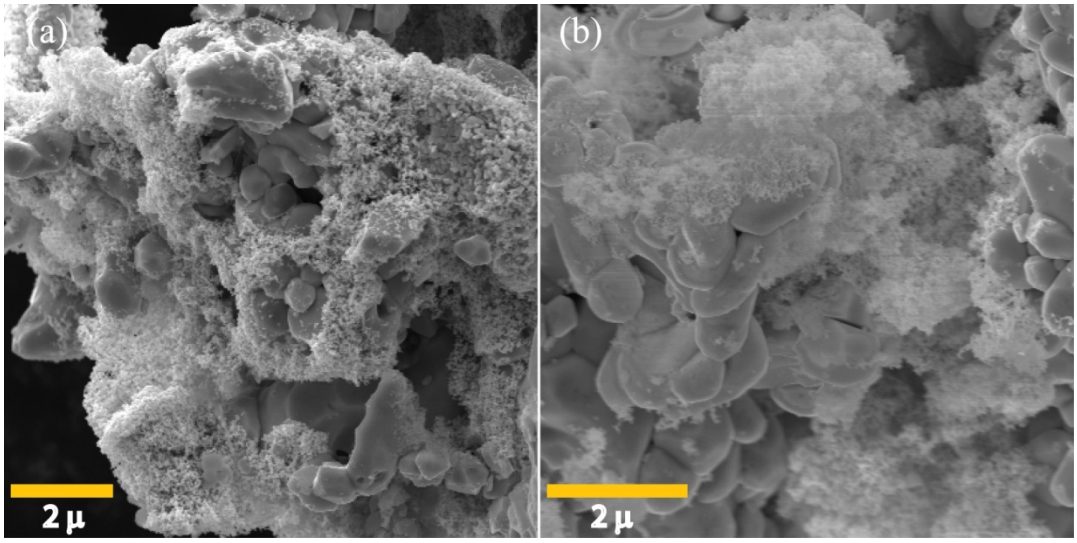

Figure 2.4: Bulk $Ni_{0.05}Mo_3Sb_{5.4}Te_{1.6}$ particles coated with NiSb nanoparticles. (a) 0.034 NiSb; (b) 0.074 NiSb by volume fraction.

2.2 Powder X-ray Diffraction

Powder X-ray technique has been in use for two reasons: for the fingerprint characterization of crystalline materials since each crystalline solid has its unique X-ray pattern, and determining their crystal structure. The X-ray diffraction technique is one of the most important characterization tools used in solid state chemistry and materials science.

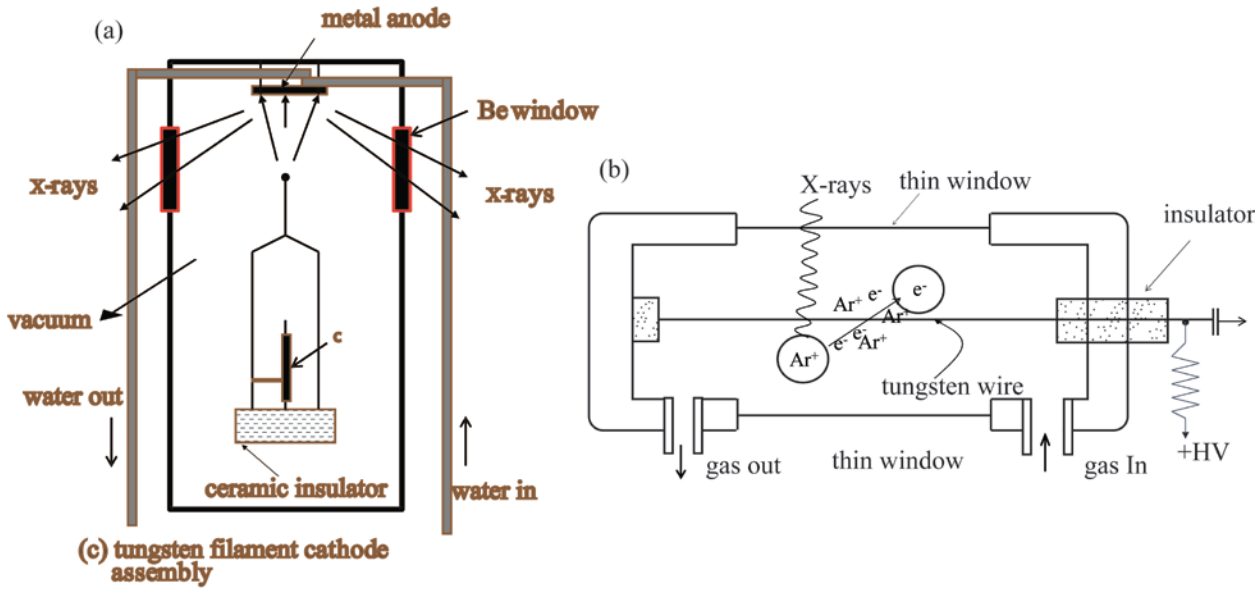

Figure 2.5: Schematic illustrating the essential components of: (a) X-ray tube; (b) Ar gas proportional counter.

Figure 2.5(a) shows X-ray production tube and Figure 2.5(b) shows the gas proportional counter used to measure the diffracted X-rays intensity. X-rays are produced when a metal target such as Cu or Mo is bombarded with a beam of high energy electrons emitted from a hot tungsten filament or thermionically emitting element. The incident beam ejects K-shell (1s) electrons of the target atoms and X-rays are emitted when the vacancies are filled by electrons from the L (2p) or M (3p) levels. This process gives K_α and K_β lines. The simplest way to filter out unwanted K_β is to use a foil of a suitable metal, for example, Ni foil is used to remove K_β, and Zr to remove Mo K_β. In modern diffractometers, a monochromatic beam is obtained using crystal monochromator, which consists of a crystal (usually graphite), oriented in such a way as to diffract only K_α lines. The mechanism of characteristic X-rays emission is shown in Figure 2.6.

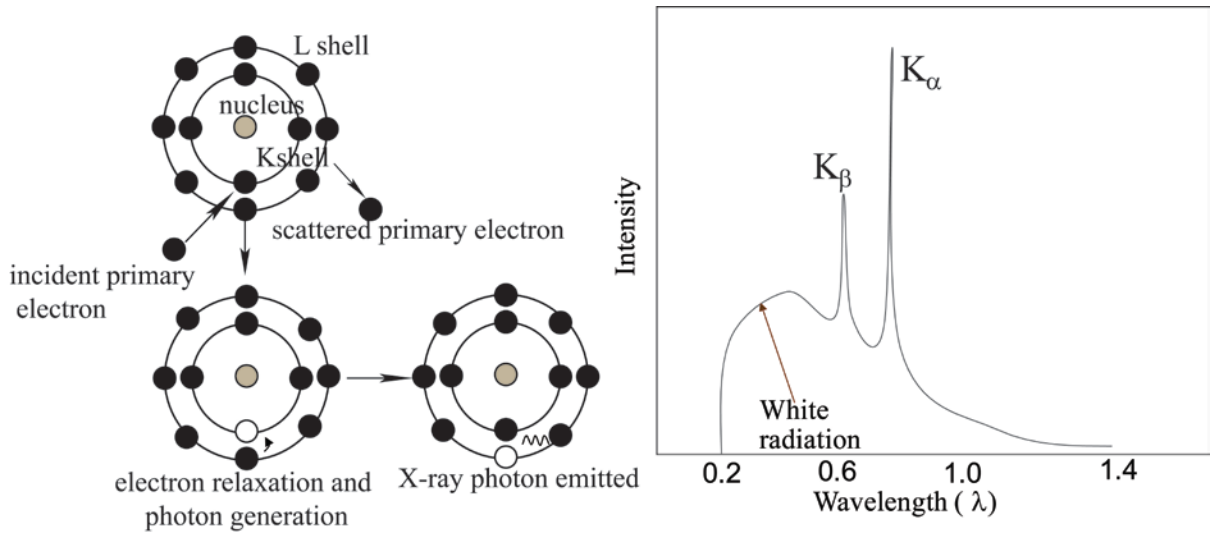

Figure 2.6: The process of inner-shell ionization, deionization and the emission of characteristic X-rays. 1.5418 Å from Cu Kα, and 0.7107 Å from Mo Kα.

For a single phase sample, a true representative of the sample with 1 μm – 10 μm particle size is required. However, for accurate results, a sample of 1 μm or smaller with a sufficient number of crystallites is preferred.[164] The sample needs to be tightly packed in the sample holder; a loosely packed sample gives peaks with poor intensities. Clearly, there are always a large number of lattice planes (hkl) with the angle θ to satisfy the Bragg's law: $n\lambda = 2d \sin\theta$.[165] Thus, randomly oriented micro-crystals diffract the beams and form a cone of angle 2θ to the incident beam, as shown in the right side of Figure 2.7.

In powder X-ray diffraction, the obtained XRD pattern will be compared with the existing phase pattern from frequently updated libraries of powder diffraction patterns, such as Inorganic Crystal Structure Database (ICSD) or International Center for Diffraction Data (ICDD). Though very suitable for qualitative analysis, such as phase purity, powder X-ray method's main limitation is that it cannot detect an amorphous phase or impurities of less than 5%.

Our XRD machine, Inel PXG 3000 powder diffractometer with a position sensitive gas proportional counter detector array, [165] is shown in Figure 2.7.

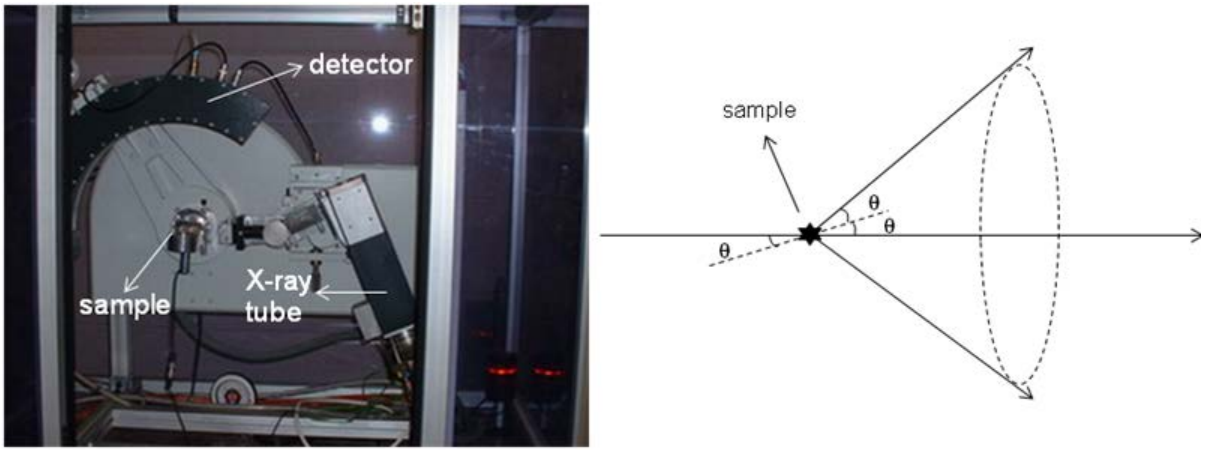

Figure 2.7: (a) Inel XRG 3000 powder X-ray diffractometer; (b) The formation of a cone of diffracted beams in PXRD.

2.3 Ball-milling

There are two methods to synthesize nanomaterials. First one is bottom-up process, where nanomaterial is synthesized from atoms and molecules. The second method is top-down, where big particles are reduced to nanoscale by grinding them (also called milling in some literatures). High energy planetary ball-milling is very suitable for the latter.

Ball-milling is a process in which the starting materials in proper stoichiometry (for alloys) or the powder from which we are interested in making nanoparticles are added to the milling pot with appropriate amount of milling balls and a suitable agent (called process control agent, PCA) and the pot is subjected to a high speed rotation, where milling balls vigorously agitate against each other and walls thereby crushing the powder to form nanoparticles or an alloy (mechanochemical synthesis or alloying mechanically).[165]

The mechanism of movement of balls and the powder is shown in the Figure 2.8. Since the rotation directions of the pot on its own axis and the disc containing this pot are opposite, the centrifugal forces are alternately synchronized.

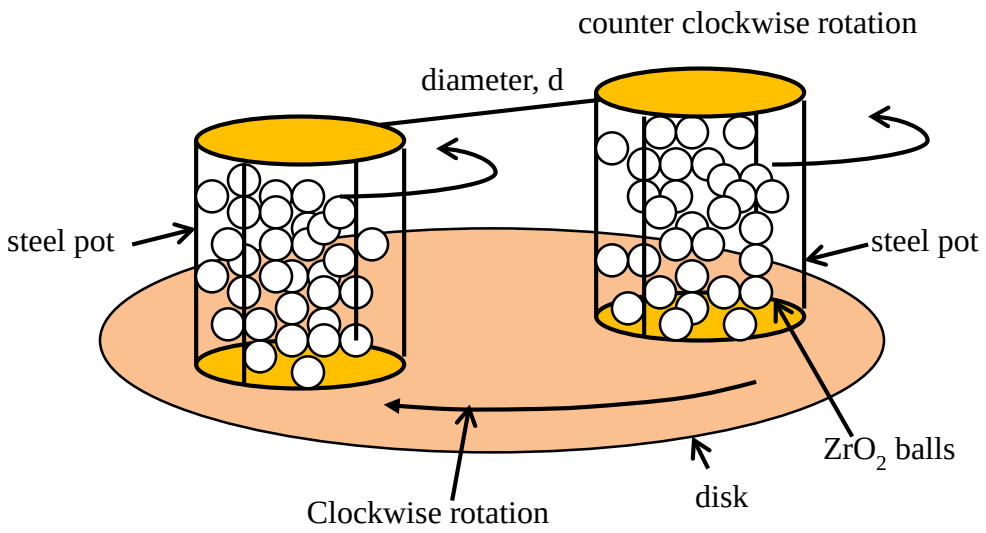

Figure 2.8: Rudimentary planetary ball-milling machine.

Thus, friction results from the hardened milling balls and the powder mixture alternately rolling on the inner wall of the pot and striking the opposite wall. The impact energy of the milling balls in the normal direction attains far higher energy than that due to gravitational acceleration. Hence, planetary ball milling is very suitable for high-speed milling.

During high energy ball-milling, particles of several 100s μm particles are subjected to repeated fracture, cold welded, and re-welded. The amount of the material trapped between two balls depends on the size of the balls and the nature of the material. Newly formed surfaces enable the particles to weld together and this leads to an increase in particle size. Thus, a broad range of particle sizes develops. With continued impact of the grinding balls, the structure of the particles is steadily refined, but the particle size continues to be the same. After milling for a certain amount of time, a steady-state equilibrium is attained when the rate of welding, which tends to increase the particle size, and the rate of fracturing are balanced. Smaller particles are able to withstand fracturing and tend to be welded into larger pieces, with an overall tendency to drive both very fine and very large particles towards an intermediate size. At this stage, the particle distribution will be narrow, because particles larger than average in size are being reduced in size, while smaller particles are agglomerated to become average in size at an equal

rate. Figure 2.9 is a rough sketch of variation in particle size with respect to time during the ball-milling process. Figure 2.10 shows the ball-milling machine with the specifications used in our experiments.

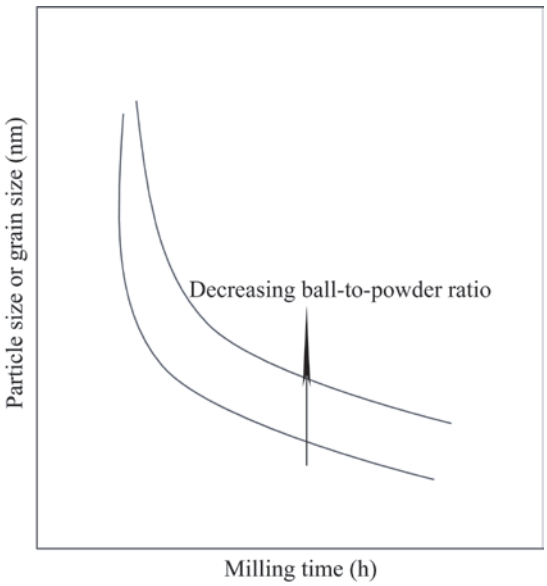

Figure 2.9: Particle and grain size refinement of particle with milling time.

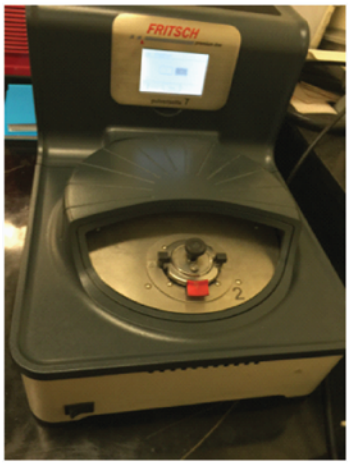

Fritsch Pulverisette 7 Premium line planetary ball-milling parameters

Grinding components	Units	Parameters
Pot diameter	mm	46.5
Pot depth	mm	13
Pot volume	ml	20
Revolution Radius	mm	70
ZrO_2 ball diameter	mm	1.86
Each ball mass	gm	0.192
Total mass of balls		can be varied
Ball density	gm cm^{-3}	5.7

Figure 2.10: Ball-mill machine and its specifications (from vendor's manual). Image is courtesy of Yixuan Shi.

Variables in Ball-milling

Alloying mechanically or nanoparticle synthesis or mixing two components by ball-milling is a complex process. To save time, it is extremely important to several variables involved to get the desired product (top-to-bottom) or phase (alloying mechanically). The following parameters play a very important role when it comes to the expected end product.

Grinding Medium

Grinding medium refers to the inner lining in the milling pot and the milling balls. It is highly recommended to have the entire grinding medium made of the same material because different materials may cause cross contamination. Typical grinding media are made of ZrO_2, steel, hardened chromium steel, stainless steel, bearing steel, or WC-Co alloy. Large size of the grinding medium is useful as more impact energy will be transferred to the powder.

Milling Atmosphere

Air may cause contamination and therefore an Ar or N_2 atmosphere is preferred. In case of a rudimentary milling pot without a gas inlet and outlet for the inert gas, it is advisable to transfer the charge to the milling pot inside a glove box.

Milling Speed (rotations per minute)

Intuitively, it is easy to guess that the faster the milling pot rotates, the higher the energy imparted from the balls to the powder will be. In a conventional mill, increasing the rotation speed will increase the speed of the balls inside the pot. Above a critical speed, the balls will not move; instead, they will adhere to the wall of the milling pot and sit idle. Therefore, rotation speed should not be above this critical speed. Balls should hit the starting material with high speed to impart high energy. However, maximum speed also rises the temperature of the pot culminating in decomposition of process control agents.

Milling Time

Milling time is a very important parameter in the milling process. Depending on the type of mill used, the times required vary depending on the intensity of milling and the temperature of milling. These times have to be decided for each combination of the above parameters and for a particular powder system.

Ball-to-Powder Ratio

The ratio of the weight of the balls to the powder (BPR), also called the charge ratio (CR), is an important variable in the milling process. If the capacity of milling pot is small (20 ml), 10:1 is the preferred ratio. The BPR has a significant effect on the time required to achieve required grain size. The higher the BPR, the shorter is the time required.

The Amount of Starting Material (volume occupied by starting materials).

It is necessary to have enough space for the balls and the powder to move freely in the milling pot. If both the amount of powder and the number of balls are small, the production rate is small. On the other hand, if both are in large quantity, there will not be enough space to move around and thus the energy of impact will be less. Generally 50% of the pot should be left empty.

Temperature of Milling

The temperature factor is very important in mechanical alloying and in nanocrystal synthesis. It has been reported that, during nanocrystal synthesis, the strain in the material was lower and the grain size larger when the material was ball-milled at high temperatures.[166] In our experiments, the milling pots were removed and cooled using a small fan when the duration of the milling time was more than 30 minutes. The pressure inside the milling pot was released and the ball-milling process continued thereafter to complete the milling time..

Type of Process Control Agents (PCA)

A process control agent (PCA), also referred to as lubricant or surfactant, is added to the powder mixture during milling to reduce cold welding. These can be solids, liquids, and even

gases. However, a majority of milling processes use organic compounds, which act like surface-active agents, and these PCA get adsorbed on the surface of the particles, minimizing the cold welding between powder particles, and thereby inhibiting agglomeration. In this thesis, ethanol was used as PCA. The amount of PCA required for a particular material depends on its chemical and thermal stability. If there is a possibility of oxide formation on the surface of the material, it is advisable not to use PCA that can decompose and contribute hydrocarbons to the material. In fact, one way of determining the effectiveness of the PCA is to determine the powder yield after milling. If the yield is high, the PCA is effective. If the yield is not high, then either the amount of PCA used is not requisite, or it is not the right PCA.

2.4 Characterization of Nanopowders Synthesized from High-Energy Planetary Ball-milling

The size and shape of the powder particles can be determined accurately using scanning electron microscopy (SEM) for micron size to several hundred nanometer particles. Transmission electron microscopy (TEM) can be used for nanometer sized particles. It is important to realize that powder particles are agglomerated and therefore care must be taken during particle size estimation. A powder particle may contain several coherently diffracting domains also called crystallites. Microscopic images give particle size or even grain size if sufficient resolution is available, whereas diffraction techniques give the crystallite size (powder XRD with a reliable standard material, for example, LaB_6, from The National Institute of Standards and Technology (NIST)).[167] Crystallite size and lattice strain (which may be attributed to prolonged high energy ball-milling) can be obtained by analyzing the peak broadening of the samples. X-ray diffraction peaks get broadened for the following reasons: (a) the instrumental effect of incoherent X-rays and poor focusing; (b) nanoparticles; (c) lattice strain in the crystal. The individual contribution of these to the total broadening can be separated using known standard techniques. The Scherrer equation [168] provides a simple estimate of the crystallite size using full-width-at-half-maximum (FWHM) of the diffraction peak of nanomaterials:

$$\boldsymbol{d = \frac{0.9\lambda}{B\cos\theta}} \qquad \textbf{Equation 2.2}$$

where d is the crystallite size, λ is the wavelength of the X-ray radiation (1.5418 Å from Cu Kα, and 0.7107 Å from Mo Kα), B is the peak FWHM and θ is the Bragg angle. One must measure the instrumental broadening by running a standard material, such as Si or LaB_6 to determine the strain-free line width. This must be subtracted from the total broadening. It is very important to use a standard with peaks in a similar 2θ range. Then the nanomaterial needs to be scanned in a similar 2θ range as that of a standard with identical combination of slits and collimators; an increase in the width of the peaks will be compared with the standard, and crystallite size can be calculated using Equation 2.2.

Instrument, Crystallite, and Strain Related XRD Line Broadening

Instrumental (B_i) related: Non-monochromacity of the x-ray due to poor focusing and unresolved α1 and α2 peaks.

Crystallite size (B_c) related: As more and more planes participate in XRD diffraction, peaks appear fat.

Strain (B_s) related: 'Residual Strain' arising from dislocations, coherent precipitates etc., leading to broadening.

Stacking faults (S_f) related: Non planar lattice planes contribute to peak broadening.

Thus, the total broadening B,[165] is: $B(FWHM) = B_i + B_c + B_s + B_{SF} + \ldots$

The next step is to separate the crystallite size broadening and the strain broadening.

Integral breadth analysis assumes that the total breadth Δθ of a peak to be the simple sum of d = 0.9λ/(B cosθ), and a new microstrain term, 4ε tanθ.

Given: $B_r = B_c + B_s$

$$B_c = \frac{k\lambda}{L\cos(\theta)}$$

$B_s = \eta\tan(\theta)$, substituting in B_c and B_S in B_r we can get

$$B_r = \frac{k\lambda}{L\cos(\theta)} + \eta\tan(\theta)$$

$$B_r\cos(\theta) = \frac{k\lambda}{L} + \eta\sin(\theta)$$

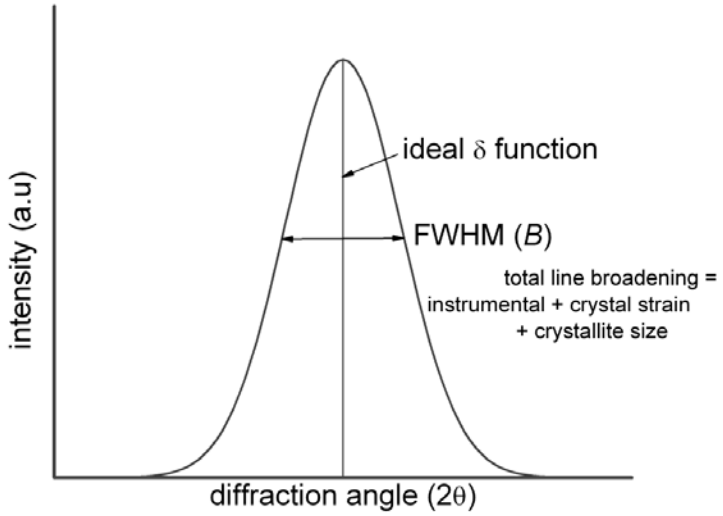

Figure 2.11: Total line broadening contribution from different sources.

The Williamson-Hall plot can be used to separate the effect of crystallite size from microstrain.[169] In this method, $B_r\cos(\theta)$ will be plotted against $\sin\theta$, which gives a straight line, the intercept of which gives the crystallite size, and the slope gives the strain.

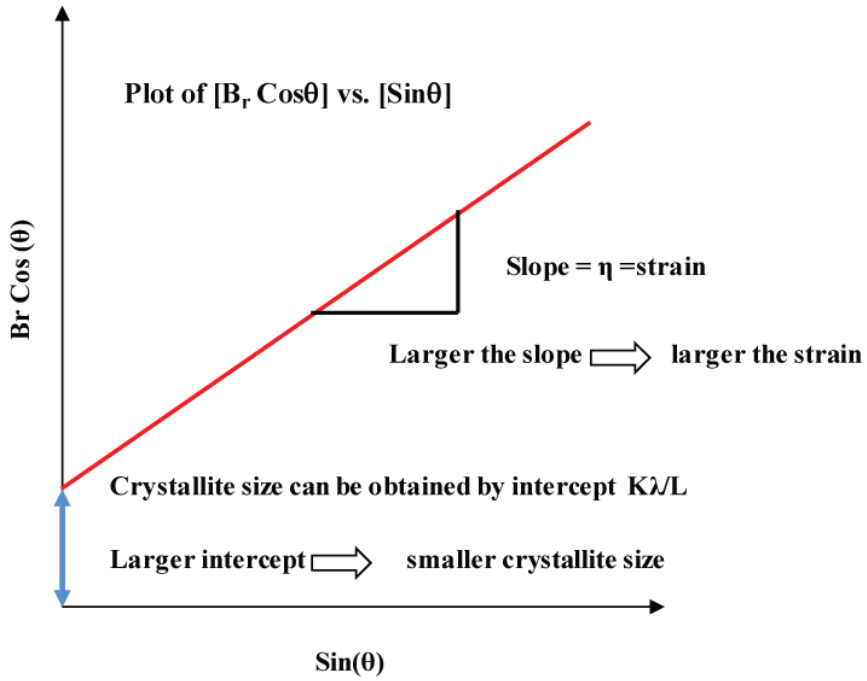

Figure 2.12: Williamson-Hall plot

Standard: Obtaining instrumental broadening

Peak No.	2θ (°)	B_i = FWHM (°)	B_i = FWHM (rad)
1			
2			
3			
4			

Nanomaterial: Obtaining crystallite broadening

Peak No	2θ (°)	Sin(θ)	B (°)	B (rad)	$B_r^2 = B^2 - B_i^2$	B_r Cosθ (rad)
1						
2						
3						
4						

Particle Size Analysis & Strain Analysis of Ball-milled $Ni_{0.05}Mo_3Sb_{5.4}Te_{1.6}$ –Worked Example

Line broadening due to instrument

Bulk Sample (as standard)			λ=0.15406 nm	
Material:	$Ni_{0.05}Mo_3Sb_{5.4}Te_{1.6}$			B^2_{Inst}
Peak (hkl)	2θ(Deg)	**FWHM(2θ)**	FWHM(Rad)=Instr. Broadening=B_{inst}	
211	22.765	**0.1753**	0.00306	9.3609E-06
310	29.5631	0.195102	0.00341	1.1595E-05
222	32.456	0.203411	0.00355	1.2604E-05
321	35.1246	0.215193	0.00376	1.4106E-05
411	40.0103	0.2225	0.00388	1.508E-05
420	42.2797	0.244531	0.00427	1.8215E-05
422	46.5246	0.251669	0.00439	1.9294E-05
440	54.2692	0.287691	0.00502	2.5212E-05
600	56.0849	0.288661	0.00504	2.5382E-05
611	57.8528	0.289542	0.00505	2.5537E-05

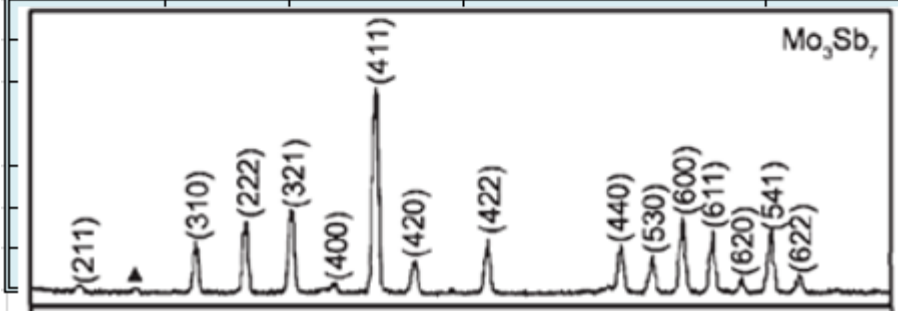

For accurate results, use (Geometric Average of Lorenzian and Gaussian shapes)

Final Broadening: Inst. Contribution is subtracted: $B_F = \sqrt{(B_o - B_{Instr})\sqrt{B_o^2 - B_{Inst}^2}}$

Line Broadening Due to Crystallite Size

Nanopowder -$Ni_{0.05}Mo_3Sb_{5.4}Te_{1.6}$										
Peak (hkl)	2θ(Deg)	θ(Rad)	cos(θ) rad	Sin(θ)	**Observed Broadening $=B_o$ (in deg)**	B_o (Rad)	Strain & Size Contribution= B_O^2	$B_F^2 = B_o^2 - B_{Inst}^2$		$B_{F\,x}$ Cosθ
211	23.036	0.20	0.9799	0.19968	**0.22541**	0.00393	1.548E-05	6.11659E-06	0.002473	0.002423
310	29.8634	0.26	0.9662	0.25767	0.293871	0.00513	2.631E-05	1.47116E-05	0.003836	0.003706
222	32.7807	0.29	0.9594	0.28218	0.30712	0.00536	2.873E-05	1.61285E-05	0.004016	0.003853
321	35.4844	0.31	0.9524	0.30473	0.330454	0.00577	3.326E-05	1.91579E-05	0.004377	0.004169
411	40.4138	0.35	0.9385	0.34541	0.366841	0.0064	4.099E-05	2.59126E-05	0.00509	0.004777
420	42.7052	0.37	0.9314	0.36411	0.364875	0.00637	4.055E-05	2.23401E-05	0.004727	0.004402
422	46.9921	0.41	0.9171	0.39869	0.412307	0.0072	5.178E-05	3.24904E-05	0.0057	0.005227
440	54.7937	0.48	0.8878	0.46015	0.533438	0.00931	8.668E-05	6.14687E-05	0.00784	0.006961
600	56.6097	0.49	0.8804	0.47416	0.566276	0.00988	9.768E-05	7.22989E-05	0.008503	0.007486
611	58.41	0.51	0.8729	0.48794	0.548797	0.00958	9.174E-05	6.62066E-05	0.008137	0.007102
							Results:			
							Intercept	**Particle Size (nm)**	**Strain(rad)**	
							0.00095	**163**	**0.0168**	

Note: To obtain FWHM for bulk (or standard) and nanopowder, always use the same 2θ range and X-ray patterns essentially under the same experimental conditions.

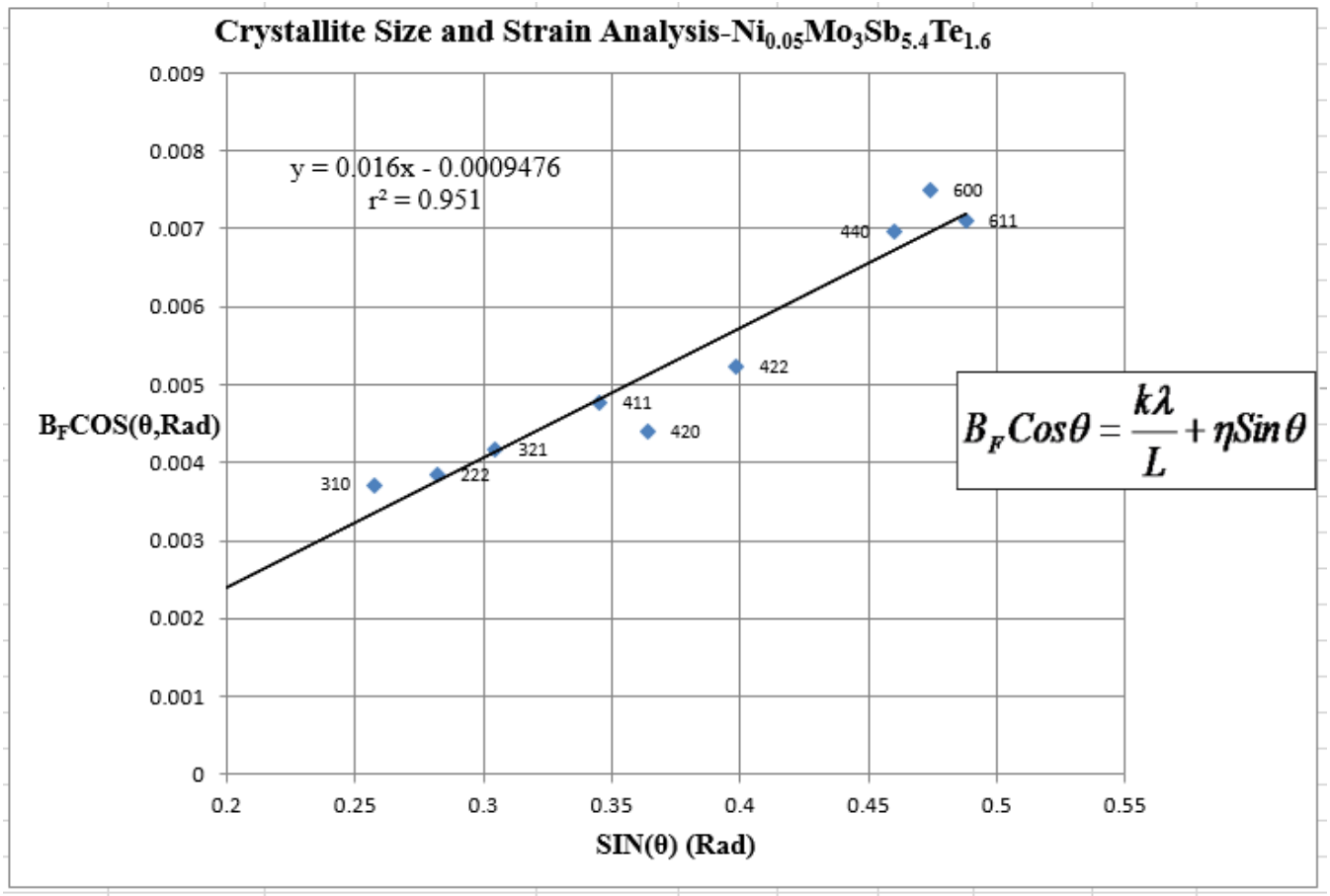

2.5 Scanning Electron Microscopy (SEM)

It has been observed that microstructures have a large impact on the TE properties of materials, especially on the thermal conductivity and the electrical conductivity.[170, 171] Microstructures also affect mechanical properties.[172, 173] For microstructural investigations, SEM is the most versatile tool that utilizes an electron beam as a sensing or illumining media, just as light in optical microscopy. SEM is capable of achieving magnification of 10,000X to 150,000X, and the limit of resolution as small as 10 nm in regular SEMs and as small as 1 nm in some sophisticated SEMs. Transmission Electron Microscopy (TEM), on the other hand, has even higher magnification, lower limits of resolution than SEM, but TEM is very expensive (couple of millions of dollars), and the maintenance costs are also high. The sample preparation for TEM investigations is time consuming (a couple of weeks in some cases), and the process

can be laborious. In addition, the interpretation of the results is not straightforward, as we need to have a solid knowledge of contrast theory to interpret microstructural features. Therefore, SEM with reasonable costs can bridge the gap between an optical microscope and TEM in terms of resolution and magnification. SEM sample preparation is easy, less time consuming, and finally easy to interpret the microstructural information. SEM comes with an elemental analysis module that provides elemental composition of the sample by analyzing the x-rays from the samples.

For our all composites morphological and microstructural studies we used University of Waterloo's Waterloo Advanced Technology Laboratory (WAT Labs)'s Zeiss Ultra | plus SEM coupled with an integrated secondary electron detector in in-lens mode (Figure 2.13)

Figure 2.13: Commercial SEM from Zeiss.

2.5.1 Specimen Preparation

For microstructural studies, a post transport property characterized disk was broken and a small piece of this sample was investigated. For sample morphological investigation, for example study size of pores, surface of the sample was analyzed. The sample under investigation was placed on an aluminum holder coated with carbon foil and transferred to SEM analysis chamber.

2.6 Transmission Electron Microscopy (TEM)

For a detailed analysis of grain boundaries and an elemental distribution, most of our samples were subjected to TEM analysis at CNRS, Université de Bordeaux, Pessac, France using JEOL 2200 FS equipped with spherical aberration (Cs) corrector. Electron-transparent specimen was prepared using Gatan's Precision Ion Polishing System (PIPS) with an operating voltage of 5 kV and low incident angle of $8^{o} - 10^{o}$ to specimen at liquid nitrogen temperature. Precautions were taken to avoid mechanical and ion beam damage.

Specimen Preparation for HRTEM

In general, the samples were grinded and then dispersed in ethanol through intense sonication. 10 microliter of the solution was dropped on the TEM grid (holey carbon) and dried in vacumm chamber. HRTEM image of 0.16 bulk/NiSb sample is displayed in the following figure.

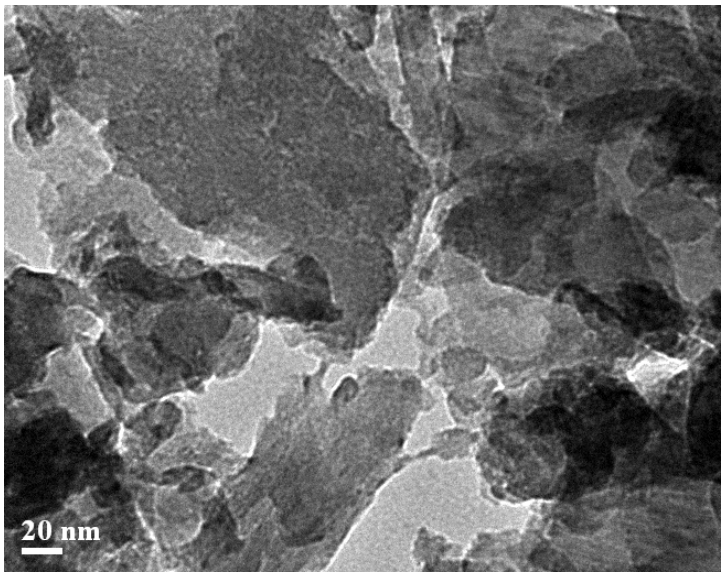

HRTEM image of 0.16 bulk/NiSb sample

2.7 Consolidation Methods

2.7.1 Hot Consolidation of Composite Powders

Hot-pressing (HP) is a pressure assisted consolidation method to obtain a densified sample of metallic or ceramics or semiconductors by inserting powder into a die and applying force uniaxially using two pressing rams (also called pressing punches).[174]

The consolidation of nanocomposites was accomplished by means of the uniaxial hot-press machine model no. FR210-30T-ASA-160-EVC equipped with high temperature vacuumed furnace system (also called heat zone) with 30 ton (27,200kg) pressing force capability built by Oxy-Gon Industries, Inc. The die used for the hot-press is shown in the Figure 2.14.

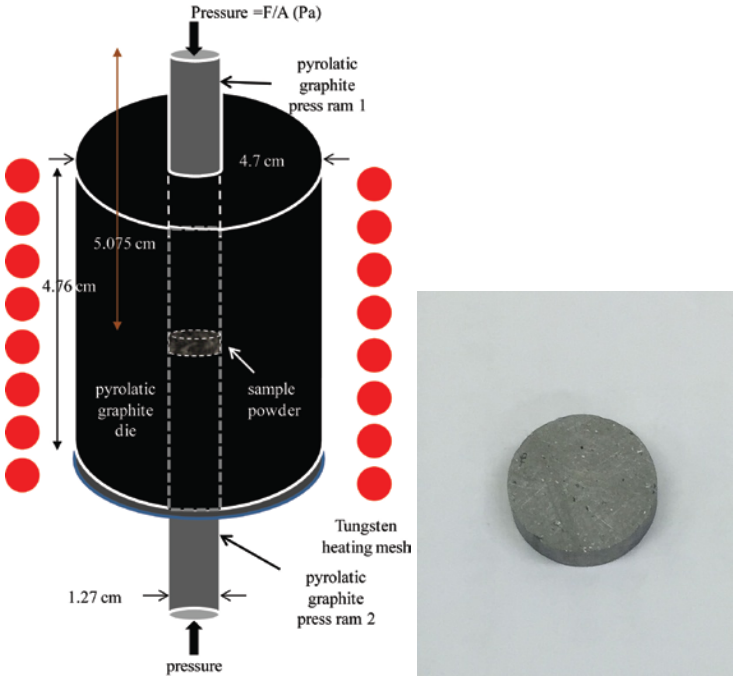

Figure 2.14: Schematic showing the essential elements of the die surrounded by the heating mesh. The right image shows a 1.26 cm diameter pellet.

It consists of two vertically aligned solid cylinders as pressing rams capable enough to provide couple of tons of force using hydraulic system and one pressing die. Both are made of pyrolytic graphite. It is also possible to use pressing rams made of titanium zirconium

molybdenum (TZM) and graphite die encased in a steel jacket to protect the die and heating mantle. The physical dimensions of the die and pressing rams are shown in the Figure 2.14; also shown is the pellet obtained by hot-pressing. In case of very high pressing force beyond 800 kg, it is strongly advisable to use a die encased in a steel shield.

The die is enclosed in furnace called “heat zone” (also called furnace). The die will be positioned in the middle of two heaters made of tungsten. The heat zone is cooled by a watercirculating jacket to avoid transfer of heat to the environment. To keep the heat zone inert an inlet port is located at the bottom of the chamber and exit port is located at the top of the chamber through an inline pressure relief valve. The pressure inside the heat zone is measured by a rough chamber pressure gauge. The gas system consists of a gas inlet valve, flowmeter, and pressure relief valve. Gas inlet gauge is connected to respective gas cylinders (Ar, N etc.). A rotary pump is used as a roughing pump. Hot- pressing usually carried out under 0.3 – 0.5 psi in nitrogen or Ar atmosphere. Connected to the furnace chamber is a hydraulic system (AUTOPAK Ne) built by Carver, Inc. This hydraulic system is capable enough to provide 30 ton load on pressing rams.

The heat zone chamber has a front right hinged door to allow full access to the workspace inside the furnace. A tungsten mesh heating element, 4” in diameter and 5” height, is encased by a shield assembly of six layers - two layers are from tungsten and four are from molybdenum radiation shields. Half portion of this assembly is located inside the furnace and the other half is mounted to the door of the furnace. Power to this heating mesh is being furnished by a special water cooled cables.

Pressing parameters such as temperature, and elapsed time inside the furnace are all monitored by a controller console Eurotherm 2704 mounted on the front control panel Oxy-Gon assembly. The pressing parameters can be set by used defined multi-step programs. Figure 2.15 shows the Oxy-Gon 30 ton capacity hot-press machine.

Figure 2.15: Uniaxial hot-pressing machine. Inset shows heat zone.

Hot-pressing was carried out as follows: a graphite foil of 1.25 cm in diameter (~same as the pressing ram's diameter) was placed on top of the ram and the ram was slowly pushed halfway inside the pressing die. From the other opening of die, sample powder of approximately 2 g was poured and tapped to settle. Then a second piece of graphite foil was placed on this side of the die and pressing ram was inserted thus the sample powder is sandwiched between two graphite foils. Figure 2.14 depicts the aforementioned procedure. After placing the die inside the heat zone, a pressing force of 700 kg is applied via the control buttons located on Carver hydraulic assembly. Once the pressure reaches 700 kg (54 MPa), the furnace door was closed and evacuated to 0.008 psi. The processing of filling the chamber with Ar was carried out using backfilling button. Once the pressure reached 0.5 psi, the pre-programmed pressing profile shown in Figure 2.16 was executed using the Eurotherm console.

Te

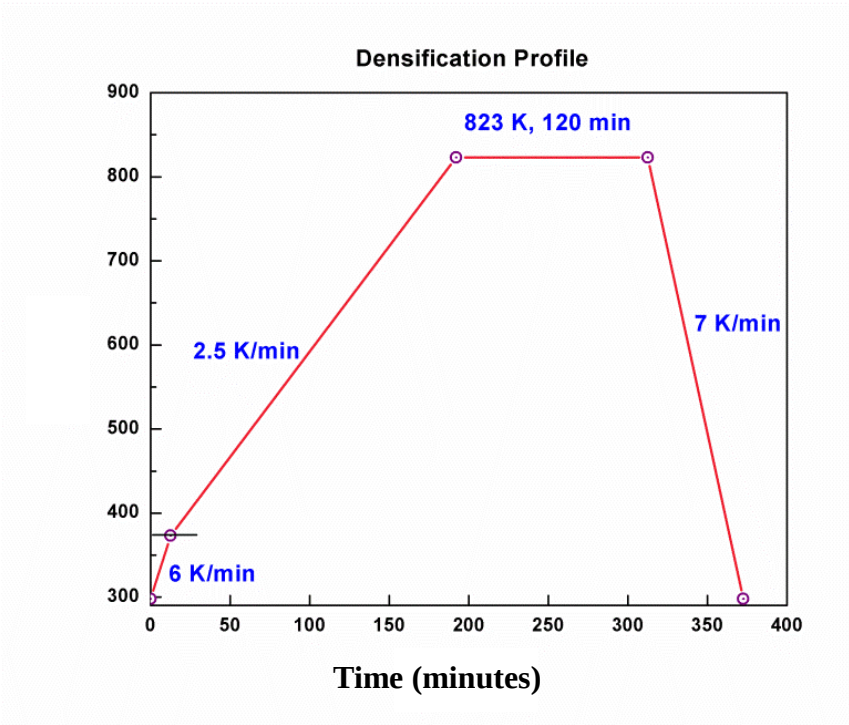

Figure 2.16: Heating profile for consolidation by hot-pressing under 700 kg of set point.

Based on the applied pressing set point, *m*, (in kg) and the area of the pressing ram *A* (in m^2), the effective force, *F*, on the sample (in Newton, N), can be calculated as (with *g* = gravity constant):

$$F = mg$$

Then pressure in Pa can be calculated according to the following relation: $P = \frac{F}{A}$

In our case for 700 kg, the pressing force was 6860 N, and the corresponding pressure was 54 MPa. For the same pressing ram and for different set points the pressures are listed in the Table 2.1. After hot-pressing the furnace was allowed to cool to room temperature and the pellet was recovered using simple cold pressing tools.

Table 2.1: Hot-press set points vs. pressure

Set point (kg)	Pressing force (N)	Pressure (MPa)
300	2940	23.2
400	3920	31.0
500	4900	38.7
600	5880	46.4
700	6860	54.2
800	7840	61.9
900	8820	69.7
1000	9800	77.4

2.7.2 Spark-Plasma Consolidation of Composite Powders

Spark-plasma sintering (SPS) is a pressure assisted sintering technique based on generating high temperature sparks in the voids between powder particles by electrical discharge at the beginning of ON-OFF DC pulse energizing.[175] The heat can go up to 10,000 ºC in a localized area inside the matrix of the material.

In SPS, a force as high as 300 tons and very high DC current generate heat that facilitates rapid mass transfer mechanism to give higher relative density than any other densification process. This technique is applicable to conductive, nonconductive, and various composite materials. It provides a very high density and strong bond between the particles. The spark energy vaporizes contaminants and oxidizes the surface of particles prior to neck formation. Joule heat is concentrated on particle surfaces, facilitating faster mass transfer through diffusion of materials into voids. Figure 2.17 illustrates cycles of DC pulse current generation, diffusion, plasma, and Joule heating inside the sintering die.

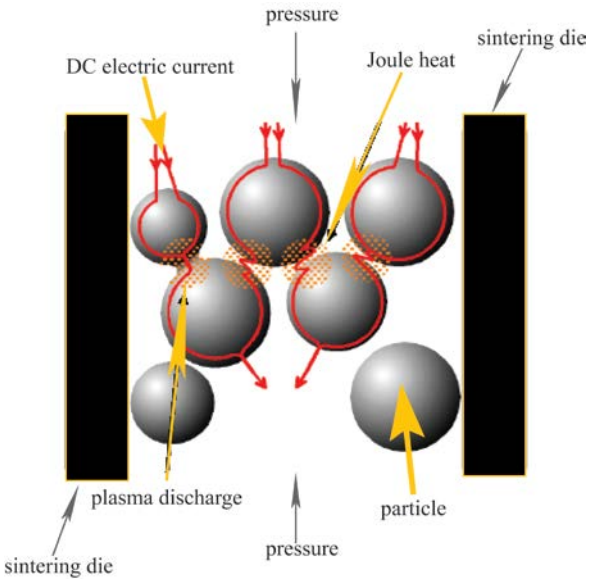

Figure 2.17: Pulsed DC current flow through powder particles.

The three Al_2O_3 containing samples and their bulk counterpart were consolidated in our investigations using spark-plasma sintering at National Institute for Materials Science (NIMS), Japan. The SPS-825 with 25.5-ton capacity from Fuji Electronic Industrial Co. was used for consolidation. The samples were heated from room temperature to 873 K under 60 MPa pressure, and were allowed to stay at that temperature for 5 minutes and then cooled to room temperature at the rate of 2.25 K/min.

2.8 Density Measurement

After consolidation by either hot-pressing or spark-plasma sintering, the densities of the samples were determined using the density measurement kit Sartorius YDK01 from Sartorius mechatronics and deionized water was used as an immersion liquid. Since composites can be porous, bubbles after the immersion of solid were not uncommon. These bubbles were removed while weighing the sample in the liquid. The following formula is used to calculate the density:

$$\rho\,(\text{density}) = W(\text{air})[\,\rho\,(\text{fluid}) - \rho\,(\text{air})] \,/\, [W(\text{air}) - W(\text{fluid})]$$

where W (air), ρ (fluid), W(fluid) are weight of the sample in air, density of fluid at room temperature, weight of sample in fluid respectively, and ρ (air) = 0.0012 g cm^{-3}.

Theoretical Composite Density and Specific Heat Calculations

The theoretical density and theoretical specific heat can be calculated using the "Rules of Mixtures", which are mathematical expressions whereby the property of the composite is expressed in terms of the quantity of its constituents as indicated below:

$$\rho_c = \sum_{i}^{n} \rho_i v_i$$

where ρ_i and v_i are the respective density and volume fractions respectively. For two component simple system: $\rho_{c=f\rho_1+(1-f)\rho_2}$ where f is the volume fraction.

Similarly, specific heat C_v can be calculated using the formula:

$$Cv = \sum_{\mathrm{k}}^{\mathrm{n}} C_{pk} \mathrm{m_k}$$

where, C_{pk} and $\mathrm{m_k}$ are specific heat and mass fraction of the kth phase.

Weight Percent to Volume Percent Conversion

On many occasions, we had to convert weight% to volume%. The following relation was used to convert weight percent to volume percent:

$$f = W_{\mathrm{nano}}\, \rho_{\mathrm{bulk}} / (W_{\mathrm{nano}}\, \rho_{\mathrm{bulk}} + W_{\mathrm{bulk}}\, \rho_{\mathrm{nano}})$$

where W_{nano} and W_{bulk} are the weights of nanoinclusion and bulk respectively. ρ_{nano} and ρ_{bulk} are the densities of nanoinclusion and bulk.

2.9 Thermal Diffusivity (α_d) Measurement

Ever since the flash method for measuring the thermal diffusivity was introduced by Parker in 1961, it has been very popular among the thermo-physical experts.[176] It became popular because of its elegance with which a thermal measurement is largely reduced to a time

measurement, a generally easier and more accurate task.

Figure 2.18: Schematics of Flashline 3000 from Anter Corporation.

For a particular temperature segment, the operating software is configured to seek optimum pulse power at which optimum operation is expected, as dictated by sample thickness. At each step, the indexing mechanism (calibrated motor) positions each sample in the beam path; then energy pulse is generated from the Xenon lamp and impinges on the sample. The transient rise in the temperature in the opposite face of the sample will be monitored by the InSb detector placed above the sample, providing thermogram. The software contains an extensive comparison program that analyzes the raw data, performs corrections according to various theories,[177, 178] and determines the "goodness of fit" regression for each of them. In general, it takes the measured data and sequentially applies the corrections to each pulse. Each corrected thermogram is then compared to the theoretical (calculated) one that represents the ideal case (very narrow pulse, no radiative heat losses, etc.). The difference within each pair will be analyzed by least-square calculations, and the one with the minimal deviation is considered to be the best.

Assuming ideal conditions of the adiabatic sample and instantaneous pulse heating, the diffusivity (cm^2sec^{-1}) is given by[176]:

$$d = 0.1388 \frac{l^2}{t_{0.5}}$$ **Equation 2.3**

where l is the thickness of the sample and $t_{0.5}$ is the time required to reach 50% of the maximal rise in temperature measured at the rear end of the sample; this rise in signal is illustrated in Figure 2.19. Heat loss from conduction, convection, and radiation will be corrected using the software. Before the measurement, the thickness of the samples will be measured with a micrometer (in our case 1.8 mm – 2.2 mm thickness is preferred) and will be sprayed with graphite paint to reduce reflection from the face on which light impinges on the material.

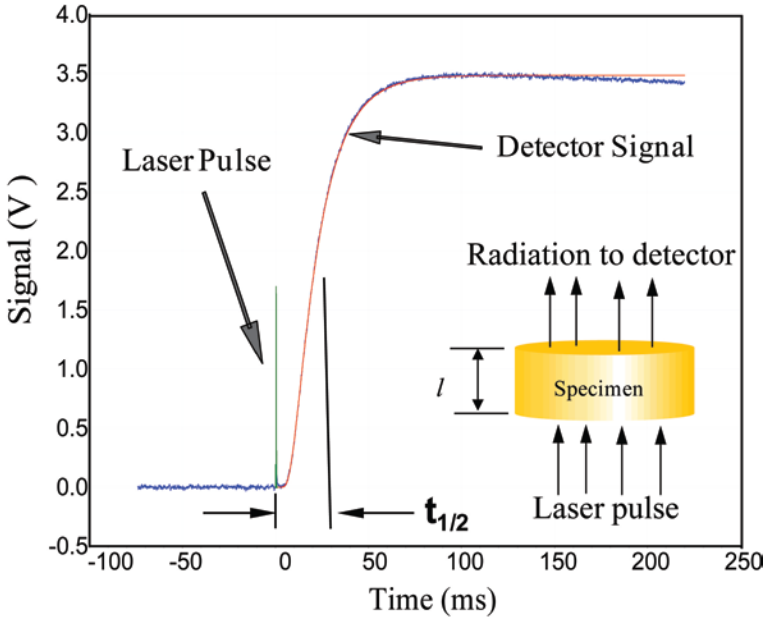

Figure 2.19: Signal rise with respect to time from Flashline 3000.

For all of our samples, the thermal diffusivity α_d was measured by means of the flash technique, [176, 177] using an Anter FlashLine^{TM} instrument (Figure 2.18), which is equipped with a Xenon flash lamp to shine light on specimens and liquid nitrogen cooled indium-antimonide (InSb) infra-red detector. A steady flow of argon was maintained throughout the experiment inside the furnace to avoid contamination of the samples. Disk-shaped pellets with a diameter of ~12.6 mm were investigated as prepared by hot-pressing (bulk/C_{60}, bulk/MWCNT, bulk/NiSb samples) and spark-plasma sintering (bulk/Al_2O_3 samples), respectively. The thermal

conductivity, κ, was obtained using $\kappa = \alpha_d \rho C_P$, where ρ is density and C_P is the specific heat estimated using the rule of mixtures (Section 2.8).

Uncertainties Associated with the Measurements

The thermal diffusivity values can be obtained by parameters such as thickness, and a characteristic time function that describes the rise in the heat from the front surface to the back surface. Since thermal diffusivity is directly related to the square of the sample thickness, errors associated with the thickness measurement lead to a significant error in diffusivity values. Errors such as a lack of parallelism on the front and back surfaces and a lack of smoothness in the samples can induce a large error margin. Thus, precautions needs to be taken while preparing the sample.[179]

2.10 Electrical Transport Properties Measurement

It has been observed that thermal and electrical properties can have a strong dependence on crystallographic direction, sometimes by orders of magnitude. Even consolidated polycrystalline samples can exhibit slight anisotropy, thus it is advisable to measure more than one sample of a given material. This will help to average any possible sample differences.

2.10.1 Simultaneous Measurement of Resistivity and Seebeck Coefficient Using ZEM 3

The electrical conductivity, σ, and the Seebeck coefficient, S, were measured simultaneously using four-probe and differential methods respectively with commercially available high temperature ULVAC-RIKO ZEM-3 system (Figure 2.20)

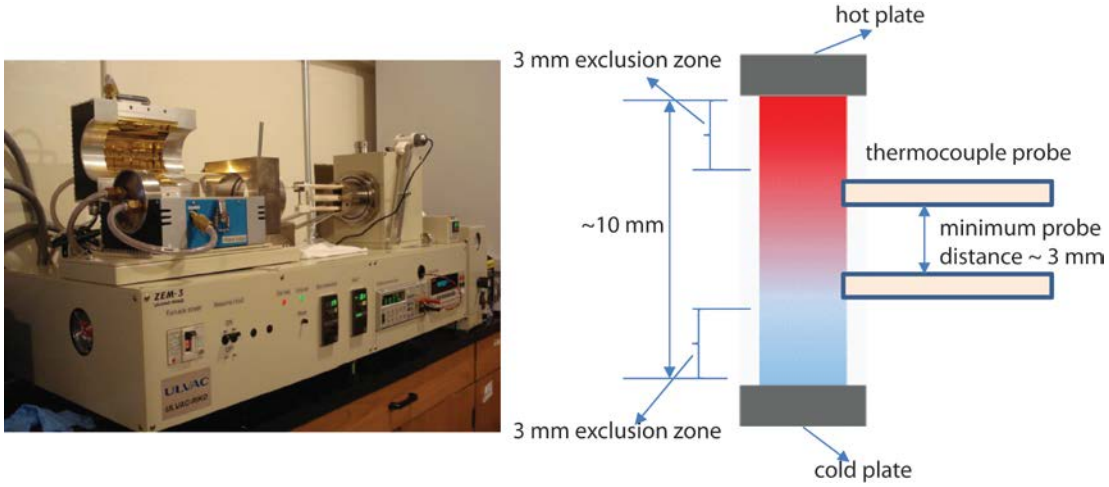

Figure 2.20: ULVAC ZEM-3 measuring system with sample and attached probes.

A low-speed diamond saw was used to cut the disk-shaped samples into quadratic prisms of 11 × 2 × 2 mm with all surfaces pairwise parallel to each other. So obtained rectangular bar was positioned between the upper and lower block of the furnace. After the sample was heated to a certain temperature, the upper block was heated to create a temperature difference. The Seebeck coefficient was determined by measuring the upper and lower temperatures T_H and T_C with the thermocouples pressed against the side of the sample followed by measuring the voltage difference between those two points of contacts. The resistance, *R*, is determined by the DC four point method, where a constant current *I* is supplied to both ends of the sample. The voltage drop d*V* between the two probes is then measured to obtain $R = \mathrm{d}V/I$. The Seebeck coefficient, *S*, and resistivity, ρ, were calculated as:

$$S = \frac{\Delta V}{\Delta T} = \frac{(V_H - V_L)}{(T_{H-}T_L)}$$

$$\rho = R\frac{A}{l}$$

where *R* is the sample resistance, *A* is the cross sectional area of the sample, and l is the distance between the probes.

S was determined from the slope of the thermo-electromotive force, ΔV, versus temperature gradient, Δ*T*, between 10 K < 15 K < 20 K and an average was taken. Inert atmosphere was maintained inside the furnace using –0.9 MPa helium pressure during the measurement.

2.10.2 Issues in Electrical Property Measurement:

Establishing excellent electrical contacts is very important when measuring the electrical properties. Large contact resistance because of impurities can result in Joule heating at the contacts, which can induce a considerable error in the electrical properties. Some TE materials are susceptible to oxide layer formation at the surface, and therefore, careful surface preparation is a crucial step in achieving good adhesion and low resistance contacts. Apart from this, most of the TE materials are semiconductors, thus, requiring metal-semiconductor contacts.

Another source of error is the placement of thermocouple probes in relation to the voltage leads. Accuracy in Seebeck coefficient measurements relies on determining the temperatures T_H and T_L, precisely at the location of the voltage probes, V_H and V_L, respectively. If we are using a differential thermocouple, care must be taken to thermally anchor the ends of the thermocouple as closely as possible to the voltage contacts and electrically insulate them from the sample.

2.11 BJH Pore Size Distribution and BET Surface Area Characterization

Porous solids have a higher surface area than the corresponding dense solids, because pore walls contribute more to the total surface area of the material. Knowing the accurate pore size and their distribution will help in elucidating the phonon scattering cross section. Pore size and particle size distribution also affect the mechanical properties of TE materials.[172] Surface area and porosity will also help us to explicate the transport properties.

Nitrogen adsorption at its boiling temperature (77 K) is the most widely used technique to determine the total surface area and pore size distribution. When a gas or vapor phase is brought into contact with a solid, a thin layer of gas will be deposited on the surface due to weak Van der Waals forces. This allows us to determine specific surface area, pore size distribution, and pore

volume. The starting point in this direction is the determination of the adsorption isotherm, and this is obtained by measuring the amount of nitrogen adsorbed across a wide range of relative pressure at 77 K. Similarly, desorption isotherm is achieved by measuring the gas removed as pressure is reduced. During desorption, evaporation of adsorbed gas evaporates from the mesopores usually takes place at a relative pressure lower than that of capillary condensation giving rise to hysteresis.

The International Union of Pure and Applied Chemistry (IUPAC) has classifies hysteresis into four groups based on pore shape, their distribution, and particle shapes.

Types H1 and H2 hysteresis: Type H1 hysteresis has been associated with porous materials with a narrow distribution of relatively uniform (cylindrical pores), whereas materials that give rise to H2 hysteresis contain more complex pore networks consisting of pores with ill-defined pore size and shape.

Types H3 and H4 hysteresis: These types of hysteresis are the characteristics of solids, consisting of aggregates or agglomerates of particles forming slit shaped pores in lose plate aggregates with nonuniform (type H3) size pores sizes or uniform (type H4) pores sizes.

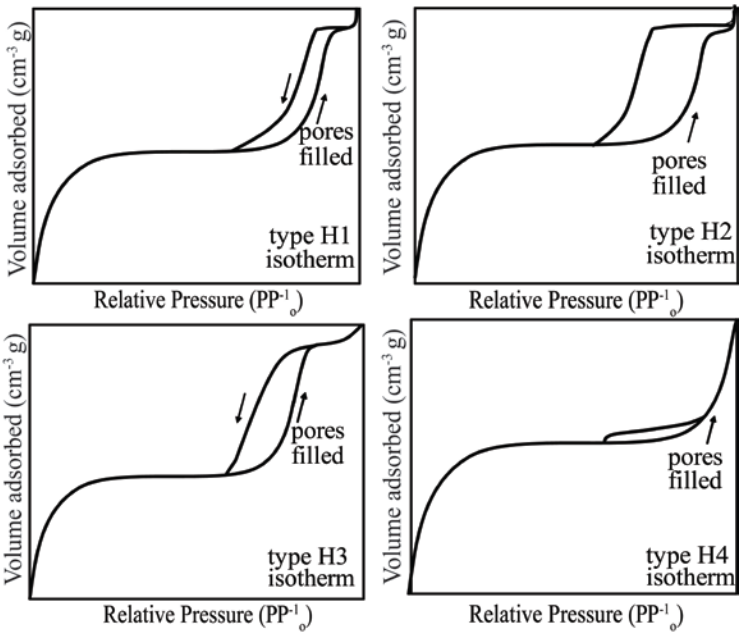

Figure 2.21: Isotherms (IUPAC classification).

IUPAC classifies pores based on their sizes: macropores (>50 nm), mesopores (2 nm – 50 nm), and micropores (< 2nm).[180] In our investigations, the composites $Ni_{0.05}Mo_3Sb_{5.4}Te_{1.6}$/SiC and $Ni_{0.05}Mo_3Sb_{5.4}Te_{1.6}/Al_2O_3$ were subjected to BET, pore size distribution and surface area results were discussed while addressing the transport properties and thermal effective properties. For pore size distribution, we applied the BJH method, put forward by Barrett, Joyner, and Halenda (BJH),[181] and for surface area we adopted the multipoint BET method. To grasp the effect of pore size distribution, surface area, and cumulative pore volume on thermal properties, nitrogen adsorption-desorption measurements were carried out at University of Waterloo using BET - Autosorb–1C (Model: AX1C–MP–LP) adsorption analyzer from Quantachrome instruments (Figure 2.23). Before the measurements, powder form of every sample of $Ni_{0.05}Mo_3Sb_{5.4}Te_{1.6}$/SiC and $Ni_{0.05}Mo_3Sb_{5.4}Te_{1.6}/Al_2O_3$ were outgassed in the degas port of the adsorption apparatus. For all samples the multiplot BET (P/P_o versus $(W((Po/P)-1))^{-1}$, were perfectly straight and had a correlation coefficient of 0.99. W is the weight of adsorbed gas at a relative pressure, P/P_o. Both composites exhibited isotherm H4. As the content of SiC and Al_2O_3

nanoparticles increased, gap between adsorption and desorption curves widened, indicating that both composites have plate like aggregates, which was further reinforced by TEM images.

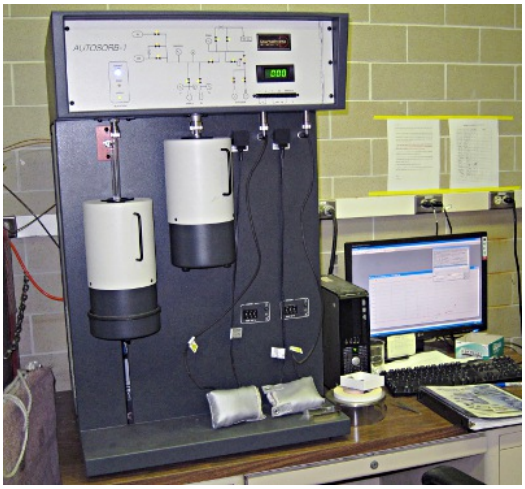

Figure 2.22: Surface area and pore size analyzer (Quantachrome Autosorb-1 Instrument).

Chapter 3

Effects of Additions of Carbon Nanotubes on the Thermoelectric Properties of $Ni_{0.05}Mo_3Sb_{5.4}Te_{1.6}$[9]

This chapter is reprinted in adapted form from my own work[107] Reprinted from J. Solid State Chem., 226, Nandihalli, Nagaraj, Gorsse, Stéphane, Kleinke, Holger, "Effects of additions of carbon nanotubes on the thermoelectric properties of $Ni_{0.05}Mo_3 Sb_{5.4} Te_{1.6}$" 164-169, Copyright 2015, with permission from Elsevier.

3.1 Experimental

3.1.1 Phase Purity Analysis

First we synthesized the bulk material $Ni_{0.05}Mo_3Sb_{5.4}Te_{1.6}$. The detailed procedure for synthesis is discussed in Section 4.1.1. CNT were produced using chemical vapor deposition. The outer diameters of the tubes were 20 nm – 50 nm, and the lengths were ~10 μm. The tubes were used without purification. All these materials were stored in a glove box filled with argon.

Once the requisite amount of bulk material was obtained, the large sample was divided into four equal parts for bulk (no CNT), 1 mass-% CNT, 2% CNT and 3% CNT. Bulk/CNT composites were prepared using ball-milling, as this method is assumed to disperse the CNT homogeneously inside the bulk matrix. Appropriate amounts of both materials were placed in a 20 ml ball-milling bowl from FRITZSCH GmbH with 5 mm ZrO_2 balls and 10 ml ethanol. The bowl was subjected to 300 rounds per minute for 20 minutes, followed by drying on a Petri dish.

---

[9] Reprinted from J. Solid State Chem., vol. 226, Nandihalli, Nagaraj, Gorsse, Stéphane, Kleinke, Holger, , "Effects of additions of carbon nanotubes on the thermoelectric properties of $Ni_{0.05}Mo_3 Sb_{5.4} Te_{1.6}$" Pages 164–169, Copyright (2013), with permission from Elsevier.

To ascertain the effect of ball-milling alone on physical properties, a part of the bulk sample was ball-milled with the same duration as the other composites and also characterized.

The process of consolidation through hot-pressing is discussed in Section 2.7.1. The disk-shaped pellets obtained in this process were of a diameter of 12.6 mm and a height of ~ 2 mm. These were polished first, and then their densities were measured using the Archimedes principle (Section 2.8). The densities are found to be 8.25 g cm^{-3}, 8.22 g cm^{-3}, 7.97 g cm^{-3}, 7.56 g cm^{-3} and 7.08 g cm^{-3} for bulk, ball-milled (BMilled), 1%, 2%, and 3% CNT respectively.

Table 3.1 Experimental densities of various $Ni_{0.05}Mo_3Sb_{5.4}Te_{1.6}$/CNT composites at 295 K.

Sample	Density of pellet ρ/(g cm^{-3})	Relative Density (%)
Bulk	8.25	94.7
BMilled	8.22	94.2
1% CNT	7.97	92.0
2% CNT	7.56	87.8
3% CNT	7.07	82.6

3.2 Characterization

Figure 3.1 illustrates the XRD patterns of pure $Ni_{0.05}Mo_3Sb_{5.4}Te_{1.6}$ (bulk), ball-milled bulk, $Ni_{0.05}Mo_3Sb_{5.4}Te_{1.6}$/CNT composites and pure CNT obtained after hot-pressing and the transport measurement. The introduction of CNT and the ball-milling did not result in the formation of any new unwanted side products.

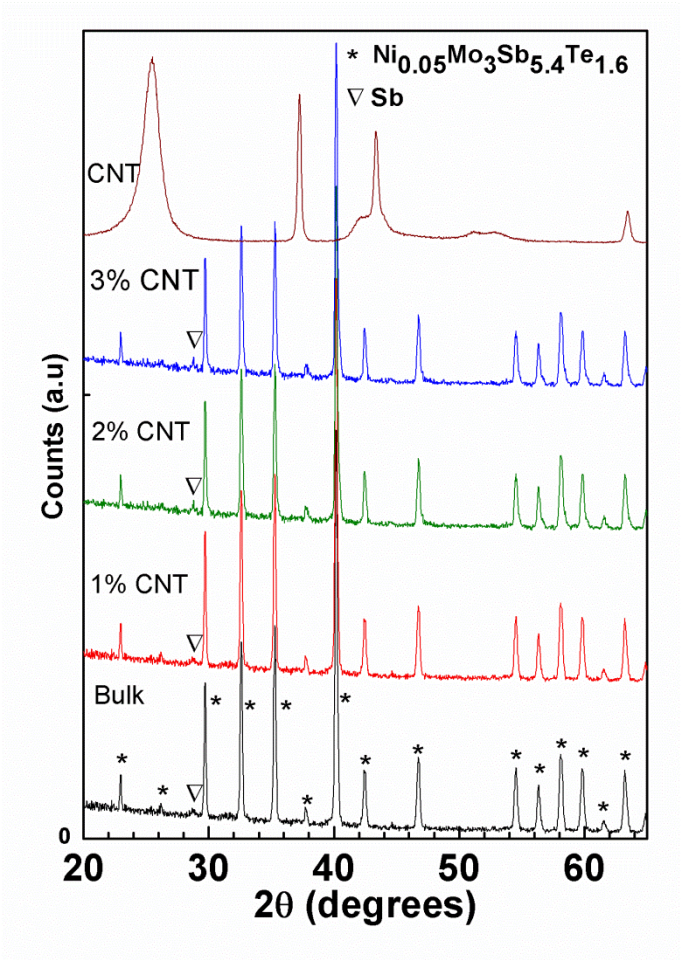

Figure 3.1: XRD patterns of (from top to bottom) pristine CNT, composites, and bulk.

Figure 3.2 shows the microstructural analysis of hot-pressed samples. Immediately after the transport property measurements, the pellets were broken and subjected to scanning electron microscopy (SEM) analysis using a Zeiss Ultra | plus SEM coupled with an integrated secondary electron detector with in-lens mode. The accelerating voltages were adjusted to capture high resolution images. Figure 3.2(a), 3.2(b), 3.2(c) and 3.2(d) respectively show SEM images of bulk, 1%, 2% and 3% CNT. Islands of CNT are found to be clustered between the grain boundaries of the particles. Figure 3.2(a) and (b) show that both bulk and composites have the same bulk particle sizes (1 μm – 2 μm); therefore, we conclude that ball-milling process itself

did not significantly alter the physical properties. Any changes must thus be coming from the CNT additions.

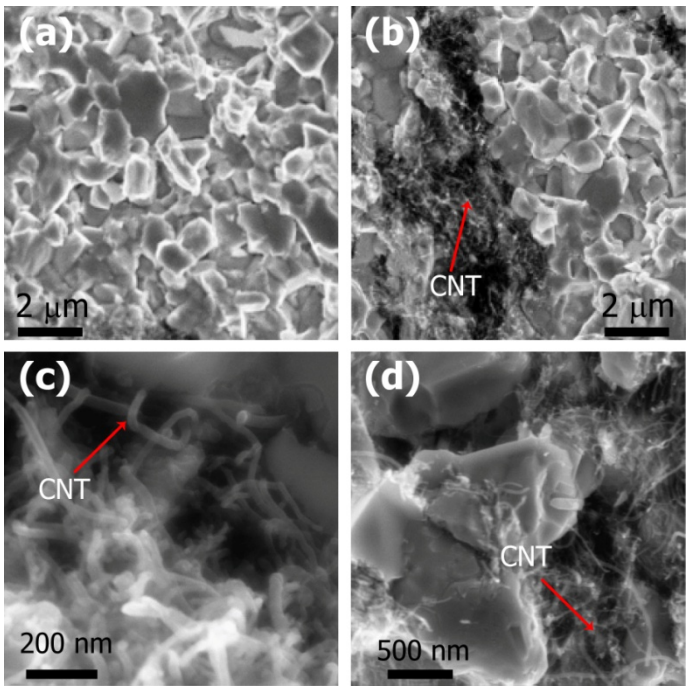

Figure 3.2: SEM images of hot-pressed (a) bulk $Ni_{0.05}Mo_3Sb_{5.4}Te_{1.6}$; (b) bulk with 1% CNT; (c) bulk with 2% CNT; (d) bulk with 3% CNT.

To investigate possible changes induced by ball-milling and hot-pressing on CNT, we determined the Raman shifts in pristine CNT and CNT present inside the composites (Figure 3.3). The samples were excited by a source with a wavelength of 633 nm, 4 mW power and an operational bandwidth from 800 to 2000 nm using Horiba Jobin Yvon LabRAM HR 800 Raman spectrometer. The disorder-induced D band, occurring between 1330 cm^{-1} and 1360 cm^{-1} in graphitic carbon structures, is expected to be observed in MWCNT.[182, 183] This band is attributed to the presence of defects such as vacancies, foreign atoms etc. Comparing the frequencies of the D band for both pristine and composite CNT (1327 cm^{-1} vs. 1328 cm^{-1}), we can see that no significant amounts of defects were created during ball-milling or hot-pressing. The same is true for the tangential G band, which remained at 1580 cm^{-1} after ball-milling and hot-pressing.

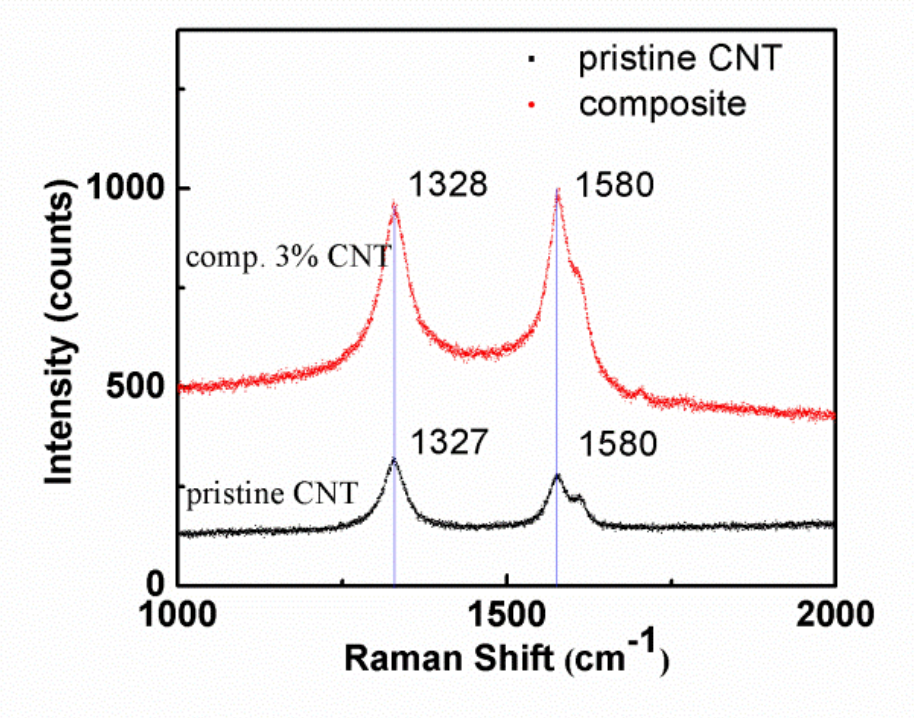

Figure 3.3: Raman spectra of pristine CNT (bottom) and bulk with 3% CNT (top)

For TEM analysis, the specimen was prepared as discussed in Section 2.6. A very minute detailed topographical visualization and the elemental mapping of carbon, molybdenum, and antimony were performed on 3% CNT. Elemental mapping was done in energy dispersive X-ray spectroscopy (EDX) configuration.

The elemental distributions are shown in Figure 3.4. The areas with high C concentration (Figure 3.4(b)) show the CNT, while the areas with high Mo and Sb contributions indicate the presence of the bulk material (Figure 3.4(c) and (d)). The latter reveal the presence of nanometer size (20 nm – 50 nm) bulk particles as well.

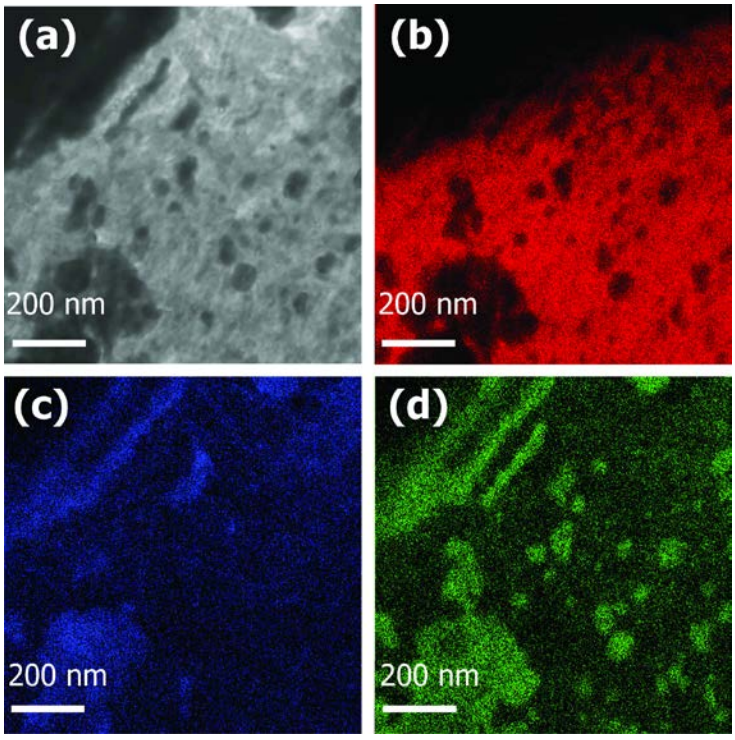

Figure 3.4: TEM images of hot-pressed bulk $Ni_{0.05}Mo_3Sb_{5.4}Te_{1.6}$ with 3% CNT. (a) Surface morphology; (b) carbon map; (c) molybdenum map; (d) antimony map.

Figure 3.5 depicts the sizes and crystallinity of the CNT. At the bottom right of Figure 3.5(b), a cross sectional view of a CNT is given: its outer diameter is ~30 nm, which matches the specifications provided by the supplier. No evidence for a reaction of the CNT with the bulk materials was found.

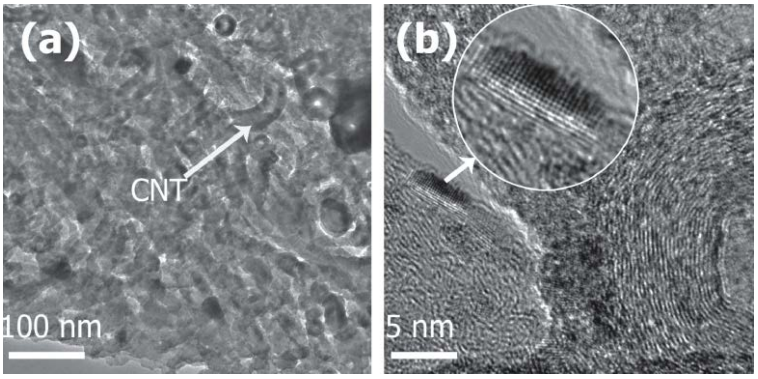

Figure 3.5: TEM images of hot-pressed bulk $Ni_{0.05}Mo_3Sb_{5.4}Te_{1.6}$ with 3% CNT showing crystalline CNT.

3.3 Physical Property Measurements

The instruments and the procedure to characterize thermal and electrical properties are covered in Sections 2.9 and 2.10 respectively.

3.4 Results and Discussion

Previously we reported the charge carrier concentration of $Ni_{0.06}Mo_3Sb_{5.4}Te_{1.6}$ to be around 4×10^{21} cm^{-3}.[184] Typically, these materials exhibit high electrical conductivity, moderate Seebeck coefficient, and relatively high thermal conductivity. The electrical conductivity of our bulk sample without CNT decreases from σ = 1400 $\Omega^{-1}cm^{-1}$ at 325 K to 950 $\Omega^{-1}cm^{-1}$ at 760 K (Figure 3.6), displaying the expected behavior. The conductivity of the ball-milled sample is insignificantly higher, and appears to follow the same temperature dependence, roughly proportional to $T^{-3/2}$ below 700 K. This temperature dependence is indicative of dominant phonon scattering if the carrier concentration remains constant, as observed before. As the content of the CNT increases, there is a systematic reduction in the conductivity, as well as a reduction in the temperature dependence, i.e. the curves become flatter with increasing CNT content approaching a $T^{-1/2}$ dependence. Both reductions can be explained with increased scattering at the increasing interfaces.

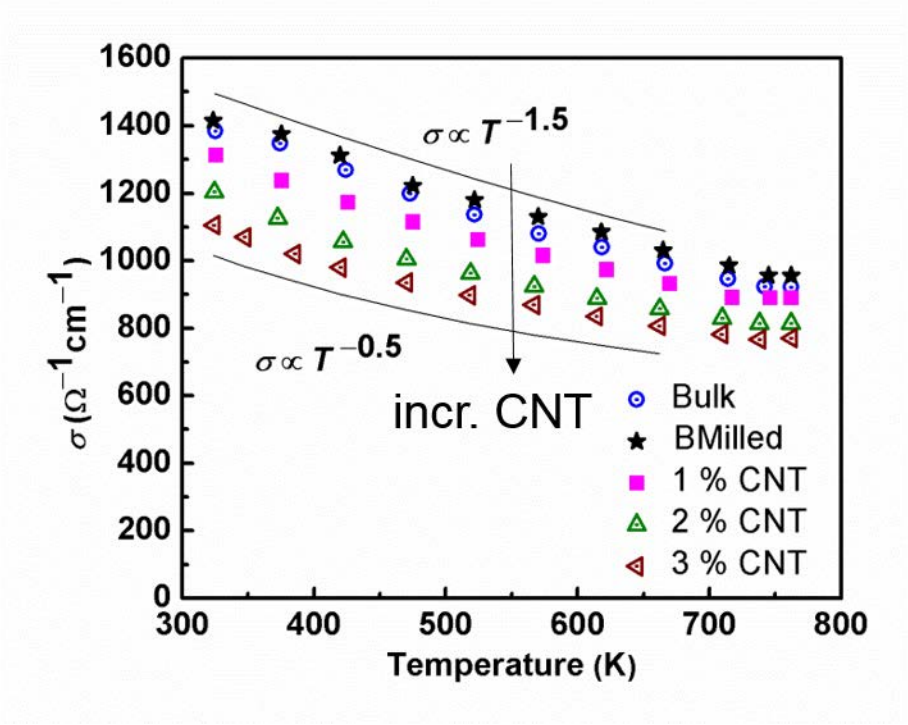

Figure 3.6: Electrical conductivity of various $Ni_{0.05}Mo_3Sb_{5.4}Te_{1.6}$/CNT composites.

For the composites at 325 K, the electrical conductivity values range from σ = 1311 $\Omega^{-1}cm^{-1}$ (1% CNT) to 1204 $\Omega^{-1}cm^{-1}$ (2% CNT) and finally 1105 $\Omega^{-1}cm^{-1}$ (3% CNT). Assuming an experimental error of ± 5%, the differences are significant. Going beyond 700 K, the conductivity starts to flatten mostly likely because of the increasing participation of the intrinsic carriers. Around 760 K, the difference between bulk and 3% CNT sample is 150 $\Omega^{-1}cm^{-1}$, which amounts to ~20% difference. To provide an overview, the high temperature data are summarized in Table 3.2.

Table 3.2: Thermoelectric properties of various $Ni_{0.05}Mo_3Sb_{5.4}Te_{1.6}$/CNT composites at 760 K.

	Bulk	BMilled	1% CNT	2% CNT	3% CNT
$\sigma/(\Omega^{-1}cm^{-1})$	950	976	870	820	780
$S/(\mu V\ K^{-1})$	140	137	140	130	135
$P.F./(\mu W\ cm^{-1}K^{-2})$	17.5	17.2	16.5	13.6	13.8
$\kappa/(W\ m^{-1}K^{-1})$	4.0	4.0	3.7	3.6	2.8
ZT	0.32	0.31	0.33	0.30	0.40

A similar trend was observed in composites of the same bulk material with C_{60}, but the decreases in the electrical conductivity for bulk/C_{60} samples were larger compared to the present composites. At 325 K, the conductivity values for bulk, 1%, 2%, and 3% C_{60} samples were σ = 1475 $\Omega^{-1}cm^{-1}$, 1114 $\Omega^{-1}cm^{-1}$, 826 $\Omega^{-1}cm^{-1}$, and 727 $\Omega^{-1}cm^{-1}$, respectively, and at 665 K, the values were 975 $\Omega^{-1}cm^{-1}$, 769 $\Omega^{-1}cm^{-1}$, 588 $\Omega^{-1}cm^{-1}$ and 546 $\Omega^{-1}cm^{-1}$, respectively. This considerable difference in electrical conductivity between the two composites likely stems from the amorphization of C_{60} under pressure, while the CNT character remained basically unchanged.

As depicted in Figure 3.7, all samples have very similar Seebeck coefficient values, all increasing from about 60 $\mu V\ K^{-1}$ at 325 K to 130 $\mu V\ K^{-1}$ - 140 $\mu V\ K^{-1}$ at 760 K. Evidently the impact of the increased scattering upon introduction of the CNT on the Seebeck coefficient is canceled by the low Seebeck coefficient of the CNT itself,[185] as the overall Seebeck coefficient results from the properties of both the bulk and the nanomaterial as well as the interfaces.[186] On the other hand, the composite Bi_2Te_3/MWCNT (0.7 mass-%) exhibits reduced electrical conductivity and significantly enhanced Seebeck coefficient compared to the respective bulk sample.[187] For example, at 297 K, bulk Bi_2Te_3 has σ = 1380 $\Omega^{-1}cm^{-1}$ and S = –83 $\mu V\ K^{-1}$, compared to the Bi_2Te_3/MWCNT composite with σ = 825 $\Omega^{-1}cm^{-1}$ and S = –114 $\mu V\ K^{-1}$. For the same material, the Seebeck coefficient increases upon MWCNT addition from –92 $\mu V\ K^{-1}$ to –124 $\mu V\ K^{-1}$ at 500 K mainly because of the decrease in carrier concentration from 8.1

$\times 10^{19}$ cm^{-3} to 1.4 $\times 10^{18}$ cm^{-3}. The same trends were found in $(Bi_{0.2}Sb_{0.8})_2Te_3$/MWCNT composites.[116]

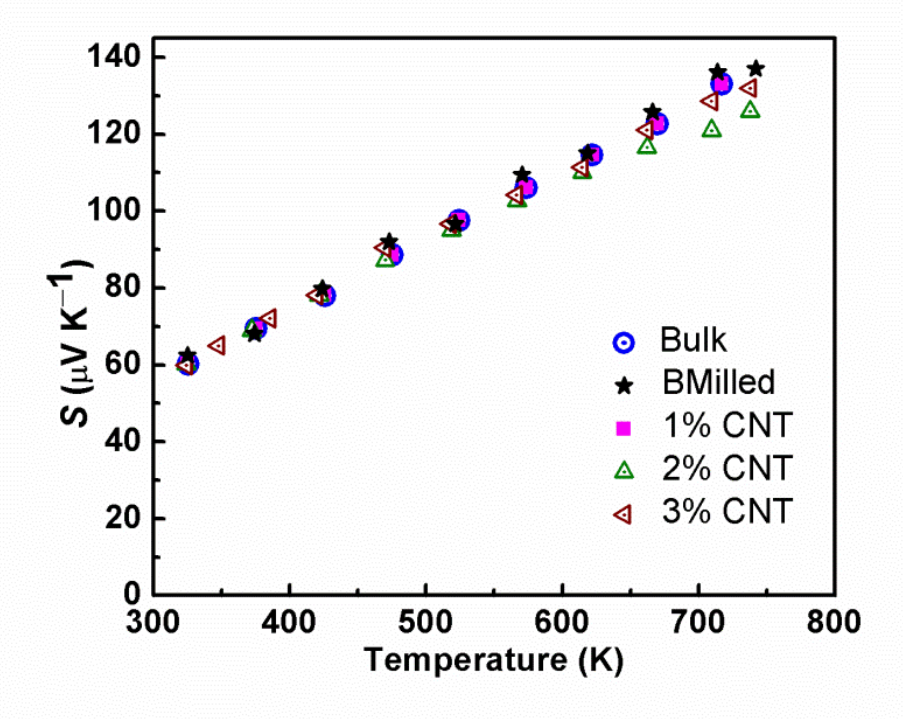

Figure 3.7: Seebeck coefficient of various $Ni_{0.05}Mo_3Sb_{5.4}Te_{1.6}$/CNT composites.

The power factor $P.F. = S^2\sigma$ increases linearly with temperature (Figure 3.8) like the Seebeck coefficient, similar to $Ni_{0.05}Mo_3Sb_{5.4}Te_{1.6}/C_{60}$.[188] *P.F.* ranges from 4 μW cm^{-1}K^{-2} to 5 μW cm^{-1}K^{-2} at 325 K. As the temperature increases, *P.F.* increases fastest for the bulk and the ball-milled bulk, surpassing 17 μW cm^{-1}K^{-2} at 760 K. For 2% and 3% CNT, *P.F.* remains below 14 μW cm^{-1}K^{-2}.

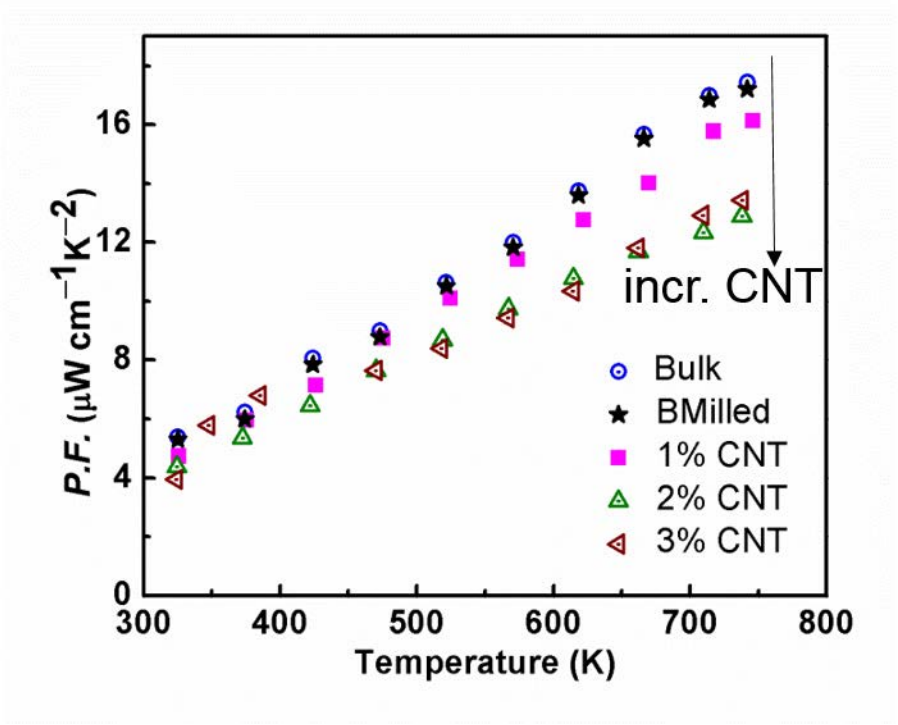

Figure 3.8: Power factor of various $Ni_{0.05}Mo_3Sb_{5.4}Te_{1.6}$/CNT composites.

The thermal conductivity data are presented in Figure 3.9. All these samples exhibit the expected negative temperature dependence of the thermal conductivity, κ. For example, κ (bulk) decreases from 5.0 W $m^{-1}K^{-1}$ at 325 K to 4.0 W $m^{-1}K^{-1}$ at 760 K. Ball-milling did not cause a significant change (assuming an experimental error of ±5%), as the κ values of the ball-milled sample without CNT are 5.1 W $m^{-1}K^{-1}$ at 325 K and 4.0 W $m^{-1}K^{-1}$ at 760 K. Adding CNT led to a significant reduction in κ, for example down to 3.8 W $m^{-1}K^{-1}$ at 325 K and 2.8 W $m^{-1}K^{-1}$ at 760 K in case of the 3% CNT sample. These reductions are smaller than in case of our previously reported composites with C_{60}, where the 3% sample showed a reduction from the bulk's value of 5.0 W $m^{-1}K^{-1}$ down to 2.5 W $m^{-1}K^{-1}$ at 325 K.

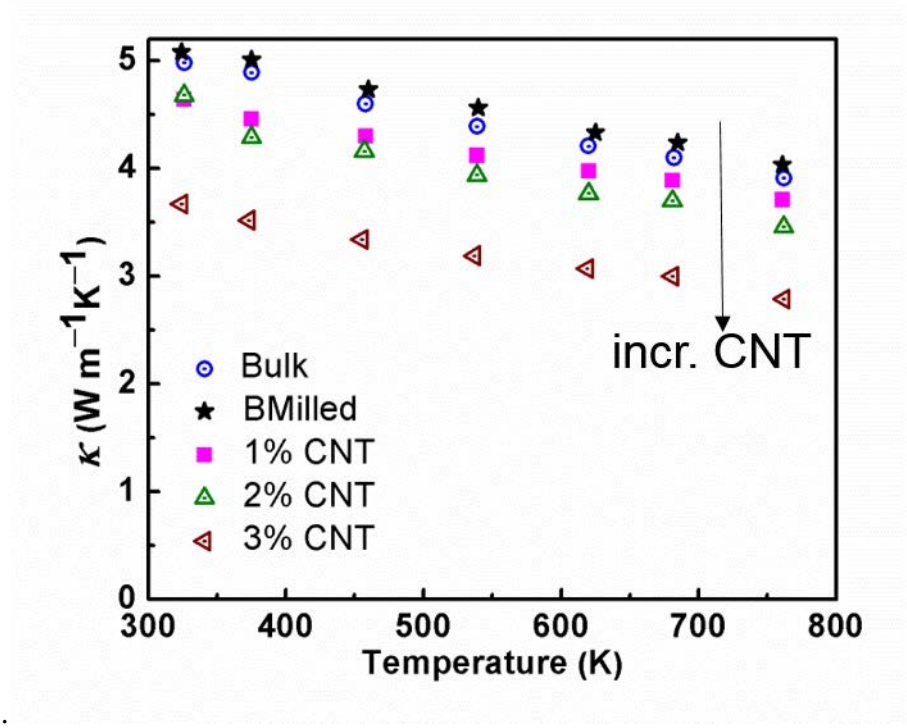

Figure 3.9: Thermal conductivity of various $Ni_{0.05}Mo_3Sb_{5.4}Te_{1.6}$/CNT composites.

To comprehend the effect of CNT on lattice thermal conductivity, we calculated κ_l for all samples by subtracting κ_e from the total thermal conductivity as discussed in Section 1.4.1.2 (Estimation of Lattice Thermal Conductivity Contribution to Total thermal Conductivity). Calculated L_0 values at various temperatures and displayed in Supplementary Information (Figure 3.12)

As shown in Figure 3.10, the lattice thermal conductivity decreases with increasing temperature - a clear indication of increased phonon-phonon scattering. Comparing the trends of these composites to previously reported $Ni_{0.05}Mo_3Sb_{5.4}Te_{1.6}/C_{60}$, we can surmise that CNT are also reducing lattice thermal conductivity. Using $L_o = 2.44 \times 10^{-8}$ V^2K^{-2}, we reported a lattice thermal conductivity κ_l of 3.6 W $m^{-1}K^{-1}$ for bulk and 2.7 W $m^{-1}K^{-1}$ for 1% C_{60} at 325 K. Similarly, using $L_o = 2.14 \times 10^{-8}$ V^2K^{-2} in our present bulk, κ_l (4.0 W $m^{-1}K^{-1}$) is larger than κ_e, and for the sample with 1% CNT, κ_l is 3.72 W $m^{-1}K^{-1}$. Comparing κ_l at 325 K for both, we can conclude that phonons are major carriers of heat in bulk as well in composites.

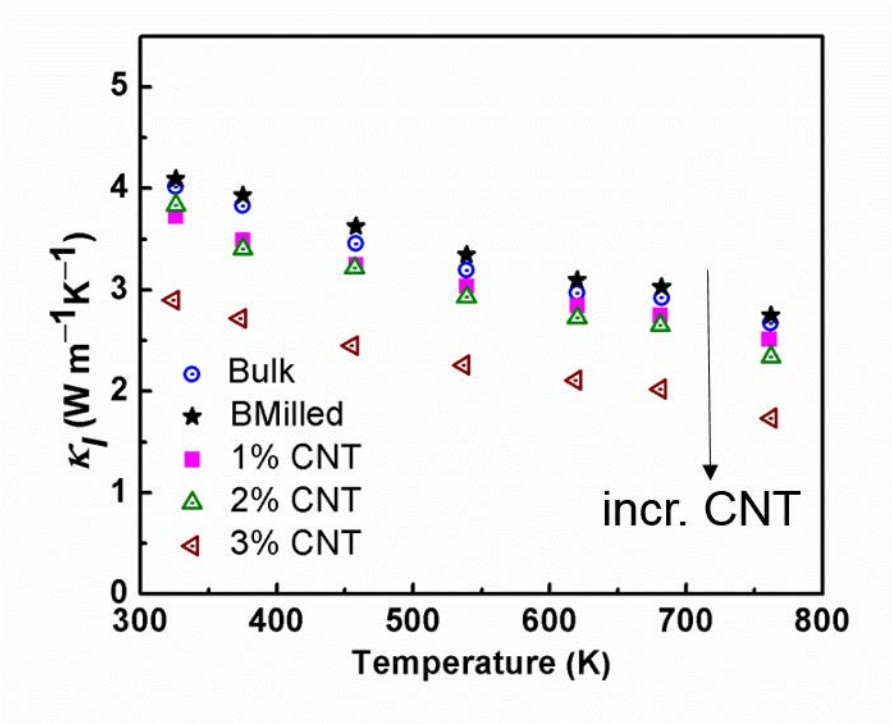

Figure 3.10: Lattice thermal conductivity of various $Ni_{0.05}Mo_3Sb_{5.4}Te_{1.6}$/CNT composites.

Finally, we calculated the *figure-of-merit*: $ZT = S^2\sigma\kappa^{-1}T$ by applying a polynomial fit to $P.F. = S^2\sigma$, and using κ as directly determined. As typical for members of the $Mo_3(Sb,Te)_7$ family,[113] *ZT* rises quickly with increasing temperature (Figure 3.11). For the bulk material, *ZT* increases from 0.035 at 325 K to 0.32 at 760 K. The ball-milled bulk without CNT behaves very similarly. The CNT additions led in part to improvements (3% CNT: *ZT* (760 K) = 0.40), in part to (insignificantly) lower *ZT* values (2% CNT: *ZT* (760 K) = 0.30). At 760 K, *ZT* improves by 25% after adding 3% CNT, because the reduction in thermal conductivity outweighs the reduction in the power factor. For the composites with C_{60} published in 2013, the *ZT* values at 665 K are 0.22, 0.25, 0.23, and 0.25 for bulk, 1%, 2% and 3% C_{60}, respectively.

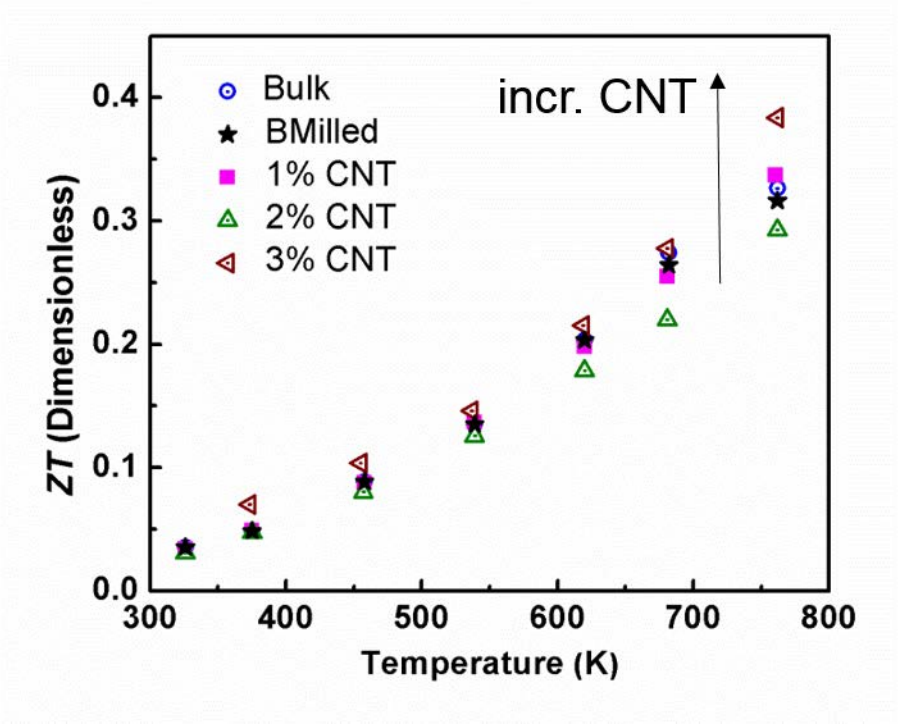

Figure 3.11: *Figure-of-merit* of various $Ni_{0.05}Mo_3Sb_{5.4}Te_{1.6}$/CNT composites.

3.5 Conclusions

For the first time we have proven that adding CNT may enhance the thermoelectric properties of $Mo_3(Sb,Te)_7$ materials. XRD analysis of hot-pressed samples revealed that CNT did not react with the bulk material. Raman characterization of free CNT and of CNT embedded in the bulk sample indicated that ball-milling and hot-pressing did not induce any noticeable defects on CNT. For 3% CNT, the reduction in thermal conductivity at 325 K is 33%, compared to 6% for 1% and 2% CNT composites. In case of the 3% CNT sample, this reduction outweighs the impeded electrical performance, ultimately yielding a significant improvement of the *figure-of-merit* by 25%. This improvement is slightly higher than the one achieved after adding CNT to $MnSi_{1.75}Ge_{0.02}$ (20%).

In the future, we intend to investigate the performance and stability of these composites beyond 760 K and the effect of using non-graphitic nanotubes (for example Bi nanowires) on the

thermoelectric properties. Apart from ball-milling, we planned to explore other methods to disperse CNT homogeneously to enhance phonon scattering, while simultaneously preserving electrical conductivity as much as possible by embedding metal nanoparticle coated CNT.

3.6 Supplementary Information

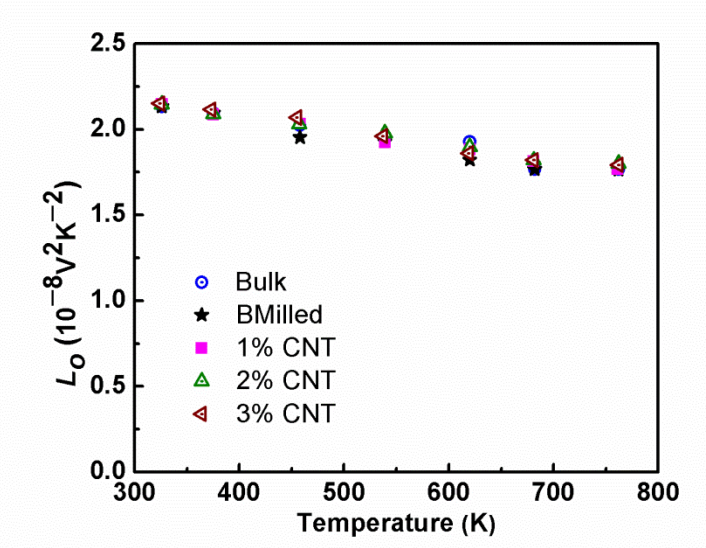

Figure 3.12: Figure showing the calculated variation in Lorenz numbers with temperature for various $Ni_{0.05}Mo_3Sb_{5.4}Te_{1.6}$/CNT composites.

Acknowledgment: Dr. Shirley Tang and Xiguang Gao for Raman spectra of MWCNT

Chapter 4

Thermoelectric Properties of $Ni_{0.05}Mo_3Sb_{5.4}Te_{1.6}$ Embedded with SiC and Al_2O_3 Nanoparticles[10]

4.1 Experimental Section

4.1.1 Synthesis

We conducted four solid-state reactions, with 4.6 g of starting materials each, to obtain enough pure phase of $Ni_{0.05}Mo_3Sb_{5.4}Te_{1.6}$ (Section 2.1.1). SiC nanoparticle powder was purchased from Alfa Aesar, whose primary particle size is 45 nm – 55 nm, according to TEM analysis. Similarly, Al_2O_3 nanopowder of 13 nm primary particle size (99.8% purity) was purchased from Sigma-Aldrich. The bulk $Ni_{0.05}Mo_3Sb_{5.4}Te_{1.6}$ obtained from four solid-state reactions was thoroughly mixed as follows: all samples were added to mortar and pestle and stirred to get one big homogeneous mixture and this mixture was added to a 50 ml vial. The vial was subjected to high frequency vibrations in the Vortex-Mixture (Fisher-Scientific) for twenty minutes and then divided into two equally sized heaps. These heaps were again divided into four of ~2.3 g each to finally add SiC and Al_2O_3 nanoparticles.

The desired amounts of SiC and Al_2O_3 nanopowders to give composites with three different volume fractions were suspended in acetone and subjected to sonication to minimize agglomeration during mixing. Small amounts of each suspension were stepwise added to bulk inside the mortar and stirred until depletion of the whole suspension, yielding two reference samples without nanoadditions and three samples each with different amounts of SiC and Al_2O_3 for a total of eight samples.

Consolidation of the SiC composites and its reference sample ("bulk") was carried out using the 30-ton Oxy-Gon hot-press (Section 2.7.1). This densification procedure yielded

[10] With the permission from the European Journal of Inorganic Chemistry. N. Nandihalli, Q. Guo, S. Gorsse, A.U. Khan, T. Mori, H. Kleinke, *Eur. J. Inorg. Chem.* 2016 (2016) 853-860.

densified disk-shaped pellets with a diameter of 12.7 mm and a thickness of ~ 2 mm. Their densities were measured using Archimedes principle (Section 2.8) and displayed in Table 4.1.

Table 4.1: Experimental densities of various $Ni_{0.05}Mo_3Sb_{5.4}Te_{1.6}$/SiC composites at 295 K.

f	Density of pellet ρ/(g cm^{-3})	Relative Density (%)
0 (bulk)	8.21	94.2
0.010	7.96	92.8
0.020	7.93	91.0
0.034	7.85	90.7

In our study, the three Al_2O_3-containing samples and bulk were consolidated using the spark-plasma sintering (SPS) technique at National Institute for Materials Science (NIMS), Japan (Section 2.7.2). The densities were determined using Archimedes' principle (Table 4.2).

Table 4.2: Experimental densities of various $Ni_{0.05}Mo_3Sb_{5.4}Te_{1.6}/Al_2O_3$ composites at 295 K.

f	Density of pellet ρ/(g cm^{-3})	Relative Density (%)
0 (bulk)	8.59	98.5
0.0100	8.36	96.5
0.0216	8.27	96.0
0.0325	8.13	95.0

4.1.2 Phase Purity Analysis

To investigate whether any side products formed during SiC inclusion or during consolidation or during transport property measurement, we subjected hot-pressed and SPS'ed samples for powder XRD analysis after all transport properties were characterized. Figure 4.1 and Figure 4.2 show XRD patterns of both batches. No changes were detected. No X-ray peaks representing SiC and Al_2O_3 appeared in any samples because of their low content. Similarly in other composites, $Bi_{0.3}Sb_{1.7}Te_3$ with SiC: f = 0.004 and $Bi_{0.5}Sb_{1.5}Te_3$ with SiC: f = 0.01, no SiC peaks were reported. [109, 189]

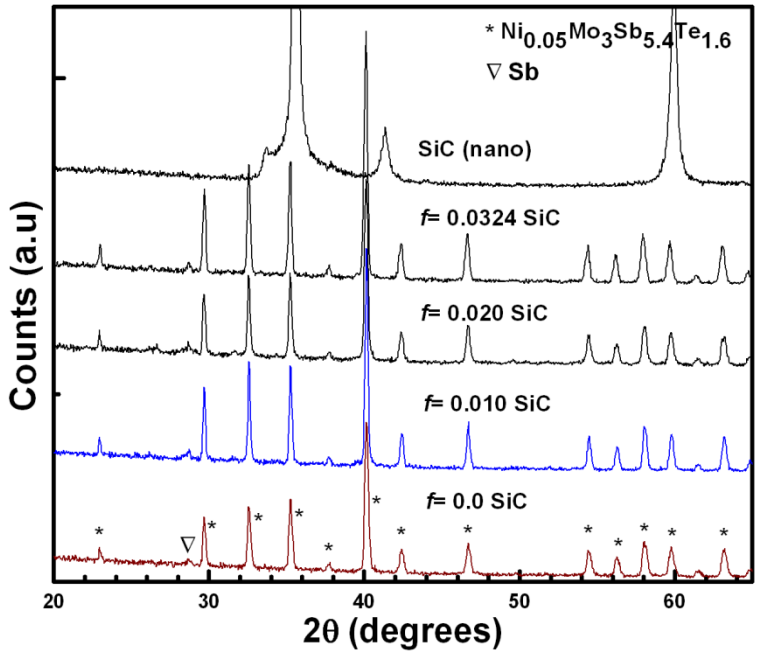

Figure 4.1: XRD patterns of pristine SiC, composites and bulk (from top to bottom).

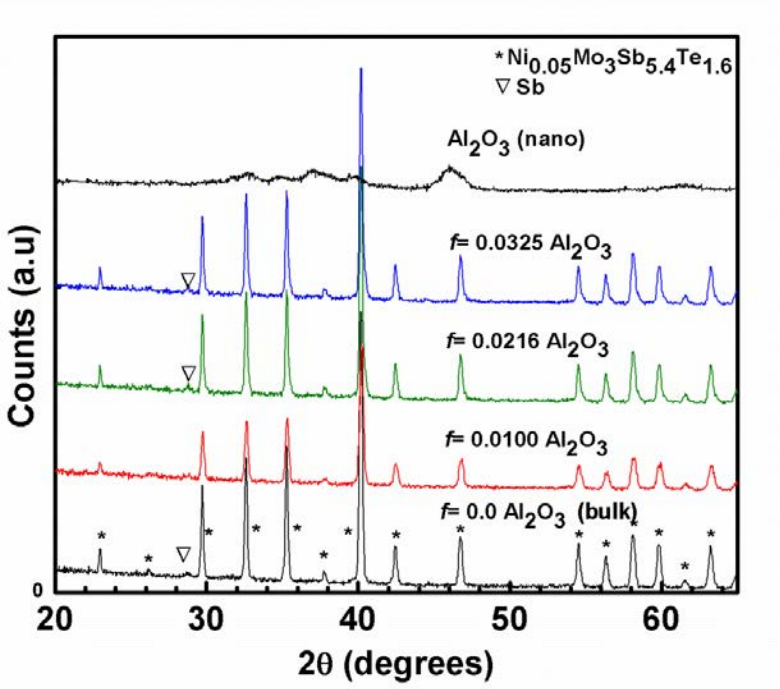

Figure 4.2: XRD patterns of pristine Al_2O_3, composites and bulk (from top to bottom).

4.1.3 Microstructural Investigations

Microstructural and morphological features were studied using University of Waterloo's Waterloo Advanced Technology Laboratory (WATLabs)'s Zeiss Ultra | plus SEM coupled with integrated secondary electron detector in in-lens mode (Section 2.5). Figure 4.3 shows the microstructures of the sample with SiC: f = 0.034 after hot-pressing. Some voids of 20 μm – 30 μm are found (Figure 4.3(a)). The bulk has a wide range of particle sizes, ranging from 2 μm to 10 μm ((Figure 4.3(b)). The SiC nanoparticles occur in agglomerated form because nanoparticles have the general tendency to form agglomeration due to their high surface energy (Figure 4.3 (c,d)).[190] It is evident that the process of nanoinclusion needs to be further optimized, noting that we had already sonicated the nanopowder in acetone to separate nanoparticles in an attempt to minimize this issue.

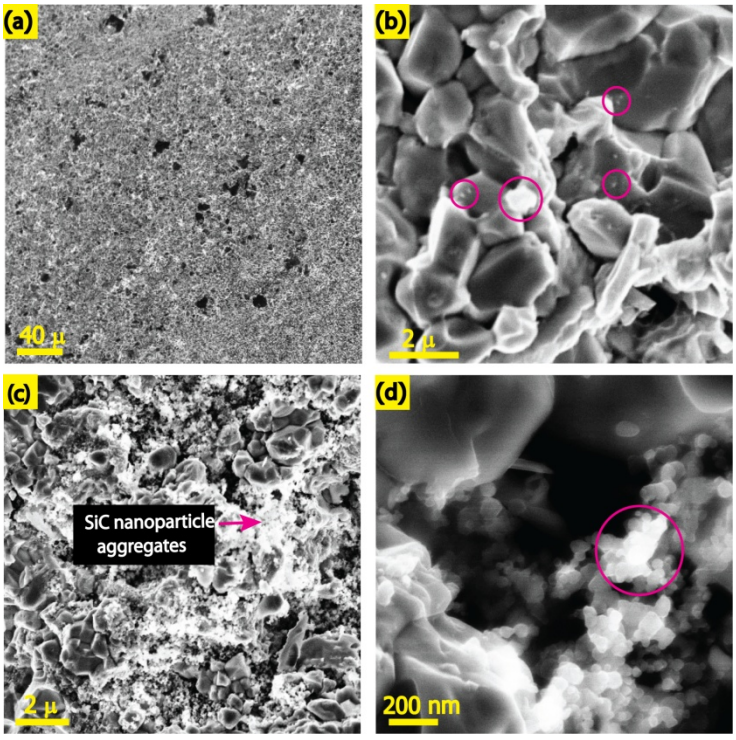

Figure 4.3: SEM images of hot-pressed $Ni_{0.05}Mo_3Sb_{5.4}Te_{1.6}$/0.034 SiC. (a) Surface with 20 µm - 30 µm voids; (b) SiC aggregates on bulk particles; (c) clumped aggregates of SiC; (d) SiC aggregates between the bulk particles.

To study micro grain boundaries, transmission electron microscopy (TEM) was applied and the procedure to prepare the sample is mentioned in Section 2.6. As obtained TEM micrographs are displayed in Figure 4.4. Figure 4.4(a) shows two different parts of the SiC: f = 0.034 sample. SiC aggregates of up to 500 nm are visible, along with clean grain boundaries, which are preferred over rough boundaries in order to not impact the electron transport too much. Figure 4.4(b-f) show elemental mappings of silicon, nickel, molybdenum, antimony, and tellurium all obtained using aforementioned TEM in energy dispersive X-ray spectroscopy (EDX) mode. The distribution of the elements Ni, Mo, Sb and Te appears to be very homogeneous throughout the sample, indicating that no element precipitated at the grain boundaries or reacted with SiC, thus leaving the bulk intact.

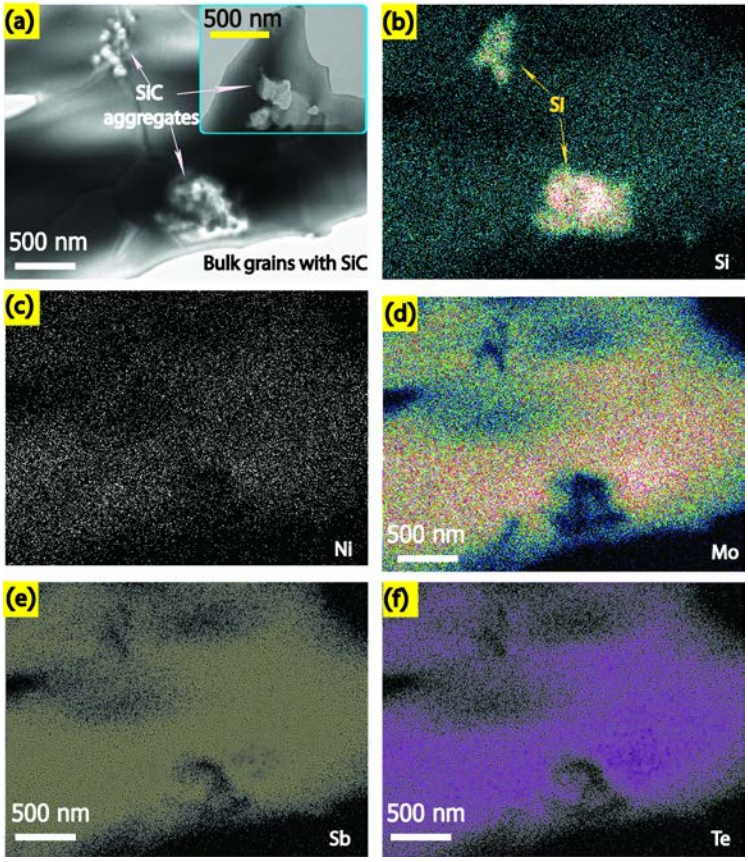

Figure 4.4: TEM images of hot-pressed $Ni_{0.05}Mo_3Sb_{5.4}Te_{1.6}$/0.034 SiC. (a) SiC aggregates on the surface of bulk particles; (b), (c), (d), (e) and (f): elemental maps of Si, Ni, Mo, Sb and Te respectively.

Figure 4.5 displays the SEM analysis of Al_2O_3: f = 0.0325 composite. Figure 4.5(a) at 100 micron magnification shows a smooth surface. At higher magnification (4.5 (b), 4.5 (c)), voids of 2 μm – 5 μm are revealed. Al_2O_3 aggregates of around 400 nm can be found (4.5(d)). The SiC sample has larger voids and a rougher surface than Al_2O_3.

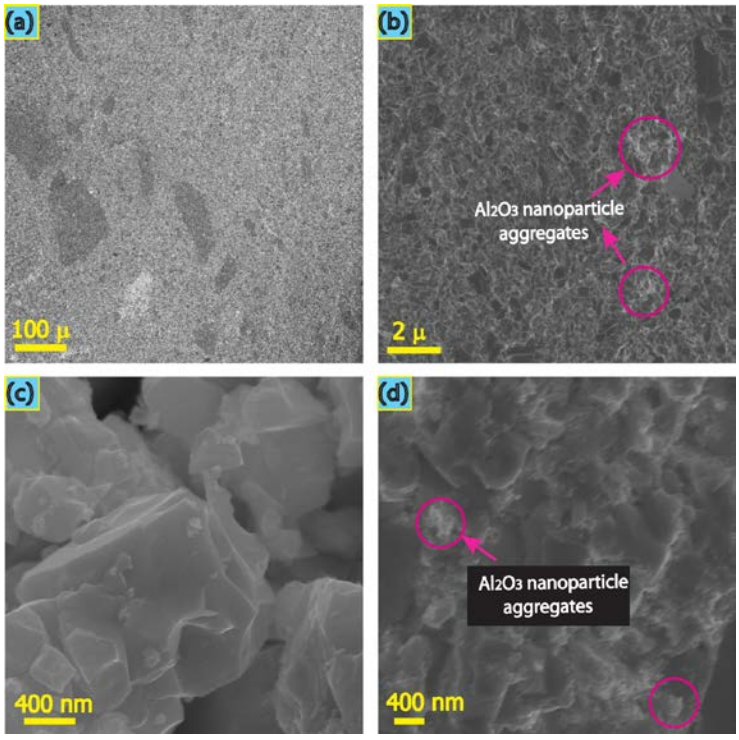

Figure 4.5: SEM images of spark-plasma sintered $Ni_{0.05}Mo_3Sb_{5.4}Te_{1.6}$/0.034 Al_2O_3. (a) Surface morphology; (b) voids of 2 µm and Al_2O_3 aggregates on bulk particles; (c) voids and bulk particles at higher magnification; (d) Al_2O_3 aggregates of 400 nm.

Listed in Table 4.3 are the surface areas and cumulative pore volumes for different volume fractions of SiC and Al_2O_3 (Section 2.11). Comparing SiC: f = 0 and 0.034 samples, there is an increase by 80% in surface area and 280% increase in cumulative pore volume for the 0.034 sample, respectively. Comparing Al_2O_3: f = 0 and 0.0325, 90% and 230% increases in surface area and cumulative pore volume were observed. These findings are in qualitative agreement with the SEM studies. Similarly, for SiC: f = 0 and 0.034, the relative densities are 94.2% and 90.7% respectively, while for Al_2O_3: f = 0 and 0.0325, the relative densities are significantly higher, namely 98.5% and 95.0% respectively.

Table 4.3: BET Surface area and BJH (Barrett-Joyner-Halenda) cumulative pore volume

Composite	Surface Area (m^2g^{-1})	Cumulative Pore Volume (cm^3g^{-1})
SiC		
$f = 0.00$	0.58	3.38×10^{-3}
$f = 0.010$	0.65	4.30×10^{-3}
$f = 0.020$	0.78	4.80×10^{-3}
$f = 0.034$	1.05	12.9×10^{-3}
Al_2O_3		
$f = 0.00$	0.47	1.84×10^{-3}
$f = 0.010$	0.49	1.61×10^{-3}
$f = 0.0216$	0.53	1.96×10^{-3}
$f = 0.0325$	0.89	5.06×10^{-3}

4.2 Results and Discussion

4.2.1 Transport Properties

The instruments and the procedure to characterize thermal and electrical properties are covered in Sections 2.9 and 2.10 respectively.

Previously we reported p-type carrier concentrations of the order of 4×10^{21} cm^{-3} for $Mo_3Sb_{5.4}Te_{1.6}$ and $Ni_{0.06}Mo_3Sb_{5.4}Te_{1.6}$.[184] With such a high carrier concentration, the electrical conductivity drops with increasing temperature, as the mobility decreases, as observed for all eight samples displayed in Figure 4.6(a) and (b) and typical for thermoelectric materials. Electrical conductivity values in excess of 10^3 $\Omega^{-1}cm^{-1}$ are expected for the $Mo_3(Sb,Te)_7$ family

of compounds at room temperature.[29, 64, 113] At 325 K, the σ values decrease from 1338 $\Omega^{-1}cm^{-1}$ (no SiC) down to 664 $\Omega^{-1}cm^{-1}$ (3.4% SiC). Assuming an error of ±5%, most of the differences are significant.

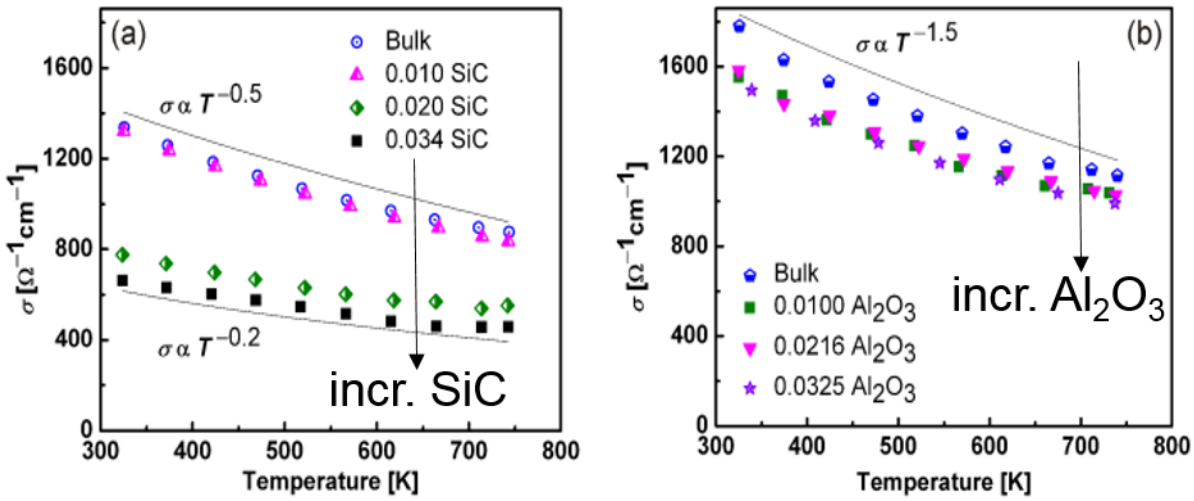

Figure 4.6: Temperature dependence of electrical conductivity of bulk and SiC (a) and bulk and Al_2O_3 composites (b).

This drop of 50% in σ for SiC*: f* = 0.034 can be explained in terms of microstructural changes coupled with charge-carrier scattering from the nanoinclusions. As the volume fraction increases, the degree of aggregation not only increases but also enhances cumulative pore volume and surface area, as the BET results demonstrate. This leads to a huge degradation in mobility due to charge-carrier scattering. For SiC: $f = 0$ and $f = 0.01$ samples, σ tends to follow $T^{-0.5}$ dependence in the entire temperature range. However as the content of SiC increases to $f =$ 0.02 and 0.034, this dependence starts to diminish to $T^{-0.2}$. A similar trend was observed in hot-pressed $CoSb_3$ bulk with 0% and 0.3 wt-% ZrO_2 (nano). Though both composites have close relative densities of 95.6% and 95.4%, there is a drop in electrical conductivity by ~72% for sample with 0.3 ZrO_2 (nano) compared to the bulk sample at 325 K. [191] In our previously reported bulk/MWCNT composites, we observed the electrical conductivity following a $T^{-1.5}$ dependency, typical for acoustic-phonon scattering mechanism.[107, 192] During consolidation

by hot-pressing, the SiC nanoparticles may have suppressed grain growth, thus enhancing porosity and surface area, and these microstructural features may be changing the charge-carrier scattering mechanism. Also, the amount of similar cumulative pore volumes for these samples may attribute to this deviation. Similarly in $La_{0.75}Fe_3CoSb_{12}$, the samples with 12.4% and 12.8% porosity showed drastic reduction in mobility by 47% and 82% respectively.[193].

The electrical conductivity curves of the Al_2O_3 containing samples are shown in Figure 4b. At 325 K, the bulk sample exhibits σ = 1780 $\Omega^{-1}cm^{-1}$, and the 3.25% sample σ = 1495 $\Omega^{-1}cm^{-1}$. In the entire temperature range from 325 K to 740 K, all samples follow $T^{-1.5}$, an indication of acoustic-phonon scattering. As the volume fraction increases, the conductivity values are very close to each other, falling within the error margin of 5%. During the SPS process, grain growth can occur due to intense Joule heating, electrical field diffusion effect, and high pressure. This leads to mass transfer that facilitate smaller particles filling voids, thus reducing porosity.[194] At high temperatures, the σ values start to converge because of the minority carrier effect.

The difference in electrical conductivity of SiC: f = 0 and Al_2O_3: f = 0 amounts to 28%, and at 740 K, the difference is still 24%. This large difference mainly stems from the 98% density of the SPSed bulk sample of the Al_2O_3 series, compared to 94% of the hot-pressed bulk sample of the SiC series.

To analyze the extent of reduction in σ stemming from the different porosity, we followed Adachi et al., and applied a correction based on the Maxwell-Eucken equation: $\sigma_p = \sigma_o (1 - p) / (1 + \beta p)$, where σ_p, σ_o are the electrical conductivity with pores and without pores, respectively, p is porosity and β is the empirical value that depends on the shape of pores, usually lying between 1 and 3.[195] At 325 K, the pore corrected electrical conductivity values are, using β = 2 for spherical pores, σ_o = 1585 $\Omega^{-1}cm^{-1}$ for 0 SiC and 868 $\Omega^{-1}cm^{-1}$ for 3.4% SiC. Similarly for the Al_2O_3 series, we obtained σ_o = 1861 $\Omega^{-1}cm^{-1}$ for 0 Al_2O_3 and 1731 $\Omega^{-1}cm^{-1}$ for 3.25% Al_2O_3. Thus, the pore effect alone cannot completely account for the reduction of the electrical conductivity with increasing amount of the nanoadditions. It has been observed that a low relative density of nanocomposites should cause poor electrical conductivity because of

charge-carrier scattering caused by the increased interface density in nanocomposites.[154, 196, 197] Thus, in comparing both composites, the higher magnitude of reduction in electrical conductivity of the SiC composites is in part due to the higher porosity that can lead to a drop in mobility. For example, $La_{0.75}Fe_3CoSb_{12}$ showed a systematic reduction in mobility with respect to the amount of porosity. Four samples with 0.3%, 0.5%, 12% and, 15% respectively, were found to have charge-carrier mobility values of 11.5, 8.2, 6.1 and, 2.1 $cm^2V^{-1}s^{-1}$.[193]

The high temperature total thermal conductivity κ is shown in Figure 4.7. The total thermal conductivity, κ, of the bulk and the SiC composites decrease steadily with increasing temperature. At 325 K, the thermal conductivity values are 5.23 W $m^{-1}K^{-1}$ for the SiC-free sample and 2.35 W $m^{-1}K^{-1}$ for the sample with 3.4% SiC. And at 740 K, the corresponding κ values are 4.00 W $m^{-1}K^{-1}$ vs. and 2.31 W $m^{-1}K^{-1}$. Similar temperature dependences were reported by us for the $Ni_{0.05}Mo_3Sb_{5.4}Te_{1.6}/C_{60}$ and $Ni_{0.05}Mo_3Sb_{5.4}Te_{1.6}$/MWCNT composites. When a considerable amount of pores exists, as in the SiC series, the pores provide more interfaces and larger surface area and therefore phonon-phonon and phonon-interface scattering becomes dominant, thus effectively reducing thermal conductivity.

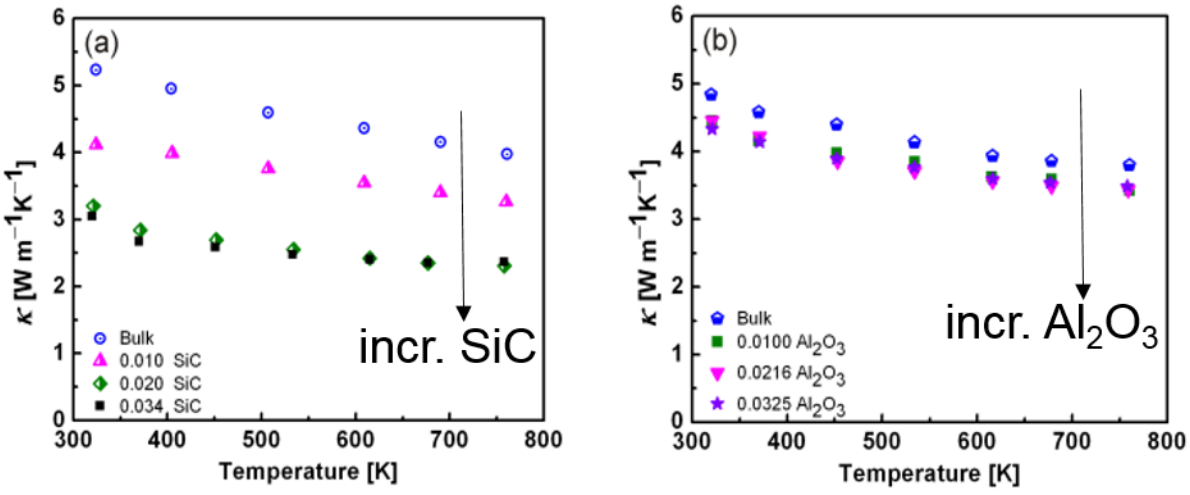

Figure 4.7: Temperature dependence of total and lattice thermal conductivity of bulk and SiC and Al_2O_3 composites.

At 325 K, the κ values for Al_2O_3: $f = 0$ and 0.0325, respectively, are: 4.84 W $m^{-1}K^{-1}$ and 4.33 W $m^{-1}K^{-1}$. All curves except for the one without Al_2O_3 are very close to each other in the entire temperature segment from 325 K to 740 K. At 740 K, all samples with Al_2O_3 have the same thermal conductivity value of $\kappa = 3.5$ W $m^{-1}K^{-1}$. In $La_{0.75}Fe_3CoSb_{12}$ (consolidated through spark plasma sintering), the sample with 0.3% porosity had $\kappa = 2.6$ W $m^{-1}K^{-1}$, compared to the sample with 15% porosity exhibiting $\kappa = 1.48$ W $m^{-1}K^{-1}$ at 300 K. [193]

Analogous to the electrical conductivity discussion, we applied the Maxwell-Eucken's equation for the thermal conductivity as well: $\kappa_p = \kappa_o (1 - p) / (1 + \beta p)$, where κ_p and κ_o are the experimental thermal conductivity and the pore-corrected one, respectively. We obtained pore corrected thermal values for SiC: $f = 0$ and 0.034 as 6.2 W $m^{-1}K^{-1}$ and 3.80 W $m^{-1}K^{-1}$, respectively, and for Al_2O_3: $f = 0$ and 0.0325 as 5.06 W $m^{-1}K^{-1}$ and 5.01 W $m^{-1}K^{-1}$, respectively. In conclusion, the changes in measured thermal conductivity with increasing amount of nanoadditions can be fully explained with the increasing porosity in case of the Al_2O_3 additions, but not in case of the SiC additions.

Lattice thermal conductivity κ_l was obtained by subtracting κ_e from the total thermal conductivity κ and displayed in Figure 4.8 (Section 1.4.1.2, and Supplementary Information at the end of this chapter).

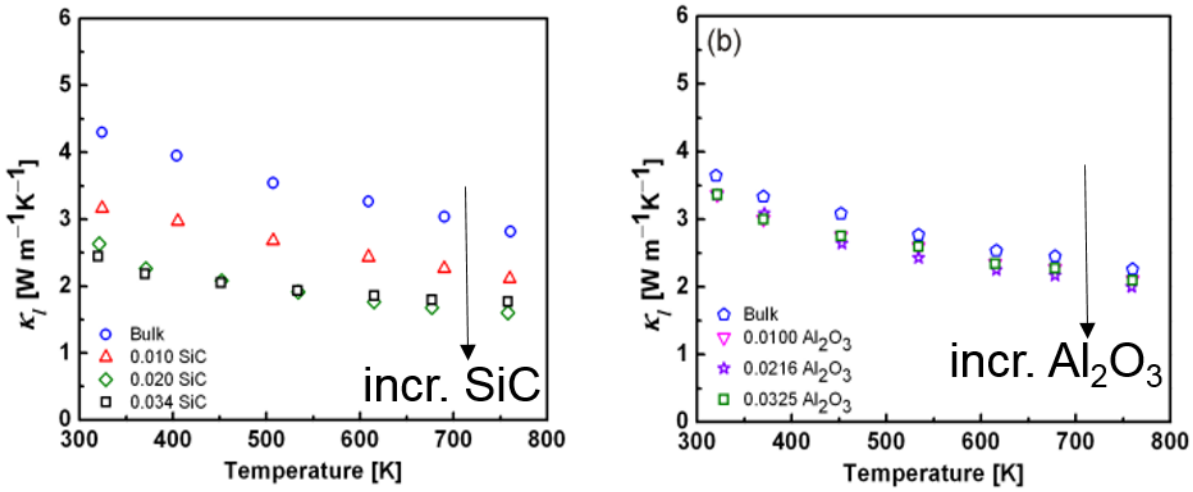

Figure 4.8: Temperature dependence of lattice thermal conductivity of bulk and SiC (a) and bulk and Al_2O_3 composites (b).

Despite the high electrical conductivity, the lattice part of the thermal conductivity, κ_l, is still the dominant component. A systematic reduction in κ_l with temperature for both composites indicates that phonon-phonon interactions are dominant, diminishing the thermal conductivity at higher temperatures. For SiC: $f = 0$ and 0.034, we obtained $\kappa_l = 4.30$ W $m^{-1}K^{-1}$ and 2.33 W $m^{-1}K^{-1}$, respectively, at 325 K. The reduction in κ_l from $f = 0$ to $f = 0.034$ amounts thus to almost 50%. This reduction in thermal conductivity is mainly due to the disruption in the coherent propagation of energy carrying phonons and inter-phonon interactions. The embedded SiC nanoparticles act as scattering centers and also reduce the cross sections available for phonons.

In case of the Al_2O_3 series, $f = 0$ and 0.0325 exhibit $\kappa_l = 3.64$ W $m^{-1}K^{-1}$ and 3.23 W $m^{-1}K^{-1}$, respectively, at 325 K. The reduction in κ_l from $f = 0$ to $f = 0.01$ is just 8%. This decrease is due to the presence of Al_2O_3 nanoparticles that exert a negative influence on the coherent flow of small wavelength phonons. However, adding more Al_2O_3 barely reduces κ_l further, indicating that high energy phonons are easily crossing the boundaries.

It has been shown in many composites, that incorporating particles with very high thermal conductivity into a bulk matrix of lower thermal conductivity increased the composite's

thermal conductivity, depending on the particles' sizes. For example, adding 2 μm diamond particles with κ = 600 W $m^{-1}K^{-1}$ to ZnS with κ = 17.4 W $m^{-1}K^{-1}$ resulted in increased thermal conductivity. On the other hand, adding 0.25 μm size diamond particles to the same ZnS matrix reduced thermal conductivity.[40]

In our case, $\kappa_{\beta\text{-SiC}}$ and κ_{Al2O3} are 320 W $m^{-1}K^{-1}$ and 30 W $m^{-1}K^{-1}$,[118] with particle sizes of 45 nm – 55 nm and 13 nm, respectively. As the particle size decreases, the surface to volume ratio becomes larger, thus increasing the interfacial surface area. An increased surface area reduces the phonon mean free path aiding in reducing thermal conductivity, as observed in case of the SiC additions.[28, 130] Due to small size of Al_2O_3, one could expect a more significant reduction in thermal conductivity when adding more and more of its nanoparticles. However, all Al_2O_3 containing samples exhibited very comparable thermal conductivity values. A possible reason may arise from agglomerations of the Al_2O_3 nanoparticles.

The Seebeck coefficient values *S* are positive in the entire temperature range from 325 K to 740 K, (Figure 4.9), indicating that the synthesized compounds are *p*-type materials like the other members of the $Mo_3(Sb,Te)_7$ family. Typically *S* starts around 60 μV K^{-1} and increases almost linearly to 140 μV K^{-1} at 760 K for samples with an Sb : Te ratio of 5.4:1.6.[113, 198] Since *S* is roughly proportional to *T*, the diffusive part of the Seebeck coefficient is dominant in these samples.[199]

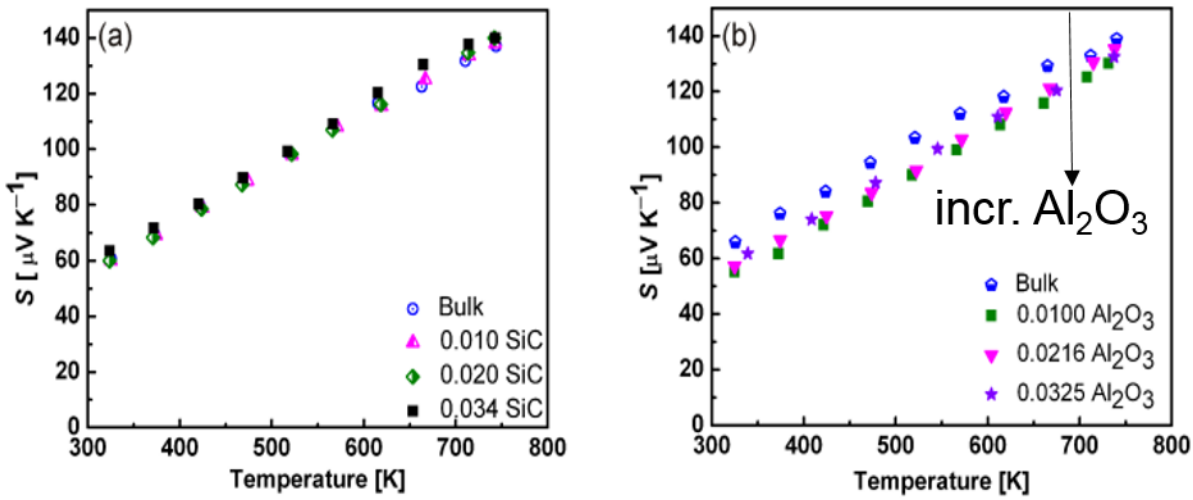

Figure 4.9: Temperature dependence of Seebeck coefficient of bulk and SiC and Al_2O_3 composites.

In Al_2O_3: $f = 0$, the Seebeck coefficient, S, starts at 66 μV K^{-1} at 325 K and increases linearly, reaching 139 μV K^{-1} at 740 K, very similar to SiC: $f = 0$, 0.02, and 0.034. In all samples with Al_2O_3, S starts around 55 μV K^{-1} and increases linearly very similar to the $f = 0$ sample, reaching 130 μV K^{-1} to 139 μV K^{-1} at 740 K. Taking into account an estimated error of ±3%, all Seebeck curves except for the one without Al_2O_3 are within error margin. The $Ni_{0.05}Mo_3Sb_{5.4}Te_{1.6}/C_{60}$ and $Ni_{0.05}Mo_3Sb_{5.4}Te_{1.6}$/MWCNT composites exhibited the same temperature dependence, and no appreciable change in Seebeck coefficient was observed with respect to the amount of C_{60} and CNT.[107, 188] In *n*-type $Co_{0.92}Ni_{0.08}Sb_{2.96}Te_{0.04}$, the bulk material and samples with 0.5 mass-%, 1%, 2% and 3% C_{60} did also not show much difference in the Seebeck coefficient in the entire temperature range from 300 K to 870 K.[200] Likewise, adding 4.77 mass-% C_{60} to $CoSb_3$ had only a minor impact on Seebeck coefficient.[153]

The calculated power factor curves, $P.F. = S^2\sigma$, are displayed in Figure 4.10. From 325 K to 740 K, *P.F.* increases from 5 μW cm^{-1}K^{-2} to 16.5 μW cm^{-1}K^{-2} with the same slope for SiC: f = 0 and 0.010 samples similar to our previous reports on $Mo_3(Sb,Te)_7$ compounds.[113] However, the samples with f = 0.020 and 0.034 exhibit significantly lower values throughout the whole temperature range measured.

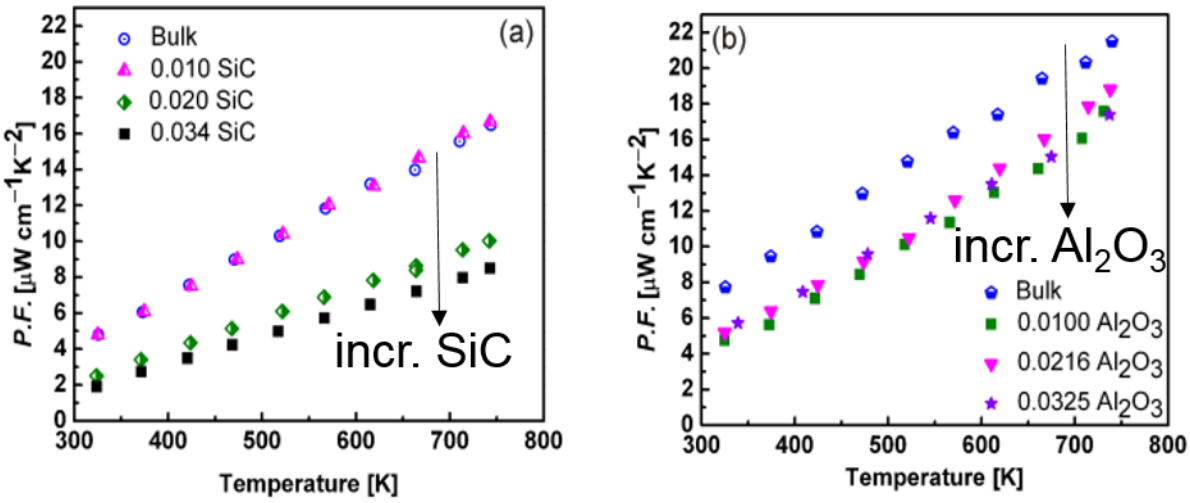

Figure 4.10: Temperature dependence of power factor of bulk and SiC and Al_2O_3 composites.

For Al_2O_3: f = 0, *P.F.* is at 7.7 μW cm^{-1}K^{-2} at 325 K and increases approximately linearly with temperature reaching 21.5 μW cm^{-1}K^{-2} at 740 K. The samples with Al_2O_3 have significantly lower values (and comparable slopes).

Since the thermal conductivity was measured at slightly different temperatures than the electrical properties, fits of the power factor were used to extract *P.F.* values corresponding to thermal conductivity measurement temperatures to calculate the *figure-of-merit, ZT*. The error margin for *ZT* is estimated as 7% using the propagation of error method. Typical for $Mo_3(Sb,Te)_7$ materials, the *ZT* values of all samples investigated here increase rapidly with temperature (Figure 4.11). From 325 K to 740 K, *ZT* for SiC: f = 0.010 increases from 0.036 to 0.38, for SiC: f = 0, from 0.030 to 0.31, and for Al_2O_3: f = 0, from 0.050 to 0.42. Thus, an improvement of 17% was observed at 740 K for the 1% SiC sample compared its bulk sample.

The difference of 35% between two bulk samples (f = 0) is quite significant, a consequence of the different consolidation technique, i.e. hot-pressing vs. spark-plasma sintering.

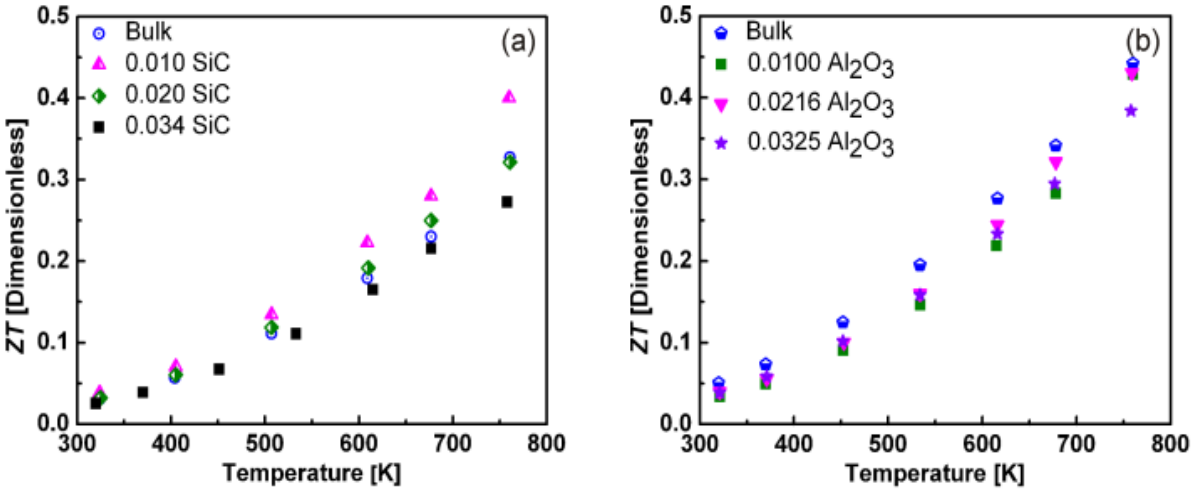

Figure 4.11: Temperature dependence of *figure-of-merit* of bulk and SiC (a) and bulk and Al2O3 composites (b).

On the other hand, the *ZT* values of Al_2O_3: f = 0.010, 0.0216 and 0.0325 are 0.41, 0.41, and 0.37, respectively, at 740 K, thus not higher than for the bulk sample of that series. In the bulk/MWCNT composite, the 21% reduction in *P.F.* was outweighed by a 40% reduction in thermal conductivity, thus leading to a 25% in increase in *ZT*. [107] It has been suggested that inclusion of insulating nanoparticles in composites can lead to enhanced *ZT*, provided the inclusions are not disrupting electrical conductivity but are scattering phonons.[201] The outcome of dispersing inert oxides in TE materials has been mixed. For example, thermal conductivity was lowered in TE materials containing some inert oxides, [202] but negative effects on the electrical performance were also reported.[201] These results show that improvements in TE properties of nanocomposites vary from case to case.

The thermoelectric properties are summarized in Tables 4.4 and 4.5 at both the minimum and maximum measurement temperatures.

Table 4.4: TE properties of $Ni_{0.05}Mo_3Sb_{5.4}Te_{1.6}$and $Ni_{0.05}Mo_3Sb_{5.4}Te_{1.6}$/SiC composites at 325 K and 740 K.

f	0 (bulk)	0.010	0.020	0.034
$\sigma/(\Omega^{-1}cm^{-1})$	1338 / 876	1322 / 836	776 / 553	664 / 458
$\sigma_o/(\Omega^{-1}cm^{-1})$	1585 / 1036	1630 / 1029	1006 / 717	868 / 712
$S/(\mu V\ K^{-1})$	61 / 137	60 /138	60 / 140	63 /140
$P.F./(\mu W\ cm^{-1}K^{-2})$	4.8 / 16.5	4.8 / 16.6	2.5 / 10.1	1.9 / 8.5
$\kappa/(W\ m^{-1}K^{-1})$	5.23 / 4.0	4.11 / 3.30	3.20 / 2.35	2.90 / 2.31
$\kappa_o/(W\ m^{-1}K^{-1})$	6.20 / 4.70	5.07 / 4.03	4.15 / 3.00	3.79 / 3.01
$\kappa_l/(W\ m^{-1}K^{-1})$	4.30 / 2.88	3.16 / 2.16	2.63 / 1.61	2.44 / 1.74
ZT	0.030 / 0.31	0.036 / 0.38	0.030 / 0.31	0.025 / 0.27

Table 4.5: Thermoelectric properties of $Ni_{0.05}Mo_3Sb_{5.4}Te_{1.6}$ and $Ni_{0.05}Mo_3Sb_{5.4}Te_{1.6}$/Al2O3 composites at 325 K and 740 K.

f	0 (bulk)	0.010	0.0216	0.0325
$\sigma/(\Omega^{-1}cm^{-1})$	1780 / 1115	1554 / 1038	1583 / 1027	1495 / 991
$\sigma_o/(\Omega^{-1}cm^{-1})$	1861 / 1165	1732 / 1149	1780 / 1155	1731 / 1169
$S/(\mu V\ K^{-1})$	66 / 139	55 / 130	57 / 135	62 / 132
$P.F./(\mu W\ cm^{-1}K^{-2})$	7.71 / 21.5	4.8 / 17.6	5.2 / 19.0	5.7 / 17.4
$\kappa/(W\ m^{-1}K^{-1})$	4.84 / 3.80	4.46 / 3.47	4.45 / 3.46	4.33 / 3.45
$\kappa_o/(W\ m^{-1}K^{-1})$	5.06 / 3.80	4.95 / 3.40	5.01 / 3.44	5.01 / 3.50
$\kappa_l/(W\ m^{-1}K^{-1})$	3.64 / 2.25	3.36 / 2.13	3.37 / 1.90	3.23 / 2.00
ZT	0.050 / 0.42	0.033 / 0.40	0.034 / 0.41	0.038 / 0.37

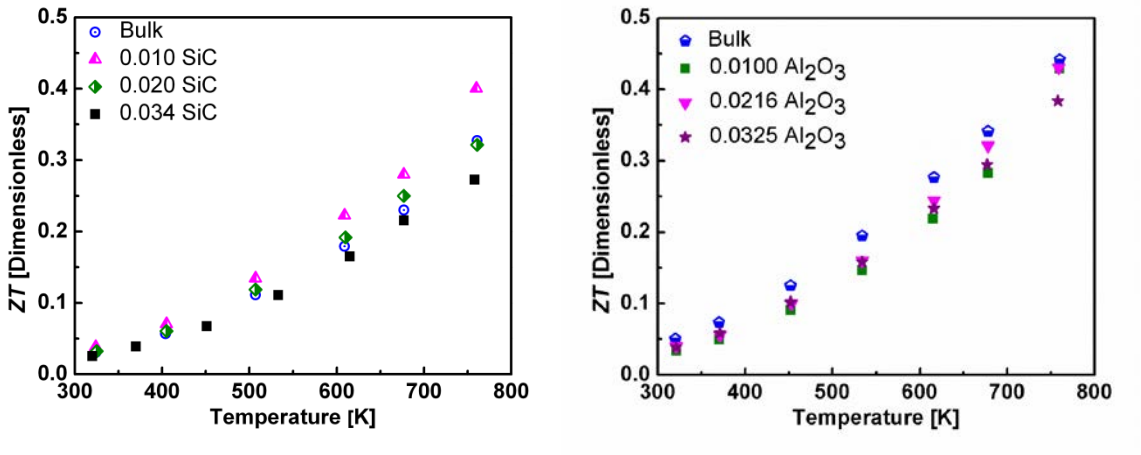

Figure 4.12: Temperature dependence of *figure-of-merit* of bulk and SiC and Al_2O_3 composites.

4.3 Conclusions

We successfully synthesized and studied the properties of $Ni_{0.05}Mo_3Sb_{5.4}Te_{1.6}$/SiC and $Ni_{0.05}Mo_3Sb_{5.4}Te_{1.6}/Al_2O_3$ nanocomposites. Addition of 0.01 SiC enhanced the thermoelectric *figure-of-merit* by 17% compared to the SiC-free sample. Increased surface area for SiC: f = 0.02 and f = 0.034 resulted in reduced electrical conductivity due to charge carrier scattering with SiC nanoparticles, pores and grain boundaries, while leaving Seebeck coefficient unchanged. Also enhanced surface area and cumulative pore volume in SiC samples facilitated inter-phonon scattering and phonon scattering with grain boundaries thus aiding in reducing thermal conductivity.

Lattice thermal conductivity is still the dominant component in both composites. There is a consistent reduction in lattice thermal conductivity with increasing SiC content in the entire temperature from 325 K to 740 K for the SiC samples. For Al_2O_3: f = 0.010 0.0216 and 0.0325, the magnitude of the lattice thermal reduction compared to the bulk sample is the same in the temperature segment of 325 K to 740 K, suggesting diffusive phonon scattering due to pores less effective. Concomitant effects of interfacial area, pore volume, and volume fraction of SiC are prevailing in abating the phonon mean free path much efficiently than Al_2O_3. The larger porosity

of the SiC samples also contributed to the phonon scattering. There was no appreciable improvement in the *figure-of-merit* for the Al_2O_3 composites.

Post transport property measurement phase analysis of composites showed no deterioration in stoichiometry of constituents in both types of composites. It is worth to investigate more on wet chemistry to coat SiC and Al_2O_3 nanoparticles on bulk particles homogeneously and reduce thermal conductivity even further. As the *figure-of-merit* for the bulk sample consolidated through SPS is 35% higher than the hot-pressed bulk sample, further investigations need to be done to optimize the consolidation parameters such as pressure, temperature and heating rate.

4.4 Supplementary Information

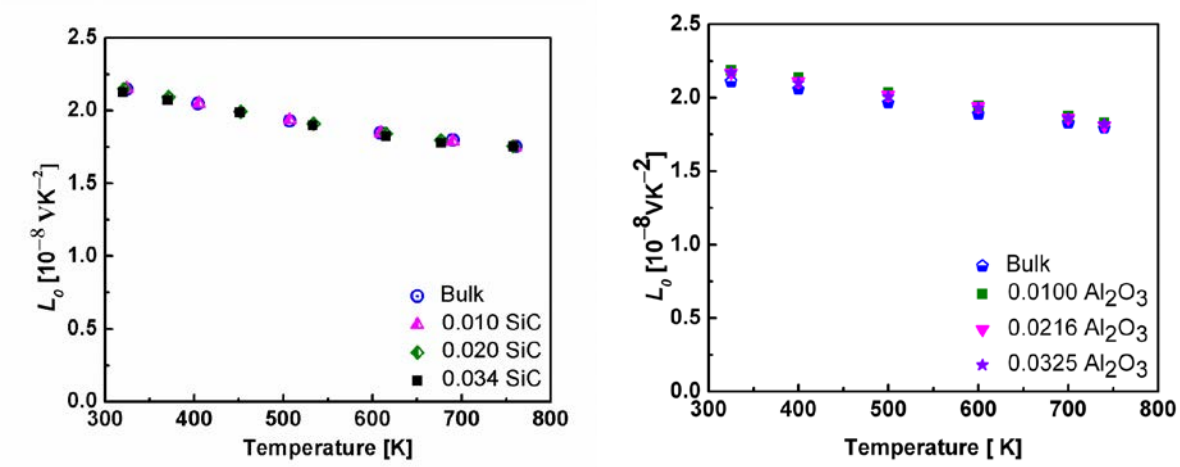

Figure 4.13: Temperature dependence of Lorenz numbers of bulk and SiC and Al_2O_3 composites

Chapter 5

Thermoelectric Properties of $Ni_{0.05}Mo_3Sb_{5.4}Te_{1.6}$ with NiSb Nanoparticles[11]

These results are yet to be published in a relevant journal.

5.1 Background

Readers are strongly advised to read Abstract (page iv), and Sections 1.4.1, 1.4.2, 1.5.5, 1.7, 1.8, and 1.9 before going through the next sections.

5.2 Experimental Section

5.2.1 Synthesis

Bulk $Ni_{0.05}Mo_3Sb_{5.4}Te_{1.6}$ was synthesized from a powder mixture of starting materials through solid-state reaction. Synthesis procedure is discussed in Section 2.1.1. All phase pure bulk materials from several reactions were transferred to 50 ml vial and subjected to high frequency vibrations in the Vortex-Mixture (Fisher-Scientific) for twenty minutes and divided into four heaps of equal mass.

NiSb nanoparticles were synthesized through a solvothermal route. The procedure can be found in Section 2.1.2. NiSb nanoparticles were dispersed in the bulk material as follows: NiSb was transferred to a 50 ml vial containing 35 ml of pure acetone and subjected to sonication to de-agglomerate the nanoparticles. 2 g of bulk material was placed into a mortar containing 10 ml of pure acetone. Small amounts of the NiSb suspension were added to mortar using a small pipette while stirring the mixture simultaneously. This procedure was repeated until depletion of the whole NiSb suspension. Through this process, we obtained four samples with NiSb in volume fraction, *f:* 0, 0.034, 0.074 and 0.16 respectively. Theoretical densities of composites were calculated using the rule of mixture discussed in Section 2.7.2. Throughout our discussion on $Ni_{0.05}Mo_3Sb_{5.4}Te_{1.6}$/NiSb, we name the samples according to their NiSb volume fraction.

[11] Nagaraj Nandihalli, Robert Liang, Stéphane Gorsse, Norman Zhou, Holger Kleinke

All composites and their reference counterpart (which we call “bulk” in our discussion) were consolidated by hot-pressing using 30-ton capacity Oxy-Gon Uniaxial Hot-Press Furnace System under Ar atmosphere.

Table 5.1: Experimental densities of bulk and various $Ni_{0.05}Mo_3Sb_{5.4}Te_{1.6}$/NiSb composites at 295 K.

f	Density of pellet ρ/(g cm^{-3})	Relative Density (%)
0 (bulk)	8.28	95.0
0.034	8.11	93.2
0.074	7.86	90.5
0.160	8.25	95.4

5.2.2 Phase and Microstructural Analysis

Phase analysis of bulk and composites was performed immediately after the synthesis, after mixing the NiSb nanoparticles, and finally after the transport property characterization (Section 2.2). Figure 5.1 shows the XRD patterns of NiSb nanoparticles; the peaks are consistent with the literature data. In these composites, as the content of NiSb increased, the intensity of NiSb peaks increased. For the bulk sample, a small amount of Sb was detected, which may have formed during consolidation or during transport property characterization. Similar to our samples, traces of Sb are reported in the family of Mo_3Sb_7 [107, 203] and $CoSb_3$ compounds [204]. For the rest of the samples, no remaining Sb was detected. The sample with 0.074 NiSb had small trace of $NiSb_2$.

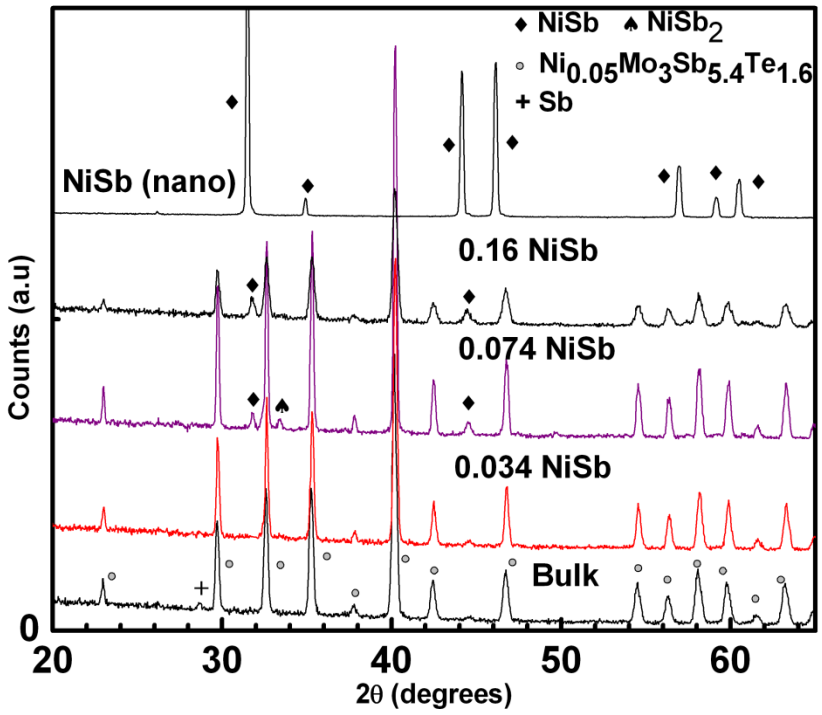

Figure 5.1: XRD patterns of NiSb, composites and bulk (from top to bottom).

Figure 5.2(a) shows the NiSb nanoparticles of approximately 60 nm synthesized via the solvothermal route. The crystallite size calculated using Scherrer's formula is ~66 nm. As depicted in Fig. 5.2(c) – (f), NiSb nanoparticles form a conductive bridge between the bulk particles for charge carriers and phonons that may enhance electrical and thermal conductivity. Figure 5.2(b) demonstrates large NiSb particles of ~100 µm -1000 µm size synthesized through solid-state reaction. Images of these particles were obtained using secondary electron image (SEI) mode.

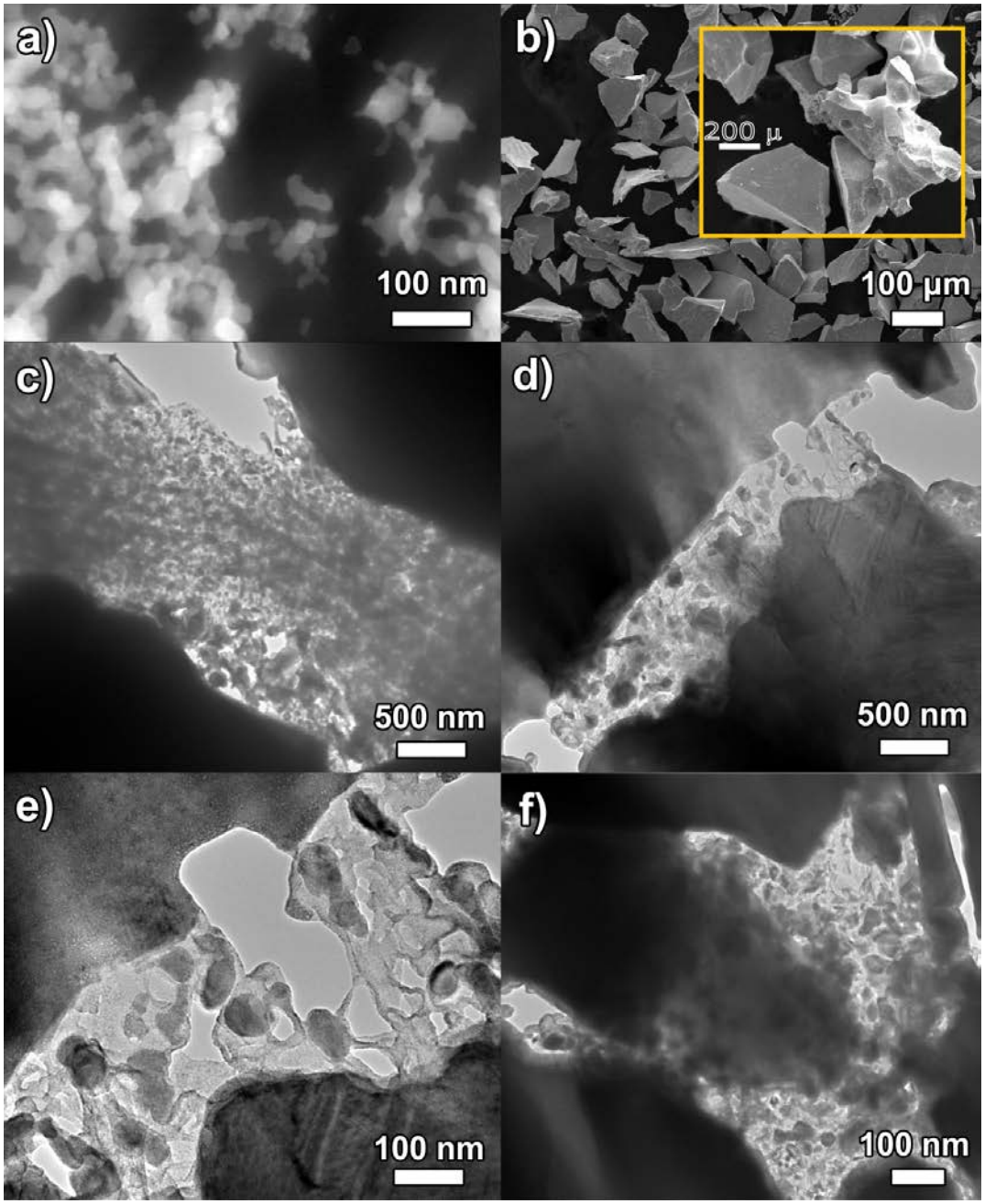

Figure 5.2: (a) EEM image of NiSb nanoparticles synthesized via solvothermal process with ~60 nm size; (b) SEM image of large NiSb particles synthesized through high temperature solid-state reaction. Inset image shows larger NiSb particles of 100 µm - 500 µm; (c) – (f): TEM images of NiSb nanoparticles forming a bridge between bulk $Ni_{0.05}Mo_3Sb_{5.4}Te_{1.6}$ particles.

Figure 5.3 displays the HRTEM images of post-transport property measured 0.16 composite taken at the McMaster University. Figure 5.3(b) shows HR image of area 8 and Figure 5.3(c) and (d) respectively show area 11 and 12. The unit cell parameters of hexagonal NiSb are 3.9399 Å, 3.9399 Å, and 5.1413 Å. For Mo_3Sb_7, the unit cell parameters are: 9.571 Å, 9.571 Å and 9.571 Å. Needles like structures in Figure 5.3(b) must be NiSb and Figure 5.3(c) and (d) are belongs to Mo_3Sb_7.

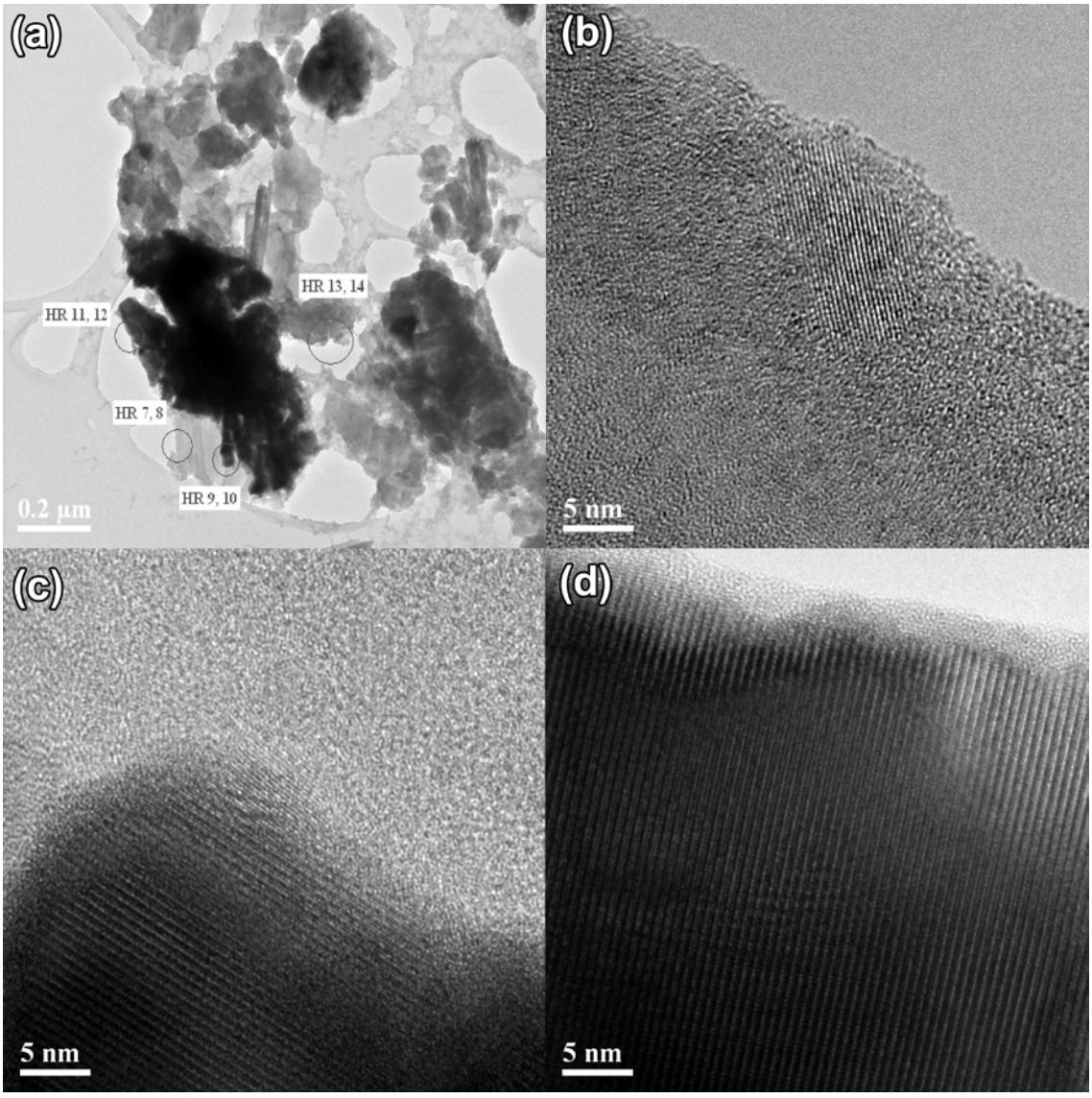

Figure 5.3: HRTEM images of 0.16 sample. Image (b) displays area, 8 and images; (c) and (d) respectively show area, 11 and 12.

SEM images of NiSb 0.034, 0.74 and 0.16 composites are shown in Figure 5.4. As Figure 5.4(a) shows, islands of NiSb nanoparticles were distributed randomly in 0.034 and somewhat homogeneously in 0.074 and 0.16 samples.

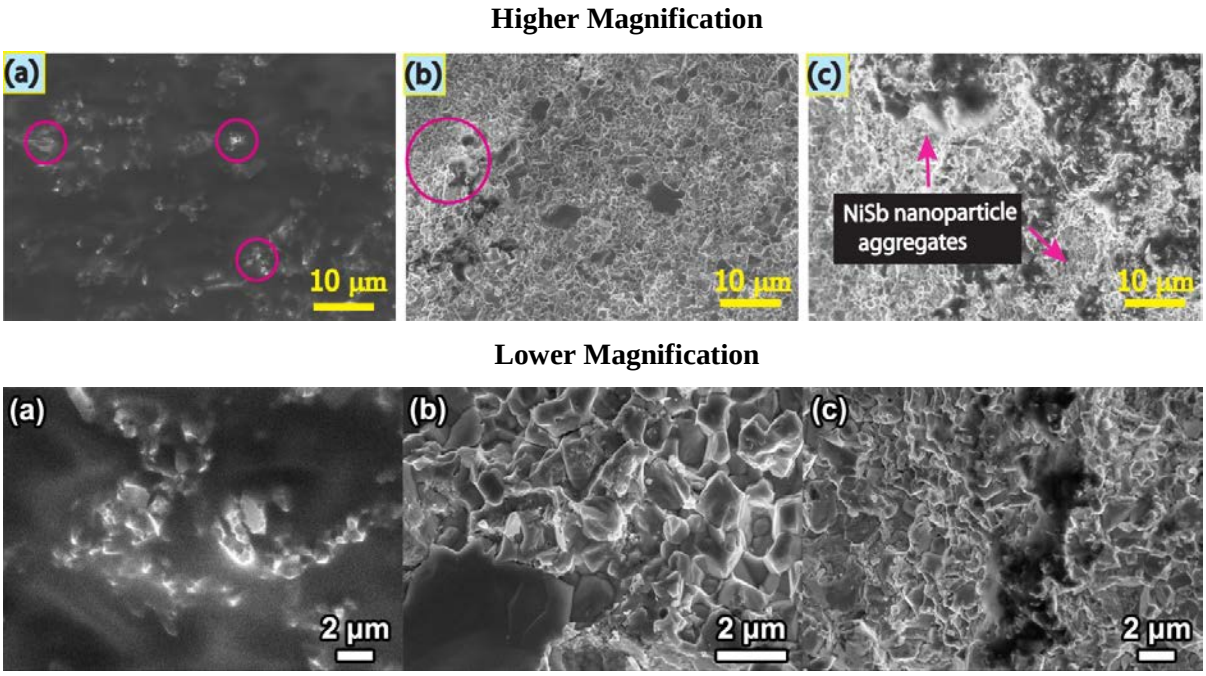

Figure 5.4: SEM image of NiSb nanocomposites (same scale for all); (a) 0.034 NiSb samples with scattered islands of NiSb particles; (b) 0.074 NiSb sample; (c) 0.16 NiSb sample. Lower panel shows the same composites in lower magnification

5.2.3 Hardness and Young Elastic Modulus Testing

Hardness testing was done on these samples by micro-indentation. The leftover samples from diamond saw cutting were mounted using phenolic resin (thickness: 1.26 cm) on a mounting hot-press (Buehler SimpliMet® 1000) at a pressure of 4300 MPa for a heating time of 5 minutes and a cooling time of 3 minutes. The mounted samples were progressively ground with 600, 800, 1200 coarse, and 1200 fine grit silicon carbide paper, then polished for a mirror-like finish using 1 µm and 0.25 µm diamond spray, sequentially, on a polishing pad under 250 rpm rotation. The hardness and elastic modulus of the polished samples were characterized using the Nanovea ST400 Optical Profilometer with built-in microindentation module using a Vicker's

indenter (radius: 100 µm). Hardness and elastic values were measured under a load of 10 N with a loading rate of 20 N min^{-1} and an unloading rate of 10 N min^{-1}; the values were obtained from the load vs. depth curve and analyzed using the Nanovea hardness software. The 95% confidence intervals were calculated from more than 30 microindentations per sample.

5.3 Physical Property Measurements

Thermal and electrical properties were characterized as discussed in Section 2.8 and 2.9.1 respectively.

5.4 Results and Discussion

5.4.1 Transport Properties

The temperature dependent electrical conductivity of bulk and NiSb composites in the 330 K – 740 K range are exhibited in Figure 5.5. At 330 K, bulk, 0.034, 0.074 and 0.16 NiSb samples have σ = 1008 $\Omega^{-1}cm^{-1}$, 1073 $\Omega^{-1}cm^{-1}$, 1190 $\Omega^{-1}cm^{-1}$, and 2653 $\Omega^{-1}cm^{-1}$ respectively. Thus, there is a gradual increase from the bulk to the 0.034 and to the 0.074 NiSb samples, while the conductivity of the 0.16 sample is 2.6 times higher than the one of the bulk.

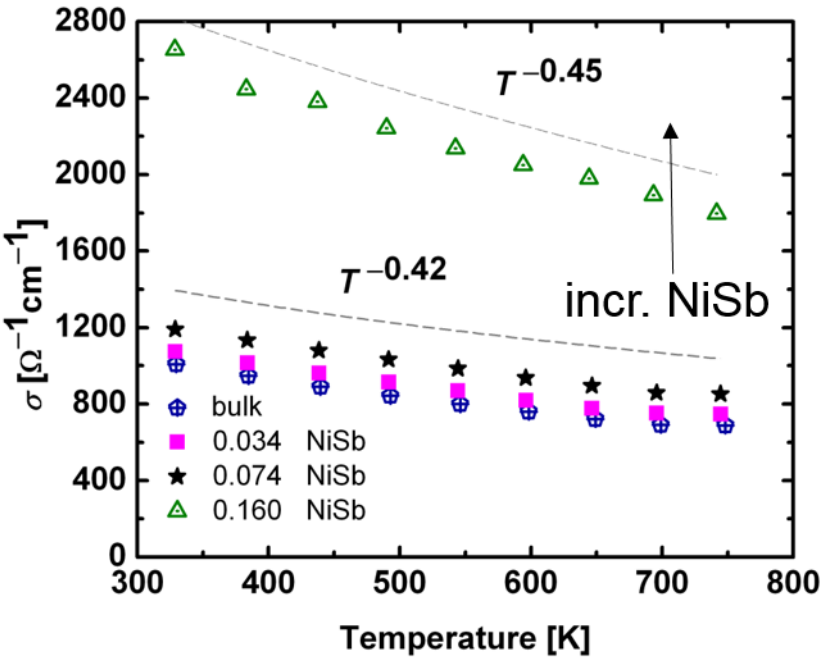

Figure 5.5: Temperature dependence of electrical conductivity of bulk and NiSb composites.

This large increase in σ for 0.16 sample can be explained by percolation theory. When particles of high thermal conductivity or electrical conductivity, such as NiSb are randomly dispersed in a bulk matrix of relatively low electrical and thermal conductivity (such as bulk in our case), clusters of particles form a percolation network.[51, 205] The distribution of the minor phase, such as NiSb in bulk phase, may follow three different types of geometric morphology of phase distributions.[205, 206] When the volume fraction of NiSb is low, particles of NiSb are statistically distributed, and many of them form random aggregates. At this stage, electrical conductivity may not improve much since these aggregates cannot form a path for charge carriers through the material. As the volumetric content of NiSb increases further, more and more NiSb nanoparticles form clusters and start to form chains.[205, 207] As we increase NiSb further, clusters are connected together forming continuous chains and at this stage there is a rapid increase in electrical or/and thermal conductivity. The volume fraction at this critical point is called the percolation threshold. It has been observed that the majority of clusters formed do

not carry current as many of them are dead-ended and the actual pathways that convey the current are called “backbones”.[131, 208, 209] In our 0.034, 0.074 and 0.16 samples, for every one hundred formula units of bulk there exist 22, 49, and 115 formula units of NiSb formula units. However, this does not augur the fact that the higher volume fraction of highly conducting nanoparticles may manifest in a low percolation threshold. To achieve a low electrical percolation threshold, well controlled dispersion of NiSb nanoparticles of a certain shape and size is very essential. Moreover, the outcome of this process should not affect the Seebeck coefficient. Compared to 3-dimensional systems, in 2-dimensional systems it is very easy to achieve low electrical percolation threshold cost effectively as the required amount of highly conductive phase is less and also the techniques are well developed. In our sample, a very straight backbone, running along a 1 cm sample from one end to another can contain back-to-back ~1.6×10^5 NiSb nanoparticles of 60 nm in diameter. This backbone conducts current without the aid of bulk particles. Using our current experimental observation, it is difficult to determine the exact percolation threshold as we do not have many experimental volume fractions. However, ~ or < 0.16 is a reasonable estimate.

A preponderance of experimental and theoretical investigations show that the percolation threshold depends on various factors such as the properties of both the bulk matrix and inclusions, the ratio of the size of nanoinclusions to the size of bulk particles, their volume fractions, and the method by which they are mixed. Kusy has studied the relation between critical volume fraction and the ratio of the size of conducting filler particles to the size of insulating particles. As this ratio decreased, the critical volume fraction was reduced. When conducting particles formed a continuous monolayer on the surface of insulating material, a percolation network was formed. However, when the conducting particles were trapped between the voids of larger bulk material, critical volume fraction was increased.[210] According to our assertion, one reason for the sudden increase in electrical conductivity is that our bulk matrix is moderately conductive, and another reason is that the almost spherical NiSb nanoparticles (highly conductive even though they are in nano size [146]), forced into interstitial regions between the bulk particles during hot-pressing, thus forming a percolation network and finally

reducing the critical volume fraction. Bhattacharya et al. have observed a considerable reduction in critical volume fraction when copper particles were 40 times smaller than bulk polymer particles.[211] In contrast to the 2.6 times increase in electrical conductivity in our case, in PVC/MWCNT (3000 W $m^{-1}K^{-1}$) composite, the increase in electrical conductivity was a much larger order of magnitude, and the electrical percolation threshold was 0.05 vol% of MWCNT. Surprisingly, for the same volume fraction, there was a 6% decrease in thermal conductivity due to high interfacial resistance (the specific surface area of CNT in this case was 190 m^2g^{-1}).[212]

Bulk epoxy containing (0.005-0.5%) MWCNT has exhibited electrical percolation threshold < 0.005 wt%. The same sample showed moderate increase in thermal conductivity with respect to the filler content. On the other hand epoxy/SWCNT (3000 W $m^{-1}K^{-1}$) composites had higher percolation threshold (0.05-0.23 wt%) and the thermal conductivity was lower than the bulk epoxy.[213]

In $Ni_{0.05}Mo_3Sb_{5.4}Te_{1.6}$/MWCNT (multi-wall carbon nanotubes) [107] composites, there was a gradual reduction in electrical conductivity as the content of MWCNT was increased despite the high electrical conductivity of CNTs.[114] Using finite element calculations, Shenogina et al. studied the electrical conductivity percolation threshold in polymer matrix/carbon nanotube composites, and found lack of percolation threshold due to poor contact between nanotubes that limits the charge carrier transfer.[214] That outcome strongly corroborates our findings, as TEM and SEM images of $Ni_{0.05}Mo_3Sb_{5.4}Te_{1.6}$/MWCNT show that the nanotubes were not dispersed homogeneously. Indeed it is very challenging to disperse CNT in solid state bulk materials and polymers.[215] Our assertion is that CNTs with their high surface area are providing more resistance at the bulk/CNT interfaces to the charge carriers.

Polymer based composites and polymer TE materials provided some encouraging results. For example poly (vinyl chloride) filled with CNTs was found to have a very low electrical percolation threshold of 0.00047.[212] Similarly, in a TE polymer composite with 20 wt% segregated network of CNT, there was an improvement in electrical conductivity and unchanged thermal conductivity and the Seebeck coefficient.[216] Composite films of poly (3-hexylthiophene) with SWCNT were demonstrated to offer a competitive thermoelectric

performance. A maximum value of σ = 1000 $\Omega^{-1}cm^{-1}$ was observed to give rise to a *P.F.* of 25 ± 6 μW $cm^{-1}K^{-2}$ for a filler content of only 8 wt-%, and a maximum of 95 ± 12 μW $cm^{-1}K^{-2}$ for 42 – 81 wt-%.[217]

In our case, TEM images of the 0.16 NiSb sample show all the features of a typical percolation network. The NiSb nanoparticle clusters are acting as a bridge between the bulk particles. In general, introducing nanoinclusions into a bulk semiconducting material leads to a reduction in mobility due to increased charge carrier scattering. On the other hand, adding a second, semimetallic or metallic phase like NiSb to a semiconducting bulk matrix can increase the average charge carrier concentration.[218, 219] The electrical conductivity of NiSb (100 μm –1000 μm size) synthesized through solid-state reaction in our laboratory was found to be ~10^5 $\Omega^{-1}cm^{-1}$ at 325 K (Supplementary Information), and even cold pressed NiSb nanoparticles exhibited $\sigma = 10^4$ $\Omega^{-1}cm^{-1}$.[146] Thus, we expect NiSb to contribute significantly to the electrical conductivity.

For a constant carrier concentration, the exponent *c* varies according to temperature dependence of the mobility and is given by $\mu \approx T^c$.[220] In the nanostructured PbTe–Pb–Sb system, a change in *c* with respect to the Pb/Sb ratio and Pb+Sb concentration was observed.[221] Invoking the above power law for the bulk, 0.034 and 0.074 NiSb samples, the value of *c* was found to be –0.42. A similar approach to 0.16 gave *c* = –0.45, i.e. a comparable but slightly faster decrease.

It is imperative to compare these results with the Bi_2Te_3/Bi composite.[222] In Bi_2Te_3, the inclusion of solvothermally synthesized 10 nm – 12 nm Bi nanoparticles doubled the electrical conductivity, and the charge carrier concentration increased from 1.5 × 10^{19} cm^{-3} to 5.5 × 10^{19} cm^{-3} and 5.8 × 10^{19} cm^{-3} for 5% and 7% volume fractions of Bi nanoparticles, respectively. However, the charge carrier mobility dropped from 122 $cm^2V^{-1}s^{-1}$ to 79 $cm^2V^{-1}s^{-1}$ and 62 $cm^2V^{-1}s^{-1}$, respectively, for the same samples due to charge carrier scattering with the Bi nanoparticles. Ag and Cu nanoparticles decorated $Bi_{0.5}Sb_{1.5}Te_3$ exhibited similar behavior, albeit with unchanged mobility.[223]

We postulate that the network of NiSb nanoparticles increases the charge carrier concentration. In a highly degenerate semiconductors, σ decays as $T^{-3/2}$, which we call acoustic scattering.[22] (Assuming the carrier concentration remain constant throughout the temperature range from 330 K -745 K, $T^{-0.5}$ decays indicates a typical alloy scattering.[88, 224])

To isolate and decipher the effect of pore volume on the electrical conductivity, we have applied a pore correction using Maxwell-Eucken relation: $\sigma_p = \sigma_o (1 - P)/(1 + \beta P)$, where σ_p is the experimental conductivity with a porosity P, σ_o the theoretical conductivity with zero porosity, and $\beta = 2$ in case of spherical pores. The calculated results are included in Figure 5.6. For the bulk sample, the difference between experimental and pore corrected σ is 159 $\Omega^{-1}cm^{-1}$ at 330 K, and at 750 K, the difference is narrowed down to 108 $\Omega^{-1}cm^{-1}$. For 0.034 NiSb, we determined at 330 K/750 K: 234 $\Omega^{-1}cm^{-1}$/163 $\Omega^{-1}cm^{-1}$, and for 0.074 NiSb: 377 $\Omega^{-1}cm^{-1}$/267 $\Omega^{-1}cm^{-1}$, and similarly for 0.16 NiSb: 383 $\Omega^{-1}cm^{-1}$/259 $\Omega^{-1}cm^{-1}$. Among all these samples, the 0.074 NiSb sample has the lowest relative density of 91%, therefore it exhibited the largest pore related reduction. Surprisingly, the difference decreases for all samples from 330 K to 750 K. One possible reason is that at 750 K, the charge carriers have higher thermal energy to overcome the pore effect compared to the charge carriers at 330 K.

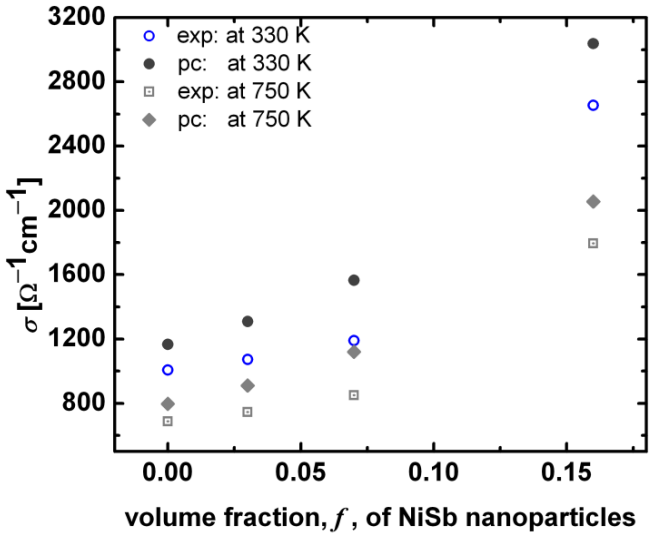

Figure 5.6: Variation of experimental and pore corrected electrical conductivity for samples of different volume fractions at 330 K and 750 K.

The Seebeck coefficient values, *S*, of all samples are positive, indicative of p-type electrical transport. *S* increases with temperature in every case here (Figure 5.7). At 330 K/745 K, for 0, 0.034, 0.074 and 0.16 volume fractions of NiSb, the Seebeck coefficient values are: 59 μV K^{-1}/131 μV K^{-1}, 55 μV K^{-1}/121 μV K^{-1}, 47 μV K^{-1}/109 μV K^{-1}, and 38 μV K^{-1} /83 μV K^{-1} respectively. The nature in the variation of Seebeck for bulk is very similar to other members of the $Mo_3(Sb,Te)_7$ family of compounds. For metals and degenerate semiconductors, the Seebeck coefficient and the electrical conductivity σ are given by the equations: $S = 8\pi^2 k_B^2 m^*/(3eh^2)(\pi/3n)^{2/3}$ [225] and $\sigma = ne\mu = ne^2\tau / m^*$, where k_B, e, h, m^*, n, and μ are: Boltzmann constant, electronic charge, Planck's constant, effective mass, charge carrier concentration, and charge carrier mobility respectively. According to the above equations, the electrical conductivity increases with increase in charge carrier concentration, while the Seebeck coefficient decreases. For the 0.16 NiSb sample, the NiSb network must have created many short-circuited paths reducing the Seebeck coefficient drastically. Our claim can further be buttressed by comparing our results with Bi_2Te_3/Bi composite, where a 20% – 25% drop in Seebeck coefficient was observed for 5% and 7% volume fractions of Bi nanoparticles.[222] Similarly, in $Bi_{0.5}Sb_{1.5}Te_3$,

addition of 0.2 wt% Ag nanoparticles lowered *S* from 233 μV $K^{-1}$to 123 μV K^{-1} with increased charge carrier concentration and unchanged mobility at 320 K.[223]

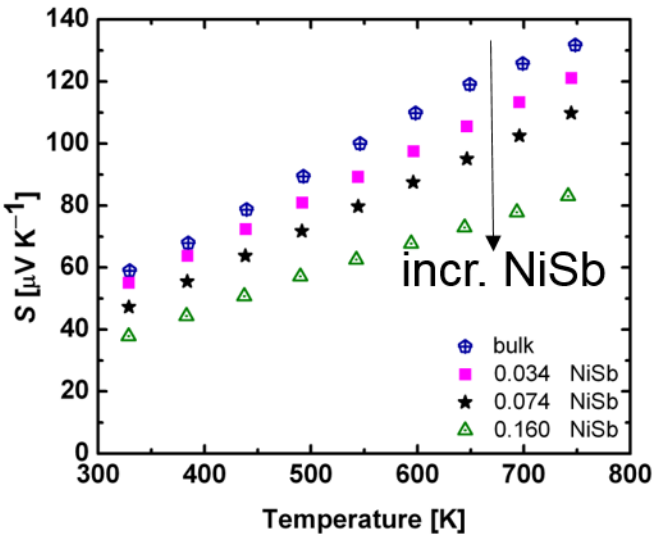

Figure 5.7: Temperature dependence of Seebeck coefficient of bulk and NiSb composites.

When metal and semiconductor come into contact, band bending at their interface produces a scattering potential, which might preferentially scatter low energy charge carriers, aiding in enhancing the Seebeck coefficient, albeit lowering mobility; this phenomenon was observed in PbTe with Pb nanoparticles [60] and PbTe with Ag nanodots.[61] and is called energy filtering effect, has been investigated theoretically[62], but this is not visible in our composites.

The thermal conductivity data is exhibited in Figure 5.8. All the samples exhibit the expected negative temperature dependence. For the bulk sample without NiSb, κ decreases from 3.7 W $m^{-1}K^{-1}$ at 320 K to 2.9 W $m^{-1}K^{-1}$ at 755 K. Similarly, for the other samples with 0.034, 0.074 and 0.16 NiSb respectively, at 320 K/755 K, the κ values are 4 W $m^{-1}K^{-1}$/3.2 W $m^{-1}K^{-1}$, 4.3 W $m^{-1}K^{-1}$/3.6 W $m^{-1}K^{-1}$, and 6.6 W $m^{-1}K^{-1}$/6.3 W $m^{-1}K^{-1}$ respectively. When phonons incident at the grain boundary, they gets diffusively scattered to produce multiple phonons of longer wavelength. These long wavelength phonons in turn scattered by grain boundaries. They

also scattered by centers such as NiSb nanoparticles that are comparable or smaller than the phonon wavelengths of bulk material. However, as TEM images show, NiSb nanoparticles are of ~60 nm, thus we can speculate that direct interactions between the phonons and NiSb particles are unlikely. The interfaces created by NiSb nanoparticles must participate in scattering phonons.[28, 130] κ is increasing with increasing volume fraction of NiSb. However, as the NiSb amount increases further, there is a competition between interfaces created by NiSb and the large thermal conductivity contribution from NiSb, which finally prevails. We can speculate that the electronic contribution to the thermal conductivity, κ_e, starts to contribute significantly at this stage. Thus, adding more and more NiSb to bulk leads to enhanced thermal conductivity, as clusters of NiSb pave the way for lattice as well as electronic thermal conduction. This is contrary to our previously reported $Ni_{0.05}Mo_3Sb_{5.4}Te_{1.6}$/MWCNT, where the thermal conductivity decreased with respect to the amount of MWCNT content, as the CNT with their high surface areas scatter phonons.[107] We are going to discuss the exact nature of heat transfer between bulk and NiSb later.

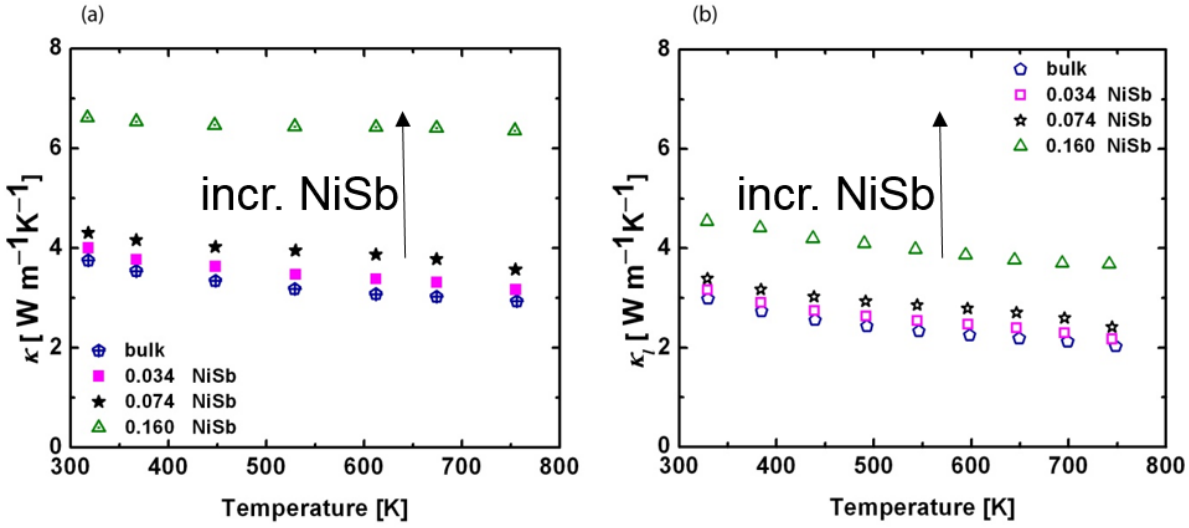

Figure 5.8: Temperature dependence of total and lattice thermal conductivity of bulk and NiSb composites.

Fig. 5.2 (c) – (f) show NiSb nanoparticles in the channel between two bulk particles. Phonons travelling between these bulk particles may face thermal boundary resistance if there is

an acoustic mismatch between the bulk and NiSb.[36, 39] If there is an acoustic match, phonons still undergo boundary scattering as there are voids between NiSb particles and bulk particles. Those clusters, which are not part of the backbones but are in contact with the bulk particles may aid in enhancing phonon scattering depending on the states of phonons available in its neighborhood. Taking into consideration the radius of the NiSb nanoparticles as 30 nm, it is possible to calculate the interface per unit volume using the relation, $3f/a$,[44, 45] where f is the volume fraction of NiSb nanoparticles and a is the radius of the nanoparticle. To estimate the interfacial per unit volume, some authors have used the relation, % vol/d, where d is the diameter of the embedded particle. [226] Respectively, for 0.034, 0.074 and 0.16, we obtained $3.5 \times 10^5 m^{-1}$, $7.5 \times 10^5\ m^{-1}$, and $16 \times 10^5\ m^{-1}$. Interfacial per unit volume is a key parameter that decides the effective thermal conductivity in bulk materials containing nanoparticles as phonon scattering agents. [24, 100, 227] The prime principle in fabricating nanocomposites is to reduce lattice thermal conductivity by incorporating a suitable nanoparticle.[23, 228, 229] For the 0.16 sample, irrespective of the very high interface per unit volume, there was no reduction in thermal conductivity. As mentioned early the only possible reason for this is the acoustic match and contribution of κ_e.

To ascertain the contribution of the lattice conductivity κ_l to the total thermal conductivity, we calculated κ_l using the Wiedemann–Franz relation: $\kappa_e = L_0 \sigma T$, with L_0 = Lorenz number, and subtract the electronic thermal conductivity κ_e from the total thermal conductivity: $\kappa_l = \kappa - \kappa_e$.[29, 230] The variation of the Lorenz numbers with respect to temperature including bulk NiSb is displayed in Figure 5.15 of the Supplementary Information.

Since bulk/NiSb composites have high electrical conductivity, the κ_e contribution to total thermal conductivity is considerable. At 320 K, for f = 0, 0.034, 0.074 and 0.16 samples, the contributions of κ_e and κ_l are: 19.5%/80.5%, 20.0%/80.0%**,** 20.5%/79.5% and, 31.0%/69.0% respectively. In case of the metallic NiSb bulk particles, κ_e contributes 87% to the total thermal conductivity (Figure 5.13 of Supplementary Information).

The estimated lattice thermal conductivity is shown in Figure 5.8(b). At 330 K, κ_l values for bulk, 0.034, 0.074 and 0.160 samples are: 2.9 W $m^{-1}K^{-1}$, 3.2 W $m^{-1}K^{-1}$, 3.4 W $m^{-1}K^{-1}$ and, 4.5 W $m^{-1}K^{-1}$ respectively. Likewise at 740 K, the κ_l values of the same samples are: 2 W $m^{-1}K^{-1}$, 2.2 W $m^{-1}K^{-1}$, 2.4 W $m^{-1}K^{-1}$, and 3.7 W $m^{-1}K^{-1}$. When it comes to the lattice thermal conductivity of our samples, three important factors come under scrutiny: (a) lattice thermal conductivity is increasing with respect to NiSb content; (b) irrespective of the amount of NiSb nanoparticle content, the difference in lattice thermal conductivity at 330 K and 740 K is ~1 W $m^{-1}K^{-1}$; (c) the variation of lattice thermal conductivity with temperature is very similar. The factor (c) indicates that in all samples the mechanism of phonons travelling, interacting with grain boundaries, and nanoparticles is the same.

As we mentioned early, the prime goal of majority of nancomposite synthesis technique is to reduce lattice thermal conductivity. In $Ba_{0.3}Co_4Sb_{12}$ with 0.5 wt% Ag nanoparticles of size 20 nm – 40 nm and 0.5 wt% Ag microparticles of size 2 mμ – 6 mμ in 1:1 wt. ratio exhibited reduction in lattice thermal conductivity compared to bulk $Ba_{0.3}Co_4Sb_{12}$. The reduction was due to the scattering of short wavelength phonons with smaller Ag nanoparticles and mid –long wavelength phonons with micron size Ag nanoparticles.[228] In this study, the variation of lattice thermal conductivity of Ag composites with respect to their bulk counterpart is very inconsistent, providing clue that phonon scattering mechanism or the magnitude of phonon scattering is different in these composites. Surprisingly, compared to our 0.16 volume fraction (15 wt% NiSb), in $Ba_{0.3}Co_4Sb_{12}$/Ag (nano, micro) the wt% of Ag (1:1 of 20 nm – 40 nm and 2 mμ – 6 μm particles) was very small (0.5 wt.%) and the variation of lattice thermal conductivity was in sharp contrast compared to bulk (assuming mechanically mixing did not change the grain boundaries drastically). Similarly, solvothermally synthesized Bi nanoparticles (semimetal, 10 nm – 20 nm in size) were incorporated into bulk Bi_2Te_3 and a considerable reduction in the lattice thermal conductivity was observed. [222]

In Bi_2Te_3/Bi (0-7% nano, semimetal, 10 nm – 20 nm in size), thermal conductivity increased from 0.98 W $m^{-1}K^{-1}$ to 1.15 W $m^{-1}K^{-1}$; however, there was a reduction in the lattice part of thermal conductivity. Similarly, $Bi_{0.5}Sb_{1.5}Te_3$ coated with 2% Ag nanoparticles exhibited

an increase in total thermal conductivity from 0.93 W $m^{-1}K^{-1}$ to 1.26 W $m^{-1}K^{-1}$ and 20% reduction in the lattice thermal conduction at 315 K. In $Ni_{0.05}Mo_3Sb_{5.4}Te_{1.6}$/MWCNT composite, we reported a systematic reduction in the lattice thermal conductivity with respect to the amount of MWCNT content as these tubes provide more interfaces, thus scattering the phonons.[107] In bulk/SiC and bulk/Al_2O_3, reduction in lattice thermal conductivity was seen. [231] Our current results are contrary to the results of these composites and provokes a question.

Mo_3Sb_7 is considered as a hole-like (p-type metallic behavior) metal with fermi level located deep inside the valence band. To optimize the charge carrier concentration, our group started to substitute Te in place of Sb to reduce hole concentration and thereby tried to make Mo_3Sb_7 semiconducting.[87] However, the process of band engineering by substituting Sb with Te has one drawback, i.e., increased κ_l.[203, 224, 232] Over the years, some research groups made attempts to explain this κ_l enhancement utilizing the Debye model of relaxation time of phonons, phonon density of states using density functional theory (DFT) calculations, inelastic neutron scattering (INS)[233], and inelastic X-ray scattering (IXS).[88, 224, 234, 235]

All the aforementioned investigations concentrated on alloys, $Mo_3Sb_{7-x}Te_x$ ($0.0 \leq x \leq 1.8$). According to Bansal et al, alloying with Te raises the fermi-level (close to the top edge of valence band) and decreases the charge carrier concentration, resulting in strong suppression of electron phonon coupling[236] (which leads to a significant increase in phonon group velocities and relaxation times), and finally in large overall stiffening of the interatomic force constant culminating in elevated lattice thermal conductivity.[234] However, in our case of bulk/NiSb nanocomposites, NiSb (or individual elements) participating in an alloy formation can be disregarded, as powder x-ray patterns show the pure phase of bulk.

We made attempts to explain the enhanced κ_l using Callaway formalism[237] of lattice thermal conductivity and for $T > \theta_D$, it is given by: $\kappa_l = (k_B/2\,\pi^2 v)\,(2\pi\, k_B T/h)\int_0^{\theta D/T} \tau_C y^2\, dy$, where τ_C is the combined relaxation time, v is an average phonon group velocity (speed of sound), which can be written as, $v^{-1} = (v_{T,1}^{-1} + v_{T,2}^{-1} + v_{L,}^{-1}) / 3$, where v_L and $v_{T,1}$, $v_{T,2}$ are longitudinal and transverse sound velocities respectively. $y = h\omega/2\pi\, k_B T$, where ω is phonon frequency. Overall phonon scattering rates, τ_C^{-1}, follows Matthiessen's sum rule[238, 239],

where different scattering processes are assumed to independent of each other, *i.e.* $\tau_C^{-1} = \tau_{ep}^{-1} + \tau_{pd}^{-1} + \tau_u^{-1} + \tau_b^{-1}$, where *ep, pd, u,* and *b* represent electron-phonon scattering, point-defect scattering, umklapp scattering (abbreviated as U-scattering or U-process), boundary and interfaces scattering. At this moment, we have ignored relaxation time terms related to dislocations, spinoidal decomposition, precipitates, normal process, phonon scattering by holes [240-242], and strain.[18, 237, 239, 243] In the above paragraph, τ_i, is phonon scattering time and τ_i^{-1} is scattering rate (also called relaxation rate) of phonons; when scattering time decreases, mfp of phonons also decreases and thereby phonons suffer more scattering, which in turn increases thermal resistance, here, *i = ep, pd, u, and b.*

Regarding the τ_{ep}^{-1}, term in our case, considering the Seebeck coefficient and electrical conductivity, we can infer that charge carrier concentration has increased. Decrease in lattice thermal conductivity with increased electrical conductivity has been observed in $La_{3-x}Te_4$, and this is attributed to softening of the lattice phonons due to weakening of the bonds as free charge carriers are added, bonding states are depopulated (p-type) and antibonding states are filled (n-type).[244] In some semiconductors, at low temperatures, hole-(electron) phonon interaction was found to play an important role in the large reduction of lattice thermal conductivity.[245-249]

Electron-phonon interaction was found to play an important role in the reduction of lattice thermal conductivity in skutterudites (n-type).[250] Likewise, doping $CoSb_3$ with Ni and Pd, as donor impurities has lifted the lattice thermal conductivity due to increased charge carrier concentration.[251] Contrary to these outcomes, in our samples, both lattice thermal conductivity and electrical conductivities are increasing with respect to NiSb volume fractions. Among the series, $Mo_3Sb_{7-x}Te_x$ ($x = 0$) has the lowest lattice thermal conductivity due to strong electron-phonon coupling and its charge carrier concentration is high (10^{22} cm^{-3} and large effective mass of $5m_e$). Thus, higher the charge carrier concentration, lower the lattice thermal conductivity among $Mo_3Sb_{7-x}Te_x$ ($0.0 < x \leq 1.8$) series according to Shi et al. (thermal resistivity varies as $p^{4/3}$).[88] The pertinent explanation is that, as the effective mass of charge the carrier increases, its interaction with phonons also increases, and the MFP of low frequency phonons will be attenuated.

However, in our case, the higher the charge carrier concentration, higher the lattice thermal conductivity. Sharp dependence of thermal resistivity due to electron-phonon scattering has been observed in some other systems.[252] Thus, we can eliminate electron-phonon coupling term, τ_{ep}^{-1} and the sole reason for the rejection is that our samples have higher charge carrier concentration. In bulk/NiSb composites, the magnitude of point defects is very small and therefore we disregard the point defect scattering in our case here.

The relaxation term for U-scattering for a system can be written as [253, 254], $\tau_u^{-1} \approx (h\gamma^2/2\pi Mv^2)\, \theta_D \omega^2 T \exp(-\theta_D/3T)$, where in γ is the Gruneisen anharmonicity parameter and M is the average mass of an atom in the crystal.

From the above equation, $B \sim (h\gamma^2/2\pi Mv^2\theta_D)$[88, 144]. The parameter B is a deterministic factor of U-scattering and since $\theta_D \alpha v$,[255] the parameter $B \alpha \theta_D^{-3}$. θ_D is a very important parameter for the phonon-phonon interaction. In $Mo_3Sb_{7-x}Te_x$ ($0.0 < x \leq 1.8$), enhanced lattice thermal conductivity was due to decreased U-scattering, which in turn was due to increased θ_D.[88]

As we mentioned earlier, in the absence of impurities and grain boundaries (means single crystal), only the U-process term remains. However, in samples like ours, we speculate that the presence of NiSb nanoparticles exerts some influence on the magnitude of phonon-phonon scattering; therefore, we have included the U-process term, similar to some authors. He et al. studied the possible mechanism of phonon scattering by nanostructures and defects by incorporating precipitates of 2% Sb, Bi, and Pb in PbTe. They also calculated the relation between relaxation times for strains, dislocations, nanoparticles, U-scattering and the normal scattering process, and phonon frequency normalized to Debye frequency. The same authors studied the effect of spinoidal decomposition of $PbTe_{0.7}S_{0.3}$ into PbTe and PbS on lattice thermal conductivity by studying U-scattering , normal phonon-phonon scattering, interfaces, boundaries, dislocations, and precipitates.[243] The Debye temperature, θ_D, of $Mo_3Sb_{5.4}Te_{1.6}$, below room temperature was found to be 326 K.[234] We speculate that in our bulk/NiSb composites θ_D increase with NiSb content. In general, harder materials have a higher θ_D and higher melting point ($\theta_D \alpha T_m$). [256] Also, there is a well established direct relation between Vickers Hardness,

H_v, and θ_D for solids: $\theta_D \ \alpha \ H_v^{1/2}$, (although this relation is for a pure bulk sample, we make a very rough assumption that it will work for composites as well).[257, 258] All these facts support our supposition that θ_D has increased in our composites with respect to NiSb content. We finally end up with enhanced θ_D and v terms in τ_u^{-1}. We conclude that enhanced lattice thermal conductivity was in part due to decreased U-scattering[259] with respect to NiSb content. Another factor to consider is that for a pure sample, a drop in κ_l with temperature follows $1/T$ if U-process exists; however, κ_l does not follow this relation strictly as several temperature dependent scattering mechanisms exist. Therefore, it is very difficult to ascertain the magnitude of U-process in our sample.

Next, we consider the effect of interfaces and boundaries taking into account of τ_b^{-1}. In Callaway model $\tau_b^{-1} = v_g/\mathrm{L}$, where L is the grain size and v_g is the group velocity. In our case, we digress from this formalism; instead, we approach well-established models on the heat transfer between two constituents in composites. Question arises on how phonons cross from bulk particles to NiSb nanoparticles and from NiSb particles to bulk particles. As TEM images show, NiSb nanoparticles settled between bulk particles and the nature of interfaces at the junction between bulk and nanoparticles decides the phonon and charge carrier transport. Interfacial characteristics was found to play a very important role in both electrical and thermal transport properties of nanocomposites. [19, 27]In general there are three types of precipitate (embedded particles)-bulk matrix interfaces: (a) coherent (with elastic strain) (b) incoherent (minimal interaction between two phases) and (c) semicoherent (misfit dislocations separated by elastic strain). Among all these, incoherent interface is the most suited for our composites, as NiSb are randomly distributed as SEM and TEM images show. Moreover, the bulk particles are arbitrary in shape and NiSb nanoparticles are like dumbbells. Thus, a systematic alignment of these particles along a certain crystallographic axis is unlikely and therefore the nature of phonon transmission is difficult to decipher, as we need more data on the spectrum of phonons.

The HRTEM images of the 0.16 sample (Figure 5.3) convey some interesting information. These images show layered structures of NiSb are deposited on the bulk material. Even though the interfaces between these two constituents is incoherent, needle structures of

NiSb, irrespective of their alignment, we speculate that these structures must be aiding in phonon transmission across the two bulk particles. Using lattice dynamics for highly mismatched materials, existence of mixture of both types of smaller particles between two bulk particles improved the thermal transport by a factor of 3.[260, 261]

Within the frameworks of theoretical studies, the acoustic mismatch model (AMM)[57], scattering mediated acoustic mismatch model (SMAMM)[262] and diffusive mismatch model (DMM)[36, 263] provide basic understanding of interfacial thermal resistance (reciprocal of thermal conductance). Based on the bulk properties of two solids forming the interfaces, AMM and DMM models calculate transmission coefficient of a phonon. The effect of interfacial adhesion strength on the interfacial thermal conductance[46] (related to phonon transmission coefficient) can be analyzed using a simple model of semi-infinite 1-dimensinal chains of masses that are connected by springs.[264] According to these calculations, the interfacial phonon transmission coefficient for a typical phonon, carrying the majority of heat, strongly increases with increasing interfacial stiffness. Higher hardness of the $f = 0.16$ sample, clearly provides a strong hint of higher interfacial stiffness compared to bulk sample in our case.

According to Majumder et al.,[265] for heat transfer to occur between metal and non-metal junction, energy transfer takes place from electrons of metal to phonons of non-metal. There are two possible pathways for this, (a) coupling between electrons of metal and phonons of non-metal (dielectrics) through anhormonic interactions at the metal-nonmetal interface; (b) coupling between electrons and phonons in the vicinity of interface of metal, and then subsequent transfer of energy from this couple to the phonon of non-metal. Since σ of NiSb is very high compared to bulk, from heuristic point of view we can consider bulk as dielectric with smaller σ and NiSb as a metal. In case (a), electron is scattered from the confining potential at the interface and emit a phonon, which subsequently transfer energy to non-metal. Yet, (a) is not applicable to materials having weaker electron-phonon scattering, such as ours. In fact this was proved in the case of Al (for which, electrical resistivity due to e-phonon scattering is only 2.74 $\mu\Omega$ cm)[266], thus in Al-diamond interface, electrons first transfer energy to phonons and then phonons transfer energy to diamond. In our composites, electrons must be transferring the energy

to phonons first, followed by energy transfer from phonons to NiSb. Now phonons of bulk must transfer energy to the phonons of NiSb. The coupling efficiency of this energy transfer depends on the phonon density of states (DOS) of bulk and NiSb in the respective Debye frequency range. However, we are not sure about the cut-off frequency (maximum energy of acoustic phonon = $h\nu_{max}$ where ν_{max} is the maximum frequency) that corresponds to the maximum DOS for both (decided by θ_D). Low Debye temperature means material has many low frequency phonons and high Debye temperature means phonons of high frequency are the carriers of heat. Suppose a phonon of frequency ω in material x can couple with phonons of the same frequency in material y, if the number of states available in y with the same frequency of phonon in x is small, then the transmission coefficients for phonons emanating from x into y must also be small. When θ_D are very different, there will a large difference in the DOS, and as a result, one expect to have a small phonon transmission coefficient (overall ph-ph transfer efficiency between two materials will be very low).[267] Only phonons of bulk whose DOS match that of NiSb within bulk cut-off frequency range can cross the interface and transfer energy to phonons of NiSb material. Rest of the phonons will eventually scatter or reflect back.[267] Thus, energy transfer will be decided by the allowed frequencies between the respective cut-off frequencies. We speculate there is a common range in DOS of NiSb and bulk that cause enhanced thermal conductance. The most compelling evidence to support our assumption comes from the investigation by Kida et al. Metal particles with relatively low θ_D (Al, Cu, Sn and Pb with 428 K, 343 Km 200K and 105 K respectively) were deposited on a very high θ_D material (Aluminium Nitrite, AlN with θ_D 1150 K). Transient Thermoreflectance (TTR) method was used to measure the thermal conductance between AlN and metal particles and was found to increase in accordance with the ratio of θ_D (metal/AlN) values. That means, composite with Al exhibited the highest thermal conductance and Pb the lowest.[268] Stevens et al. [269] and Stoner Maris did the similar studies.[43, 270] All the models we discussed have their own limitations and not a single model is applicable to myriads of types of material composites.

Interfacial adhesion depends strongly on the angular alignment of the two constituent particles (low angle or high angle), strain, and many other factors. Variation of lattice thermal

conductivity for all samples show that the nature of interfaces and the allowed frequencies of phonons are the same. The relaxation rate, τ_b^{-1}, is given by, $\tau_b^{-1} = v\,(1\text{-}t) / L(3/4)t$. Where, $t = (t_{12} + t_{21}) / 2$, an average phonon transmittivity at the interface and is estimated using $t_{12} = v_2\,U_2 / (v_1\,U_1 + v_2\,U_2)$. Here t_{12} is the phonon transmittivity from medium 1 to 2, and U is the density of phonon energy and L is the sample segment. Interfacial thermal boundary resistance, R, (also called Kapitza resistance)[271, 272] can be expressed as, $R = 4\,(v_1\,U_1 + v_2\,U_2) / v_2U_2\,v_2U_2$.[273, 274] Using the heat capacity and sound velocity within the media, it is possible to estimate R.

Now regarding the terms, we ignored: dislocations, normal processes, spinoidal decomposition, precipitates, strain, and normal process, there are voluminous reports on the role of these factors on the lattice thermal conductivity. [18, 243, 275, 276] In these studies, the embedded nanostructures are generated endotoxially inside the bulk matrix, whereas these nanostructures do not disturb the flow of charge carriers, but disturb the phonons. Since NiSb nanoparticles are mixed manually in our case, we assume there is no strain and thus we can easily eliminate spinoidal decomposition and strain factors.

Finally, regarding phonon scattering by holes, many experimental studies show that theory of this type of interaction explained by Ziman[242] has some limitations.[277, 278] However, in our case hole-electron combination, photon generation and a subsequent interaction of photon and phonon that affect phonon propagation is minimal and we ignore phonon scattering by holes.

In conclusion, U-scatterings were suppressed due to commonality in DOS within the cut-off frequencies of both materials (high ph-ph transfer efficiency). More experimental studies are needed to find out phonon DOS of both materials. The exact nature of lattice vibrations at the interfaces needs further investigation. We argue that needle like structures of NiSb are enhancing the phonon transmission between bulk particles.

It has been observed that the composite thermal conductivity (κ_{eff}) with respect to filler volume fraction, f, follows scaling law and is given by, $(\kappa_{eff} - \kappa_{bulk})/(\kappa_{filler} - \kappa_{bulk}) = (f - \Phi_c/1 - \Phi_c)^t$, where κ_{filler} the thermal conductivity of high thermally conducting phase (NiSb in our case). K_{bulk} is the thermal conductivity of low conducting phase (bulk in our case) and Φ_c is the critical

volume fraction of high thermally conducting phase.[212] Conductivity exponent, *t*, lies between 1.65 and 2, depending on the dimension of the embedded particle.[131] Unfortunately, the literature on thermal conductivity percolation threshold is very limited. Industrial epoxy containing unpurified SWCNT by 1% wt has increased thermal conductivity by 126% at room temperature.[279] In our case, 0.16 NiSb nanoparticles have increased the thermal conductivity by 76% at room temperature.

To determine the pore corrected thermal conductivity, we used the following relation from Maxwell-Eucken: $\kappa_p = \kappa_o (1 - P)/(1 + \beta P)$, where κ_p is the experimental thermal conductivity with porosity P, κ_o the theoretical thermal conductivity with zero porosity, and β = 2 for spherical pores. Pore corrected values are plotted in Figure 5.9 with respect to the volume fractions of NiSb at 320 K and 755 K. For the bulk sample, the difference in experimental and pore corrected kappa is 0.55 W $m^{-1}K^{-1}$at 320 K, and at 755 K the difference is 0.4 W $m^{-1}K^{-1}$. For 0.160 NiSb, the difference between experimental and pore corrected at 320 K and 755 K are the same, which is 0.9 W $m^{-1}K^{-1}$.

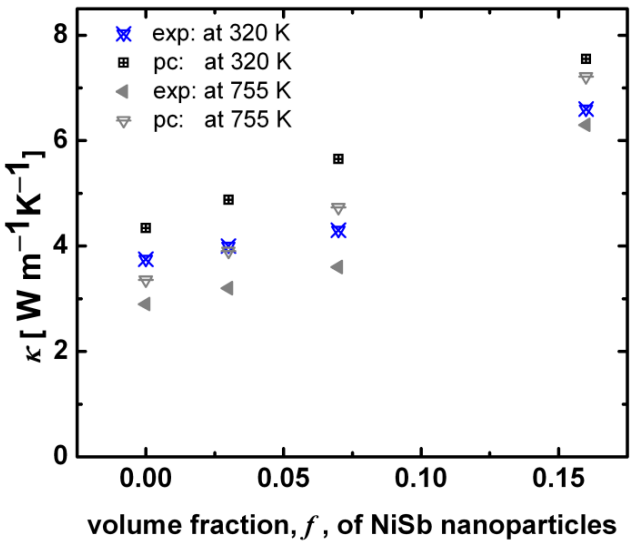

Figure 5.9: Variation of experimental and pore corrected thermal conductivity for samples of different volume fractions at 320 K and 755 K.

Similar to the Seebeck coefficient, the power factor, *P.F.* = $S^2\sigma$ increases approximately linearly with temperature (Figure 5.10). A similar trend was observed in $Ni_{0.05}Mo_3Sb_{5.4}Te_{1.6}$/MWCNT.[107] For all samples, *P.F.* lies within the range *of* 2.5 μW $cm^{-1}K^{-2}$ to 3.8 μW $cm^{-1}K^{-2}$. With increasing temperature, the rise in *P.F.* is higher for the bulk and 0.160 NiSb samples. At 750 K, for 0, 0.034, 0.074 and 0.160 NiSb samples are 12.0 μW $cm^{-1}K^{-2}$, 10.6 μW $cm^{-1}K^{-2}$, 9.9 μW $cm^{-1}K^{-2}$, and 12.4 μW $cm^{-1}K^{-2}$. For the 0.160 NiSb sample, the main contributing factor to *P.F.* is the enhanced electrical conductivity by 163%.

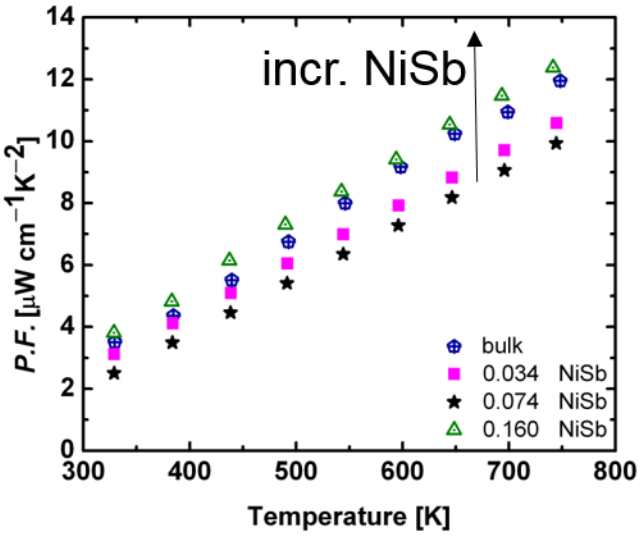

Figure 5.10: Temperature dependence of *P.F.* of bulk and NiSb composites.

The transport properties of bulk NiSb material (100 μm – 1000 μm particle size) are displayed in the Supplementary Information. The Seebeck coefficient of NiSb bulk material is ~11 μV K^{-1} around room temperature. Different authors have reported different values based on the synthesis conditions, e.g. ~5 μV K^{-1} at 350 K by Katsuyama et al.[280] and 35 μV K^{-1} at 300 K for NiSb nanocrystals of 60 nm - 80 nm size by Li et al.[146] At 300 K, bulk Ag has one of the highest electrical conductivity (6.3×10^5 Ω^{-1} cm^{-1}) of any solid, and Bi has a quite high absolute Seebeck coefficient of about −70 μV K^{-1}; both have similar density and do not form a solid solution. A Bi/Ag composite showed improved electrical properties and less reduction in Seebeck coefficient, thus improving *P.F.* by 50% by the addition of 24% volume fraction of Ag, which is below the percolation threshold.[125] Contrary to this, solvothermally synthesized NiSb nanoparticles of 60 nm – 80 nm, cold-pressed at 4 MPa, have an electrical conductivity of 10^4 Ω^{-1} cm^{-1} and a Seebeck coefficient of ~35 μV K^{-1} at 300 K (very high density samples may exhibit even better electrical properties compared to cold pressed samples).[146] Similarly, $Ni_{0.05}Mo_3Sb_{5.4}Te_{1.6}$ has a Seebeck coefficient of ~60 μV K^{-1}, and NiSb has a very high electrical conductivity of 10^4 Ω^{-1} cm^{-1}. Both NiSb and $Ni_{0.05}Mo_3Sb_{5.4}Te_{1.6}$ have similar densities (8.23 g cm^{-3} and 8.28 g cm^{-3}) and do not form sediments during consolidation as TEM micrographs

show. The $Ni_{0.05}Mo_3Sb_{5.4}Te_{1.6}$/NiSb composite exhibited decreased Seebeck values even for a sample with NiSb volume fraction as small as 0.034. While the TEM micrograph of Bi/Ag (24% volume fraction) showed islands of μm size Ag particles on Bi matrix, TEM images show NiSb nanoparticles of ~60 nm in size. As explained earlier, the possible reason for reduction of the Seebeck coefficient in $Ni_{0.05}Mo_3Sb_{5.4}Te_{1.6}$/NiSb samples is the enhanced charge carrier concentration. On the other hand, the μm size Ag particles were not well connected and some randomly formed Ag particles might have aided in electrical conductivity, without significantly changing charge carrier concentration. Using electrical conductivity, Seebeck coefficient and thermal conductivity at the same temperature segments, we have calculated the *figure-of-merit, ZT*, from 330 K to 740 K (Figure 5.11). The *ZT* values for all samples at 330 K with increasing NiSb content are: 0.031, 0.026, 0.019 and 0.019, respectively, and at 740 K, these values reach: 0.31, 0.24, 0.20 and, 0.14 respectively. The reduction in *ZT* by 36% for NiSb: $f = 0.16$ is due to deleterious enhancement in thermal conductivity by 113% and 34% decrease in Seebeck coefficient. The enhancement of the electrical conductivity by 163% was not enough to compensate the loss by thermal conductivity enhancement and reduction in Seebeck coefficient. This investigation suggests that even small amounts of NiSb nanoparticles with 60 nm in size bring the composite beyond both the electrical and thermal percolation thresholds.

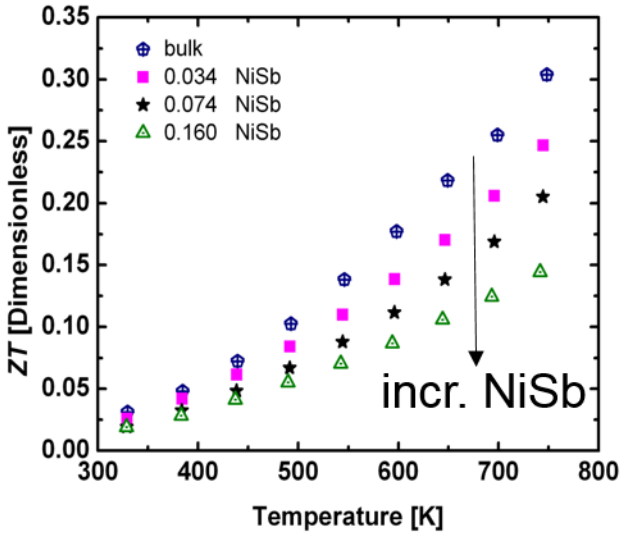

Figure 5.11: Temperature dependence of *figure-of-merit* of bulk and NiSb composites.

5.5 Mechanical Properties

The Vickers hardness and elastic modulus of the bulk with 0.034 NiSb were 3.3 GPa and 116 GPa; this represents a 1.5 times increase in the Vickers hardness (from 2.2 GPa) and a 2.2 times increase in the elastic modulus of the bulk sample from 52 GPa. An addition of 0.074 NiSb nanoparticles increased the Vickers hardness to 3.5 GPa and decreased the elastic modulus to 96 GPa from the 0.034 NiSb sample. At high loadings of NiSb nanoparticles, 0.160, the Vickers hardness increased to 3.9 GPa and the elastic modulus decreased to 69.0 GPa. Thusly, the hardness of the $Ni_{0.05}Mo_3Sb_{5.4}Te_{1.6}$ bulk improved with the addition of NiSb nanoparticles up to 0.160; the elastic modulus initially increased with small additions of NiSb nanoparticles of 0.034, but decreased with further increased additions of NiSb nanoparticles. The increased hardness is due to grain size; the increased number of nanoparticles with nanometer scale grains will increase the hardness in accordance to the Hall-Petch relationship [281]. The elastic modulus decreased with the addition of NiSb nanoparticles due to high surface-to-volume ratio of nanoparticles, nanoparticle-bulk interaction, and nanoparticle-nanoparticle interaction, which causes phase separation as indicated by TEM images from Fig. 5.2.

The variability in the hardness and elastic modulus values could be due to a heterogeneous pile-up, caused by large variations in grain sizes in these materials [282]. Indenting inside the grain, or grain boundaries, or at defects will form different amounts of pile-up, thus increasing variability using the microindenter.

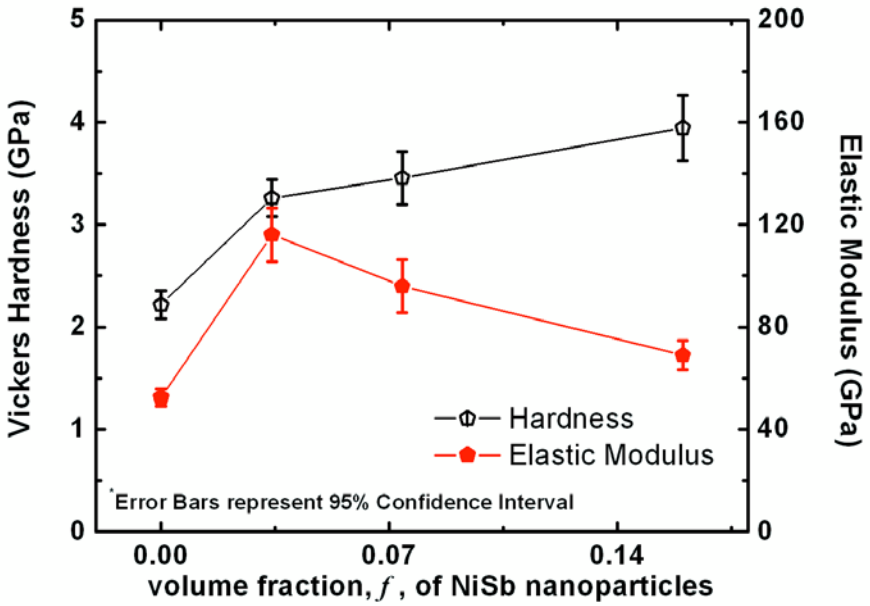

Figure 5.12: Variation of mechanical properties with respect to NiSb content.

5.6 Conclusion

In this research, we successfully synthesized NiSb nanoparticles of ~60 nm in size through a solvothermal route, and incorporated them into bulk materials in different volume fractions. Our efforts to reduce thermal conductivity were not successful, but we succeeded in enhancing electrical conductivity. Combined with a large reduction in the Seebeck coefficient, the *figure-of-merit* decreased with increasing NiSb content. Nevertheless, our investigation provided some very interesting results.

At 330 K, for the 0.16 sample, the electrical conductivity increased 2.6 times compared to the bulk as highly conductive NiSb nanoparticle clusters formed between the bulk particles, thus

aiding in enhancing the electrical and thermal conductivity. TEM images of the 0.16 sample show all the typical characteristics of a percolation network. The electrical percolation network exists in the 0.16 sample and electrical percolation threshold was ~ or < 0.16 volume fraction of NiSb. Applying the power law to the electrical conductivity yielded $T^{-0.42}$ variation for bulk, 0.034 and 0.074 samples, revealing that charge scattering mechanism for all these samples is the same. The electrical conductivity of sample 0.16 decays as $T^{-0.45}$. The pore related reduction in electrical conductivity becomes larger with the increase in the volume fraction of NiSb.

The thermal conductivity increases with respect to the amount of NiSb content. Variation in the lattice thermal conductivity from 330 K to 755 K for all samples shows that phonons are undergoing the same scattering mechanism. Adopting Callaway formalism for lattice thermal conductivity, we concluded that suppressed electron-phonon interaction is not the reason for the enhanced lattice thermal conductivity; rather, it is due to a possible reduced U-process. Assuming the Debye temperature of composites has increased, we speculate ph-ph transfer efficiency exists between bulk and NiSb particles, due to the overlap in spectrum in DOS of phonons. Electron-phonon coupling, defects, precipitates, strain, and dislocations are not the contributing factors. Detailed investigation of impedance matching of constituents is needed to explain the collective variation of lattice thermal conductivity. The total interfacial per unit area due to the presence of NiSb nanoparticles is less effective in phonon scattering. In the 0.16 sample, the electronic contribution to the total thermal conductivity is 30%, whereas for the rest of the samples it is 20%. We argue that needle like structures of NiSb are enhancing the phonon transmission between bulk particles.

We also synthesized NiSb particles of larger size through solid-state reaction to understand the impact of the NiSb particles on the effective TE properties. Another very important outcome of this study is how a small amount of NiSb nanoparticles can enhance electrical conductivity and thermal conductivity of moderately conductive material.

Materials scientists are interested in designing materials designed to have very high thermal conductivity for thermal management in electronic packaging systems and for numerous industrial applications. Power levels for the next generation microprocessor could be as high as

70 W – 200 W; this very high power density is the main source of heat mainly due to Joule heating. To keep the device function reliable and to avoid premature failure, it is very important to extract the dissipated heat using high thermal conductivity materials.[283] Combined with these results, there is a systematic enhancement in hardness with respect to NiSb; thus bulk/NiSb composites are capable of better withstanding stress that arises from a temperature gradient during the operation. Composites with these qualities have found applications in various industries.

In the near future our focus is to pursue wet chemistry techniques such as nanocoating our bulk particles similar to $CoSb_3$ nanocoating on bulk $CoSb_3$ and $CoSb_3$ nanocoating on bulk $La_{0.9}CoFe_3Sb_{12}$[144, 284] to reduce thermal conductivity.

5.7 Supplementary information

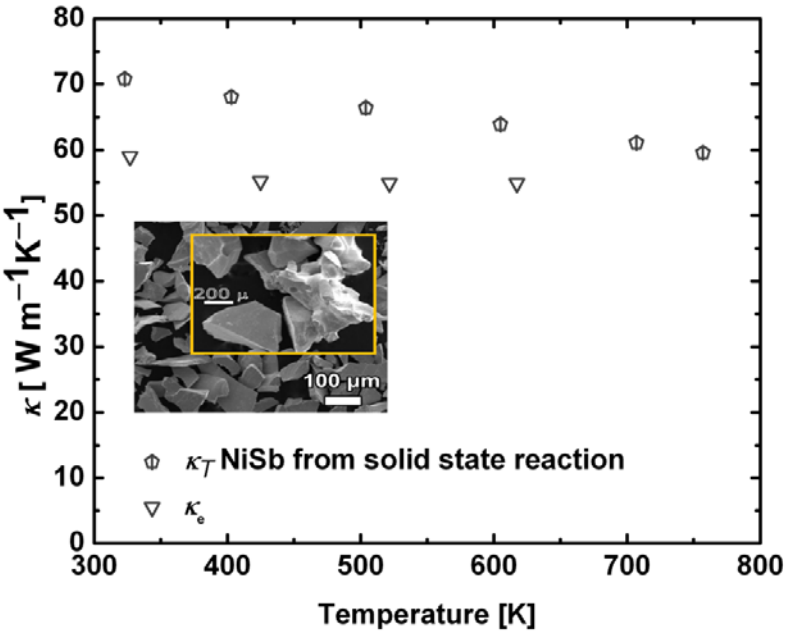

Figure 5.13: Temperature dependence of total thermal conductivity of large NiSb particles synthesized through high temperature solid-state reaction. Inset shows NiSb particles of larger size.

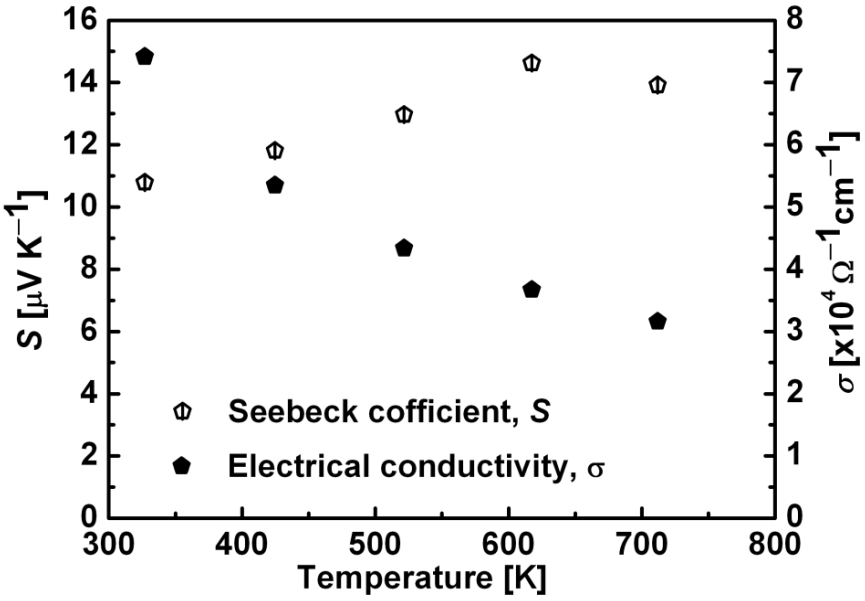

Figure 5.14: Temperature dependence of electrical conductivity and Seebeck coefficient of bulk NiSb particles synthesized through high temperature solid-state reaction. Particle sizes were the same (100 μm – 1000 μm) as displayed in the thermal conductivity plot in 55.12

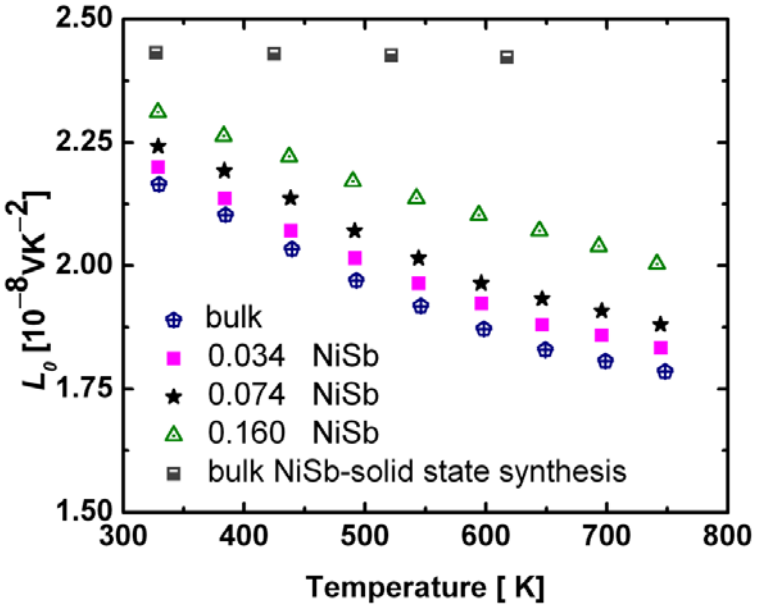

Figure 5.15: Temperature dependence of Lorenz numbers of bulk/NiSb composites.

Chapter 6

Effective Thermal Properties of $Ni_{0.05}Mo_3Sb_{5.4}Te_{1.6}$ Thermoelectric Material Embedded with SiC and Al_2O_3 Nanoparticles[12]

The results of this investigation are yet to be published in a relevant journal.

6.1 Background

This chapter extensively covers the effective thermal properties and thermal boundary resistance (Kapitza resistance) of $Ni_{0.05}Mo_3Sb_{5.4}Te_{1.6}$/SiC and $Ni_{0.05}Mo_3Sb_{5.4}Te_{1.6}/Al_2O_3$ composites adopting various Effective Media Approximations (EMA). It also covers mechanical properties of composites and their relation to their effective thermal properties. Surface area and pore size distributions are used to correlate their effect on thermal conductivity. Readers are strongly advised to read Section 1.4.1 and 1.9 before reading the next sections.

6.2 Experimental Section

6.2.1 Synthesis

The procedure for synthesizing bulk $Ni_{0.05}Mo_3Sb_{5.4}Te_{1.6}$ is similar to the one we reported in our previous paper on $Ni_{0.05}Mo_3Sb_{5.4}Te_{1.6}$/MWCNT.[107] Once required amount of the material is obtained from several reactions, we mixed them using high frequency Vortex mixer (Fisher Scientific) for 20 min and divided the sample into two equal portions. First portion was divided into four equal portions of 2.3 g of material each. We dispersed SiC in volume fractions, f = 0, 0.01, 0.02 and 0.034. First requisite amount of bulk material was added to mortar; appropriate amount of SiC nanoparticles in high purity acetone suspension was sonicated for 15 minutes; small amount of suspension was added to mortar containing bulk dropwise, and stirred with pestle until acetone evaporates. The process continued until the whole suspension depletes.

[12] Nagaraj Nandihalli, Robert Liang, Stéphane Gorsse, Norman Zhou, Takao Mori, Holger Kleinke

The sample without SiC ($f = 0$) was retained as a reference (also called bulk). Consolidation of the composite was carried out using the 30-ton Oxy-Gon hot-press at The University of Waterloo. A similar procedure was followed for other samples; their densities were measured using Archimedes principle and displayed in Table 6.1. For bulk/Al_2O_3 composites, nanoparticles of Al_2O_3 in volume fractions, $f = 0$, 0.01, 0.0216 and 0.0325 were added. Sample with zero volume fraction was retained as a reference sample.

Table 6.1: Experimental densities of various $Ni_{0.05}Mo_3Sb_{5.4}Te_{1.6}$/SiC composites at 295 K.

f	Density of pellet ρ/(g cm^{-3})	Relative Density (%)
0 (bulk)	8.21	94.2
0.010	7.96	92.8
0.020	7.93	91.0
0.034	7.85	90.7

The three Al_2O_3-containing samples were consolidated using the SPS technique at National Institute for Materials Science (NIMS), Japan (Section 4.5.2 for details). The densities were determined using Archimedes' principle (Table 6.2).

Table 6.2: Experimental densities of various $Ni_{0.05}Mo_3Sb_{5.4}Te_{1.6}/Al_2O_3$ composites at 295 K.

f	Density of pellet ρ/(g cm^{-3})	Relative Density (%)
0 (bulk)	8.59	98.5
0.0100	8.36	96.5
0.0216	8.27	96.0
0.0325	8.13	95.0

6.2.2 Phase and Microstructural Characterization

Immediately after the transport properties were characterized, the hot–pressed and SPSed samples were ground into powder and subjected to XRD phase analysis. As XRD patterns in Figure 6.9 and Fig. 6.10 (Supplementary Information) show, no discernible SiC and Al_2O_3 peaks were observed due to their small amount. Small amount of Sb phase was detected.

The inner part of cracked consolidated samples and their outer surfaces were subjected to SEM and TEM analysis to study the microstructural features such as particle size, grain boundaries, pore shapes, their distribution, and also their phase purity. We have reported SEM and TEM analysis for bulk/SiC and SEM analysis for bulk/Al_2O_3. In either case it is possible to detect and estimate the approximate particle aggregate sizes inside the bulk.

SEM located at University of Waterloo's Waterloo Advanced Technology Laboratory (WAT Labs)'s Zeiss Ultra | plus SEM coupled with integrated secondary electron detector in in-lens mode was used to study microstructural features (Section 2.5). Fig. 6.1 shows the microstructures of cracked disk of SiC: $f = 0.034$ and its polished surface. Figure 6.1(a) shows well-polished 0.034 SiC disk. The surface is rough, and voids of ~10 μm are found to be distributed randomly. Fig. 5.1(b) shows bulk particles of varying sizes ranging from 2 μm – 10 μm. Bulk particles are dotted with SiC nanoparticle in agglomerated form because nanoparticles have higher surface energy for agglomeration.[285] Distribution of SiC aggregates are shown in Fig. 6.1(c). This shows that intense sonication did not help to de–agglomerate clumped SiC nanoparticles, leading to islands of SiC particles within composites. These agglomerates are plate like rather than spherical. As shown in Figure 6.1(d), some SiC aggregates with diameters ranging from several tens to one hundred nanometers are observed between grain boundaries of bulk particles.

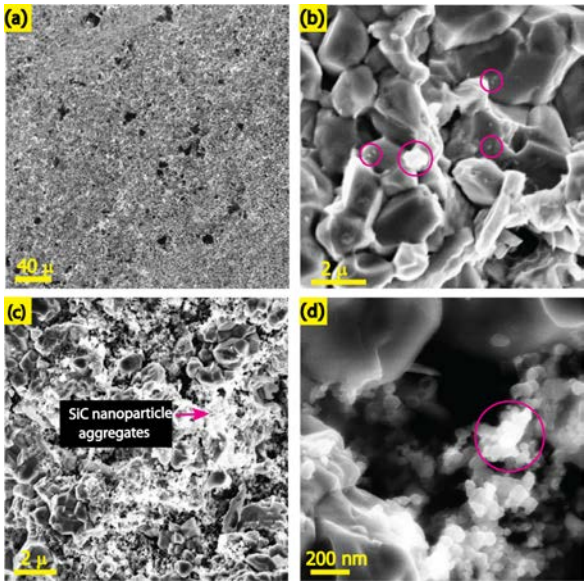

Figure 6.1: SEM images of hot–pressed $Ni_{0.05}Mo_3Sb_{5.4}Te_{1.6}$/0.034 SiC. (a) Surface with 20 µm – 30 µm voids; (b) SiC aggregates on bulk particles; (c) clumped aggregates of SiC; (d) SiC aggregates between the bulk particles.

Grain boundaries (GB) and elemental analysis to confirm the existence of SiC and pure phase of bulk was done using transmission electron microscopy (TEM). As obtained TEM micrographs of SiC: $f = 0.034$ are displayed in Figure 6.2(a). 500 nm aggregates of SiC are clearly visible. In some places clean grain boundaries (GB) are also visible. Figure 6.2 (b-f) shows elemental mappings of silicon, nickel, molybdenum, antimony, and tellurium, all obtained using aforementioned TEM in energy dispersive X-ray spectroscopy (EDX) configuration. The distribution of those elements were homogeneous throughout the samples we analyzed, indicating that no element precipitated or decomposed during consolidation.

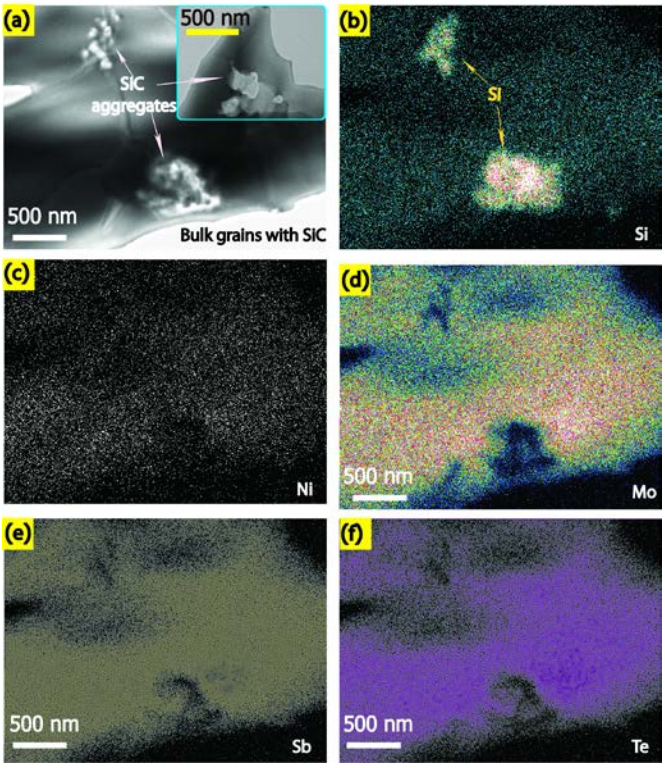

Figure 6.2: TEM images of hot–pressed $Ni_{0.05}Mo_3Sb_{5.4}Te_{1.6}$/0.034 SiC disk. (a) SiC aggregates on the surface of bulk particles; (b), (c), (d), (e) and (f): elemental maps of Si, Ni, Mo, Sb, Te respectively.

Figure 6.3 shows the SEM analysis inside the cracked Al_2O_3: f = 0.0325 disk as well as its polished surface. Fig. 6.3(a) at 100 micron magnification shows the smooth surface. At 2 μm magnification, Figure 6.3(b) shows distribution of 2 μm – 5 μm size voids. Figure 6.3(d) shows Al_2O_3 aggregates of around 400 nm. Compared to Al_2O_3 sample, SiC sample has larger voids and rougher surface.

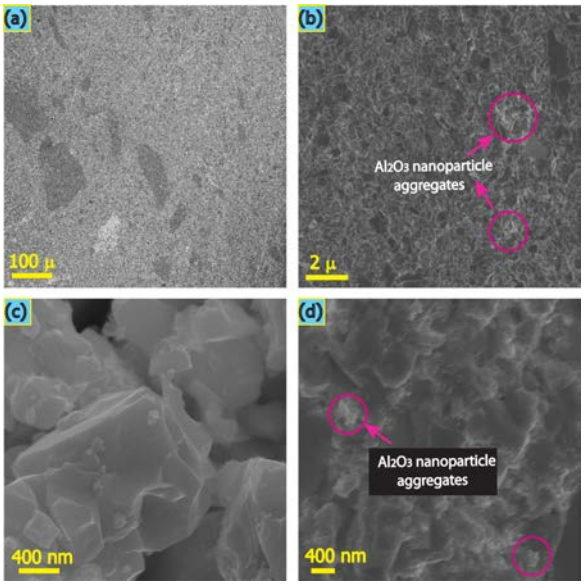

Figure 6.3: SEM images of spark-plasma sintered $Ni_{0.05}Mo_3Sb_{5.4}Te_{1.6}$/0.034 Al_2O_3. (a) Surface morphology; (b) voids of 2 µm and Al_2O_3aggregates on bulk particles; (c) voids and bulk particles at higher magnification; (d) Al_2O_3 aggregates of 400 nm.

6.2.3 BET Surface Area and BJH Pore Size Distribution

Shown in Figure 6.4 and Figure 6.5 are the pore size distribution for two types of composites, calculated using BJH method. The distribution of pore size is discrete; it does not follow any specific pattern. Sample SiC: $f = 0$ and 0.01 exhibit the same distribution. The pore sizes for SiC: $f = 0$, 0.01 are centered at 2 nm, 5.6 nm, 17 nm and 1.9 nm, 4.3 nm, and 14.7 nm. This is expected considering the small amount of SiC in $f = 0.01$ sample. Similarly, for SiC: $f = 0.02$ and 0.034, the pore sizes shift to both lower and higher diameters, i.e. 1.8 nm, 3.8 nm, 9.6 nm and 25 nm. And for SiC: $f = 0.034$, the pore size shift to 1.7 nm, 3.4 nm, 9.5 nm and 24.8 nm. For Al_2O_3: $f = 0$ sample pores are centered around 3 nm, 7.8 nm and 20 nm; for Al_2O_3: $f = 0.01$, pores are congregated around 2.5 nm, 5.6 nm and 17 nm. Al_2O_3: $f = 0.034$ has the bulk type of pattern with 2.7 nm, 7.8 nm and 20 nm.

Surface area and BJH cumulative pore volumes on the other hand exhibit specific pattern. Surface area and cumulative pore volume for both batches, increase steadily up f ~0.02, there is a sudden increase in both parameters for SiC: f = 0.032 and Al_2O_3: f = 0.0325. If we compare SiC :f = 0.00 and 0.034 samples, there is an increase by 80% in surface area and 282% increase in cumulative pore volume respectively. Similarly, for Al_2O_3: f = 0.0325, 90% and 174% increase in surface area and cumulative pore volume compared to Al_2O_3: f = 0. This suggests that there is a considerable increase in surface to volume ratio as f increases especially for SiC samples.

Table 6.3: BET surface area and BJH (Barrett-Joyner-Halenda) cumulative pore volume, and pore volume distribution.

Composite	Surface Area (m^2g^{-1})	Cumulative Pore Volume ($cm^3\ g^{-1}$)
SiC		
f = 0.00	0.584	3.40×10^{-3}
f = 0.010	0.650	4.29×10^{-3}
f = 0.020	0.782	4.81×10^{-3}
f = 0.034	1.047	12.9×10^{-3}
Al_2O_3		
f = 0.00	0.470	1.84×10^{-3}
f = 0.010	0.491	1.61×10^{-3}
f = 0.0216	0.535	1.96×10^{-3}
f = 0.0325	0.893	5.06×10^{-3}

As nitrogen adsorption isotherms indicate, for SiC: f = 0, and 0.01, the shapes of isotherm are almost the same. However, for SiC: f = 0.02 and 0.034, the width between adsorption and desorption curves is well pronounced. Isotherms of SiC: f = 0.02 and 0.034 belong to category H3 or H4 (Section 2.11). This kind of hysteresis indicates the existence of non-rigid aggregates

of plate-like particles forming slit shaped pores, with uniform (type H4) or nonuniform (type H3).[286, 287]

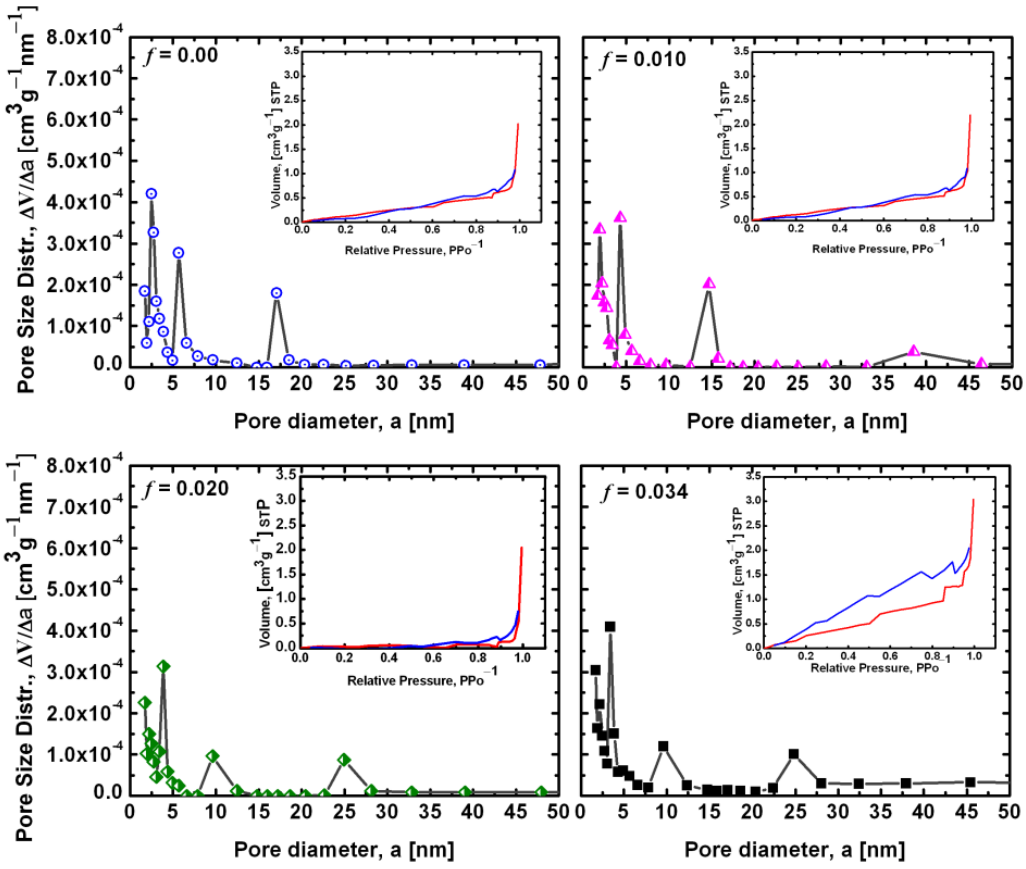

Figure 6.4: Pore size distributions calculated from adsorption data using the BJH method for bulk/SiC.

Table 6.4: Pore volume distribution according to their sizes in $Ni_{0.05}Mo_3Sb_{5.4}Te_{1.6}$/SiC composites.

SiC *f*	Pore Vol (0–50 nm) $cm^3\ g^{-1}$	Micropore Volume $cm^3\ g^{-1}$	Mesopore Volume $cm^3\ g^{-1}$	Macropore Volume $cm^3\ g^{-1}$	% Macropore 50–500 nm	% Mesopore 2–50 nm	% Micropore < 2 nm
0	1.30×10^{-3}	1.28×10^{-4}	1.15×10^{-3}	2.10×10^{-3}	62.1	34.0	3.8
0.010	1.12×10^{-3}	1.14×10^{-4}	1.00×10^{-3}	3.70×10^{-3}	76.8	20.9	2.4
0.020	1.11×10^{-3}	1.09×10^{-4}	1.85×10^{-3}	3.20×10^{-3}	74.2	23.3	2.5
0.0340	2.11×10^{-3}	2.64×10^{-4}	1.85×10^{-3}	1.00×10^{-2}	83.7	14.3	2.0

Similarly, for Al_2O_3: f = 0 and 0.01, the isotherms look similar; for Al_2O_3: f = 0.0216 and 0.0325, the width increases, indicating the existence of more plate-like aggregates as the content is increased. Isotherms of both bulk materials show plate-like structures; however, as the content of SiC and Al_2O_3 increases, the isotherm shape changes. Thus, we can conclude that both composites have plate-like loose aggregates. Although the estimation of pore size distribution are not very accurate, we still consider macropore distribution and their volume in interpreting thermal related properties. While predicting the effective thermal properties of SiC-reinforced aluminum matrix, the shape of SiC was taken as spherical even though they had angular and flat-plate shapes while the model assumes the embedded particles are spherical in shape. However, in our case, as TEM and BET isotherms show, the embedded SiC and Al_2O_3 aggregates must have turned into loose aggregates of plate-like structure under intense uniaxial pressure. The SEM microstructural investigation of hot-pressed Ti_3SiC_2 with 20 vol% SiC composite, under pressure of 45 MPa and temperature of 1773 K, showed plate-like structures of SiC. [288] Using all these facts treating SiC and Al_2O_3 aggregates in our bulk as loose plates is well justified.

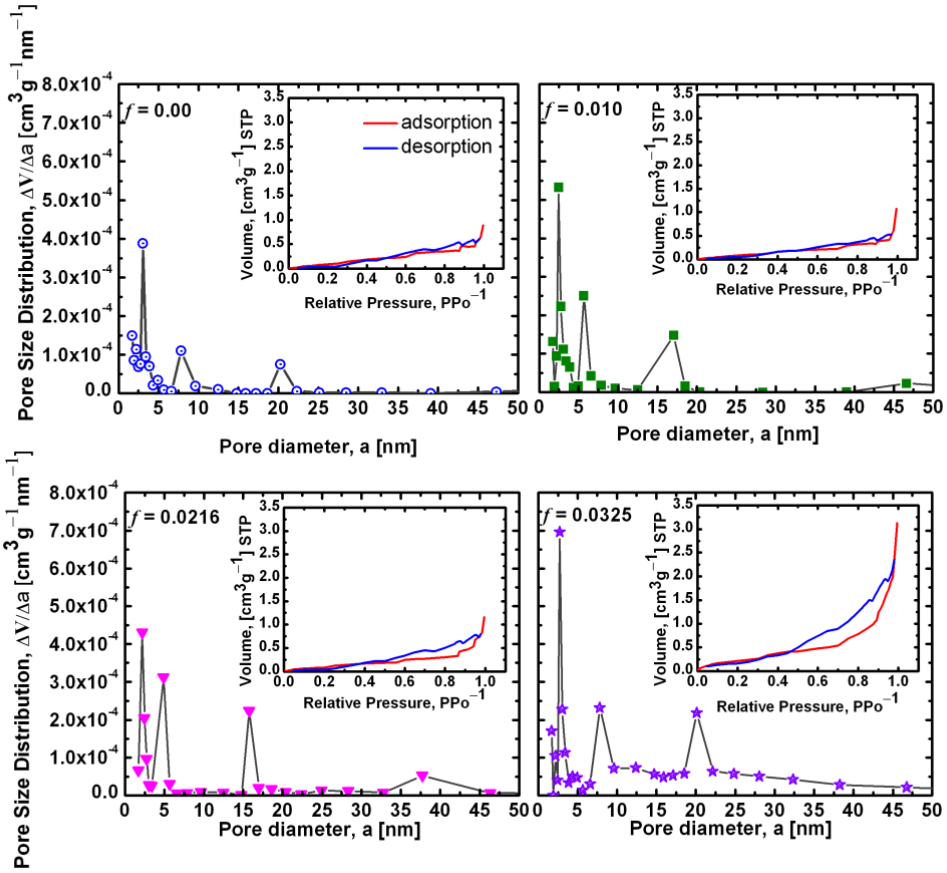

Figure 6.5: Pore size distributions calculated from adsorption data using the BJH method for bulk/Al_2O_3.

Table 6.5: Pore volume distribution according to their sizes in $Ni_{0.05}Mo_3Sb_{5.4}Te_{1.6}/Al_2O_3$ composites.

Al_2O_3 *f*	Pore Vol (0–50nm) $cm^3\ g^{-1}$	Micropore Vol $cm^3\ g^{-1}$	Mesopore Vol $cm^3\ g^{-1}$	Macropore Vol $cm^3\ g^{-1}$	% Macropore 50–500 nm	% Mesopore 2–50 nm	%Micropore < 2 nm
0	7.92×10^{-4}	7.44×10^{-5}	7.20×10^{-4}	1.05×10^{-3}	56.0	39.0	4.0
0.010	1.07×10^{-3}	8.04×10^{-5}	9.90×10^{-4}	5.40×10^{-4}	33.5	61.5	5.0
0.0216	1.25×10^{-3}	9.30×10^{-5}	1.16×10^{-3}	7.10×10^{-4}	36.2	59.0	4.7
0.0325	3.00×10^{-3}	2.52×10^{-4}	2.74×10^{-3}	2.60×10^{-3}	46.4	49.0	4.5

6.2.4 Hardness and Young Elastic Modulus Testing

Hardness testing was done on these samples by micro–indentation. Left over samples from diamond saw cutting for electrical conductivity were mounted using phenolic resin (diameter: 1.25”, thickness: and 0.5”) on a mounting hot-press (Buehler SimpliMet ® 1000) at a pressure of 4300 psi under a heating time of 5 min and a cooling time of 3 min. The mounted samples were progressively ground with 600, 800, 1200 coarse, and 1200 fine grit silicon carbide paper then polished for a mirror-like finish using 1 μm and 0.25 μm diamond spray, sequentially, on a polishing pad under 250 rpm rotation. The hardness and elastic modulus of the polished thermoelectric samples were characterized using the Nanovea ST400 Optical Profilometer with built-in micro–indentation module using a Vicker’s indenter (radius: 100 μm).

Micro–indentation is based on ASTM E2546 and ISO 14577. It uses a method in which a Vicker’s indenter tip is driven into a specific site of the material being tested by applying an increasing normal load. When reaching a pre-set maximum value, the normal load is maintained for 20s, followed by a reduction of the normal load until complete relaxation occurs. Hardness was measured under a load of 10 N with a loading rate of 20 N min^{-1}, and an unloading rate of 10 N min^{-1}; the values were obtained from the load vs. depth curve and analyzed using the

Nanovea hardness software. The elastic modulus was determined using Oliver and Pharr's method.[289]

6.3 Thermal Property Measurements

The procedure to measure thermal properties is discussed in Section 2.9

Table 6.6: Thermal conductivity parameters for SiC and Al_2O_3 composites at 325 K.

Composite	κ (W $m^{-1}K^{-1}$)
SiC	
$f = 0.00$	5.23
$f = 0.010$	4.11
$f = 0.020$	3.16
$f = 0.034$	2.90
Al_2O_3	
$f = 0.00$	4.83
$f = 0.010$	4.46
$f = 0.0216$	4.45
$f = 0.0325$	4.33

6.4 Results and Discussion:

6.4.1 Effective Thermal Properties

Shown in Figure 6.6 and Figure 6.7 is the normalized effective thermal conductivity, $\kappa_{comp} / \kappa_{bulk}$, for $Ni_{0.05}Mo_3Sb_{5.4}Te_{1.6}$/SiC and $Ni_{0.05}Mo_3Sb_{5.4}Te_{1.6}/Al_2O_3$, respectively. Also shown in the figures is Nan et al.'s MG–EMA fit with experimental data assuming that the embedded nanoparticles are not spherical but rather laminated flat plates. Prediction of B–EMA

for effective properties and L–V upper and lower bounds for effective properties are also displayed. We have not shown B–EMA prediction for SiC because it is very similar to bulk/Al_2O_3. The L–V lower bound is obtained in the limiting case where a scalar quantity called effective thermal conductivity $m_o = 0$ was used (m_o^{-1} is called the formation factor in porous media literature). The formation factor generally applies to porous composites and decides the effective thermal boundary resistance. Thus, nanoparticles of a certain shape and size within composites are replaced by non-conducting voids. Included in the plots is the effective thermal conductivity due to the presence of porosity for both composites obtained by using Maxwell's EMA for porous media. B–EMA and pore modified Maxwell's EMA predictions are close.

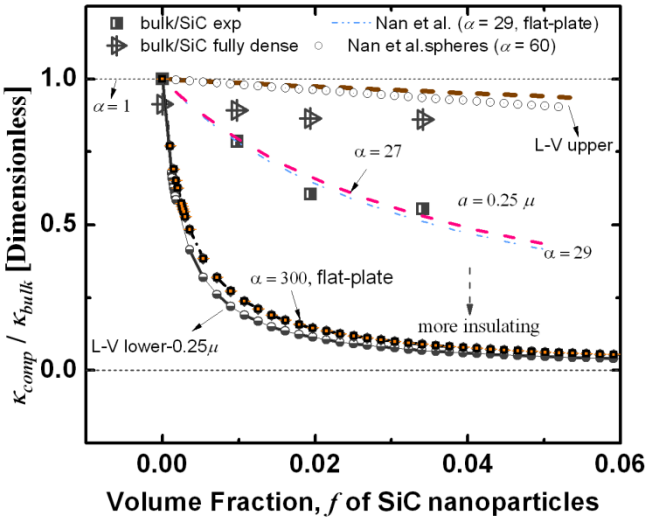

Figure 6.6: Normalized composite thermal conductivity for $Ni_{0.05}Mo_3Sb_{5.4}Te_{1.6}$/SiC composites with pore corrected, non-pore corrected, and prediction of effective thermal conductivity from different EMAs, L–V upper and lower bounds.

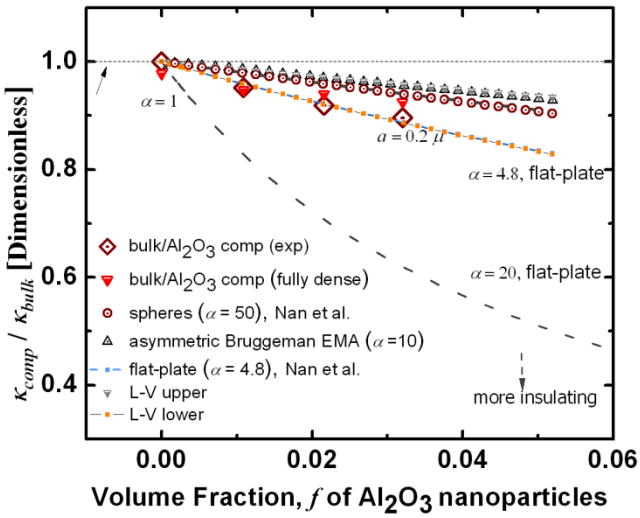

Figure 6.7: Normalized composite thermal conductivity for $Ni_{0.05}Mo_3Sb_{5.4}Te_{1.6}/Al_2O_3$ composites with pore corrected, non-pore corrected, prediction of effective thermal conductivity from different EMAs, L–V upper and lower bounds.

Not taking into consideration the interfacial effects, the effective thermal conductivity of composites lies between two extremities determined by the thermal conductivities of their constituents; and if we consider interfacial effects, κ_{comp} can cross the two extremities.[35]

In ZnS/diamond composites[40], experimental measurements of the thermal conductivity of the composites lie below the limit of completely insulating case of $\alpha \rightarrow \infty$. Although we accept the author's rationale that this discrepancy may be due to embedded smaller particles that had elliptical shapes, thus changed the volume fraction, our assertion is that, as the particles become smaller, their shape distribution becomes wide leading to microstructural changes that could change the thermal boundary resistance.

Next we tried Nan et al.'s MG-EMA prediction assuming embedded particles are spherical (Equation 1.6) for both types of composites, and obtained $\alpha = 40$, and corresponding, $a_k = 1.5$ μm and $R_{Bd} = 2.86 \times 10^{-6}\ m^2KW^{-1}$ for SiC composite. Similarly, for Al_2O_3, $\alpha = 50$, which gave $a_k = 1.0$ μm and $R_{Bd} = 2.0 \times 10^{-6}\ m^2KW^{-1}$. We did not show the limiting case of $\alpha \rightarrow$

∞ ($1/\alpha = 0$) as it is very close to $\alpha = 40$. As the Al_2O_3 plot shows, we have applied B–EMA model (Equation 1.4) and found $\alpha = 10$, which translated into $a_k = 2.0$ μm and $R_{Bd} = 0.41 \times 10^{-6}$ m^2KW^{-1}. These results are expected because the model we invoked is similar to MG–EMA derived by Hasselman and Johnson[34] for particulates with spherical particles..

L–V upper bounds are close to the effective properties predicted by Maxwell for both types of composites. The close proximity of L-V upper bounds to Maxwell's prediction is not surprising either, given that L–V lower bounds consider a monotonic increase in thermal conductance with respect to nanoparticle parameters. This model is similar to the Hashin–Shtrikman upper limit for isotropic composites with perfectly bonded interfaces, i.e., composites of high density without pores. As mentioned in the introduction, the interfacial thermal barrier to heat flow in composites arises from imperfect mechanical contact.[46]

Considering L–V lower bounds for both composites, there is a big difference between SiC and Al_2O_3 composites. For bulk/SiC composites, $\kappa_{comp}/\kappa_{bulk}$ falls precipitously, from 1 to 0.65 for small increment of $f = 0$ to $f = 0.001$, and from $\kappa_{comp}/\kappa_{bulk} = 0.2$, it proceeds asymptotically to x–axis.

SiC L–V lower bound prediction treats composite with homogeneously suspended particles, and predicts sharp bounds on lower effective thermal conductivity with limiting case of $m_o = 0$. Although for SiC samples, the experimental data lies within both L–V upper and lower bounds, the predicted sharp drop for lower bound and its asymptotic trend provoke a question on the contribution of total surface area due to the pores. We have made an attempt to explain this discrepancy in the coming paragraphs. The bounds for bulk/Al_2O_3 are tighter than the bounds for bulk/SiC composites.

Contrary to SiC L–V lower bound, L–V lower bound for bulk/Al_2O_3 composites on the other hand predicts very sharply. For 0.2 μm radius of Al_2O_3 aggregate, we found the bound is perfectly agreeing with our experimental results. L–V upper bound for both bulk/SiC and bulk/Al_2O_3 as shown in the Figure 6.6 lies close to $\alpha = 1$.

We calculated the Kapitza radius using a dimensionless parameter, α, obtained by fitting Equation 1.5 with experimental data for the particle size, a, taken from SEM and TEM images, and other pertinent parameters. The values of a_k are found to be 7.25 μm and 0.96 μm respectively for SiC and Al_2O_3. The thermal boundary resistance, R_{Bd}, was calculated via the relation, $a_k = R_{Bd}\ \kappa_{bulk}$. Respectively for SiC and Al_2O_3: R_{Bd} is 3.8×10^{-5} m^2KW^{-1} and 0.2×10^{-6} m^2KW^{-1}. Thermal boundary conductance, R_{Bd}^{-1} values are 2.63×10^4 m^2KW^{-1} and 5.00×10^6 m^2KW^{-1} for composites with SiC and Al_2O_3, and these parameters were used to estimate L–V bounds. These parameters are listed in Table 6.8. An almost 200% difference in R_{Bd} values between these two types of composites raises questions about the differences in microstructures. Thermal conductivity of particle and its size alone are not enough to explain this difference.

Table 6.7: Some pertinent parameters used in effective property estimation.

Constituents	κ (W $m^{-1}K^{-1}$)	Particle radius (μm)
$Ni_{0.05}Mo_3Sb_{5.4}Te_{1.6}$/SiC		
		>100
$\kappa_{\beta\text{-}SiC}$	320	0.25
$Ni_{0.05}Mo_3Sb_{5.4}Te_{1.6}/Al_2O_3$		
		>100
κ_{Al2O3}	30	0.20

In ZnS/diamond composite (ZnS with κ_{bulk} = 17.4 W $m^{-1}K^{-1}$) with 2 μm diamond particles (κ = 600 W $m^{-1}K^{-1}$), Kapitza radius a_k is found to be ~1.5 μm and the corresponding thermal boundary resistance $R_{Bd} = 6 \times 10^{-8}$ m^2KW^{-1}.[40] A large value of a_k = 7.25 μm for bulk/SiC composite (far larger than the mean free path of dominant phonons l, in our composite), suggest that the probability that phonons make attempts and succeed in crossing the barrier is very low according to the relation $a_k = l / \eta_p$, where η_p is the probability with which phonon can

transmit across the interface. This is one strong indication that bulk/SiC composite is exhibiting large thermal boundary resistance, compared to bulk/Al_2O_3 composites.

To gauge the degree of change in α we have shown different values of α for flat-plate particles for both composites. As the plots show, change in α is very sharp in bulk/Al_2O_3 composites compared to bulk/SiC indicating that even if there is a small change in particle size, there is no appreciable change in thermal boundary resistance in bulk/SiC composites.

For a bulk $SrTiO_3$, incorporated with 55 nm nanoparticles from the same material, thermal conductivity was reduced by 50% at 300K, and 24% at 1000 K compared to the bulk. The Kapitza interfacial thermal resistance was found to be 5.0×10^{-9} m^2KW^{-1}at 300K and 3.41×10^{-9} m^2KW^{-1} at 1000K.[130]

Listed in Tables 6.9 are the R_{Bd} and the Kapitza radius for a few well-known TE alloys at 300 K and R_{Bd} between artificial diamonds and metals (Table 6.10). Based on molecular dynamics with multi–scale modeling and finite element calculations, it has been observed that for <111> tilts in GB in cubic SiC/SiC (fiber) composites, the thermal conductivity is very sensitive to the tilt angle. For example, for 1^o tilt, thermal boundary resistance was 0.8×10^{-10} m^2KW^{-1}, and at 15^o the R_{Bd} was 7×10^{-10} m^2KW^{-1}. Thus the orientations of SiC nanoparticles and their aggregates change the nature of conductivity.[290, 291]

Table 6.8: Thermal boundary resistance and the Kapitza radius for present composites at 325 K.

Composite	Thermal boundary resistance, R_{Bd} (m^2KW^{-1})	Kapitza radius a_K (μm)	Interfacial thermal conductance ($m^{-2}K^{-1}W$)
$Ni_{0.05}Mo_3Sb_{5.4}Te_{1.6}$/SiC	3.75×10^{-5}	7.25	2.63×10^4
$Ni_{0.05}Mo_3Sb_{5.4}Te_{1.6}/Al_2O_3$	0.20×10^{-6}	0.96	5.00×10^6

Table 6.9: Thermal boundary resistance and Kapitza radius for few TE alloys at 300 K.[129]

Polycrystals	Thermal boundary resistance, R_{Bd} (m^2KW^{-1})	Kapitza radius a_K (μm)
p-Bi_2Te_3/Sb_2Te_3	1.4×10^{-5}	2.66
$Si_{0.3}Ge_{0.7}$	1.10×10^{-7}	0.86
n-$Si_{0.635}Ge_{0.365}$	1.15×10^{-9}	0.49
$Si_{0.7}Ge_{0.3}$	9.50×10^{-9}	0.62

Regarding to the sharp drop in the effective property for SiC nanoparticles embedded in bulk, the lower bounds are explicitly functions of interfacial surface area, interfacial barrier conductivity, constituent's thermal conductivities and their volume fraction. We speculate that this asymptotic behavior of lower bound is related to the increased interfacial surface area for a fixed volume fraction according to the L–V model.[292]

Table 6.10: R_{Bd} values between artificial diamond and some metals ($\times 10^{-5}$ m^2KW^{-1}) at 323 K.[43]

Composite	Pb	Au	Al	Ti
BaF_2	16.1	25	10	7.25
Sapphire	18.2	22.0	9.5	8.93
Diamond	32.3	25.0	21.7	10.0

Assuming SiC aggregates are flat-plates, we adopted Nan et al.'s flat plate model and obtained R_{Bd} of 3.8×10^{-5} $m^2K\ W^{-1}$ for bulk/SiC composite. However, we believe that particle size alone does not account for this thermal boundary resistance but rather that pore volume and

surface area are also a contributing factor leading to a sharp fall in effective thermal properties of SiC composites.

BET results show that SiC composites have considerable pore volume and surface area which contribute to a higher thermal boundary resistance. This fact is backed by studying the effect of porosity on thermal boundary resistance in alumina ceramics and refractories. Taking into consideration the influence of pore content using an effective media theory, a 70% jump in thermal boundary resistance (2.2×10^{-8} $m^2K\ W^{-1}$) was found for alumina with a 0.3 pore volume fraction compared to dense alumina (1.3×10^{-8} m^2KW^{-1}). We made a very crude approximation of interfacial surface area, S_i, contributions from 0.25 μm and 0.5 μm SiC particles. In the relation, $S_i = 3f/a$, [45] the embedded particles were assumed to be spherical with radius a. For volume fractions of SiC: $f = 0.034$, S_i values are found to be 4.0×10^5 m^{-1} and 1.9×10^5 m^{-1}, respectively. Thus, the asymptotic behavior in the L–V limits was s attributed to the enhanced interfacial surface area due to porosity. In a majority of EMA studies, the interfaces are treated as ideal. However, as our study shows, in heterogeneous materials, such as our composites consisting of domains of different materials, microstructures play a very important role in deciding the effective properties. Thus, for modeling the effective thermal properties, study of microstructures is very important.[49, 170]

Although many models to predict the effective thermal conductivities have many limitations of their own, these models are still useful in predicting effective properties for perfect and imperfect interfaces.[33, 34, 40, 41, 293, 294]

6.4.2 Mechanical Properties and their Relation to Thermal Properties

As we mentioned in the introduction, the poor mechanical bonding between the matrix and embedded nanoparticles along with the thermal expansion mismatch between the constituents will affect the thermal properties of the samples. To appraise this claim qualitatively, we measured Vickers hardness and elastic modulus of all composites, and the results are displayed in Figure 6.8. For SiC: $f = 0$ and Al_2O_3: $f = 0$, Vickers hardness was found

to be 4.66 GPa and 5.50 GPa respectively. For SiC samples, irrespective of SiC content, hardness and elastic modulus did not improve. For SiC: f = 0.01, hardness dropped sharply from 4.66 GPa to 1.11 GPa, a 320% drop. For SiC: f = 0.0216 and SiC: f = 0.0340, hardness values are 2.16 GPa and 0.68 GPa, respectively. Irrespective of SiC high elastic modulus (450 GPa) and hardness (2800 GPa) its presence in our composite did not improve the mechanical properties. One possible reason is the amount of macropore volume. In SiC: f = 0.0340 macropore volume is 80% higher than Al_2O_3: f = 0.0325. However, in Al_2O_3: f = 0.0216 and 0.0325 mesopore and micropore volume had increased.

On the other hand, for Al_2O_3: f = 0.01, hardness increased from 5.36 GPa to 6.55 GPa, a 22 % increase. For Al_2O_3: f = 0.0216 and Al_2O_3: f = 0.0325, ~ 4 GPa. As we see from the plots, the error margins for $Ni_{0.05}Mo_3Sb_{5.4}Te_{1.6}$/SiC are large compared to $Ni_{0.05}Mo_3Sb_{5.4}Te_{1.6}/Al_2O_3$, indicating that composites with SiC are not very homogeneous. Since we used small samples to measure the mechanical properties, a large error margin is expected; both composites are fabricated through manual routes, therefore, inhomogeneous distribution of nanoparticles may manifest in variation of hardness and elastic modulus. SiC and Al_2O_3, have a diamond and a corundum crystal structure, respectively; and as constituents of the composites, their effect on the consolidation process,especially on grain boundary alignment, and their role in grain growth are still not known. Compared to both composites, Al_2O_3 composites have higher mechanical strength (> 95% of theoretical density), and this is one of the reasons why these composites have lower R_{Bd} compared to SiC composites.

The porosity not only reduces the thermal conductivity, but also decreases the hardness and elastic modulus to a certain extent. Figure 6.8 shows there is a relation between the cumulative pore volume and the mechanical properties of the sample. As the cumulative pore volume increases, specifically the macropore volume, the hardness and elastic modulus decrease; this is the case in the samples with increasing SiC volume fractions, in which the macropore volume correlates well with the hardness and elastic modulus values obtained. The exception to these results is the Bulk/Al_2O_3 sample with f = 0.0325, which has a pore volume that is much

larger than other lower volume fractions of Al_2O_3, but the hardness does not decrease and the elastic modulus increases substantially. This exception due to the increased micropore and mesopore volume concentration and wider distribution. The pore distribution and the shape of the pores can affect the mechanical properties as well. The adsorption isotherms (Figures 6.4 and 6.5) of bulk/SiC and bulk/Al_2O_3 are of Type H3 (IUPAC) that have slit-like pores or plate-like particles as seen in the SEM images. Slit-like or ellipsoidal pores tend to have a weaker structure compared to spherical pores because of the combination of a less connected solid phase network and greater stresses and deformations near the high-curvature regions of the pore.[289] From this study, we can conclude that the poor mechanical properties of bulk/SiC result in higher thermal boundary resistance and larger Kapitza radius of 7.25 μm. We also think that SiC nanocomposites' mechanical properties can be improved with a good consolidation technique, and implementing such a technique is one of our future research plans.

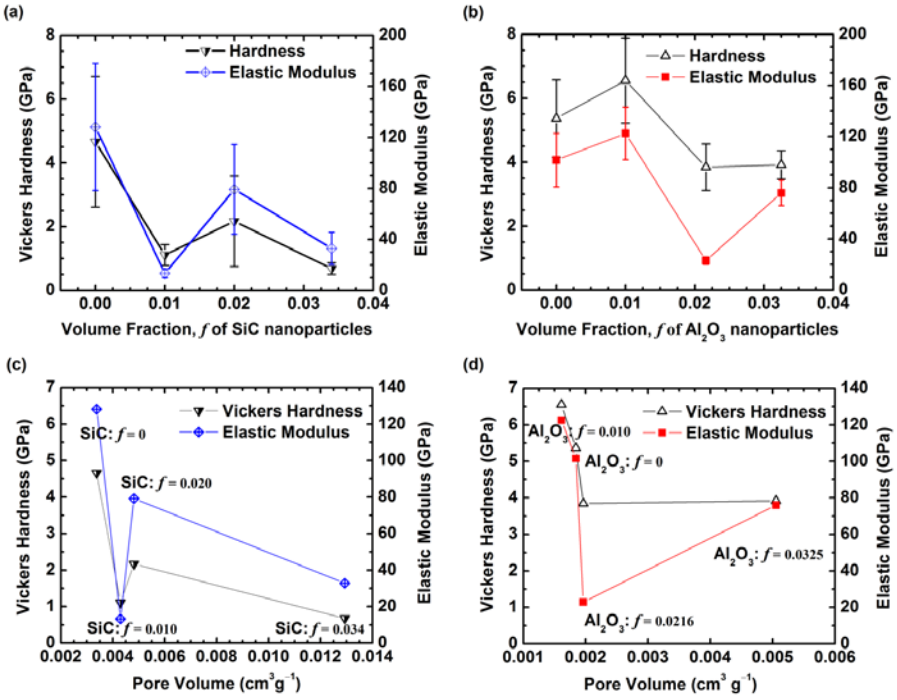

Figure 6.8: Vickers hardness and elastic modulus of (a) $Ni_{0.05}Mo_3Sb_{5.4}Te_{1.6}$/SiC and (b) $Ni_{0.05}Mo_3Sb_{5.4}Te_{1.6}/Al_2O_3$ composites as a function of volume fraction. Vickers hardness and elastic modulus as a function of pore volume of (c) $Ni_{0.05}Mo_3Sb_{5.4}Te_{1.6}$/SiC and (d)

Although we executed our effective property calculations based on the particle size estimated from SEM and TEM, variations in the distribution of particle size and their spatial distribution can cause uncertainties about the effective properties. Taking into consideration, it is very illuminating to analyze the approach taken by Dunn and Taya [295], where the embedded particles were modeled as confocal spheroids, that allowed them to modulate particles from thin flakes to continuous fiber and then different density distribution were functions facilitated to simulate completely random, in-plane or aligned distribution to predict the effective properties. Close agreement was obtained for ZnS/diamond composite. A similar study was done by Davis and Artz using Finite Element Analysis (FEA).[41] Interested readers can also refer to an article by Hatta and Taya.[296] These kinds of studies will facilitate tuning the effective properties.

6.5 Conclusions

We successfully synthesized and studied the effective thermal properties of bulk/SiC and bulk/Al_2O_3 nanocomposites at 325 K.

We performed simple MG–EM approximations to study the Kapitza thermal boundary resistance. The model used by Nan et al. MG-EMA for flat-plate composites predicts a Kapitza radius of: 7.25 μm and 0.96 μm respectively for SiC and Al_2O_3 , and the corresponding R_{Bd} values were found to be: 3.8×10^{-5} m^2KW^{-1} and 0.2×10^{-6} m^2KW^{-1}. The L–V upper bound for both operates close to $\alpha = 1$; the lower bound for SiC predicts a huge drop and asymptotic pattern in effective property for $Ni_{0.05}Mo_3Sb_{5.4}Te_{1.6}$/SiC. We made attempts to explain this drop taking into consideration interfacial surface area. For bulk/Al_2O_3 L–V, the lower bound fits well with the experimental data. The L–V bounds for interfacial thermal conductance and its relation to composite thermal conductivity were studies and explained taking into consideration of experimental data. The parameters we obtained were approximate.

Apart from the shape, size, and spatial distribution of the embedded particles, as well as their thermal and chemical properties of their constituents, we argue that microstructures play a very role in determining the effective properties of our composites. Also the 200% difference in

thermal boundary resistance of SiC and Al_2O_3, is not only due to the difference in particle size and respective thermal properties of the constituents, but also to the microstructural variations between them.

As many articles have pointed out the bonding between the constituents at the interface determines the effective property. In our case, we found SiC composites have poor mechanical properties, and this is one of the reasons for its high thermal boundary resistance. An enhanced surface area due to the presence of SiC nanoparticles and porosity are also contributing factors in yielding Kapitza radius of 7.25 μm compared to 0.96 μm for Al_2O_3 composites. Since the effective properties are coupled strongly to microstructures, a detailed understanding of these structures is important to predict these properties. Techniques such as x-ray micro-tomography, which provides high-resolution 3-dimensional phase information of a composite in a nondestructive manner, is very important.[152]

Finally, we need to consider on EMA theories, which can help us in predicting and estimating thermal boundary resistance. These can also aid in achieving finite κ_{comp}, and simultaneously, help us in enhancing the charge carrier flow across the same boundaries, a process which is very important in enhancing the TE transport properties.

6.6 Supplementary Information

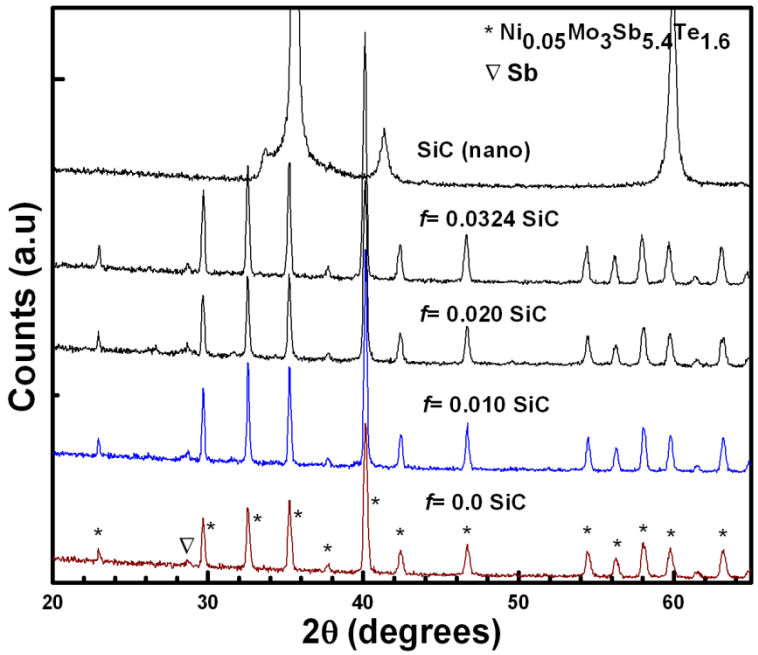

Figure 6.9: XRD patterns of pristine SiC, composites and bulk (from top to bottom).

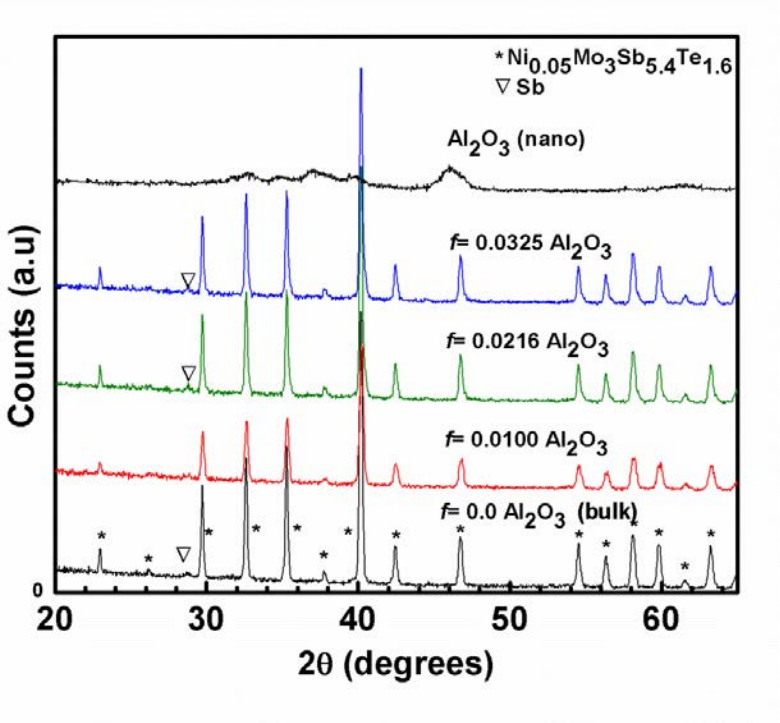

Figure 6.10: XRD patterns of pristine Al_2O_3, composites and bulk (from top to bottom).

Chapter 7

Improved Power Factor by Coating NiSb Nanoparticles on Bulk $Ni_{0.05}Mo_3Sb_{5.4}Te_{1.6}$ Particles[13]

These results are yet to be published in a relevant journal.

7.1 Experimental Section

7.1.1 Synthesis

The process of synthesizing bulk $Ni_{0.05}Mo_3Sb_{5.4}Te_{1.6}$ through solid-state reaction can be found in our previously reported article on $Ni_{0.05}Mo_3Sb_{5.4}Te_{1.6}$/MWCNT.[107] The process of coating NiSb nanoparticles on bulk particles through solvothermal process is discussed in Section 2.1.3. We ran three such reactions for 0.034, 0.074, and 0.16 by volume fraction of NiSb.

The sample with zero volume fraction (f = 0) was retained as a reference sample. The rule of mixture was used to calculate the theoretical densities and specific heats of composites (Section 2.8). The end product was subjected to powder XRD for phase analysis and SEM analysis for NiSb nanoparticle distribution on bulk particles.

Consolidation of these samples was carried out under uniaxial pressure of 56 MPa of pressure at 925 K for two hours. Throughout the consolidation, samples were kept under ar atmosphere. So obtained disks of ~2 mm thickness and 1.26 mm in diameter were subjected to density measurement and the densities are listed in Table 7.1.

[13] Nagaraj Nandihalli, Robert Liang, Norman Zhou, Holger Kleinke

Table 7.1: Experimental densities of bulk and various $Ni_{0.05}Mo_3Sb_{5.4}Te_{1.6}$/NiSb composites at 295 K.

f	Density of pellet ρ/(g cm^{-3})	Relative Density (%)
0 (bulk)	8.0	91.7
0.034	7.8	89.6
0.074	8.3	95.7
0.160	8.2	94.9

7.1.2 Phase Analysis

The XRD patterns of bulk particles coated with 0.074 and 0.16 NiSb volume fraction, before hot- pressing is exhibited in Figure 7.1. As the Figure shows, noticeable pattern of NiSb exists for both composites. As the content was increased the intensity of NiSb pattern increased. We did not see any NiSb peak in 0.034 NiSb due to the small amount of NiSb and therefore have not shown in the Figure. No other peaks were seen, indicating that the process of nanocoating did not affect the bulk material.

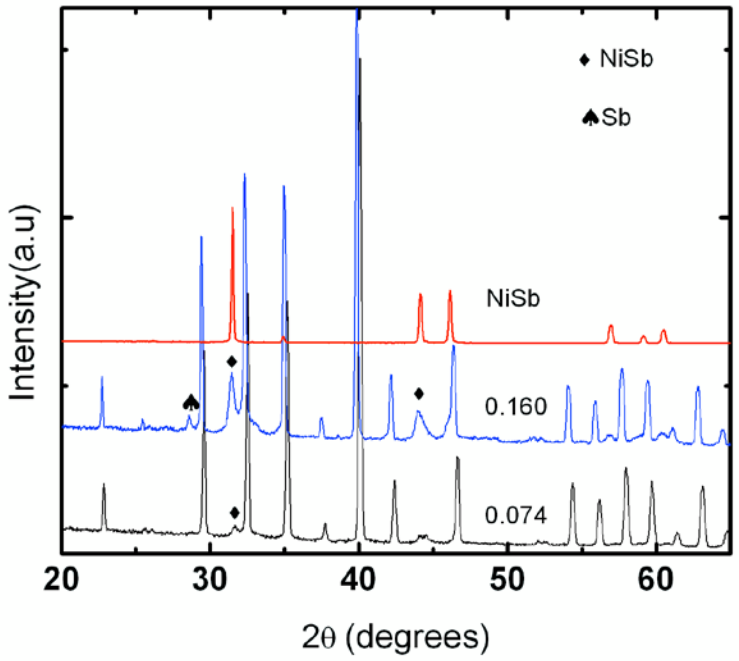

Figure 7.1: X-ray patterns of NiSb, composites and bulk before hot-press (from top to bottom).

Bulk powder coated with NiSb nanoparticles of different volume fractions were subjected to SEM analysis to investigate microstructures and exhibited in Figure 7.2. The images in Figure 7.2 clearly show nanoparticles of NiSb are coated on larger bulk particles.

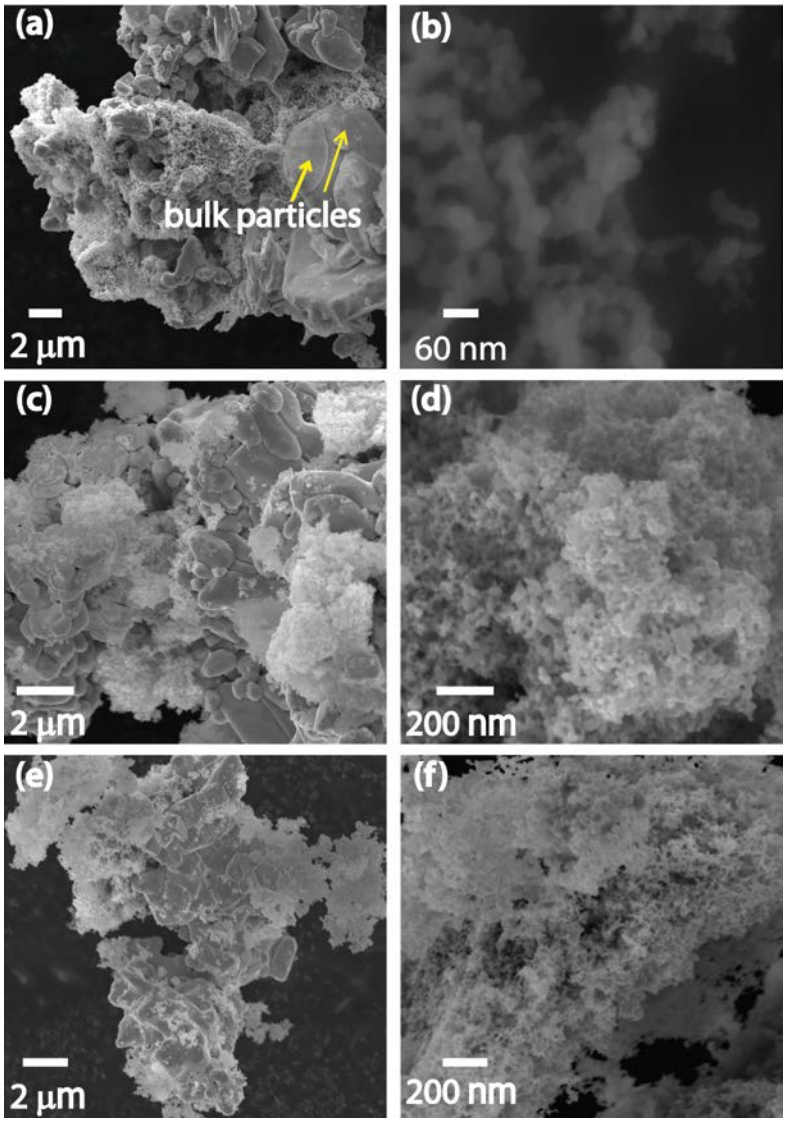

Figure 7.2: SEM images of pre hot-pressed $Ni_{0.05}Mo_3Sb_{5.4}Te_{1.6}$/NiSb powders. (a) 0.034 NiSb nanoparticles on bulk particles; (b) NiSb nanoparticles synthesized separately; (c), (d) 0.074 sample; (e) and (f) 0.16 NiSb sample.

The thickness of the coating is difficult to measure accurately. However, 100 nm – 300 nm is a good and reasonable estimate. NiSb nanoparticles, which were synthesized separately, are shown in Figure 7.2(b). The approximate size of NiSb is estimated to be 60 nm – 80 nm.

After transport property characterization, portion of the hot-pressed samples were ground into powder and subjected to powder XRD (Figure 7.3). As it is very evident, $NiSb_2$ peaks are visible and their intensities are increasing with respect to the amount of NiSb nanoparticles. Since these peaks appeared after the hot-pressing, NiSb must have scavenged some Sb from the bulk material during the hot-pressing to form $NiSb_2$.

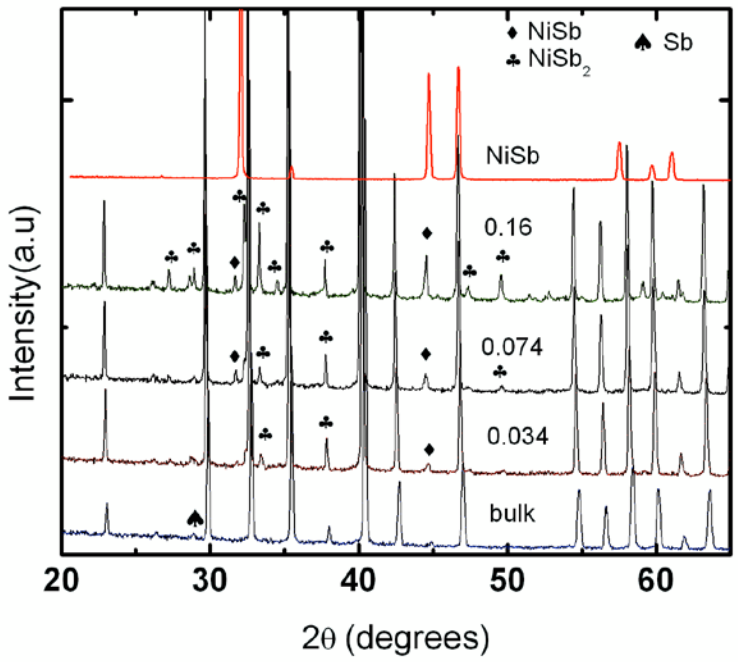

Figure 7.3: X-ray patterns of NiSb, composites and bulk after hot-press (from top to bottom).

7.2 Physical Property Measurements

The instruments and the procedures to characterized both the electrical and thermal properties can be found in Section 2.9 and 2.10.1.

7.3 Results and Discussion

7.3.1 Transport Properties

The temperature dependence of the electrical conductivity is exhibited in Figure 7.4.

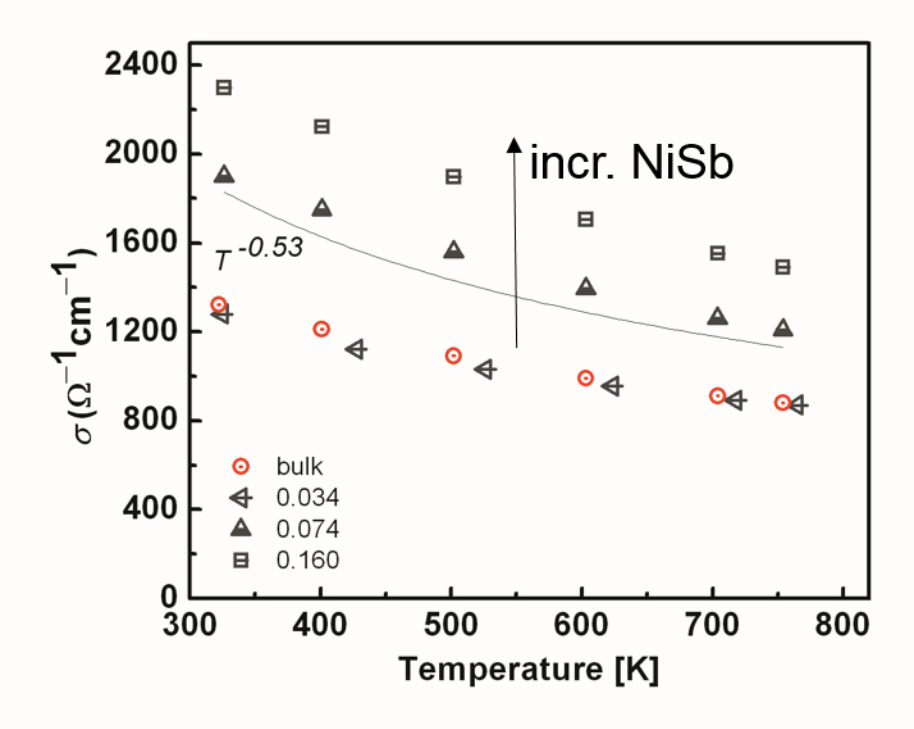

Figure 7.4: Temperature dependence of electrical conductivity of bulk and NiSb composites.

Drop in the electrical conductivity with respect to temperature indicates highly degenerate semiconductor, similar to the family of $Mo_3(Sb,Te)_7$ compounds.[113] For bulk and NiSb: f = 0.034 samples, the electrical conductivity starts in the neighborhood of 1322 $\Omega^{-1}cm^{-1}$; there is no noticeable difference between these samples throughout the temperature from 322 K to 750 K. The volume fraction 0.034 NiSb is not enough to enhance the electrical properties even though it is highly conductive (0.7×10^4 $\Omega^{-1}cm^{-1}$, Figure 7.8 in Supplementary Information). At 322 K, for 0.075 NiSb sample, the electrical conductivity jumps to 1901 $\Omega^{-1}cm^{-1}$. This jump in σ can be explained by taking into consideration of NiSb cluster formation that provides least resistive path to charge carriers. In 0.034 NiSb sample, we presume NiSb nanoparticles are

randomly coated on the bulk particles; they are not connected to each other and therefore there is no change in electrical conductivity. However, as the volumetric content of NiSb is increased, NiSb coated bulk particles make good contact with each other providing least resistant path to charge carriers from one end to the other end. Similarly, for 0.16 NiSb sample, the electrical conductivity jumps to 2300 $\Omega^{-1}cm^{-1}$. Samples 0.074 and 0.16 tend to follow $T^{-0.53}$. On the other hand for bulk and 0.034 NiSb samples, slope is less compared to 0.074 and 0.16 sample.

Plotted in Figure 7.5(a) and (b) are the temperature dependence of total and lattice contribution from 325 k to 740 K.

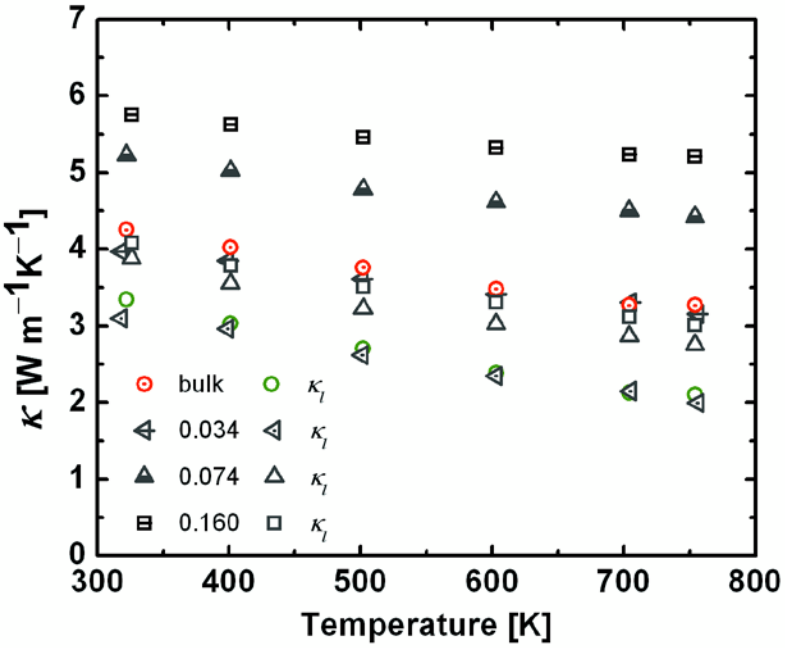

Figure 7.5: Temperature dependence of total and lattice thermal conductivity of bulk and NiSb composites.

The thermal conductivity was obtained similar to our previous composite, $Ni_{0.05}Mo_3Sb_{5.4}Te_{1.6}$/MWCNT.[107] NiSb nanoparticles have increased thermal conductivity in 0.074 and 0.16 NiSb samples; at 325 K, 0.074 and 0.16 NiSb sample have 5. 23 W $m^{-1}K^{-1}$ and 5.7 W $m^{-1}K^{-1}$ respectively, compared to 4.2 W $m^{-1}K^{-1}$ and 3.9 W $m^{-1}K^{-1}$ for bulk and 0.034

samples. One possible reason for unchanged thermal conductivity in 0.034 sample is the role of interfaces in scattering phonons, while the randomly formed NiSb layers did not contribute in enhancing thermal conductivity. When the size of the embedded particle (such as NiSb in our case) is greater than the phonon wavelength of bulk material ($Ni_{0.05}Mo_3Sb_{5.4}Te_{1.6}$ in our case), the effective thermal conductivity of the composites increases monotonically with respect to the volumetric concentration of highly conducting particles.[51] However, for smaller volume fractions, the increase in thermal conductivity is less gradual as the network of highly conducting particles is not formed yet. As the content is increased, they form a continuous path between two ends of the material and these paths are less treacherous for phonons and thermal conductivity increases more rapidly.[50] In 0.074 and 0.16 NiSb samples, well connected network of highly conductive NiSb particles (70 W $m^{-1}K^{-1}$ measured in our lab, please see Figure 7.9 in Supplementary Information) are responsible for increased thermal conductivity. Among all the samples, 0.074 and 0.16 are showing less temperature dependence, which is indicative of less inter phonon scattering and interface scattering. In ZnS/diamond composites, opposite effect was seen. While the 0.4 μm – 4 μm size embedded diamond particles increased the composite thermal conductivity, 0.1 μm – 0.5 μm diamond particles have reduced thermal conductivity of the composites monotonically. Thus, the nature of the interface between the bulk and embedded particle, their thermal conductivity, their acoustic match, physical bonding between them, size of the embedded particles (surface to volume ratio), chemical adherence, and the amount of porosity at the interface play a very important role in deciding the effective thermal conductivity of the composites.[38, 39, 46] [36, 44, 292, 297]

To comprehend the effect of NiSb nanoparticle on bulk to the lattice thermal conductivity, we calculated κ_l for all samples by subtracting κ_e from the total thermal conductivity as discussed in Section 1.4.1.2 (Estimation of Lattice Thermal Conductivity Contribution to total thermal Conductivity). Temperature dependence of Lorenz numbers of bulk and NiSb composites are displayed in Supplementary Information (Figure 7.10).

Lattice thermal conductivity, κ_l, was obtained by subtracting κ_e from the total thermal conductivity. κ_e was obtained using Wiedemann-Franz law: $\kappa_e = L_0 \sigma T$, L_0 is the Lorenz number,

which was obtained using the Seebeck coefficient data assuming our bulk and composites follow single-parabolic model and multiple scattering mechanisms.[29, 30]

At 325 K, bulk and 0.034 have κ_l of 3.3 W $m^{-1}K^{-1}$ and 3.0 W $m^{-1}K^{-1}$ respectively, indicating that NiSb nanoparticles are less effective in preventing phonon contribution to total thermal conductivity. Contrary to this, 0.074 and 0.16 samples have κ_l of 3.8 W $m^{-1}K^{-1}$ and 4 W $m^{-1}K^{-1}$ respectively. Since NiSb is metallic in conductivity, κ_l contribution to total thermal conductivity is less than the electronic contribution, κ_e (Figure 7.8 in Supplementary Information). Thus, we expect to see lower κ_l compared to bulk, which is not the case here. One possible reason is the higher relative densities of both of these composites, i.e. 95.7% and 94.9%. Pores are less effective in preventing phonon contribution to the thermal conductivity. Another plausible reason is the less acoustic mismatch between bulk and NiSb particles. Similar to our results, Bi particles incorporated into nanostructured PbTe have increased lattice thermal conductivity due to small acoustic mismatch between Pb and Bi.[77]

Figure 7.6 shows the variations of Seebeck coefficient with respect to temperature for bulk and various bulk/NiSb composites.

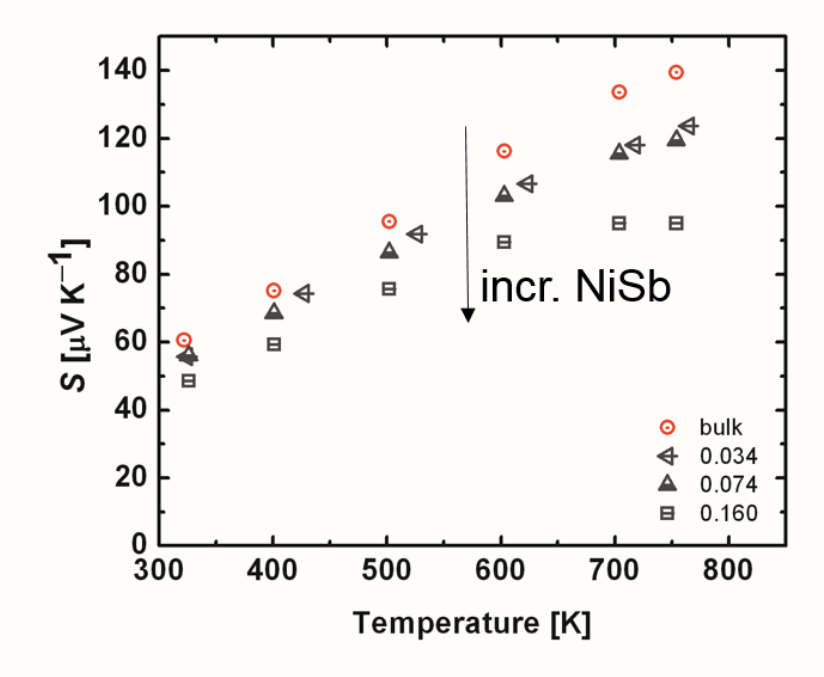

Figure 7.6: Temperature dependence of Seebeck coefficient of bulk and NiSb composites.

The bulk sample has relatively higher slope than the rest of the sample. This behavior is typical for $Mo_3(Sb,Te)_7$ family of compounds. At 322 K, bulk, 0.034, 0.074, and 0.16 samples have Seebeck coefficient of 60 μV K^{-1}, 55 μV K^{-1}, 56 μV K^{-1}, and 48 μV K^{-1}. Sample 0.034 and 0.074 have the same variation in all the temperature segments. Comparing the electrical conductivity of 0.074 (1901 Ω^{-1} cm^{-1} at 322 K) to 0.034 (1280 Ω^{-1} cm^{-1} at 322 K), and respective Seebeck coefficient at the same temperature viz. 55 μV K^{-1}, 56 μV K^{-1}, clearly indicates that, for sample 0.074 reciprocal relationship between the electrical conductivity and Seebeck coefficient is decoupled. This kind of decoupled pattern has been observed in the TE properties of $Ni_{0.05}Mo_3Sb_{5.4}Te_{1.6}$/MWCNT and n-type Skutterudite compound with fullerene as nanoinclusions.[200] Sample 0.16 has linier variation of Seebeck coefficient between 322 K to 600 K. Beyond 600 K, Seebeck coefficient starts to saturate.

The variation of *P.F.* with respect to temperature is similar to the Seebeck coefficient. At 325 K, *P.F.* lies between 4 to 6 μW$cm^{-1}K^{-2}$ (Figure 7.7). However, sample 0.074 NiSb maintained dominance among all samples from 322 K to 700 K and the main contributing factor

in enhanced *P.F.* is the elevated electrical conductivity. Competing with this sample is sample 0.16, but due to the drop in Seebeck coefficient of this sample, *P.F.* starts to saturate at 700 K. At 400 K, 500 K, and 600 K, sample 0.074 has 22%, 16%, and 11.3% increase in *P.F.* compared to bulk.

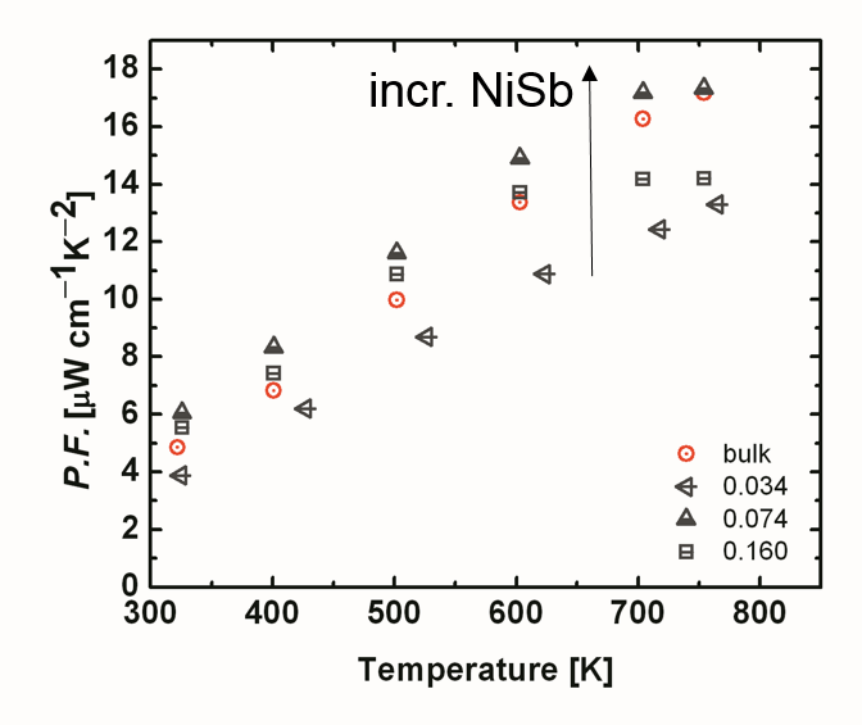

Figure 7.7: Temperature dependence of *P.F.* of bulk and NiSb composites.

The effect of $NiSb_2$ on bulk transport properties needs investigation. However, looking at the Seebeck coefficient and the electrical conductivity, we need to explore how it is possible to suppress the growth of $NiSb_2$ during hot-pressing by using some additives.

7.4 Conclusion

For the first time we have shown that $Ni_{0.05}Mo_3Sb_{5.4}Te_{1.6}$ can be coated with NiSb nanoparticles of size 60 nm – 80 nm through the solvothermal nanoplating technique. The process of nanoplating did not affect the bulk material. For samples with 0.074 and 0.16 NiSb particles, there was an enhancement in the electrical conductivity, and this is the main

contributing factor in elevating *P.F.* for 0.074 by 16%. Between 400 K and 600 K, this sample has the highest power factor of all. There was no improvement in *P.F.* for sample 0.16. For samples 0.074 and 0.16, thermal conductivity was increased, whereas for 0.034 NiSb sample, thermal conductivity stayed the same. For 0.16 NiSb sample, hot-pressing is responsible for the formation of $NiSb_2$. We are of the opinion that if we are able to prevent $NiSb_2$, we can improve TE properties even further. In the near future more investigation will be carried out to coat bulk material with other nanoparticles such as $CoSb_3$ or ZnO.

7.5 Supplementary Information

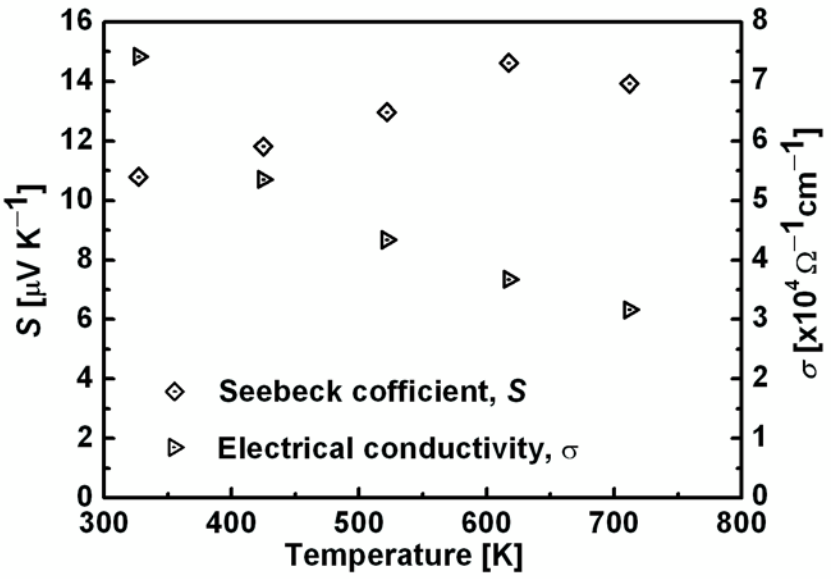

Figure 7.8: Electrical conductivity and Seebeck coefficient of bulk NiSb particles (100 nm – 10000 nm) synthesized through solid-state reaction.

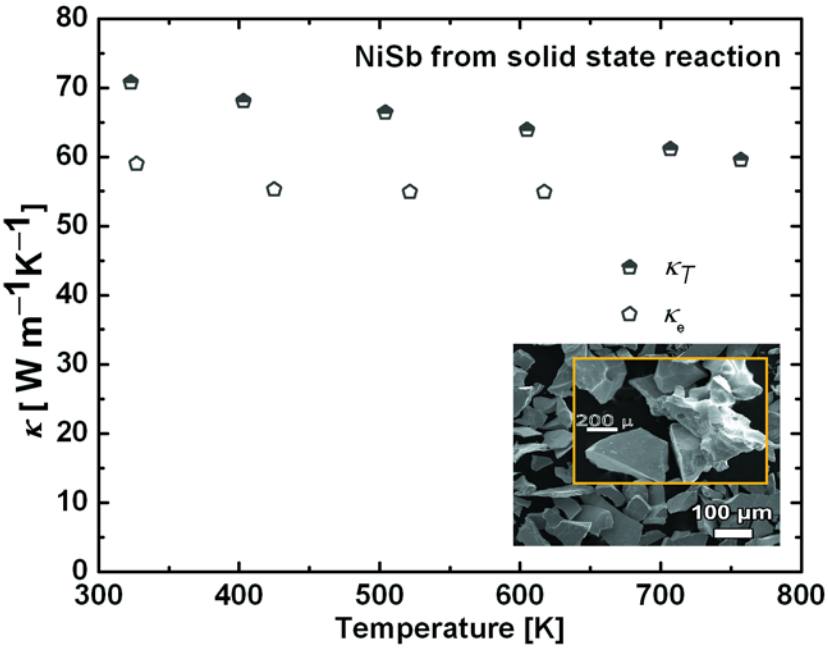

Figure 7.9: Temperature dependence of total thermal conductivity of large NiSb particles (100 nm – 1000 nm) synthesized through solid-state reaction.

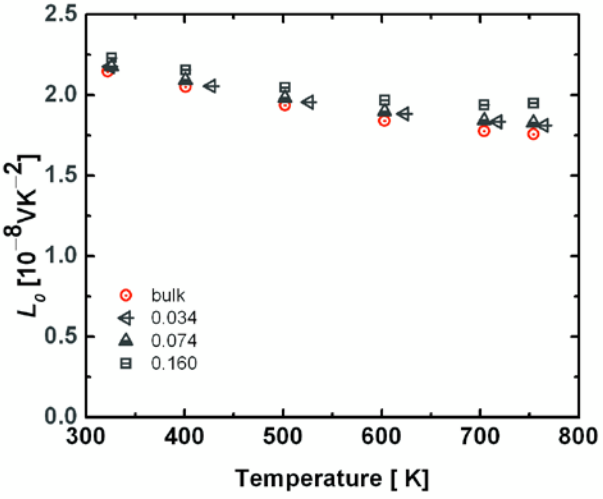

Figure 7.10: Temperature dependence of Lorenz numbers of bulk/NiSb composites.

Chapter 8

Thermoelectric Properties of Composites Made of $Ni_{0.05}Mo_3Sb_{5.4}Te_{1.6}$ and Fullerene[14]

Background: Readers are advised to read Abstract for Chapter 8 on page vi, and Material Choice for Our Composites (Section 1.9).

8.1 Experimental Section

8.1.1 Syntheses and Analyses

We conducted four solid-state reactions, with 4.6 g of starting materials each, to obtain enough pure phase of $Ni_{0.05}Mo_3Sb_{5.4}Te_{1.6}$ (Section 2.1.1). This big sample was then divided into four equal parts, three thereof getting mixed thereafter with 1, 2, and, 3 mass% C_{60} (obtained from Alfa Aesar, 98% C_{60}, 2% C_{70}), respectively. 1 mass% C_{60} correspond to 0.96 mol C per mol $Ni_{0.05}Mo_3Sb_{5.4}Te_{1.6}$; thusly the 3% sample contains almost as many carbon as molybdenum atoms. To form the composites, the bulk material was added to an agate mortar containing 10 ml acetone. Likewise, C_{60} was added to a vial containing acetone in the desired amount. Next, the C_{60}/acetone suspension was stepwise introduced to the mortar, with pure acetone added at the end to ensure that no C_{60} remained in the vial. The mixture was continuously stirred with a pestle until acetone completely dried. The whole process took approximately 45 min.

Hot-pressing was performed at the Clemson University under argon, applying a pressure of 150 MPa at 923 K for 1 h in each case. The so-obtained pellets were polished first and then

---

[14] Reprinted J. Solid State Chem., vol. 203, Nagaraj Nandihalli, Ali Lahwal, Daniel Thompson, Tim C. Holgate, Terry M. Tritt, Véronique Dassylva-Raymond, László I. Kiss, Elisabeth Sellier, Stéphane Gorsse, Holger Kleinke, "Thermoelectric properties of composites made of $Ni_{0.05}Mo_3Sb_{5.4}Te_{1.6}$ and fullerene" Pages 25–30., Copyright (2013), with permission from Elsevier.

cut into proper pieces for the various physical property measurements using a low-speed diamond saw.

The properties of the pellets with nominal 2% and 3% C_{60} were measured at Clemson, while the thermal properties of the other two samples were determined at the Université du Québec à Chicoutimi and their electrical properties at the University of Waterloo.

8.1.2 Physical Property Measurements

Seebeck coefficient, S, and electrical conductivity, σ, were simultaneously determined in a helium atmosphere using an ULVAC ZEM system, a ZEM-2 in Clemson and a ZEM-3 in Waterloo. Thermal conductivity, κ, was calculated from $\kappa = \rho C_P \alpha$, the product of the experimentally determined material's density, ρ, the specific heat, C_P, via the Dulong–Petit approximation, and the thermal diffusivity, α was measured utilizing a laser flash system (NETZSCH LFA 457 in Clemson, Anter FlashLine^{TM} 3000 in Chicoutimi). To verify the Dulong–Petit approximation, the specific heat of the 0% C_{60} and the 1% C_{60} samples were also determined in Chicoutimi via differential scanning calorimetry using a DSC 8000 from PerkinElmer. The samples exhibited no sign of decay after either process.
Minor differences were found between the experimentally determined specific heat and the Dulong–Petit values, as shown in the supplementary information. For example, using the measured C_P values instead of Dulong–Petit's C_P, the largest ZT value was 0.27 instead of 0.25 for the 1% C_{60} sample, compared to 0.24 instead of 0.23 for the sample without C_{60}. For consistency however, we used Dulong–Petit in all calculations presented as results in this work, noting that the improvement in ZT would be larger when using the experimentally determined C_P values (0.269/0.235 = 14% vs. 10%).

8.1.3 Structural Analysis

After measuring the physical properties, a pellet of the sample with 1% C_{60} was crushed and ground into fine powder. Its X-ray powder diffractogram was obtained after irradiating the powder over a period of 15 h on a Bruker D8 diffractometer, equipped with a Våntec-1 detector,

using Cu*K*α radiation in the range from 15° to 100° in 2θ at a step size of 0.025° in Bragg–Brentano geometry. A Rietveld refinement [298] was performed to verify purity/stability after the measurement using the GSAS program [299] and [300] via the graphical interface EXPGUI.[301]

8.1.4 Scanning Electron Microscopy (SEM)

Parts of the hot-pressed sample with 1% C_{60} were ground into fine powder, and then analyzed by means of standardless energy dispersive spectroscopy (EDXS, LEO 1530, with integrated EDAX Pegasus 1200 detector) using an acceleration voltage of 25 kV at WATLABS at the University of Waterloo. No evidence for the formation of any carbides were found, all selected grains appeared to be based on Ni-containing Mo antimonide-telluride. Not considering carbon in the elemental analysis, the atomic percents as determined on six different crystals averaged to 0.9: 29.4: 51.9: 16.3, which compares well to the nominal Ni: Mo: Sb: Te ratio of 0.5: 29.9: 53.7: 15.9. Because the Ni–K peaks were relatively small compared to the background, the Ni concentration could not be determined reliably. Consequently, the calculated Ni content seemed to vary a lot between the selected grains, ranging from 0.7 at% to 1.4 at%, but those variations are not significant.

8.1.5 Transmission Electron Microscopy (TEM)

Ion-etched specimens of the hot-pressed sample with 1% C_{60} were analyzed with a JEOL 2200 FS at the Université de Bordeaux. Compositional maps of the composite material were determined by energy dispersive X-ray spectroscopy (EDX) (Section 2.6).

8.1.6 Results and Discussion

As mentioned above, a large sample of nominal composition $Ni_{0.05}Mo_3Sb_{5.4}Te_{1.6}$ was synthesized first and then divided into four parts, and three parts thereof were then mixed with different amounts of C_{60}. The Rietveld refinement of the sample with nominal 1 mass% C_{60}, obtained after the physical property measurements, is depicted in Figure 8.1. Final residual values were R_P = 0.034, R_{wP} = 0.052, and R_F^2 = 0.051. Traces of MoO_2(refined to amount to

4(4) mass%) and Sb_2Te (0.8(9) mass%) seem to be present in all samples, with their strongest peaks occurring at 26.0° and 28.4°, respectively. The occurrence of MoO_2 most likely originated from oxygen present in the unpurified tellurium, and then traces of Sb_2Te formed because of the Mo-deficiency caused by the formation of MoO_2.

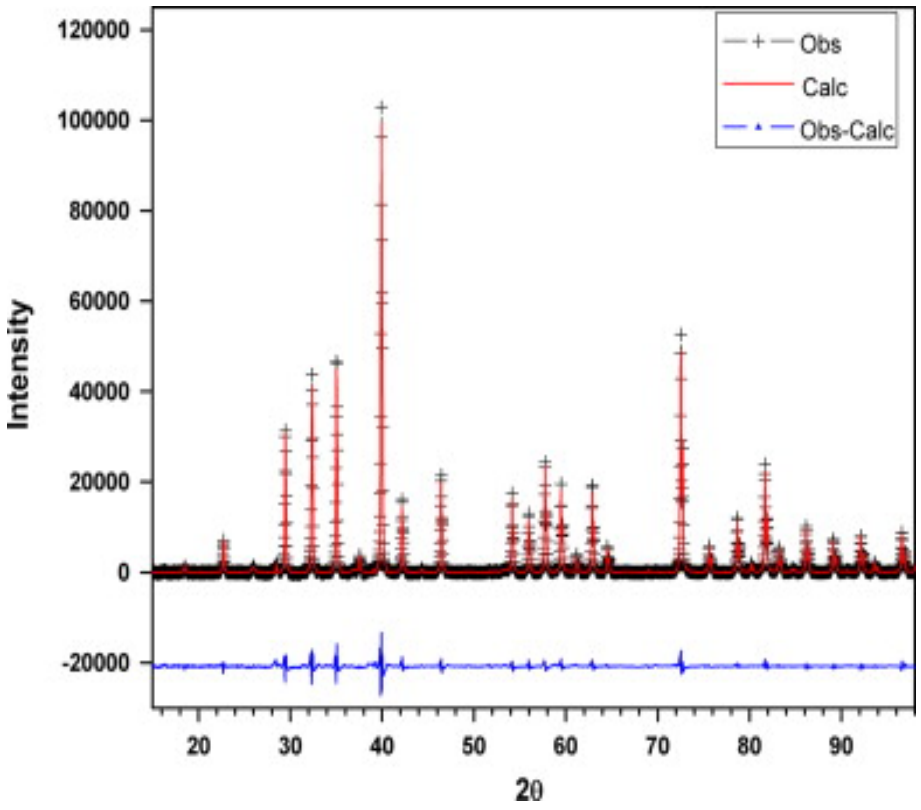

Figure 8.1: Rietveld refinement of $Ni_{0.05}Mo_3Sb_{5.4}Te_{1.6}$ with 1 mass% C_{60}, obtained after the physical property measurements.

No peaks could be assigned to any crystalline C-containing phase, which indicates that no significant amount of (crystalline) carbide or graphite was formed, in agreement with the TEM images. The refined lattice parameter and atomic positions are compared to earlier investigations in Table 8.1, demonstrating that the bulk materials are isostructural.

Table 8.1: Crystallographic data of various samples.[15]

Rietveld Analysis				
Formula	a (Å)	X (Mo)	X (Sb2)	Method
Mo_3Sb_7	9.559(3)	0.3432(2)	0.16220(8)	CCD
Mo_3Sb_7	9.561(1)	0.3451(8)	0.1633(3)	Rietveld
$Mo_3Sb_5Te_2$	9.563(1)	0.3407(5)	0.1634(2)	Rietveld
$Ni_{0.04}Mo_3Sb_7$	9.5734(6)	0.3432(2)	0.16235(9)	CCD
$Ni_{0.05}Mo_3Sb_{5.4}Te_{1.6}$	9.56628(3)	0.3436(3)	0.16270(9)	Rietveld

This structure comprises face-condensed pairs of $Mo(Sb,Te)_8$ square antiprisms, which are interconnected to infinite linear chains by nonclassical Sb–Sb bonds between the pairs. These bonds result in Sb_8 cubes Figure 8.2, with all faces being capped by Mo atoms. Thus, the chains interpenetrate each other at these cubes to form a three-dimensional structure. The Ni position in the Sb_8 cube is nominally filled to only 10%, corresponding to $0.10 \times 28 = 2.8$ electrons, while surrounded by 8 Sb atoms with 51 electrons each. With the scattering power being proportional to the square of the absolute electron numbers, the Ni occupancy cannot be refined reliably. Likewise, we did not refine the mixed occupancies of Sb and Te, for these elements are neighbors in the periodic table and have thus almost equivalent scattering power. Therefore, the occupancy of the *Q*1 site (*Q* = Sb, Te) was fixed according to the nominal Sb/Te ratio, again assuming that the more electronegative Te atom prefers the site with weaker *Q*–*Q* interactions [87] and [302]: Numerous such *Q*–*Q* interactions are present in this compound, with lengths of 2.89 Å between the Sb_8 cubes, 3.11 Å along the cube edges, and 3.38 Å within the *Q*1 squares between the Mo atoms.

[15] Space group *Im* $\bar{3}$*m*, Ni on (0, 0, 0); Mo on (*x*, 0, 0); *Q*1 = Sb1/Te1 on (¼, 0, ½); Sb2 on (*x*, *x*, *x*). CCD stands for Charge Coupled Device, in X-ray crystallography

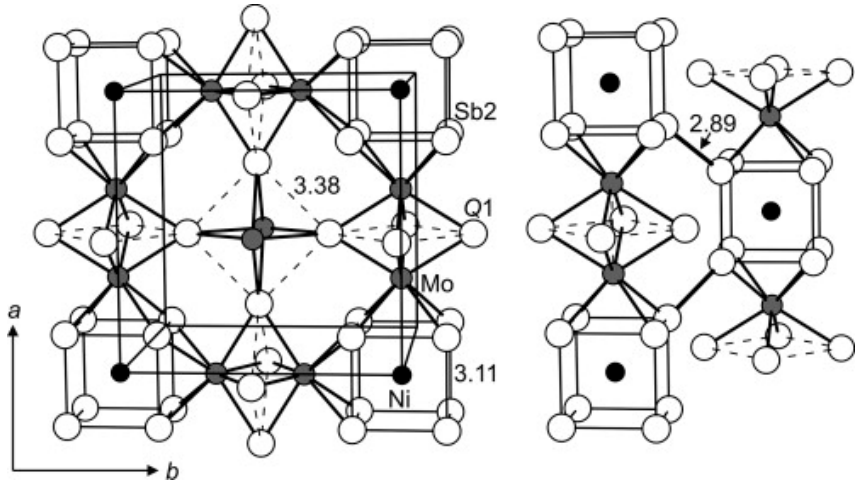

Figure 8.2: Crystal structure (left) and two interconnected chains (right) of $Ni_{0.05}Mo_3Sb_{5.4}Te_{1.6}$. Distances between the Sb and Te atoms are given in Å.

Figure 8.3(a) shows a representative bright field image at low magnification of the composite nanostructure. The dark areas stem from the bulk $Ni_{0.05}Mo_3Sb_{5.4}Te_{1.6}$ samples, and the crystallite sizes range from a few tenth of a micrometer to a few micrometers. The brighter areas between these dark crystallites represent the carbon additions, with particle sizes typically around 50 nm. The C_{60} particles have polymerized during hot-pressing, resulting in amorphous nanoparticles of carbon. A detail of the nanostructure is shown in Figure 8.3(b) along with the corresponding C Figure 8.3(c) and Sb Figure 8.3(d) compositional maps, which confirms the character postulated above for both the thermoelectric bulk and the carbon particles. No reaction between carbon and the bulk material and neither the formation of metallic carbides were detected.

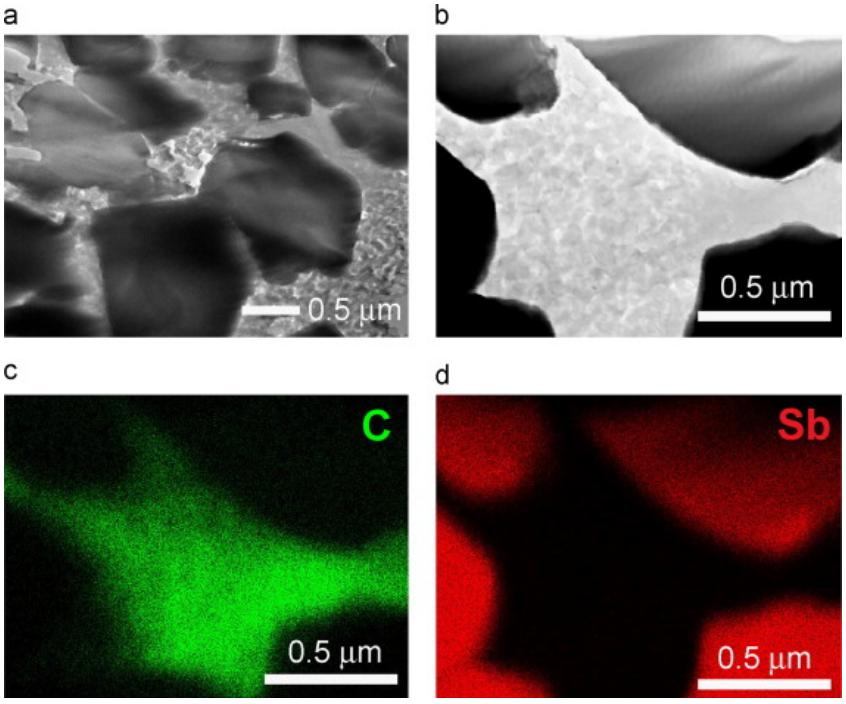

Figure 8.3: TEM images of $Ni_{0.05}Mo_3Sb_{5.4}Te_{1.6}$ with 1 mass% C_{60}.

As shown before, the samples with an Sb/Te ratio larger than 5:2 are p-type semiconductors with a rather high carrier concentration. For example, we measured p-type carrier concentrations of the order of 10^{21} cm^{-3} on $Mo_3Sb_{5.4}Te_{1.6}$ and $Ni_{0.06}Mo_3Sb_{5.4}Te_{1.6}$ [184]. All electrical conductivity values measured thus far on hot-pressed pellets of similar stoichiometry were in excess of 10^3 Ω^{-1} cm^{-1} at room temperature, and decrease with increasing temperature, while the Seebeck coefficient was 50 µV K^{-1} −60 µV K^{-1} around 300 K, increasing linearly with increasing temperature. These temperature dependences were to be expected for materials with high charge carrier concentration [225], [303] and [304].

The here-investigated hot-pressed bulk material, $Ni_{0.05}Mo_3Sb_{5.4}Te_{1.6}$, is no exception. Its (positive) Seebeck coefficient values increase linearly from S = 57 µV K^{-1} at 300 K to 110 µV K^{-1} at 665 K Figure 8.4. The samples with C_{60} additions appear to have slightly lower$S$ values that decrease with increasing amount of C_{60}. The smallest values are S = 57 µV K^{-1} (1% C_{60} added), 56 µV K^{-1} (2% C_{60}), and 53 µV K^{-1} (3% C_{60}), the latter two measured at slightly higher temperature, namely at 323 K instead of at 300 K.

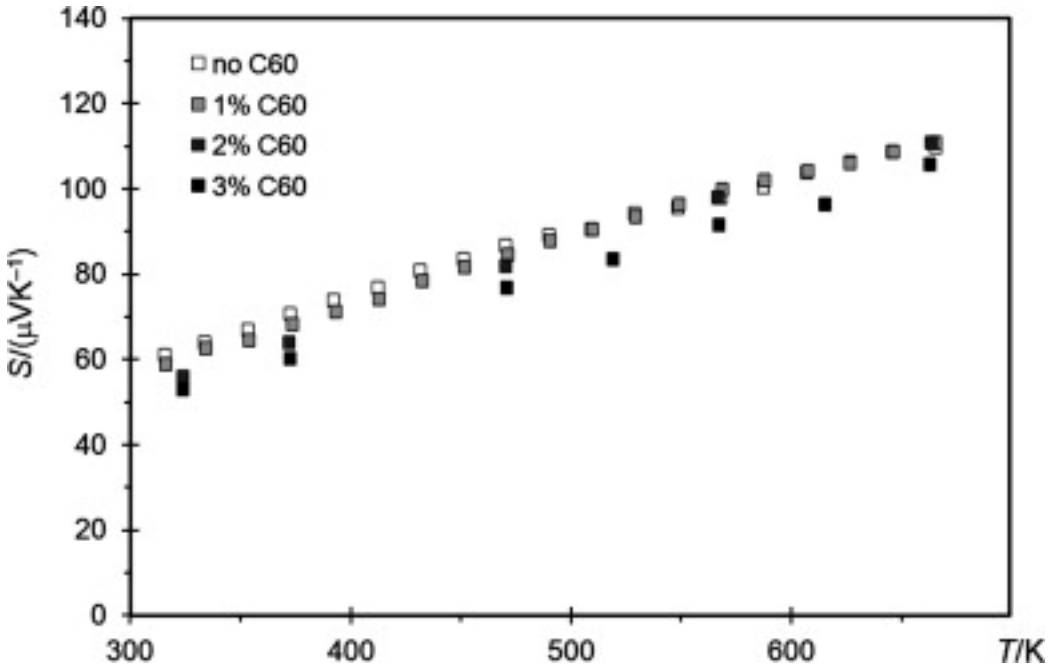

Figure 8.4: Seebeck coefficient of various $Ni_{0.05}Mo_3Sb_{5.4}Te_{1.6}/C_{60}$ samples.

The high-temperature data are summarized in Table 2. With an estimated experimental error of ±3%, i.e. 2 μV K^{-1}–3 μVK^{-1}, the differences in *S* are not significant. Likewise, adding of up to 4.77% C_{60} to $CoSb_3$ had only a minor impact on the Seebeck coefficient [153]; in the case of Ba*x*Co_4Sb_{12}; however, the composites with C_{60} had a lower carrier (and Ba) concentration and thus a larger Seebeck coefficient.[155] That this is not the case here suggests that the composites exhibit a carrier concentration comparable with the bulk material, as also observed for $CoSb_3$.[153]

Table 8.2: Thermoelectric properties of various $Ni_{0.05}Mo_3Sb_{5.4}Te_{1.6}/C_{60}$ samples around 665 K.

Property	No C_{60}	1%C_{60}	2% C_{60}	3% C_{60}
S ($\mu V\ K^{-1}$)	110±3	111±3	111±3	105±3
σ ($\Omega^{-1}\ cm^{-1}$)	975±49	770±39	590±30	590±30
P.F. ($\mu W\ cm^{-1}\ K^{-2}$)	11.7±0.8	9.48±0.62	7.12±0.47	6.64±0.44
κ ($W\ m^{-1}\ K^{-1}$)	3.75±0.15	2.65±0.11	2.18±0.09	1.83±0.07
ZT (Dulong–Petit)	0.228±0.18	0.251±0.20	0.232±0.18	0.250±0.19
ZT (meas. Cp)	0.235±0.18	0.269±0.21	-	-

The electrical conductivity of the bulk $Ni_{0.05}Mo_3Sb_{5.4}Te_{1.6}$ sample without C_{60} decreases from σ = 1480 $\Omega^{-1}\ cm^{-1}$ at 300 K to 980 $\Omega^{-1}\ cm^{-1}$ at 665 K Figure 8.5, thus, again displaying normal behavior for a $Mo_3(Sb,Te)_7$ sample. Adding more and more C_{60} causes a continuing decrease in these values, while the linear negative temperature dependence prevails. The room temperature values are 1120 $\Omega^{-1}\ cm^{-1}$ (1% C_{60} added), 830 $\Omega^{-1}\ cm^{-1}$(2% C_{60}), and 730 $\Omega^{-1}\ cm^{-1}$ (3% C_{60}), respectively. Assuming an experimental error of ±5%, which corresponds up to 74 $\Omega^{-1}\ cm^{-1}$, the differences of up to 750 $\Omega^{-1}\ cm^{-1}$ are of course significant. While the same tendency of decreasing conductivity with increasing C_{60} addition occurred in Ba*x*Co_4Sb_{12}, the temperature dependence changed therein in contrast to the $Ni_{0.05}Mo_3Sb_{5.4}Te_{1.6}$, turning into a positive dependence starting at 2.12% C_{60}.[155] The latter was deduced to arise from dominant carrier-boundary scattering at high C_{60} concentrations, while we found no evidence here for a change in the scattering mechanism, as the temperature dependence does not change for the C-containing composites, aside from obtaining flatter curves for the samples with more carbon. The latter is a consequence of increased impurity scattering.

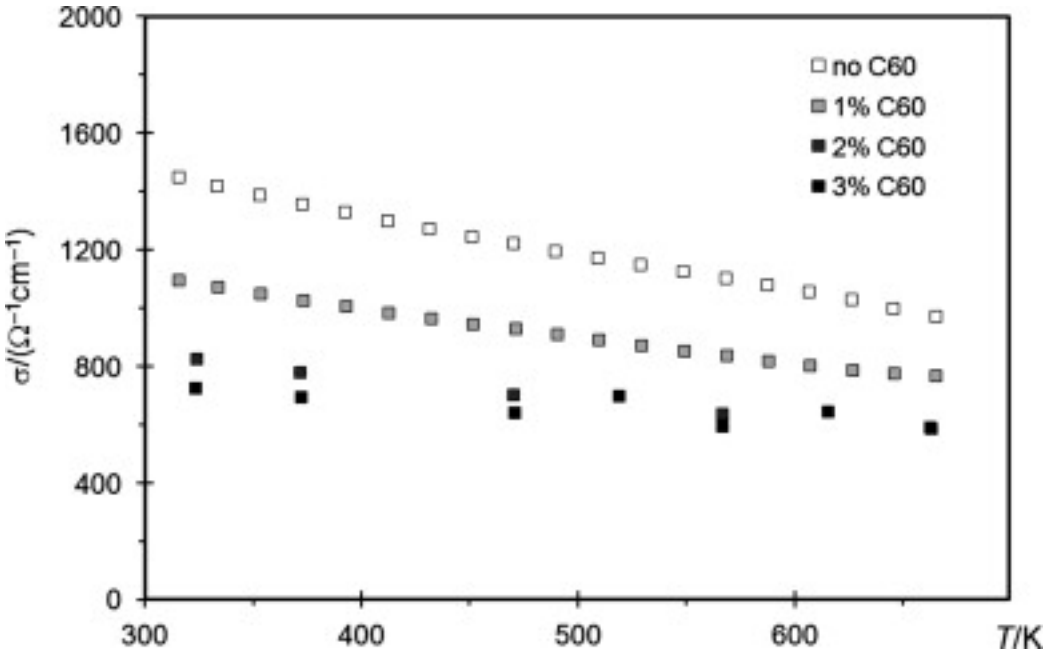

Figure 8.5: Electrical conductivity of various $Ni_{0.05}Mo_3Sb_{5.4}Te_{1.6}/C_{60}$ samples.

The power factor, $P.F. = S^2\sigma$, i.e. the numerator of Z, increases in a linear fashion with increasing temperature Figure 8.6 like the Seebeck coefficient, as also observed for the previously published $Mo_3(Sb,Te)_7$ cases. [113] Around 300 K, *P.F.* of the 1% C_{60} sample is with 3.6 μW cm^{-1} K^{-2} 25% smaller than the sample without C_{60} (4.8 μW cm^{-1} K^{-2}), and at 660 K 19% smaller (9.5 μW cm^{-1} K^{-2} vs. 11.7 μW cm^{-1} K^{-2}), noting that *P.F.* here generally decreases with increasing carbon content because of the decrease in σ. Except for the 2% and 3% samples, all *P.F.* values are significantly different Table 8.2. To counter that decrease in *P.F.* following the additions of C_{60}, the thermal conductivity – the denominator of Z – of the 1% C_{60} sample would thus have to be more than 25% lower than that of the bulk sample to result in a higher *figure-of-merit*.

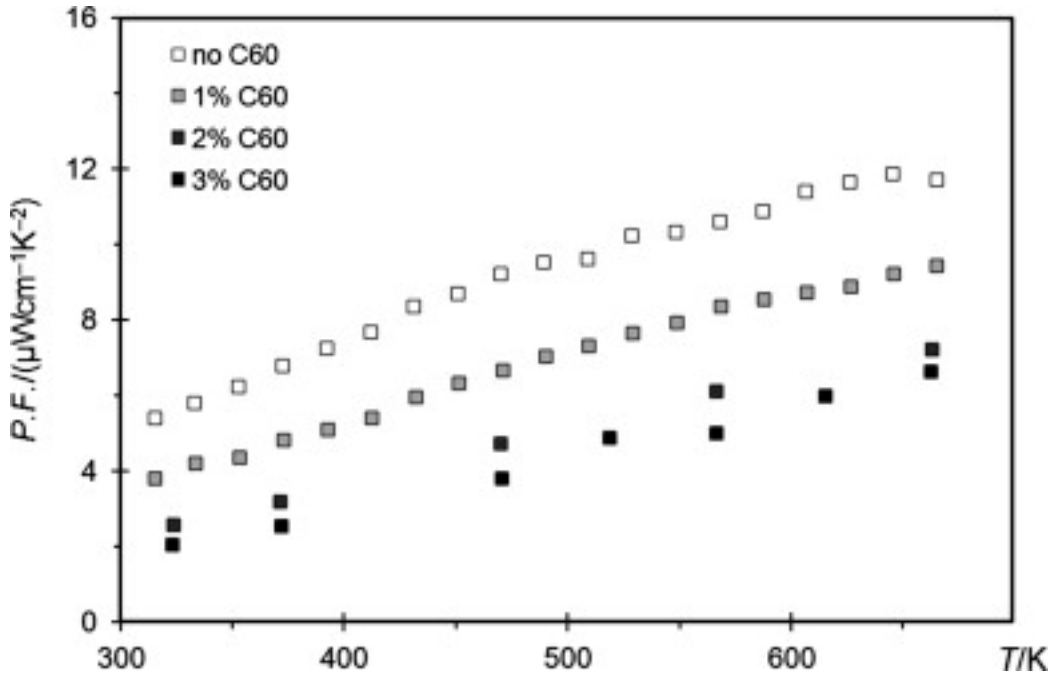

Figure 8.6: Power factor of various $Ni_{0.05}Mo_3Sb_{5.4}Te_{1.6}/C_{60}$ samples.

For comparison, the maximum *P.F.* of $Yb_{14}MnSb_{11}$, one of the leading high temperature p-type thermoelectric materials above 900 K, was originally reported to reach 6 μW $cm^{-1}K^{-2}$ at 1200 K [305], and later improved to reach almost 7 μW cm^{-1} K^{-2} by substituting some Mn for Al.[306] $Ba_xCo_4Sb_{12}$, on the other hand, exhibited *P.F.*(300 K) of almost 20 μW cm^{-1} K^{-2} and just above 20 μW cm^{-1} K^{-2} for the composite containing 0.43% C_{60}, for its increase in *S* outweighed the decrease in σ.

As expressed in the Wiedemann–Franz law [307], the electronic contribution to the thermal conductivity is proportional to the product of the temperature and the electrical conductivity, which decreases with increasing temperature in this case. Likewise, the lattice thermal conductivity should follow the same trend.[88] The high temperature thermal conductivity data on the $Ni_{0.05}Mo_3Sb_{5.4}Te_{1.6}$ composites exhibit the expected negative temperature dependence Figure 8.7. Like the electrical conductivity, σ, the thermal conductivity, κ, decreases with increasing C_{60} content: The values for the bulk sample vary from κ = 4.7 W $m^{-1}K^{-1}$ at 323 K to 3.8 W $m^{-1}K^{-1}$ at 673 K, and for example for the 1% C_{60} sample from 3.6 W $m^{-1}K^{-1}$ at 323 K to 2.7 W $m^{-1}K^{-1}$ at 673 K. With experimental errors of

4%, i.e. of the order of 0.1 W $m^{-1}K^{-1}$, the values are significantly different. The decrease at 673 K amounts to 30%, and thus outweighs the decrease of the 25% decrease of the power factor, so that the *figure-of-merit ZT = T P.F.* κ^{-1} will be higher.

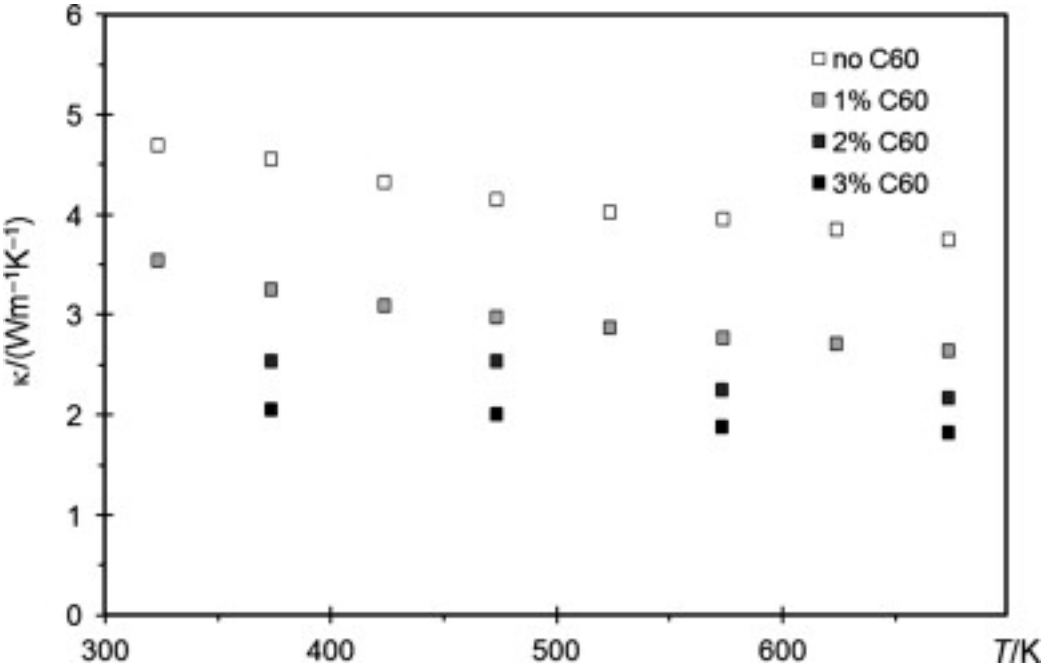

Figure 8.7: Thermal conductivity of various $Ni_{0.05}Mo_3Sb_{5.4}Te_{1.6}/C_{60}$ samples.

To verify whether or not the decrease in κ upon C_{60} addition is caused by increased electron and phonon scattering, we estimated the electronic thermal conductivity, κ_e, via the Wiedemann–Franz law (Section 1.4.1.2).

Because κ and σ were obtained at slightly different temperatures, we used a fit to the σ curves to interpolate σ at the required temperatures, e.g. 323 K. Using the Sommerfeld value, $L_0 = 2.44\times10^{-8}$ W Ω K^{-2}, we obtained at 323 K κ_l = 3.6 W $m^{-1}K^{-1}$ for the bulk, compared to 2.7 W $m^{-1}K^{-1}$ for the 1% sample and 1.4 W $m^{-1}K^{-1}$ for the 3% sample Figure 8.8. However, because the Lorenz number varies depending on the material and on the temperature [308], $L_0 = 2.1\times10^{-8}$ W Ω K^{-2} might be a more appropriate number, which was calculated for these $Mo_3(Sb,Te)_7$ materials around 323 K.[88] With this smaller Lorenz number, κ_e is smaller and thus κ_l larger (in both cases), here 3.7 W $m^{-1}K^{-1}$ (bulk) and 2.8 W $m^{-1}K^{-1}$ (1% C_{60}). It is

therefore, concluded that irrelevant of which (constant) L_0 is used, that the C_{60} additions increase both electron and phonon scattering.

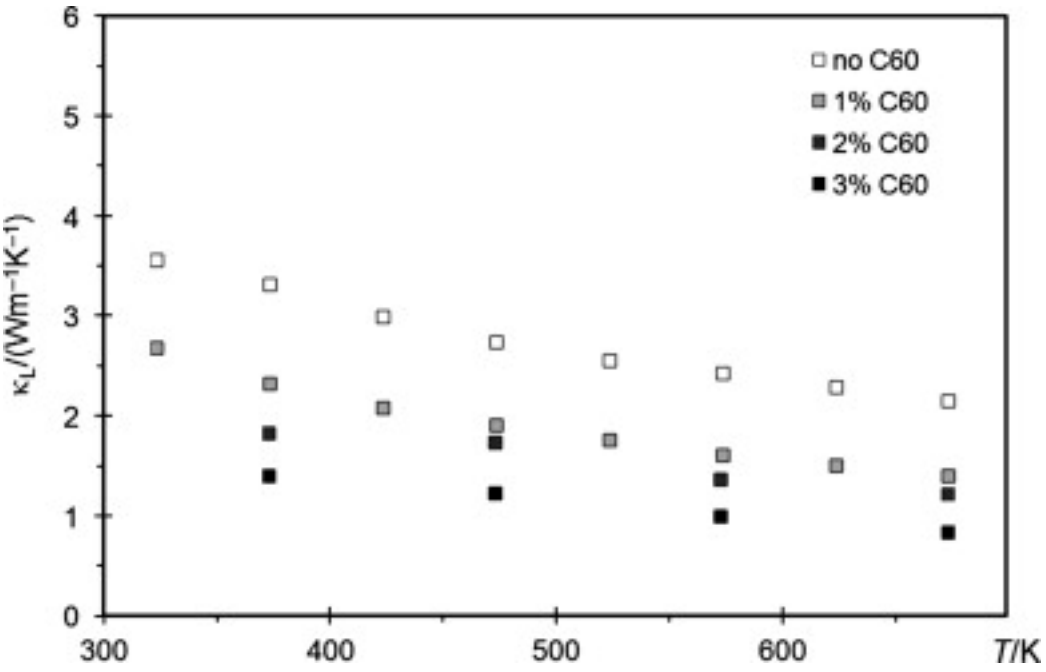

Figure 8.8: Lattice thermal conductivity of various $Ni_{0.05}Mo_3Sb_{5.4}Te_{1.6}/C_{60}$ samples.

The *figure-of-merit*, $ZT = S^2\sigma\kappa^{-1}T$, was calculated for the temperatures at which κ was measured, using a fit of the power factor curves, $P.F. = S^2\sigma$. Like other $Mo_3(Sb,Te)_7$ materials investigated before, *ZT* increases sharply with increasing temperature Figure 8.9, e.g. for the bulk sample from 0.04 at 323 K to 0.23 at 673 K. With *ZT* (673 K) = 0.25 for both $Mo_3Sb_{5.6}Te_{1.4}$ [88] and $Ni_{0.05}Mo_3Sb_{5.3}Te_{1.7}$ [90], the bulk $Ni_{0.05}Mo_3Sb_{5.4}Te_{1.6}$ sample analyzed here is very typical for this kind of material. While the *ZT* values of the C_{60}composites are practically equivalent with the bulk at low temperatures, they are higher at higher temperatures, culminating in *ZT* = 0.25 for both the 1% and 3% composites. The largest improvement is thus 10% (14% when using the experimentally derived C_P values), which is at the border of significance Table 8.2 [229], [309] and [310].

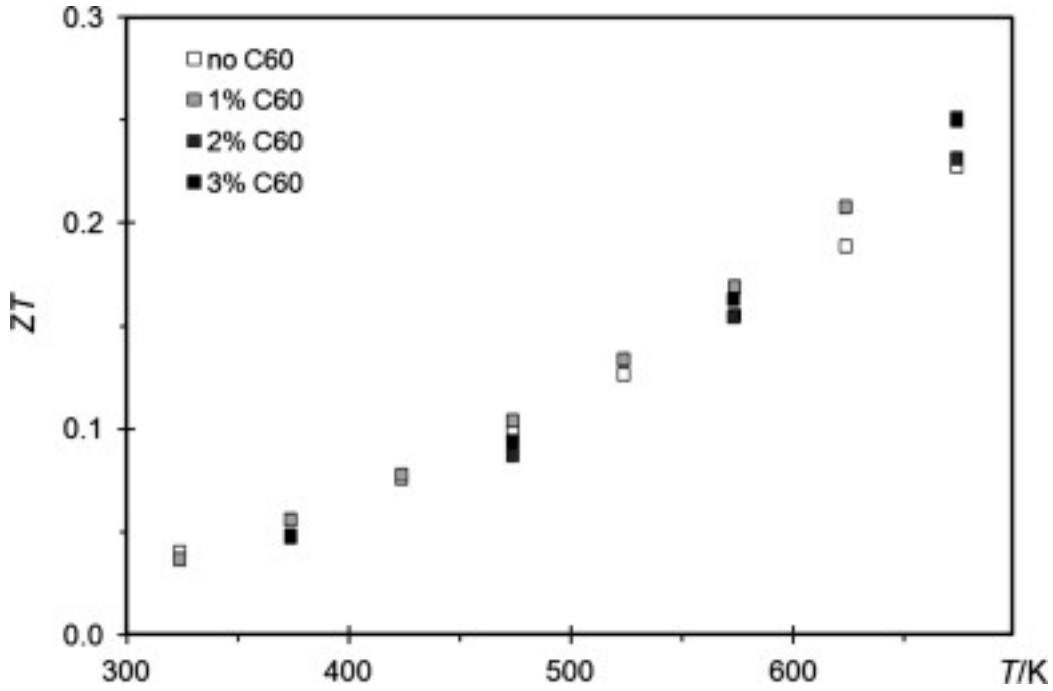

Figure 8.9: ***Figure-of-merit*** **of various $Ni_{0.05}Mo_3Sb_{5.4}Te_{1.6}/C_{60}$ composites.**

8.2 Conclusions

Using $Ni_{0.05}Mo_3Sb_{5.4}Te_{1.6}$ as a representative, we have demonstrated here for the first time, that the thermoelectric properties of $Mo_3(Sb,Te)_7$ materials may be improved via composite formation, here using additions of 1–3 mass% C_{60}. Rietveld refinements and TEM investigations performed after hot-pressing and the physical property measurement indicated that the bulk material remained intact during the processing. The C_{60} polymerized during the hot-pressing and turned into amorphous nanoparticles with typical sizes around 50 nm. Adding more and more C_{60} led to increased electron and phonon scattering, which reflected on lower electrical conductivity, lower total thermal conductivity and lower phonon contribution to the thermal conductivity.

As the Seebeck effect remained basically unaffected by the carbon additions, the change of the *figure-of-merit* depended on whether the electrical conductivity decreased more than the thermal conductivity or vice versa. While all materials exhibited comparable *ZT* values at low temperatures, the composites containing carbon appeared to perform better at elevated

temperatures, noting that these experimentally determined improvements were of the order of the experimental errors and thus not significant.

Ongoing research will reveal the best amount of C_{60}, including attempts with smaller C_{60} additions, and whether using other forms of carbon will yield significantly different results. Extended measurements at higher temperatures will be attempted to investigate the long-term high temperature stability of these composites and to verify whether the differences in performance continue to increase at temperatures above 700 K.

Acknowledgments

Financial support from the Natural Sciences and Engineering Research Council and the Canada Research Chair program (CRC for H.K.) is appreciated. The work at Clemson University is supported by DOE/EPSCoR Implementation Grant (no. DE-FG02-04 ER-46139), and the SC EPSCoR cost-sharing program.

8.3 Supplementary Information

A figure of C_P measurements and a figure comparing ZT deduced from measured C_P with the one from Dulong–Petit's C_P.

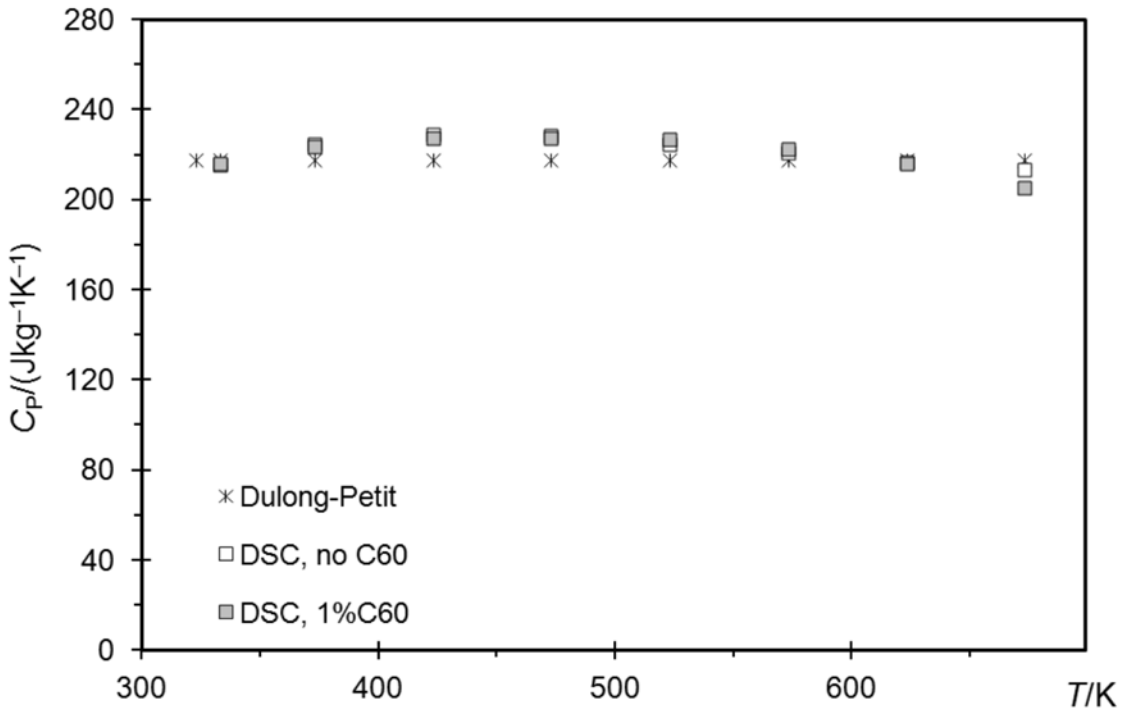

Figure 8.10: Specific heat obtained from DSC data vs. Dulong-Petit approximation.

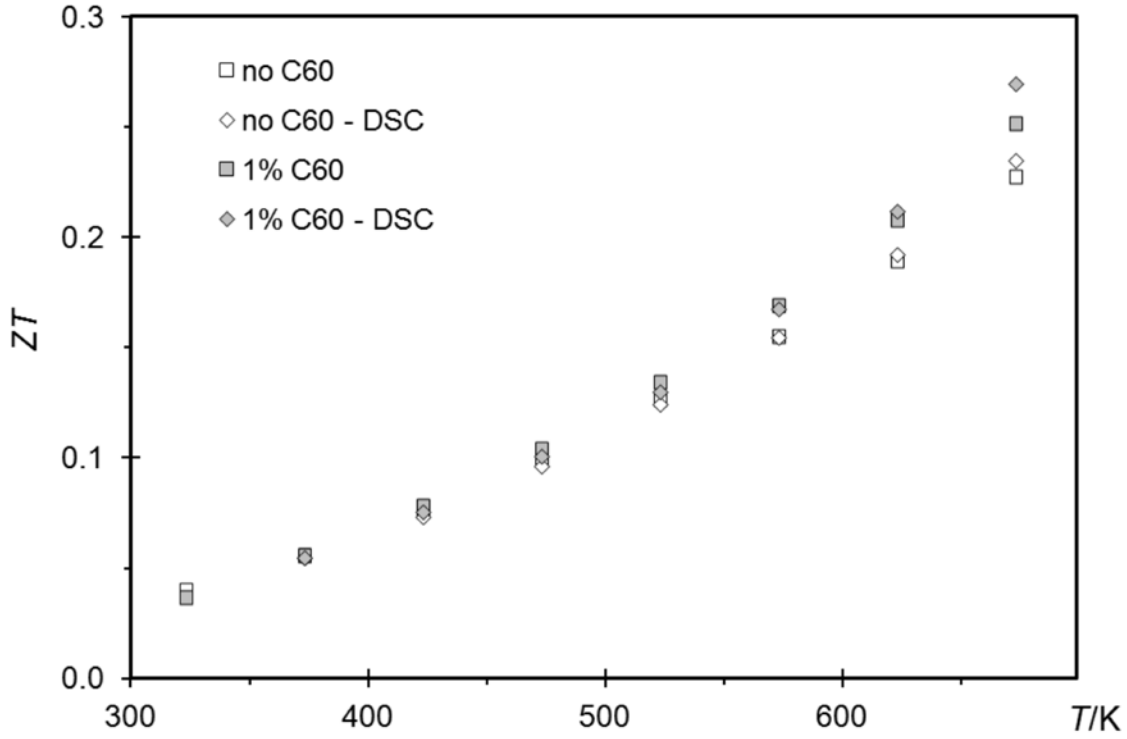

Figure 8.11: ***Figure-of-merit*** **using the specific heat from DSC data vs. Dulong-Petit approximation.**

Chapter 9
Conclusion and Future Work

9.1 Conclusions

The question arises of why some materials are very suitable candidates for our bulk material as nanoinclusions. Since our bulk material is found to have high charge carrier concentration (10^{21} cm^{-3}), any inclusion that enhances the charge carrier concentration can degrade the Seebeck coefficient as the bulk/NiSb composites study show. In bulk/C_{60}, bulk/MWCNT, bulk/SiC, bulk/Al_2O_3 composites, charge carriers are scattered by embedded particles and the interfaces they created, thereby reducing the charge carrier mobility.

Spark-plasma sintering (SPS) is a very suitable consolidation technique (the *figure-of-merit* for the bulk sample consolidated through SPS is 35% higher than the hot-pressed bulk sample); however, our opinion is that densification profile for hot-press needs to be optimized to achieve very high relative densities.

Our study on bulk/Al_2O_3 shows that variation of electrical conductivity with temperature in samples with very high relative densities tends to follow $T^{-3/2}$, a typical acoustic phonon scattering. However, samples with low relative densities deviate from this pattern due to microstructures such as porosity ($T^{-0.43}$ in bulk/SiC composites). The nature of electrical conductivity of MWCNT in our composites needs more investigation. As we discussed in Chapter 5, some polymers with MWCNT exhibit a very low electrical percolation threshold. However, in a material such as ours, this result was not observed and requires further investigation.

In bulk/C_{60}, bulk/MWCNT, bulk/SiC, bulk/Al_2O_3 composites, there is a systematic reduction in the lattice part of the thermal conductivity. Contrary to this, in bulk/NiSb composites, lattice thermal conductivity increased. As we pointed out in Chapter 5, needle like structures of NiSb must be playing a role in enhancing the thermal conductivity. Also in bulk/C_{60}, bulk/MWCNT, bulk/SiC composites, Seebeck coefficient is less sensitive to microstructure.

Summary of *figure-of-merits* (*ZT*) for Different Composites

bulk/MWCNT			at 765 K
ZT of bulk	0.32		
	mass%	*ZT*-comp	*ZT*-comp/ZT bulk
	0	0.32	1.00
	1%	0.33	1.03
	2%	0.3	0.94
	3%	0.38	1.19

bulk/C_{60}			at 675 K
ZT of bulk	0.23		
	mass%	*ZT*-comp	*ZT*-comp/ZT bulk
	0	0.23	1.00
	1%	0.25	1.09
	2%	0.23	1.00
	3%	0.25	1.09

bulk/SiC			
ZT o fbulk	0.33		at 760 K
	f	*ZT*-comp	*ZT*-comp/ZT bulk
	0	0.33	1.00
	0.01	0.4	1.21
	0.02	0.32	0.97
	0.034	0.30	0.91

bulk/CNP			
ZT of bulk	0.32		at 755 K
	mass%	*ZT*-comp	*ZT*-comp/ZT bulk
	0.00	0.32	1.00
	0.05	0.34	1.06
	1.00	0.3	0.94
	1.50	0.31	0.97

bulk/Al_2O_3			at 760 K
ZT of bulk	0.42		
	f	*ZT*-comp	*ZT*-comp/ZT bulk
	0	0.42	1.00
	0.01	0.40	0.95
	0.0216	0.41	0.97
	0.0325	0.37	0.88

bulk/NiSb			at 750 K
ZT of bulk	0.3		
	f	*ZT*-comp	*ZT*-comp/ZT bulk
	0	0.30	1.00
	0.034	0.24	0.80
	0.074	0.20	0.67
	0.16	0.15	0.50

Note: bulk/CNP (carbon nanoparticles)-CNP were coated on bulk through solvothermal process using glucose as the starting material

9.2 Future Work

There are debatable issues on the nature of charge carrier transport through the inner walls of MWCNT. It is still not clear whether the charge carriers flow through the outer wall or/and through the inner walls. In our opinion, it is very advisable to use carbon nanowires (very small diameter) as nanoinclusions. If charge carriers indeed flow though the outer wall, then the inner walls simply occupy space in the composites, thus reducing the mechanical integrity of composites. Environmentally benign Bi nanowires are also very suitable candidates for bulk/Bi (nanowire) composites that can enhance electrical conductivity, leave the Seebeck coefficient unaffected, and reduce lattice thermal conductivity.

Engineering a conducive interface that facilitates suitable electrical (filtering effect) and thermal conductivity (enhanced phonon scattering) is one of the options we have to enhance the *figure-of-merit*.

Since SPS is a suitable consolidation technique, our contention is that, with a suitable nanomaterial (carbon nanowires, graphene, micron sized refractory materials such as SiC, ZrO_2 and Al_2O_3), it is possible to reduce the lattice thermal conductivity of bulk material (provided that the materials are dispersed homogeneously).

In my experience, it is very challenging to disperse CNT very homogeneously inside the bulk material. In the future, we intend to investigate the performance and stability of bulk/CNT composites beyond 760 K and the effect of using non-graphitic nanotubes (for example inexpensive Bi nanowires) on the thermoelectric properties. The electrical conductivity of metal (Cu, Ag, Ni) coated CNT is not well understood; we are exploring wet chemistry or solventless techniques [311] to coat CNT with different metal particles. Apart from ball-milling, we plan to explore other methods that disperse CNT homogeneously to enhance phonon scattering, while simultaneously preserving electrical conductivity as much as possible.

It is also worthwhile to investigate wet chemistry techniques to coat SiC and Al_2O_3 nanoparticles on bulk particles homogeneously (using some surfactant). We are also optimistic that bulk material with larger alumina particles consolidated through SPS can improve the TE properties. The thermal boundary resistance (Kapitza resistance) of SiC, is higher than that of

Al_2O_3 composites mainly due to the microstructures of bulk/SiC rather than the embedded particles.

In bulk/NiSb (solvothermally coated) composites, we observed the formation of $NiSb_2$. In the future, we need to explore avenues to prevent the formation of $NiSb_2$ by using some additives. Also we are planning to coat bulk material with $CoSb_3$ or ZnO nano particles using either a solvothermal process or low energy colloidal synthesis.

9.3 Collaborators

During my doctoral studies, our group was collaborated with various groups. These groups, and their contribution are listed in the following paragraphs

(1) Stéphane Gorsse

CNRS, Université de Bordeaux, ICMCB, and Bordeaux INP, ICMCB, UPR 9048, 33600 Pessac,France

TEM microstructural and elemental analysis of the following composite: bulk/$C_{60,}$ bulk/MWCNT, and bulk/NiSb

(2) Robert Liang and Y. Norman Zhou

Centre of Advanced Materials Joining, Department of Mechanical and Mechatronics Engineering and Waterloo Institute for Nanotechnology, University of Waterloo, Waterloo, Ontario, Canada N2L 3G1

NiSb nanoparticle synthesis, mechanical property measurement of bulk/NiSb, bulk/SiC and bulk/Al_2O_3 composites. Developed method and synthesis of NiSb nanoparticles coating on bulk material through solvothermal process with acid digester. Carbon nanoparticle coating on bulk particles. HRTEM and SEM images of bulk/NiSb composites with elemental analysis (EDS). Participated in effective property calculations of bulk/NiSb, bulk/SiC composites; BET

measurement; edited and polished many figures and text to specified formats for publication.

(3) Atta Ullah Khan and Takao Mori

National Institute for Materials Science, Tsukuba, Ibaraki Prefecture 305-0047, Japan

Spark-plasma sintering (SPS) of the following composites:
bulk/SiC and bulk/Al_2O_3, bulk/ZrO_2, bulk/NiO, and ball-milled samples
Transport property characterization of bulk/Al_2O_3 composites

(4) Ali Lahwal, Daniel Thompson,Tim C. Holgate, and Terry M. Tritt

Department of Physics and Astronomy, Clemson University, Clemson, SC, USA 29634

Helped in hot-pressing and thermal conductivity characterization of bulk/C_{60} composite

(5) Véronique Dassylva-Raymond and László I. Kiss

Specific heat analysis of bulk/C_{60} composites

(6) Elisabeth Sellier

CREMEM, Université de Bordeaux, F-33405 Talence, France
TEM microstructural and elemental mapping of bulk/C_{60} composites

Bibliography

[1] R. Stone, *Introduction to internal combustion engines*. Palgrave Macmillan, 2012.

[2] T.B. Johansson, N. Nakićenović, *Global Energy Assessment: Toward a Sustainable Future*. Cambridge University Press, 2012.

[3] R.R. Furlong, E.J. Wahlquist, *Nuclear news* 42 (1999) 26-35.

[4] H. Goldsmid, *Thermoelectric refrigeration*. Springer, 2013.

[5] A.F. Ioffe, *Physics of Semiconductors*. Academic Press, New York City, NY, 1960.

[6] D. Kraemer, B. Poudel, H.P. Feng, J.C. Caylor, B. Yu, X. Yan, Y. Ma, X. Wang, D. Wang, A. Muto, *Nat. Mater.* 10 (2011) 532-538.

[7] D. Rowe, C. Bhandari, *Modern Thermoelectrics*. Holt, Rinehart and Winston, London, 1983.

[8] E.J.R. Rao R. Tummala, Alan G. Klopfenstein, *Microelectronics packaging handbook*. Springer US, 1997.

[9] G. Min, D. Rowe, *Solid-State Electron.* 43 (1999) 923-929.

[10] F. Völklein, G. Min, D. Rowe, *Sens. Actuators, A* 75 (1999) 95-101.

[11] I. Chowdhury, R. Prasher, K. Lofgreen, G. Chrysler, S. Narasimhan, R. Mahajan, D. Koester, R. Alley, R. Venkatasubramanian, *Nat. Nanotechnol.* 4 (2009) 235-238.

[12] T. Haruyama, *Cryogenics* 41 (2001) 335-339.

[13] H. Stachowiak, S. Lassue, A. Dubernard, E. Gaviot, *Flow Meas. Instrum.* 9 (1998) 135-141.

[14] A. Van Herwaarden, P. Sarro, *Sens. Actuators, A* 10 (1986) 321-346.

[15] G. Joshi, X. Yan, H. Wang, W. Liu, G. Chen, Z. Ren, *Adv. Energy Mater.* 1 (2011) 643-647.

[16] K.F. Hsu, S. Loo, F. Guo, W. Chen, J.S. Dyck, C. Uher, T. Hogan, E. Polychroniadis, M.G. Kanatzidis, *Science* 303 (2004) 818-821.

[17] W.S. Liu, Q. Zhang, Y. Lan, S. Chen, X. Yan, Q. Zhang, H. Wang, D. Wang, G. Chen, Z. Ren, *Adv. Energy Mater.* 1 (2011) 577-587.

[18] K. Biswas, J. He, Q. Zhang, G. Wang, C. Uher, V.P. Dravid, M.G. Kanatzidis, *Nat. Chem.* 3 (2011) 160-166.

[19] W. Liu, X. Yan, G. Chen, Z. Ren, *Nano Energy* 1 (2012) 42-56.

[20] T.M. Tritt, *Thermal conductivity: theory, properties, and applications*. Springer Science & Business Media, 2004.

[21] P. Klemens, *Proc. Phys. Soc. London, Sect. A* 68 (1955) 1113.

[22] S. Wang, *Fundamentals of semiconductor theory and devices physics*. Prentice-Hall, Inc., 1989.

[23] Y. Lan, A.J. Minnich, G. Chen, Z. Ren, *Adv. Funct. Mater.* 20 (2010) 357-376.

[24] M.S. Jeng, R. Yang, D. Song, G. Chen, *J. Heat Transfer* 130 (2008) 042410.

[25] B. Poudel, Q. Hao, Y. Ma, Y. Lan, A. Minnich, B. Yu, X. Yan, D. Wang, A. Muto, D. Vashaee, *Science* 320 (2008) 634-638.

[26] M.S. Dresselhaus, G. Chen, M.Y. Tang, R. Yang, H. Lee, D. Wang, Z. Ren, J.P. Fleurial, P. Gogna, *Adv. Mater.* 19 (2007) 1043-1053.

[27] D. Medlin, G. Snyder, *Curr. Opin. Colloid Interface Sci.* 14 (2009) 226-235.

[28] M.-S. Jeng, R. Yang, D. Song, G. Chen, *J. Heat Transfer* 130 (2008) 042410.

[29] Q. Guo, H. Kleinke, *J. Solid State Chem.* 215 (2014) 253-259.

[30] V.I. Fistul, J. Blakemore, *Heavily doped semiconductors*. Plenum Press, New York, 1969.

[31] R. Prasher, *Proc. IEEE* 94 (2006) 1571-1586.

[32] J.C. Maxwell, *A treatise on electricity and magnetism*. Oxford University Press, 1904.

[33] D.A.G. Bruggeman, *Ann. Phys. (Leipzig)* 24 (1935) 636-679.

[34] D. Hasselman, L.F. Johnson, *J. Compos. Mater.* 21 (1987) 508-515.

[35] C.W. Nan, R. Birringer, D.R. Clarke, H. Gleiter, *J. Appl. Phys.* 81 (1997) 6692-6699.
[36] E.T. Swartz, R.O. Pohl, *Rev. Mod. Phys.* 61 (1989) 605.
[37] J. Ordonez-Miranda, J. Alvarado-Gil, *Compos. Sci. Technol.* 72 (2012) 853-857.
[38] D. Hasselman, K.Y. Donaldson, A.L. Geiger, *J. Am. Ceram. Soc.* 75 (1992) 3137-3140.
[39] P.L. Kapitza, *Collected Papers of P.L. Kapitza*. Pergamon Press, Oxford, 1965.
[40] A. Every, Y. Tzou, D. Hasselman, R. Raj, *Acta Metall. Mater.* 40 (1992) 123-129.
[41] L. Davis, B. Artz, *J. Appl. Phys.* 77 (1995) 4954-4960.
[42] K. Schlichting, N. Padture, P. Klemens, *J. Mater. Sci.* 36 (2001) 3003-3010.
[43] R. Stoner, H. Maris, T. Anthony, W. Banholzer, *Phys. Rev. Lett.* 68 (1992) 1563.
[44] R. Lipton, B. Vernescu, *J. Appl. Phys.* 79 (1996) 8964-8966.
[45] R. Lipton, B. Vernescu, *Proc. R. Soc. Lond. A* 452 (1996) 329-358.
[46] H. Bhatt, K.Y. Donaldson, D.H. Hasselman, R. Bhatt, *J. Am. Ceram. Soc.* 73 (1990) 312-316.
[47] W. Leung, A. Tam, *J. Appl. Phys.* 63 (1988) 4505-4510.
[48] G. Milton, *J. Appl. Phys.* 52 (1981) 5286-5293.
[49] S. Torquato, M. Rintoul, *Phys. Rev. Lett.* 75 (1995) 4067.
[50] D. Stauffer, A. Aharony, *Introduction to percolation theory*. Tailor & Francis, London, UK, 1985.
[51] W. Tian, R. Yang, *Computer modeling in engineering and sciences* 24 (2008) 123.
[52] Z. Tian, H. Hu, Y. Sun, *Int. J. Heat Mass Transfer* 61 (2013) 577-582.
[53] D.G. Cahill, W.K. Ford, K.E. Goodson, G.D. Mahan, A. Majumdar, H.J. Maris, R. Merlin, S.R. Phillpot, *J. Appl. Phys.* 93 (2003) 793-818.
[54] J. Francl, W. Kingery, *J. Am. Ceram. Soc.* 37 (1954) 99-107.
[55] I. Sumirat, Y. Ando, S. Shimamura, *J. Porous Mater.* 13 (2006) 439-443.
[56] G. Chen, Oxford University Press, New York, 2005.
[57] W. Little, *Can. J. Phys.* 37 (1959) 334-349.
[58] D.M. Rowe, *CRC Handbook of Thermoelectrics*. CRC Press, Boca Raton, FL, 1995.
[59] H.J. N. F. Mott, *The Theory of the Properties of Metals and Alloys*. Dover Publications, 1936.
[60] J.P. Heremans, C.M. Thrush, D.T. Morelli, *Phys. Rev. B: Condens. Matter* 70 (2004) 115334.
[61] B. Paul, A. Kumar, P. Banerji, *J. Appl. Phys.* 108 (2010) 064322.
[62] S.V. Faleev, F. Léonard, *Phys. Rev. B* 77 (2008) 214304/1-214304/9.
[63] A. Akhiezer, I. Akhiezer, V. Bary'yakhtar, *Soviet Journal of Experimental and Theoretical Physics* 38 (1974) 167.
[64] X. Shi, Y. Pei, G.J. Snyder, L. Chen, *Energy Environ. Sci.* 4 (2011) 4086-4095.
[65] S. Kirkpatrick, *Rev. Mod. Phys.* 45 (1973) 574.
[66] B. Poudel, Q. Hao, Y. Ma, Y. Lan, A. Minnich, B. Yu, X. Yan, D. Wang, A. Muto, D. Vashaee, X. Chen, J. Liu, M.S. Dresselhaus, G. Chen, Z. Ren, *Science* 320 (2008) 634-638.
[67] W. Xie, J. He, H.J. Kang, X. Tang, S. Zhu, M. Laver, S. Wang, J.R. Copley, C.M. Brown, Q. Zhang, *Nano Lett.* 10 (2010) 3283-3289.
[68] D.-K. Ko, Y. Kang, C.B. Murray, *Nano Lett.* 11 (2011) 2841-2844.
[69] D.M. Rowe, *Thermoelectrics Handbook: Macro to Nano*. CRC Press, Taylor & Francis Group, Boca Raton, FL, USA, 2006.
[70] C.B. Vining, W. Laskow, J.O. Hanson, R.R. Van der Beck, P.D. Gorsuch, *J. Appl. Phys.* 69 (1991) 4333-4340.
[71] G. Joshi, H. Lee, Y. Lan, X. Wang, G. Zhu, D. Wang, R.W. Gould, D.C. Cuff, M.Y. Tang, M.S. Dresselhaus, *Nano Lett.* 8 (2008) 4670-4674.

[72] X. Wang, H. Lee, Y. Lan, G. Zhu, G. Joshi, D. Wang, J. Yang, A. Muto, M. Tang, J. Klatsky, *Appl. Phys. Lett.* 93 (2008) 193121.
[73] H. Wang, J.-F. Li, C.-W. Nan, M. Zhou, W. Liu, B.-P. Zhang, T. Kita, *Appl. Phys. Lett.* 88 (2006) 092104.
[74] M. Zhou, J.-F. Li, T. Kita, *J. Am. Chem. Soc.* 130 (2008) 4527-4532.
[75] J.P. Heremans, V. Jovovic, E.S. Toberer, A. Saramat, K. Kurosaki, A. Charoenphakdee, S. Yamanaka, G.J. Snyder, *Science* 321 (2008) 554-557.
[76] G.J. Snyder, E.S. Toberer, *Nat. Mater.* 7 (2008) 105-114.
[77] J.R. Sootsman, R.J. Pcionek, H. Kong, C. Uher, M.G. Kanatzidis, *Chem. Mater.* 18 (2006) 4993-4995.
[78] Q. Guo, A. Assoud, H. Kleinke, *Adv. Energy Mater.* 4 (2014).
[79] G.S. Nolas, D.T. Morelli, T.M. Tritt, *Annu. Rev. Mat. Sci.* 29 (1999) 89-116.
[80] B.C. Sales, D. Mandrus, R.K. Williams, *Science* 272 (1996) 1325-1328.
[81] G.S. Nolas, J.L. Cohn, G.A. Slack, S.B. Schujman, Appl. Phys. Lett., 1998, pp. 178-180.
[82] D.T. Morelli, G.P. Meisner, C. B., S. Hu, C. Uher, *Phys. Rev. B.* 56 (1997) 7376-7383.
[83] G.S. Nolas, M. Kaeser, R.T.I. Littleton, T.M. Tritt, *Appl. Phys. Lett.* 77 (2000) 1855-1857.
[84] J.S. Dyck, W. Chen, C. Uher, L. Chen, X. Tang, T. Hirai, *J. Appl. Phys.* 91 (2002) 3698-3705.
[85] G. Rogl, A. Grytsiv, P. Rogl, E. Bauer, M. Hochenhofer, R. Anbalagan, R. Mallik, E. Schafler, *Acta Mater.* 76 (2014) 434-448.
[86] H. Xu, Ph.D thesis, " New Arsenides and Antimonides as Thermoelectric Materials and Chalcogenides with Distorted Square Nets". The University of Waterloo, 2010
[87] E. Dashjav, A. Szczepenowska, H. Kleinke, *J. Mater. Chem.* 12 (2002) 345-349.
[88] X. Shi, Y. Pei, G.J. Snyder, L. Chen, *Energy Environ.Sci.* 4 (2011) 4086-4095.
[89] N. Soheilnia, E. Dashjav, H. Kleinke, *Can. J. Chem.* 81 (2003) 1157-1163.
[90] H. Xu, K. Kleinke, T. Holgate, H. Zhang, Z. Su, T. Tritt, H. Kleinke, *J. Appl. Phys.* 105 (2009) 053703.
[91] L. Hicks, M. Dresselhaus, *Phys. Rev. B: Condens. Matter* 47 (1993) 12727.
[92] L. Hicks, T. Harman, X. Sun, M. Dresselhaus, *Phys. Rev. B: Condens. Matter* 53 (1996) R10493.
[93] R. Venkatasubramanian, E. Slivola, T. Colpitts, B. O'Quinn, *Nature* 413 (2001) 597-602.
[94] S.M. Lee, D.G. Cahill, R. Venkatasubramanian, *Appl. Phys. Lett.* 70 (1997) 2957-2959.
[95] G. Chen, A. Shakouri, *J. Heat Transfer* 124 (2002) 242-252.
[96] D. Rowe, C. Bhandari, *Applied Energy* 6 (1980) 347-351.
[97] C. Moelle, M. Werner, F. SzuÈcs, D. Wittorf, M. Sellschopp, J. Von Borany, H.-J. Fecht, C. Johnston, *Diamond Relat. Mater.* 7 (1998) 499-503.
[98] D. Rowe, V. Shukla, *J. Appl. Phys.* 52 (1981) 7421-7426.
[99] C.J. Vineis, A. Shakouri, A. Majumdar, M.G. Kanatzidis, *Adv. Mater.* 22 (2010) 3970-3980.
[100] M.S. Dresselhaus, G. Chen, M.Y. Tang, R. Yang, H. Lee, D. Wang, Z. Ren, J.P. Fleurial, P. Gogna, *Adv. Mater.* 19 (2007) 1043-1053.
[101] J. Mi, X. Zhao, T. Zhu, J. Tu, *Appl. Phys. Lett.* 92 (2008) 9905.
[102] A.S. Henry, G. Chen, *J. Comput. Theor. Nanosci.* 5 (2008) 141-152.
[103] S.K. Bux, R.G. Blair, P.K. Gogna, H. Lee, G. Chen, M.S. Dresselhaus, R.B. Kaner, J.P. Fleurial, *Adv. Funct. Mater.* 19 (2009) 2445-2452.
[104] M.G. Kanatzidis, *Chem. Mater.* 22 (2009) 648-659.
[105] H. Kleinke, *Chem. Mater.* 22 (2009) 604-611.
[106] J.P. Makongo, D.K. Misra, X. Zhou, A. Pant, M.R. Shabetai, X. Su, C. Uher, K.L. Stokes, P.F. Poudeu, *J. Amer. Chem. Soc.* 133 (2011) 18843-18852.

[107] N. Nandihalli, S. Gorsse, H. Kleinke, *J. Solid State Chem.* 226 (2015) 164-169.
[108] P. Alboni, X. Ji, J. He, N. Gothard, T.M. Tritt, *J. Appl. Phys.* 103 (2008) 113707.
[109] J. Li, Q. Tan, J.F. Li, D.W. Liu, F. Li, Z.Y. Li, M. Zou, K. Wang, *Adv. Funct. Mater.* 23 (2013) 4317-4323.
[110] A. Minnich, M. Dresselhaus, Z. Ren, G. Chen, *Energy Environ. Sci.* 2 (2009) 466-479.
[111] T. Zou, X. Qin, D. Li, B. Ren, G. Sun, Y. Dou, Y. Li, L. Li, J. Zhang, H. Xin, *J. Appl. Phys.* 115 (2014) 053710.
[112] J.-H. Bahk, A. Shakouri, *Appl. Phys. Lett.* 105 (2014) 052106.
[113] H. Xu, K.M. Kleinke, T. Holgate, D. Rossouw, G. Botton, T.M. Tritt, H. Kleinke, *J. Alloys Compd.* 504 (2010) 314-319.
[114] T. Ebbesen, H. Lezec, H. Hiura, J. Bennett, H. Ghaemi, T. Thio, *Nature* 382 (1996) 54-56.
[115] S. Xie, W. Li, Z. Pan, B. Chang, L. Sun, *J. Phys. Chem. Solids* 61 (2000) 1153-1158.
[116] Y. Yeo, T. Oh, *Mater. Res. Bull.* 58 (2014) 54-58.
[117] N.D.Y. Truong, H. Kleinke, F. Gascoin, *Dalton Trans.* 43 (2014) 15092-15097.
[118] H.O. Pierson, *Handbook of Refractory Carbides & Nitrides: Properties, Characteristics, Processing and Apps*. Noyes Publications, Westwood, NJ, USA, 1996.
[119] J.J. Berzelius, *Ann. Phys. Chem.*, 1, 169-230 (1824) 204-30.
[120] J. Li, Q. Tan, J.-F. Li, D.-W. Liu, F. Li, Z.-Y. Li, M. Zou, K. Wang, *Adv. Funct. Mater.* 23 (2013) 4317-4323.
[121] J.-F. Li, J. Liu, *Phys. Status Solidi A* 203 (2006) 3768-3773.
[122] D.W. Liu, J.F. Li, C. Chen, B.P. Zhang, L. Li, *J. Micromech. Microeng.* 20 (2010) 125031.
[123] P.F. Becher, G.C. Wei, *J. Am. Ceram. Soc.* 67 (1984) C-267-C-269.
[124] T.S. Basu, R. Yang, S.J. Thiagarajan, S. Ghosh, S. Gierlotka, M. Ray, *Appl. Phys. Lett.* 103 (2013) 083115.
[125] J. Heremans, C. Jaworski, *Appl. Phys. Lett.* 93 (2008) 122107.
[126] R. Armstrong, *Int. J. Refract. Met. Hard Mater* 19 (2001) 251-255.
[127] J.W. Anthony, *Handbook of mineralogy: Arsenates, phosphates, vanadates. arsenates, phosphates, vanadates*. Mineral Data Pub., 2000.
[128] F. Ren, E. Case, E. Timm, H. Schock, *J. Alloys Compd.* 455 (2008) 340-345.
[129] C.W. Nan, R. Birringer, *Phys. Rev. B: Condens. Matter* 57 (1998) 8264.
[130] Y. Wang, K. Fujinami, R. Zhang, C. Wan, N. Wang, Y. Ba, K. Koumoto, *Appl. Phys Express* 3 (2010) 031101.
[131] D.S. McLachlan, M. Blaszkiewicz, R.E. Newnham, *J. Am. Ceram. Soc.* 73 (1990) 2187-2203.
[132] P. Vaqueiro, A.V. Powell, *J. Mater. Chem.* 20 (2010) 9577-9584.
[133] J. Sharp, S. Poon, H. Goldsmid, *Phys. Status Solidi A* 187 (2001) 507-516.
[134] J.R. Szczech, J.M. Higgins, S. Jin, *J. Mater. Chem.* 21 (2011) 4037-4055.
[135] G. Schierning, *physica status solidi (a)* 211 (2014) 1235-1249.
[136] T. Ikeda, L.A. Collins, V.A. Ravi, F.S. Gascoin, S.M. Haile, G.J. Snyder, *Chem. Mater.* 19 (2007) 763-767.
[137] X. Zhao, X. Ji, Y. Zhang, B. Lu, *J. Alloys Compd.* 368 (2004) 349-352.
[138] Y. Zhang, T. Zhu, J. Tu, X. Zhao, *Mater. Chem. Phys.* 103 (2007) 484-488.
[139] X. Ji, B. Zhang, Z. Su, T. Holgate, J. He, T.M. Tritt, *Phys. Status Solidi A* 206 (2009) 221-228.
[140] B. Zhang, J. He, X. Ji, T.M. Tritt, A. Kumbhar, *Appl. Phys. Lett.* 89 (2006) 163114-163114.
[141] P. Alboni, X. Ji, J. He, N. Gothard, T.M. Tritt, *Appl. Phys. Lett.* 103 (2008) 113707.
[142] X. Ji, J. He, Z. Su, N. Gothard, T.M. Tritt, *J. Appl. Phys.* 104 (2008) 034907.

[143] X. Ji, J. He, P. Alboni, Z. Su, N. Gothard, B. Zhang, T.M. Tritt, J. Kolis, *Physica Stat. Sol. A* 1 (2007) 229-231.
[144] P. Alboni, X. Ji, J. He, N. Gothard, T.M. Tritt, *J.Appl.Phys* 103 (2008) 113707.
[145] L. Kumari, W. Li, J.Y. Huang, P.P. Provencio, *J. Phys. Chem. C* 114 (2010) 9573-9579.
[146] C. Li, J. Hu, Q. Peng, X. Wang, *Mater. Chem. Phys.* 110 (2008) 106-109.
[147] G.S. Nolas, G.A. Slack, S.B. Schujman, *Semicond. Semimet.* 69 (2001) 255-300.
[148] J. Xu, H. Kleinke, *J. Comput. Chem.* 29 (2008) 2134-2143.
[149] S. Gorsse, P. Bauer Pereira, R. Decourt, E. Sellier, *Chem. Mater.* 22 (2009) 988-993.
[150] S. Gorsse, P. Bellanger, Y. Brechet, E. Sellier, A. Umarji, U. Ail, R. Decourt, *Acta Mater.* 59 (2011) 7425-7437.
[151] V. Kulbachinskii, V. Kytin, V. Blank, S. Buga, M.Y. Popov, *Semiconductors* 45 (2011) 1194-1198.
[152] N. Gothard, J. Spowart, T.M. Tritt, *Phys. Stat. Sol. A,* 207 (2010) 157-162.
[153] X. Shi, L. Chen, J. Yang, G. Meisner, *Appl. Phys. Lett.* 84 (2004) 2301-2303.
[154] N. Gothard, T. Tritt, J. Spowart, *J.Appl.Phys* 110 (2011) 023706.
[155] X. Shi, L. Chen, S. Bai, X. Huang, X. Zhao, Q. Yao, C. Uher, *J. Appl. Phys.* 102 (2007) 103709.
[156] S.V. Faleev, F. Léonard, *Phys. Rev. B: Condens. Matter* 77 (2008) 214304.
[157] J.F. Li, W.S. Liu, L.D. Zhao, M. Zhou, *NPG Asia Mater,* 2 (2010) 152-158.
[158] K. Nielsch, J. Bachmann, J. Kimling, H. Böttner, *Adv. Energy Mater.* 1 (2011) 713-731.
[159] A. Soni, Y. Shen, M. Yin, Y. Zhao, L. Yu, X. Hu, Z. Dong, K.A. Khor, M.S. Dresselhaus, Q. Xiong, *Nano Lett.* 12 (2012) 4305-4310.
[160] S.R. Elliott, *The Physics and Chemistry of Solids*. John Wiley & Sons Ltd, 1998.
[161] C.N.R. Rao, A. Müller, A.K. Cheetham, *The chemistry of nanomaterials: synthesis, properties and applications*. John Wiley & Sons, 2006.
[162] L. Manna, D.J. Milliron, A. Meisel, E.C. Scher, A.P. Alivisatos, *Nat. Mater.* 2 (2003) 382-385.
[163] K. Byrappa, M. Yoshimura, *Handbook of hydrothermal technology*. William Andrew, 2012.
[164] D.K. Smith, *Powder Diffr.* 16 (2001) 186-191.
[165] C. Suryanarayana, M.G. Norton, *X-ray diffraction: a practical approach*. Springer Science & Business Media, 2013.
[166] L. Hong, C. Bansal, B. Fultz, *Nanostruct. Mater.* 4 (1994) 949-956.
[167] D.R. Black, D. Windover, A. Henins, D. Gil, J. Filliben, J.P. Cline, *Adv. X-Ray Anal.* 53 (2009) 172-179.
[168] P. Scherrer, *Phys* 2 (1918) 98-100.
[169] G. Williamson, W. Hall, *Acta Metall.* 1 (1953) 22-31.
[170] S. Torquato, *Int. J. Solids Struct.* 37 (2000) 411-422.
[171] D. Liu, W. Tuan, *Acta Mater.* 44 (1996) 813-818.
[172] R.D. Schmidt, E.D. Case, Z. Lobo, T.R. Thompson, J.S. Sakamoto, X.-Y. Zhou, C. Uher, *J. Mater. Res.* 49 (2014) 7192-7212.
[173] H. Muta, K. Kurosaki, S. Yamanaka, *J. Alloys Compd.* 350 (2003) 292-295.
[174] C.C. Koch, *Nanostructured materials: processing, properties and applications*. William Andrew, 2006.
[175] M. Tokita, Proceeding of NEDO International Symposium on Functionally Graded Materials, Japan, 1999, pp. 22.
[176] W. Parker, R. Jenkins, C. Butler, G. Abbott, *J. Appl. Phys.* 32 (1961) 1679-1684.
[177] R.D. Cowan, *J. Appl. Phys.* 34 (1963) 926-927.
[178] T. Azumi, Y. Takahashi, *Rev. Sci. Instrum.* 52 (1981) 1411-1413.

[179] L. Clark III, R. Taylor, *J. Appl. Phys.* 46 (1975) 714-719.
[180] S. Gregg, K. Sing, *Adsorption, Surface Area and Porosity*. Academic Press, Inc., New York, 1982.
[181] E.P. Barrett, L.G. Joyner, P.P. Halenda, *J. Am. Chem. Soc.* 73 (1951) 373-380.
[182] A. Jorio, M.A. Pimenta, A.G. Souza Filho, R. Saito, G. Dresselhaus, M.S. Dresselhaus, *New J. Phys.* 5 (2003) 139.
[183] J.H. Lehman, M. Terrones, E. Mansfield, K.E. Hurst, V. Meunier, *Carbon* 49 (2011) 2581-2602.
[184] H. Zhang, J. He, B. Zhang, Z. Su, T.M. Tritt, N. Soheilnia, H. Kleinke, *J. Electron. Mater.* 36 (2007) 727-731.
[185] N. Kang, L. Lu, W.J. Kong, J.S. Hu, W. Yi, Y.P. Wang, D.L. Zhang, Z.W. Pan, S.S. Xie, *Phys. Rev. B* 67 (2003) 033404/1-4.
[186] Y. Gelbstein, *J. Appl. Phys.* 105 (2009) 023713/1-5.
[187] K.T. Kim, S.Y. Choi, E.H. Shin, K.S. Moon, H.Y. Koo, G.-G. Lee, G.H. Ha, *Carbon* 52 (2013) 541-549.
[188] N. Nandihalli, A. Lahwal, D. Thompson, T.C. Holgate, T.M. Tritt, V. Dassylva-Raymond, L.I. Kiss, E. Sellier, S. Gorsse, H. Kleinke, *J. Solid State Chem.* 203 (2013) 25-30.
[189] D.W. Liu, J.F. Li, C. Chen, B.P. Zhang, *J. Electron. Mater.* 40 (2011) 992-998.
[190] C.B. Murray, C. Kagan, M. Bawendi, *Annu. Rev. Mater. Sci.* 30 (2000) 545-610.
[191] C. Stiewe, Z. He, D. Platzek, G. Karpinski, E. Müller, S. Li, M. Toprak, M. Muhammed, *Materialwiss. Werkstofftech.* 38 (2007) 773-776.
[192] H. Muta, K. Kurosaki, S. Yamanaka, *J. Alloys Compd.* 350 (2003) 292-295.
[193] L. Yang, J. Wu, L. Zhang, *J. Alloys Compd.* 364 (2004) 83-88.
[194] M. Omori, *Mater. Sci. Eng., A* 287 (2000) 183-188.
[195] J. Adachi, K. Kurosaki, M. Uno, S. Yamanaka, *J. Alloys Compd.* 432 (2007) 7-10.
[196] J. Martin, G. Nolas, W. Zhang, L. Chen, *Appl. Phys. Lett.* 90 (2007) 222112.
[197] X. Fan, J. Yang, Z. Xie, K. Li, W. Zhu, X. Duan, C. Xiao, Q. Zhang, *J. Phys. D: Appl. Phys.* 40 (2007) 5975.
[198] F. Gascoin, J. Rasmussen, G.J. Snyder, *J. Alloys Compd.* 427 (2007) 324-329.
[199] R.D. Barnard, *Thermoelectricity in Metals and Alloys*. Taylor and Francis LTD, London, UK, 1972.
[200] T. Itoh, K. Ishikawa, A. Okada, *J. Mater. Res.* 22 (2007) 249-253.
[201] N. Scoville, C. Bajgar, J. Rolfe, J.-P. Fleurial, J. Vandersande, *Nanostruct. Mater.* 5 (1995) 207-223.
[202] F. Brochin, B. Lenoir, X. Devaux, R. Martin-Lopez, H. Scherrer, *J. Appl. Phys.* 88 (2000) 3269-3275.
[203] C. Candolfi, B. Lenoir, A. Dauscher, E. Guilmeau, J. Hejtmanek, J. Tobola, B. Wiendlocha, S. Kaprzyk, *Phys. Rev. B: Condens. Matter* 79 (2009) 035114.
[204] Z. He, C. Stiewe, D. Platzek, G. Karpinski, E. Muller, S. Li, M. Toprak, M. Muhammed, *J. Appl. Phys.* 101 (2007) 043707-043707-7.
[205] D. Stauffer, A. Aharony, *Introduction to percolation theory*. CRC press, 1994.
[206] C.W. Nan, *Prog. Mater Sci.* 37 (1993) 1-116.
[207] C.W. Nan, Y. Shen, J. Ma, *Annual Review of Materials Research* 40 (2010) 131-151.
[208] A. Skal, B. Shklovskii, *SOVIET PHYSICS SEMICONDUCTORS-USSR* 8 (1975) 1029-1032.
[209] W. Evans, R. Prasher, J. Fish, P. Meakin, P. Phelan, P. Keblinski, *Int. J. Heat Mass Transfer* 51 (2008) 1431-1438.
[210] R. Kusy, *J. Appl. Phys.* 48 (1977) 5301-5305.

[211] S. Bhattacharya, A. Chaklader, *Polym.-Plas. Technol. Eng.* 19 (1982) 21-36.
[212] Y.P. Mamunya, V. Davydenko, P. Pissis, E. Lebedev, *Eur. Polym. J.* 38 (2002) 1887-1897.
[213] A. Moisala, Q. Li, I. Kinloch, A. Windle, *Compos. Sci. Technol.* 66 (2006) 1285-1288.
[214] N. Shenogina, S. Shenogin, L. Xue, P. Keblinski, *Appl. Phys. Lett.* 87 (2005) 133106.
[215] P.M. Ajayan, J.M. Tour, *Nature* 447 (2007) 1066-1068.
[216] C. Yu, Y.S. Kim, D. Kim, J.C. Grunlan, *Nano Lett.* 8 (2008) 4428-4432.
[217] C. Bounioux, P. Díaz-Chao, M. Campoy-Quiles, M.S. Martín-González, A.R. Goñi, R. Yerushalmi-Rozen, C. Müller, *Energy Environ. Sci.* 6 (2013) 918-925.
[218] J.P. Heremans, C.M. Thrush, D.T. Morelli, *J. Appl. Phys.* 98 (2005) 063703.
[219] H.-H. Xie, C. Yu, T.-J. Zhu, C.-G. Fu, G.J. Snyder, X.-B. Zhao, *Appl. Phys. Lett.* 100 (2012) 254104.
[220] I.I. Ravich, *Semiconducting lead chalcogenides*. Springer Science & Business Media, 2013.
[221] J.R. Sootsman, H. Kong, C. Uher, J.J. D'Angelo, C.I. Wu, T.P. Hogan, T. Caillat, M.G. Kanatzidis, *Angew. Chem. Int. Ed.* 120 (2008) 8746-8750.
[222] S. Sumithra, N.J. Takas, D.K. Misra, W.M. Nolting, P. Poudeu, K.L. Stokes, *Adv. Energy Mater.* 1 (2011) 1141-1147.
[223] K.-H. Lee, H.-S. Kim, S.-I. Kim, E.-S. Lee, S.-M. Lee, J.-S. Rhyee, J.-Y. Jung, I.-H. Kim, Y. Wang, K. Koumoto, *J. Electron. Mater.* 41 (2012) 1165-1169.
[224] C. Candolfi, B. Lenoir, A. Dauscher, J. Hejtmanek, J. Tobola, *Phys. Rev. B: Condens. Matter* 79 (2009) 235108.
[225] N.F. Mott, H. Jones, *The Theory of the Properties of Metals and Alloys*. Dover Publications, New York, NY, 1958.
[226] C. Kang, H. Kim, S.G. Park, W. Kim, *Appl. Phys. Lett.* 96 (2010) 213114.
[227] W. Kim, J. Zide, A. Gossard, D. Klenov, S. Stemmer, A. Shakouri, A. Majumdar, *Phys. Rev. Lett.* 96 (2006) 045901.
[228] X. Zhou, G. Wang, L. Zhang, H. Chi, X. Su, J. Sakamoto, C. Uher, *J. Mater. Chem.* 22 (2012) 2958-2964.
[229] X. Yan, G. Joshi, W. Liu, Y. Lan, H. Wang, S. Lee, J. Simonson, S. Poon, T. Tritt, G. Chen, *Nano Lett.* 11 (2010) 556-560.
[230] C. Candolfi, B. Lenoir, C. Chubilleau, A. Dauscher, E. Guilmeau, *J. Phys. Condens. Matter* 22 (2010) 025801.
[231] N. Nandihalli, Q. Guo, S. Gorsse, A.U. Khan, T. Mori, H. Kleinke, *Eur. J. Inorg. Chem.* 2016 (2016) 853-860.
[232] C. Candolfi, B. Lenoir, C. Chubilleau, A. Dauscher, E. Guilmeau, *J. Phys.: Condens. Matter* 22 (2010) 025801.
[233] R.M. Levy, *Principles of solid state physics*. Academic Press Inc., New York, New York, 1968.
[234] D. Bansal, C.W. Li, A.H. Said, D.L. Abernathy, J. Yan, O. Delaire, *Phys. Rev. B: Condens. Matter* 92 (2015) 214301.
[235] C. Candolfi, B. Lenoir, A. Dauscher, M. Koza, M. De Boissieu, M. Sternik, K. Parlinski, *Phys. Rev. B: Condens. Matter* 84 (2011) 224306.
[236] G. Grimvall, *The electron-phonon interaction in metals*. North-Holland Amsterdam, 1981.
[237] J. Callaway, H.C. von Baeyer, *Phys. Rev.* 120 (1960) 1149.
[238] A. Matthiessen, *Ann. Physik* 2 (1864) 19.
[239] P. Klemens, F. Seitz, D. Turnbull, *Solid state physics*. Academic Press, New York, 1958.
[240] M. Singh, *Phys. Rev. B: Condens. Matter* 23 (1981) 2983.
[241] M. Singh, Ph. D thesis, Banaras Hindu University, Varanasi, India, 1974.

[242] J.M. Ziman, *Electrons and phonons: the theory of transport phenomena in solids*. Oxford University Press, 1960.
[243] J. He, S.N. Girard, M.G. Kanatzidis, V.P. Dravid, *Adv. Funct. Mater.* 20 (2010) 764-772.
[244] O. Delaire, A.F. May, M.A. McGuire, W.D. Porter, M.S. Lucas, M.B. Stone, D.L. Abernathy, V. Ravi, S. Firdosy, G. Snyder, *Phys. Rev. B: Condens. Matter* 80 (2009) 184302.
[245] M. Singh, G. Verma, *Phys. Rev. B: Condens. Matter* 7 (1973) 2626.
[246] M. Singh, *Phys. Rev. B: Condens. Matter* 18 (1978) 2950.
[247] H. Albany, G. Laurence, *Solid State Commun.* 7 (1969) 63-66.
[248] K. Suzuki, N. Mikoshiba, *J. Phys. Soc. Jpn.* 31 (1971) 186-189.
[249] B.L. Bird, N. Pearlman, *Phys. Rev. B: Condens. Matter* 4 (1971) 4406.
[250] J. Yang, D. Morelli, G. Meisner, W. Chen, J. Dyck, C. Uher, *Phys. Rev. B: Condens. Matter* 65 (2002) 094115.
[251] H. Anno, K. Matsubara, Y. Notohara, T. Sakakibara, H. Tashiro, *J. Appl. Phys.* 86 (1999) 3780-3786.
[252] A. Poujade, H. Albany, *Phys. Rev.* 182 (1969) 802.
[253] D. Morelli, J. Heremans, G. Slack, *Phys. Rev. B: Condens. Matter* 66 (2002) 195304.
[254] G.A. Slack, S. Galginaitis, *Phys. Rev.* 133 (1964) A253.
[255] O.L. Anderson, *J. Phys. Chem. Solids* 24 (1963) 909-917.
[256] Y. Zhu, J. Lian, Q. Jiang, *J. Phys. Chem. C* 113 (2009) 16896-16900.
[257] S. Abrahams, F. Hsu, *J. Chem. Phys.* 63 (1975) 1162-1165.
[258] D.B. Sirdeshmukh, L. Sirdeshmukh, K. Subhadra, *Micro-and Macro-properties of Solids*. Springer, 2006.
[259] Y. Zhang, X. Ke, C. Chen, J. Yang, P. Kent, *Phys. Rev. B: Condens. Matter* 80 (2009) 024304.
[260] R.J. Stevens, L.V. Zhigilei, P.M. Norris, *Int. J. Heat Mass Transfer* 50 (2007) 3977-3989.
[261] D. Kechrakos, *J. Phys.: Condens. Matter* 3 (1991) 1443.
[262] R. Prasher, *Appl. Phys. Lett.* 94 (2009) 1905.
[263] D. Young, H. Maris, *Phys. Rev. B: Condens. Matter* 40 (1989) 3685.
[264] C. Caroli, R. Combescot, P. Nozieres, D. Saint-James, *J. Phys. C: Solid State Phys.* 4 (1971) 916.
[265] A. Majumdar, P. Reddy, *Appl. Phys. Lett.* 84 (2004) 4768-4770.
[266] M. Huberman, A. Overhauser, *Phys. Rev. B: Condens. Matter* 50 (1994) 2865.
[267] M. Battabyal, O. Beffort, S. Kleiner, S. Vaucher, L. Rohr, *Diamond Relat. Mater.* 17 (2008) 1438-1442.
[268] M. Kida, L. Weber, C. Monachon, A. Mortensen, *J. Appl. Phys.* 109 (2011) 064907.
[269] R.J. Stevens, A.N. Smith, P.M. Norris, *J. Heat Transfer* 127 (2005) 315-322.
[270] R. Stoner, H. Maris, *Phys. Rev. B: Condens. Matter* 48 (1993) 16373.
[271] I. Khalatnikov, *Zhurnal Eksperimentalnoi I Teoreticheskoi Fiziki* 22 (1952) 687-704.
[272] I.M. Khalatnikov, P.C. Hohenberg, *An introduction to the theory of superfluidity*. WA Benjamin New York, 1965.
[273] G. Chen, *Phys. Rev. B: Condens. Matter* 57 (1998) 14958.
[274] C. Dames, G. Chen, *J. Appl. Phys.* 95 (2004) 682-693.
[275] J. Androulakis, K. Hsu, R. Pcionek, H. Kong, C. Uher, J. D'Angelo, A. Downey, T. Hogan, M. Kanatzidis, *Adv. Mater.* 18 (2006) 1170-1173.
[276] J. Zou, D. Kotchetkov, A. Balandin, D. Florescu, F.H. Pollak, *J. Appl. Phys.* 92 (2002) 2534-2539.
[277] C.R. Whitsett, D.A. Nelson, *Phys. Rev. B: Condens. Matter* 5 (1972) 3125.

[278] C. Crosby, C. Grenier, *Phys. Rev. B: Condens. Matter* 4 (1971) 1258.
[279] M. Biercuk, M.C. Llaguno, M. Radosavljevic, J. Hyun, A.T. Johnson, J.E. Fischer, *Appl. Phys. Lett.* 80 (2002) 2767-2769.
[280] S. Katsuyama, M. Watanabe, M. Kuroki, T. Maehata, M. Ito, *J. Appl. Phys.* 93 (2003) 2758-2764.
[281] G. Li, K. Gadelrab, T. Souier, P.L. Potapov, G. Chen, M. Chiesa, *Nanotechnology* 23 (2012) 065703.
[282] R.W. Rice, *Mechanical properties of ceramics and composites: grain and particle effects*. CRC Press, 2000.
[283] S.L. Shindé, J. Goela, *High thermal conductivity materials*. Springer, 2006.
[284] X. Ji, J. He, P. Alboni, Z. Su, N. Gothard, B. Zhang, T.M. Tritt, J. Kolis, *physica status solidi (RRL)-Rapid Research Letters* 1 (2007) 229-231.
[285] K. Nanda, A. Maisels, F. Kruis, H. Fissan, S. Stappert, *Phys. Rev. Lett.* 91 (2003) 106102.
[286] S. Lowell, J.E. Shields, M.A. Thomas, M. Thommes, *Characterization of porous solids and powders: surface area, pore size and density*. Springer Science & Business Media, 2012.
[287] G. Leofanti, M. Padovan, G. Tozzola, B. Venturelli, *Catal. Today* 41 (1998) 207-219.
[288] X. Tong, T. Okano, T. Iseki, T. Yano, *J. Mater. Res.* 30 (1995) 3087-3090.
[289] W.C. Oliver, G.M. Pharr, *J. Mater. Res.* 7 (1992) 1564-1583.
[290] P. Crocombette, L. Gelebart, *J. Appl. Phys.* 106 (2009) 083520.
[291] C. Kohler, *physica status solidi (b)* 234 (2002) 522-540.
[292] R. Lipton, B. Vernescu, Proc. R. Soc. London, Ser. A, The Royal Society, 1996, pp. 329-358.
[293] J. Ordonez-Miranda, R. Yang, J.J. Alvarado-Gil, *Appl. Phys. Lett.* 98 (2011) 233111.
[294] A. Minnich, G. Chen, *J. Appl. Phys.* 91 (2007) 073105.
[295] M.L. Dunn, M. Taya, *J. Appl. Phys.* 73 (1993) 1711-1722.
[296] H. Hatta, M. Taya, *J. Appl. Phys.* 58 (1985) 2478-2486.
[297] D.S. Smith, S. Fayette, S. Grandjean, C. Martin, R. Telle, T. Tonnessen, *J. Am. Ceram. Soc.* 86 (2003) 105-111.
[298] R. Von Dreele, J. Jorgensen, C. Windsor, *J. Appl. Crystallogr.* 15 (1982) 581-589.
[299] L.C. Larson, Von Dreele, R.B, *LANSCE, MSH805, Los Alamos National Laboratory, NM 87545, USA, 1995*.
[300] A.C. Larson, R.B. Von Dreele, *Los Alamos National Laboratory, NM, 2000*.
[301] B.H. Toby, *J. Appl. Crystallogr.* 34 (2001) 210-213.
[302] C. Candolfi, B. Lenoir, A. Dauscher, J. Tobola, S.J. Clarke, R.I. Smith, *Chem. Mater.* 20 (2008) 6556-6561.
[303] G.D. Mahan, J.O. Sofo, *Proc. Natl. Acad. Sci. USA* 93 (1996) 7436-7439.
[304] A. Rao, X. Ji, T.M. Tritt, *Mat. Res. Bull.* 31 (2006) 218-223.
[305] S.R. Brown, S.M. Kauzlarich, F. Gascoin, G.J. Snyder, *Chem. Mater.* 18 (2006) 1873-1877.
[306] C.A. Cox, E.S. Toberer, A.A. Levchenko, S.R. Brown, G.J. Snyder, A. Navrotsky, S.M. Kauzlarich, *Chem. Mater.* 21 (2009) 1354-1360.
[307] R. Franz, G. Wiedemann, *Ann. Phys.* 165 (1853) 497-531.
[308] G. Kumar, G. Prasad, R. Pohl, *J. Mater. Sci.* 28 (1993) 4261-4272.
[309] H. Wang, W.D. Porter, H. Böttner, J. König, L. Chen, S. Bai, T.M. Tritt, A. Mayolet, J. Senawiratne, C. Smith, *J. Electron. Mater.* 42 (2013) 654-664.
[310] H. Wang, W.D. Porter, H. Böttner, J. König, L. Chen, S. Bai, T.M. Tritt, A. Mayolet, J. Senawiratne, C. Smith, *J. Electron. Mater.* 42 (2013) 1073-1084.

[311] Y. Lin, K.A. Watson, M.J. Fallbach, S. Ghose, J.G. Smith Jr, D.M. Delozier, W. Cao, R.E. Crooks, J.W. Connell, *ACS Nano* 3 (2009) 871-884.